LAPLACE TRANSFORM ANALYTIC ELEMENT METHOD FOR TRANSIENT GROUNDWATER FLOW

by
Kristopher L. Kuhlman

A Dissertation Submitted to the Faculty of the

DEPARTMENT OF
HYDROLOGY & WATER RESOURCES

In Partial Fulfillment of the Requirements
For the Degree of

DOCTOR OF PHILOSOPHY
WITH A MAJOR IN HYDROLOGY

In the Graduate College

THE UNIVERSITY OF ARIZONA

2008

THE UNIVERSITY OF ARIZONA
GRADUATE COLLEGE

As members of the Dissertation Committee, we certify that we have read the dissertation prepared by Kristopher L. Kuhlman entitled "Laplace transform analytic element method for transient groundwater flow simulation" and recommend that it be accepted as fulfilling the dissertation requirement for the Degree of Doctor of Philosophy

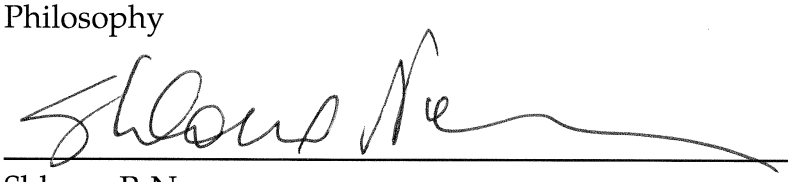

Date: April 24, 2008

Shlomo P. Neuman

Date: April 24, 2008

Arthur W. Warrick

Date: April 24, 2008

Paul A. Hsieh

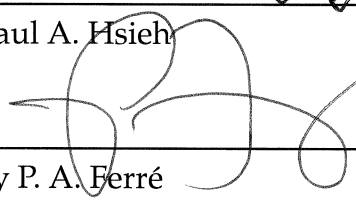

Date: April 24, 2008

Ty P. A. Ferré

Date: April 24, 2008

Barry D. Ganapol

Date: April 24, 2008

Cholik Chan

Final approval and acceptance of this dissertation is contingent upon the candidate's submission of the final copies of the dissertation to the Graduate College.

I hereby certify that I have read this dissertation prepared under my direction and recommend that it be accepted as fulfilling the dissertation requirement.

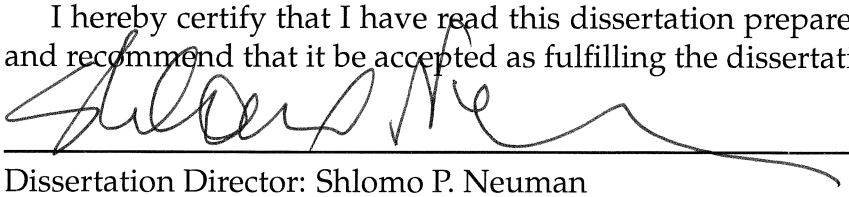

Date: April 24, 2008

Dissertation Director: Shlomo P. Neuman

STATEMENT BY AUTHOR

This dissertation has been submitted in partial fulfillment of requirements for an advanced degree at The University of Arizona and is deposited in the University Library to be made available to borrowers under rules of the Library.

Brief quotations from this dissertation are allowable without special permission, provided that accurate acknowledgment of source is made. Requests for permission for extended quotation from or reproduction of this manuscript in whole or in part may be granted by the head of the major department or the Dean of the Graduate College when in his or her judgment the proposed use of the material is in the interests of scholarship. In all other instances, however, permission must be obtained from the author.

SIGNED: Kristopher L. Kuhlman

ACKNOWLEDGMENTS

This research was supported by the United States Geological Survey National Institutes for Water Resources Grant Program (award 200AZ68G) and by the C.W. & Modene Neely fellowship through the National Water Research Institute, in Fountain Valley, California.

I thank my advisor, Shlomo Neuman, who conceptualized the LT-AEM, for being my mentor and teacher these last six years. He has both inspired and challenged me to do things I would not have otherwise imagined possible. I thank Alex Furman, who made the idea of the LT-AEM happen, for setting me in the right direction at the beginning. Art Warrick proposed the idea behind the work in Appendix F after my oral comprehensive exam. Ty Ferré has given me a glimpse into the world of teaching, which I hope to pursue in my career. Each of my major and minor committee members have both directly and indirectly given me advice and insight into problems and ideas I have encountered in graduate school. I feel fortunate to interact with such a group of people, whom I consider to be my advisors.

I thank my current and past colleagues in the department, including Bwalya Malama, Junfeng Zhu, Andreas Englert, Andrew Hinnell, Raghu Suribhatla, and Liang Xue, for many interesting discussions and projects over the years.

I would not have applied to the HWR graduate program, were it not for the help and encouragement of my boss, Dennis Williams, and various co-workers at Geoscience Support Services, in Los Angeles. I worked there as a consultant for nearly four years, where they fostered my interest in groundwater-related things. This practical experience has been the foundation for everything I have learned in graduate school.

Obviously, my ability to have done any of this comes from my supportive family. My wife, Sarah, and mother-in-law, Sue, have selflessly proof-read drafts, papers, abstracts, and applications for me. My Mother and Father set me in the right direction, supported me along the way, and basically made me who I am; they were the first teachers I ever had. My Father would be the proudest of what I am accomplishing here.

To my dad.

Table of Contents

TABLE OF CONTENTS—*Continued*

TABLE OF CONTENTS—*Continued*

TABLE OF CONTENTS—*Continued*

LIST OF FIGURES

LIST OF FIGURES—*Continued*

LIST OF FIGURES—*Continued*

LIST OF FIGURES—*Continued*

LIST OF TABLES

ABSTRACT

The Laplace transform analytic element method (LT-AEM), applies the traditionally steady-state analytic element method (AEM) to the Laplace-transformed diffusion equation (Furman and Neuman, 2003). This strategy preserves the accuracy and elegance of the AEM while extending the method to transient phenomena. The approach taken here utilizes eigenfunction expansion to derive analytic solutions to the modified Helmholtz equation, then back-transforms the LT-AEM results with a numerical inverse Laplace transform algorithm. The two-dimensional elements derived here include the point, circle, line segment, ellipse, and infinite line, corresponding to polar, elliptical and Cartesian coordinates. Each element is derived for the simplest useful case, an impulse response due to a confined, transient, single-aquifer source. The extension of these elements to include effects due to leaky, unconfined, multi-aquifer, wellbore storage, and inertia is shown for a few simple elements (point and line), with ready extension to other elements. General temporal behavior is achieved using convolution between these impulse and general time functions; convolution allows the spatial and temporal components of an element to be handled independently.

Comparisons are made between inverse Laplace transform algorithms; the accelerated Fourier series approach of de Hoog et al. (1982) is found to be the most appropriate for LT-AEM applications. An aquifer test application and synthetic examples are shown for several illustrative forward and parameter estimation simulations to illustrate LT-AEM capabilities. Extension of LT-AEM to three-dimensional flow and non-linear infiltration are discussed.

Chapter 1
BACKGROUND

1.1 Motivation

Water is imperative to life. In places where surface water is ephemeral or contaminated, water supply either comes from groundwater or must be imported. The majority of the Earth's non-frozen fresh water is groundwater. To understand and predict the movement of groundwater in the subsurface we rely on sparse measurements of head and aquifer properties (wells are expensive and geophysics is only indirectly related to the hydrologic problem), interpreted and extrapolated using groundwater flow simulations.

Models are simplified representations of reality. Hydrologists utilize conceptual models (e.g. Bear, 1988, §4.5.1), analytic models (e.g. Bruggeman, 1999), numerical models (e.g. Bear and Verruijt, 1987), and even physical-analog models (e.g. Bear and Zaslavsky, 1968, §12). In reality, subsurface geology and hydrology are heterogeneous, complex, and difficult to characterize (e.g. Neuman and Di Federico, 2003); we accept that our models will not capture every detail of reality. For well-understood physical processes (e.g., porous media flow, heat conduction, neutron diffusion, or elastic waves), we simulate an equation which is believed to adequately describe observed behavior as a proxy for the actual physical process. There are a few fundamental equations of mathematical physics which have been studied extensively because they appear repeatedly (Laplace, diffusion, and advection-dispersion equations). When a process is identified as being governed by one of these equations, we can immediately adopt a large body of previously-derived analytic results and numerical methods.

While it is always necessary to eventually justify equations and solutions with

observations, that is not being done here. We are focused on solving the governing equations. Solving a diffusion problem produces a solution useful to hydrologists or any field where diffusion is believed to describe the problem.

1.2 AEM introduction

The analytic element method (AEM) provides semi-analytic solutions to linear porous media flow problems, through superposition of fundamental solutions (elements) that represent physical entities in the hydraulic system. AEM has largely been developed by Strack and his colleagues since the early 1980s; a historical summary of AEM publications and contributors is recounted by Kraemer (2007). The first AEM application was a steady 2D system, with an infinitesimally-thick clay layer between two aquifers (Strack and Haitjema, 1981a,b). Inhomogeneous aquifer properties or area source terms were handled using polygons of line doublets and dipoles, which created the jump in discharge potential (due to change in aquifer properties) or stream-function required in the solution. The fundamental elements in this approach were derived using line and area integrals of the 2D Green's function for Laplace's equation ($-\ln r$), over the desired curve or area (Strack, 1989). This early AEM approach came out of Strack's work with the boundary element method (BEM) (Strack and Haitjema, 1981a); it is very similar to BEM in both philosophy and implementation.

Most AEM applications have been concerned with two-dimensional steady groundwater flow (Laplace and Poisson equations), but AEM has been extended to 3D (e.g. Fitts, 1989, 1991), transient (discussed in next section), multi-aquifer (e.g. Bakker and Strack, 2003; Bakker, 2006), electrical geophysical (Furman et al., 2002), and linearized unsaturated (e.g. Warrick and Knight, 2002; Furman and Warrick, 2005) flow problems. Strack (1989; 1999; 2003) and Haitjema (1995) cover the traditional line integral approach in great detail. This technique is not used here, but

it could be applied to derive additional types of LT-AEM elements, following the analogies drawn by Duffin (1971) between Laplace's equation and the LT-AEM governing equation (introduced in §2.1).

The traditional AEM and the Laplace transform AEM (LT-AEM) described here partially fill a gap in available modeling tools between the analytic solutions derived for simple geometries (e.g., radially-symmetric flow to a well (Theis, 1935)) and distributed-parameter gridded models (e.g., finite element (Istok, 1989) or finite difference (McDonald and Harbaugh, 1988) methods). AEM and LT-AEM provide flexibility and computational efficiency, while retaining the accuracy and much of the elegance of an analytic solution.

AEM is not intended as a replacement for gridded models, but there are many situations where AEM and LT-AEM are more appropriate than a finite difference or finite element model. Often, due to lack of detailed information about the subsurface or interest in simplicity, the assumption of homogeneous aquifer properties is adequate. Applications of AEM include the EPA WhAEM2000 software for the federally-mandated wellhead protection program (Kraemer et al., 2007), NAGROM, the Dutch national groundwater model (de Lange, 2006), and numerous smaller cases (Strack, 2003). In AEM models, the complexity of the problem is proportional to the number of physical entities in the domain, rather than the grid spacing. Hunt et al. (1998) and Kelson et al. (2002) demonstrate how AEM can be used during the planning stage to improve complex gridded models. AEM and LT-AEM make good learning tools, because the solution they compute is accurate and efficient. Kraemer (2007) lists 8 steady-state AEM program implementations freely available for use in academic settings.

Dagan et al. (2003), Fiori et al. (2003), and Janković et al. (2003) have investigated the use of steady AEM solutions for simulating flow through a large number of non-intersecting elements to explore topics pertaining to random heterogeneity. Because non-overlapping, non-intersecting convex elements (e.g., circles, spheres,

spheroids) cannot tessellate a domain (there is an interconnected background between the elements), additional theoretical complications arise. They have illustrated that AEM solutions can be used to investigate randomly heterogeneous flow problems.

An active area of research in the AEM community is extension of the method to transient flow problems. AEM is well suited for boundary value problems defined by the Laplace and Poisson equations; extensions to transient flow governed by the diffusion equation, an initial value problem, have taken several directions.

1.2.1 Transient AEM

Haitjema and Strack (1985) were the first to attempt an extension of AEM to transient groundwater flow; their approach was discontinuous in time, using a grid to simulate the effects of transient storage. The space discretization of this approach offset the mesh-free benefit of AEM. Haitjema (1991) approximated transient interface flow (e.g., between fresh and sea water) near a well with explicit time marching between steady-state Poisson solutions, using vortex rings to represent the interface. Zaadnoordijk (1988) and Zaadnoordijk and Strack (1993) took an approach that combined steady and transient elements, using area source elements to approximate transient storage. The method had many restrictions, including that there be no net transient withdrawal from the aquifer, requiring additional non-physical elements to be placed at a large distance to cancel local transient effects. The point and line source elements derived in this approach accounted for both time and space behavior, significantly increasing their complexity. Several of the expressions they derived contained temporal convolution integrals, which were looked up in tables or evaluated numerically. The different combinations of space and time behaviors to be considered, quickly rises to an unmanageable number. Due to these limitations, the approach was neither accurate nor straight-

forward. Zaadnoordijk (1998) also explored the combination of both transient and steady well solutions; he found this lead to complications on both theoretical and implementation levels that were not easily resolved.

Bakker (2004c) used a temporal Fourier transform to modify the governing equation. The Fourier transform allowed him to better apply the AEM, similar to LT-AEM, but without some of the benefits which the Laplace transform brings (see Appendix A for comparison of these transforms). He arrived at essentially the same governing equation used here through a Fourier transform, but he restricted the approach to periodic time behavior (a finite number of sinusoidal harmonics). This, coupled with the assumption of no initial conditions, limited the method's application to oscillatory problems (e.g., seasonal fluctuations caused by a river). Bakker (2004b) proposed using Fejér averaging to smooth oscillations that arose when expanding discontinuous time behaviors. While this approach did smooth the oscillatory behavior, it can be thought of as a re-implementation of a numerical inverse Fourier or Laplace transform algorithm. In general, there exist more efficient and accurate ways to sum potentially divergent Fourier series than Fejér averaging (§D.2).

Most recently, Strack (2006) outlined an approximate AEM approach in which localized transient, leaky, or non-constant material property *local perturbation* elements are superimposed on a constant property, confined, steady background, with transient effects approximated using finite differences. The full details of Strack's latest method have not yet been given, only an abstract of the approach is provided.

Furman and Neuman (2003) first used AEM to solve the Laplace-transformed transient flow problem; the transform converts the initial value problem into a boundary value problem, where the time dependence is expressed through the Laplace parameter. They illustrated the method for point and circular matching elements. LT-AEM back-transforms the Laplace space solution into the time do-

main using a numerical inverse Laplace transform algorithm. In contrast to the Fourier transform approach of Bakker (2004c), the Laplace transform and its numerical inverse removes the restriction of periodic time behavior and allows for the incorporation of initial conditions (Kuhlman and Neuman, 2006).

1.2.2 Laplace-transform based methods

The Laplace transform is a commonly-used tool for developing both analytic and numerical solutions to transient diffusion problems. When it is possible to analytically invert the transformed solution, a closed-form time-domain solution is obtained. Working in the petroleum industry, van Everdingen and Hurst (1949) were the first to methodically use the Laplace transform to find solutions for flow in porous media. Carslaw and Jaeger (1959) utilized the Laplace transform extensively to find analytic solutions for numerous geometries in heat conduction problems.

When analytic inversion of the Laplace-space solution is not possible, or if the solution is too complicated to be of practical use, asymptotic solutions may be useful. Hantush (1960) analytically developed the solution for the modified theory of leaky aquifers in Laplace space, computing numerical results using asymptotic expansions at early and late time. Sternberg (1969) approximated the inverse solution for flow to a well within a circular inhomogeneity by neglecting what he considered to be insignificant terms in the Laplace-space expression, allowing an approximate analytic inversion. Both of these problems now are trivially solvable using LT-AEM (with numerical inversion). Furman and Neuman (2003) showed that the Sternberg's approximations led to an inaccurate solution that produced inconsistent results. We show how the leaky Hantush (1960) solution is easily solved and extended to other sources using LT-AEM (see Chapter 4).

Moench and Ogata numerically inverted analytic Laplace-space solutions for

radial dispersion (1981) and flow to a well under various aquifer conditions (1984) using the Stehfest (1970) algorithm. Hemker and Maas (1987) numerically inverted the transient multi-layer flow problem, comparing results using the numerical inversion algorithms of Schapery (1962) and Stehfest (1970). Numerical approaches were used instead of developing analytic or asymptotic solutions, the same route taken here by the LT-AEM. Many semi-analytic solutions for simple geometries have been developed in the hydrology literature, because of the flexibility gained from utilizing numerical Laplace transform inversions, often in conjunction with other integral transforms (e.g. Tartakovsky and Neuman, 2007; Malama et al., 2007, 2008).

The numerical inverse Laplace transform approach has been used to extend the related BEM to transient diffusion problems (e.g. Liggett and Liu, 1983; Brebbia et al., 1984; Davies and Crann, 2002). For transient groundwater flow Liggett and Liu (1983, §10.1.2) inverted the transient perturbation of a solution from the corresponding steady solution (analogous to the approach taken recently by Strack (2006) in the time domain), an inverse technique introduced by Schapery (1962). Few Laplace-space BEM methods utilize inverse algorithms which require complex values of the Laplace parameter, restricting the number of applicable inverse algorithms, to the methods of Stehfest (1970) and Piessens (1972). Finlayson (1972, p.56) indicates that Laplace transforms have been utilized in solving different types of method of weighted residual solutions, since as early as 1955. In hydrology, the Laplace transform has successfully been used with finite element solutions by Sudicky and McLaren (1992) for simulation of advective-dispersive transport, by Ye et al. (2004) for simulation of stochastic moment-based flow equations, and by Morales-Casique and Neuman (2008) for stochastic moment-based advective-dispersive transport.

1.3 Dissertation overview

In Chapter 2, we introduce the governing equation (§ 2.1) and the fundamental concepts that LT-AEM is based upon, including those of superposition (§ 2.2) and convolution (§ 2.4). Separation of variables and eigenfunction expansion are used to derive elements which satisfy the governing equation (§ 2.3). After deriving the elements and combining them to solve more general problems with superposition and convolution, the desired boundary conditions must be enforced using the AEM process of boundary matching (§ 2.5), which gives enough information to finally solve the coefficient problem (§ 2.6). The head or flux is then calculated in a straightforward manner from the known coefficients (§ 2.7).

Once the supporting concepts are introduced, specific LT-AEM 2D elements are derived for circular (§ 3.1), elliptical (§ 3.2) and Cartesian (§ 3.3) coordinates. Some discussion regarding the extension of the methods to 3D problems is outlined in § 3.4. As an extension of the elements just derived, general methods for deriving distributed source terms are given (§ 4.1). In Chapter 4 several homogeneous source terms of interest to hydrologists are derived, including leaky (§ 4.2.1), multi-layer (§ 4.2.2), unconfined (§ 4.2.3), and damped wave (§ 4.2.4) source terms.

Perhaps the most crucial component to the success of the LT-AEM, the inverse Laplace transform algorithm, is introduced in Chapter 5. Several different algorithms are outlined and compared, including the Post-Widder (§ 5.3.1), Schapery (§ 5.3.2), Fourier series (§ 5.3.3), and Möbius transformation (§ 5.3.4) approaches.

Chapter 6 illustrates two inverse-modeling applications of LT-AEM. One to interpret a two-well unconfined aquifer test near a river using PEST (Doherty, 2007). The second estimates the geometry associated with a synthetic problem using SCEM-UA (Vrugt et al., 2003b).

Several appendices supplement the material presented above. General properties of the Laplace transform are given in Appendix A. The metric coefficients of

the coordinate systems for which elements are derived in Chapter 3 are given in Appendix B, along with example calculations regarding the calculation of the Jacobian (§ B.2), which is required to project a vector quantity (in this case Darcy flux) in one coordinate system onto a vector in another system. We present a discussion on the relationship between LT-AEM and the method of weighted residuals in Appendix C. Details regarding convergence of Fourier series and eigenfunction expansions are given in Appendix D. The Mathieu function used for eigenfunction expansion in elliptical coordinates are discussed in detail in Appendix E, since they are typically unfamiliar.

The last appendix is an application of the eigenfunction expansion approach used here in elliptical coordinates. In this application, we solve non-linear steady-state infiltration into unsaturated soil from an elliptical cavity.

Chapter 2
LT-AEM FOUNDATION

In this chapter the governing equation is derived and the fundamental principles of convolution and superposition are introduced. We introduce the method of eigenfunction expansion, which is used later to derive elements of various geometries. Through examples, boundary matching is developed and we solve for the coefficients using either a direct or iterative approach.

2.1 Governing equation

Transient, confined groundwater flow in an elastic aquifer is governed by the diffusion equation; Jacob (1940) was the first to derive it from physical principles in the hydrology literature. While non-linear porous media flow is associated with variably-saturated conditions (e.g. Warrick, 2003, §6), gas flow (e.g. Millington, 1959), unconfined flow (e.g. Bear, 1988, §8), flow at high Reynolds numbers (e.g. Nield and Bejan, 2006, §1.5), or flow associated with large transient changes (e.g. Vásquez, 2007, §1.2.1), the linear diffusion equation is considered adequate for most confined flow applications. Non-linear problems can often be approximated adequately by linearizing them. Warrick and Knight (2002, 2004), Furman and Warrick (2005), and Appendix F use a set of non-linear transformations to linearize and solve the non-linear steady-state Richards equation. The governing partial differential equation (PDE) used here is

$$bK\nabla^2 h(\mathbf{x},t) + bG(\mathbf{x},t) = bS_s\frac{\partial h(\mathbf{x},t)}{\partial t}, \tag{2.1}$$

where $\mathbf{x}$ is a vector of general spatial coordinates, t is time $[\mathrm{T}]$, b is aquifer thickness $[\mathrm{L}]$, h is hydraulic head $[\mathrm{L}]$, G is a volumetric source term $[1/\mathrm{T}]$, K is hydraulic

conductivity $[\mathrm{L/T}]$, and S_s is specific storage $[1/\mathrm{L}]$. AEM problems are developed in free space, and therefore they tacitly include the requirement that the solution is bounded at infinity. Head, boundary conditions on specified curves, and source terms are generally functions of both time and space, while the aquifer properties are assumed to be constant scalars. More generally, K is isotropic (a tensor), but homogeneous anisotropic regions can be transformed into equivalent isotropic ones (Bear and Dagan, 1965). Representing boundaries and inhomogeneities in anisotropic domains presents additional complications for this type of transformation (Suribhatla, 2007), but the method is feasible for some simple coordinate systems. The transformation will, for example, deform circles into ellipses, as mentioned in section 3.2.4.

Due to the superposition of different geometries in LT-AEM, it is not always possible to simplify the overall problem into dimensionless quantities; fundamental dimensions of key parameters and variables are given in brackets. For two-dimensional problems, unless otherwise stated, a unit aquifer thickness, b, is assumed without loss of generality.

Girinskii (1946) and Strack (1976) established what is now the AEM tradition of working with discharge potential $[\mathrm{L}^2/\mathrm{T}]$, $\Phi = Khb + C$, where C is an arbitrary reference that we conveniently set to zero. Applying the Laplace transform (see Appendix A) to (2.1), written in terms of Φ with $G \equiv 0$, gives

$$\alpha \nabla^2 \bar{\Phi}(\mathbf{x}) = \bar{\Phi}(\mathbf{x}) p - \Phi_0(\mathbf{x}), \tag{2.2}$$

where $\alpha = K/S_s$ is hydraulic diffusivity $[\mathrm{L}^2/\mathrm{T}]$, p is the complex transform parameter $[\mathrm{T}^{-1}]$, $\bar{\Phi}$ is the transformed discharge potential $[\mathrm{L}^2]$, and Φ_0 is the initial value of Φ. Change in head from a zero initial condition is also equated with drawdown (common in aquifer testing). To render (2.2) homogeneous, we set $\Phi_0 = 0$, without loss of generality. Non-zero initial conditions are introduced using impulse area sources (Kuhlman and Neuman, 2006). This yields the homogeneous Yukawa

(Duffin, 1971) or modified Helmholtz equation

$$\nabla^2\bar{\Phi}(\mathbf{x}) - \kappa^2\bar{\Phi}(\mathbf{x}) = 0, \tag{2.3}$$

where $\kappa^2 = p/\alpha$ is analogous to the wave number used in physics (Graff, 1991, §1.1.2); later the definition of κ will be modified, due to the presence of distributed source terms (Chapter 4).

LT-AEM elements can be developed by applying the Laplace transform ($\mathcal{L}$) to a known solution of (2.1), many of which can be found in the heat conduction (e.g. Carslaw and Jaeger, 1959) or diffusion (e.g. Crank, 1975) literature. Equivalently, solutions for (2.3) may be derived directly in Laplace space; the Yukawa or modified Helmholtz equation appears frequently in seismic geophysics (e.g. Ben-Menahem and Singh, 2000), elastics (e.g. Graff, 1991), acoustics (e.g. Morse and Ingard, 1968), and physics (e.g. Duffin, 1971), as the space-dependent portion of the solutions to both the wave and diffusion equations. Equation 2.3 degenerates to the steady-state Laplace equation as $\kappa \to 0$, which corresponds to small Laplace parameter and large time (see Appendix A). Since the final time-domain solution is computed using a numerical inverse Laplace transform ($\mathcal{L}^{-1}$), the elements derived directly in Laplace space are not required to have known analytic inverses (but the inverse must exist); the numerical approach only requires numerical values of the solution.

2.2 Superposition

Spatial superposition is one of the fundamental ideas upon which LT-AEM is built. It is a consequence of the linearity of the boundary condition and governing equation; if the boundary conditions are homogeneous, superposition is simple. Combining non-homogeneous differential equations (DE) and boundary conditions is possible using superposition, but it requires keeping track of the net inhomoge-

neous terms, so their sum still satisfies the DE and/or boundary condition (i.e., boundary matching).

If $u_1(\mathbf{x})$ and $u_2(\mathbf{x})$ are two solutions of a homogeneous linear DE, then $c_1 u_1(\mathbf{x}) + c_2 u_2(\mathbf{x})$, where c_1 and c_2 are arbitrary constants, is also a solution (Courant and Hilbert, 1962, §5.1). More generally, any number of homogeneous solutions, $u_1(\mathbf{x})$, $u_2(\mathbf{x}), \ldots$ with constants $c_1, c_2, \ldots$ can be combined into a convergent series

$$v(\mathbf{x}) = \sum_{n=1}^{\infty} c_n u_n(\mathbf{x}), \tag{2.4}$$

where $v(\mathbf{x})$ is then also a solution to the same DE with the same homogeneous boundary conditions. This concept is used in eigenfunction expansion to build up solutions for general problems from individual harmonics. For the standard Sturm-Liouville problem (homogeneous boundary conditions specified at the ends of a finite interval), $u_n(\mathbf{x})$ is an eigenfunction and the integer sum index correspond to the eigenvalues (the eigenvalues can be mapped onto the integers). If the homogeneous solution $u(\mathbf{x}, \beta)$ instead depends on the continuous parameter β, new solutions can be composed using the more general form

$$v(\mathbf{x}) = \int c(\beta) u(\mathbf{x}, \beta)\, \mathrm{d}\beta. \tag{2.5}$$

The integral form of superposition is used in Sturm-Liouville problems over infinite intervals, where integer eigenvalues are insufficient to resolve an arbitrary condition. In LT-AEM the integral superposition case is not carried out explicitly; the integral is approximated numerically by a sum (i.e., only (2.4) is actually implemented).

2.3 Element derivation using eigenfunction expansion

The method of eigenfunction expansion is used to derive LT-AEM elements in Laplace space that are solutions to (2.3), following the general approach of Furman

and Neuman (2003); see Appendix D for convergence properties and theoretical implications of this approach. The eigenfunction expansion (EE) approach produces analytic solutions that can represent an arbitrary boundary condition along certain non-intersecting constant coordinate curves. The governing Laplace-space partial differential equation (PDE) involves 2 or 3 independent variables (depending on the dimension, D). EE leads to an exact solution to the PDE in certain coordinate systems, comprised of the tensor product of the solutions to the component ordinary differential equations (ODE) (Gustafson, 1999, §2.9.1), found through separation of variables. This is represented as

$$\bar{\Phi}^k(\mathbf{x}) = \prod_{i=1}^{D} \bar{\Phi}^k(x_i), \tag{2.6}$$

where $\bar{\Phi}^k(x_i)$ is a solution to the separated ODE for the coordinate x_i related to element k. For certain geometries, (2.3) can be separated into ODEs with solutions in terms of a complete set of orthogonal eigenfunctions (i.e., special functions).

Completeness ensures that any smooth function can be represented exactly by the infinite family of eigenfunctions (MacCluer, 2004, §11.3). Orthogonality is the functional equivalent to perpendicularity of 3D vectors; each function is *maximally independent* over the range of definition (MacCluer, 2004, §5.1). Orthogonality is defined for the complex function ϕ and ψ as

$$\int_a^b \phi_n(x_i)\psi_m^*(x_i)\,\mathrm{d}x_i = c\delta_{nm} \tag{2.7}$$

where $a \leq x_i \leq b$, c is a constant, δ_{nm} is the Kronecker delta, and $*$ indicates complex conjugation. More generally, (2.7) can involve a weigh function, but for the current applications this is always unity.

In EE one expands boundary conditions in eigenfunctions, then the solution is computed everywhere else using the coefficients determined from the boundary expansion. The second-order ODEs associated with finite boundaries encountered

in this work have solutions of the form,

$$\bar{\Phi}^k(x_i) = \sum_{j=0}^{N-1} \left[a_{ij}^k \, \phi_j(x_i) + b_{ij}^k \, \psi_j(x_i) \right] + R_N^k, \quad i = 1, \ldots, D \tag{2.8}$$

where ϕ_j and ψ_j are the eigenfunctions associated with the j^{th} eigenvalue and coordinate, x_i. a_{ij}^k and b_{ij}^k are generalized Fourier series coefficients [L^2] that must be determined for element k. The residual, R_N, arises from truncating the infinite expansion. In this case, the eigenvalues are the integers (j), because the domain is finite. In cases where the domain size becomes infinite, the eigenfunctions will become real numbers. When expanding a general function or boundary behavior, the sum of all the eigenfunctions, corresponding to the spectrum of eigenvalues, must be used (i.e., the form of (2.4)).

Upon recombination of the ODE solutions to form a solution to the PDE, products of coefficients are consolidated. For a two-dimensional problem this results in

$$\bar{\Phi}^k(x_1, x_2) = \sum_{j=0}^{N-1} \left[A_j^k \phi_j(x_1) + B_j^k \psi_j(x_1) \right] \left[\xi_j(x_2) + \zeta_j(x_2) \right] + R_N^k, \tag{2.9}$$

where ϕ and ψ are the basis functions for x_1 and ξ and ζ are the basis functions for x_2. There are $2N$ coefficients to determine for element k (A_j^k and B_j^k) and one residual term.

(2.9) constitutes an *exact* expression for $\bar{\Phi}^k(\mathbf{x})$, since $R_N^k \to 0$ as $N \to \infty$, due to the completeness of the eigenfunctions. Convergence is at least $\mathcal{O}(N^{-2})$ for smooth functions with continuous first derivatives (details in section D.2). The condition of smoothness is not overly restrictive for PDEs arising from physical problems; in cases where discontinuous functions must be expanded (e.g., intersecting elements), convergence will be degraded, but often the situation can be improved with series transformation and acceleration techniques (Oleksy, 1996).

LT-AEM utilizes a two-step solution process. The first step solves for the coefficients of the eigenfunctions in (2.9) using collocation, based on a desired ar-

rangement of elements, source terms, material properties, and the number and spacing of collocation points (§2.6). The second step evaluates (2.9) for various values of the independent variables, x_i, using the known coefficients (§2.7). One can evaluate the solution anywhere and analytically manipulate the solution (e.g., differentiate and integrate $\bar{\Phi}(\mathbf{x})$ for fluxes or streamfunction), a benefit of LT-AEM over gridded solutions.

LT-AEM uses the concepts of active and passive elements. Passive elements have specified strength (A_j^k and B_j^k are known before run-time), while active elements have total head or flux specified so that the coefficients of different elements depend on each other.

2.3.1 Geometric considerations

The geometry of the problem, the coordinate system used to solve the problem, and the behavior of the eigenfunctions that arise from separation of variables are interrelated. All coordinate systems in which (2.3) is separable can be derived from Cartesian coordinates using conformal mapping (Morse and Feshbach, 1953, p.499); the geometry can therefore also be related to the mapping function used to derive the working coordinate system. Table 2.1 categorizes elements related to Helmholtz-separable 2D coordinates where EE can be performed. 3D Helmholtz-separable coordinates are considered in section 3.4. Elliptical coordinates are the most general 2D coordinates; polar, parabolic, and Cartesian coordinates can be obtained by moving the elliptical foci together or moving one or both of the foci to ∞, respectively. The "concentration points" of the coordinate systems (singular points in the conformal mapping function) are related to the singularities of the ODEs obtained from separating the PDE (Moon and Spencer, 1961b, §6). The solution of ODEs can be characterized by the location and type of singularities that arise, both geometrically and analytically (Ince, 1956, §20).

coordinate system	finite boundary	singular element	infinite boundary	modified Helmholtz special functions
Cartesian	*none*	∞ line	line	exponential
circular	circle	point	ray	modified Bessel
elliptical	ellipse	line segment	hyperbola	modified Mathieu
parabolic	*none*	semi-∞ line	parabola	parabolic cylinder

TABLE 2.1. Helmholtz-separable 2D coordinate systems

Singular elements are the fundamental unit of the coordinate system, arising when one or more of the coordinates $\to 0$ (Arscott and Darai, 1981); they are generally sources or sinks (see Table 2.1), due to their reduced dimensionality. Areas can either be defined by finite boundaries, leading to a finite areas, or alternatively by infinite lines, leading to infinite areas. Circles and ellipses partition the 2D domain most conveniently; their perimeters have finite length and they encompass a finite area, resulting in periodic Sturm-Liouville expansions along their boundaries. For circular and elliptical coordinates, the finite boundary is parametrized by an angle; for the physical problems considered here, the function must be 2π periodic in this angle.

As derived and implemented here, LT-AEM elements should not touch or overlap. When elements do intersect, the boundary condition along their circumference will not be periodic, significantly degrading convergence. The Gibb's phenomenon and some potential methods to alleviate it are discussed in section D.2, as well as by Janković (1997) in the context of steady-state AEM.

2.3.2 Sturm-Liouville

The types of ODEs solved here can be related to those in Sturm-Liouville theory. The ODEs that arise from separation of variables (2.8) can be written in the general form of the Liouville equation

$$\frac{\mathrm{d}}{\mathrm{d}z}\left[p(z)\frac{\mathrm{d}\psi}{\mathrm{d}z}\right] + \psi\left[q(z) + \lambda r(z)\right] = 0 \tag{2.10}$$

where λ is the separation constant, the problem is considered over the range $a \leq z \leq b$, and the functions p, q, and r are characteristic of the coordinate system used in separating the governing PDE into ODEs (Morse and Feshbach, 1953, p.719). Equation 2.10 has boundary conditions associated with it at $z = a$ and $z = b$, whose type determines the nature of the solution. Simple, homogeneous boundary conditions lead to a one-to-one correspondence between λ and ψ, often signified by λ_n and ψ_n, since the eigenvalues can be mapped onto the non-zero integers. This is referred to as the standard Sturm-Liouville problem, but it does not arise in the current application.

A boundary condition that ensures the independent variable is periodic, $\psi(a) = \psi(a + 2\pi) = \psi(b)$, similarly leads to integer eigenvalues, but due to the ambiguity in the boundary condition there is a duality of eigenfunctions for each eigenvalue (Morse and Feshbach, 1953, p.726). This periodic domain leads to the singular Sturm-Liouville problem. When expanding a circular boundary in polar coordinates ($r = r_0, -\pi \leq \theta \leq \pi$), the n^{th} eigenfunctions are $\sin(n\theta)$ and $\cos(n\theta)$, the eigenvalues which force these functions to be periodic in 2π are found to be the integers by inspection. The eigenfunctions and eigenvalues in elliptical coordinates also exhibit this even/odd duality, and can be mapped onto the integers, but the numerical values of the eigenvalues depend on parameters appearing in the ODE therefore they must be computed in a more general manner (see Appendix E).

Another deviation from the standard Sturm-Liouville case occurs when the length of the domain becomes infinite; the totality (i.e., spectrum) of the eigenvalues for the Sturm-Liouville problem changes from the denumerably infinite integers to an infinite continuum of real numbers. For example, Cartesian coordinates or curves of constant angle in circular or elliptical coordinates lead to this type of infinite domain (Courant and Hilbert, 1962, §5.12). When the boundary being expanded becomes infinite in length there is no simple periodicity in the independent variable, and no manner to parametrize the entire curve with a finite

quantity.

This transition is illustrated through the relation between a Fourier series and Fourier transform, both of which are ways of representing a continuous function using trigonometric series (Morse and Feshbach, 1953, p.454). We begin with a type of standard Sturm-Liouville problem, the Fourier sine series of $f(x)$ in the region $0 \leq x \leq \ell$, with conditions $f(0) = f(\ell) = 0$;

$$f(x) = \sum_{n=0}^{\infty} A_n \sin\left(\frac{n\pi x}{\ell}\right), \tag{2.11}$$

which, using orthogonality, leads to the integral coefficient expressions

$$A_n = \frac{2}{\ell} \int_0^{\ell} f(x) \sin\left(\frac{n\pi x}{\ell}\right) \, \mathrm{d}x, \tag{2.12}$$

that inserted back into (2.11) gives

$$f(x) = \frac{2}{\ell} \sum_{n=0}^{\infty} \left[\int_0^{\ell} f(\zeta) \sin\left(\frac{n\pi\zeta}{\ell}\right) \, \mathrm{d}\zeta \right] \sin\left(\frac{n\pi x}{\ell}\right). \tag{2.13}$$

We introduce the variable k, which at discrete values is $k_n = n\pi/\ell$; the spacing between the discrete values is $\Delta k = k_{n+1} - k_n = \pi/\ell$. This simplifies (2.13) to

$$f(x) = \frac{2}{\pi} \sum_{n=0}^{\infty} \Delta k \left[\int_0^{\ell} f(\zeta) \sin\left(k_n \zeta\right) \, \mathrm{d}\zeta \right] \sin\left(k_n x\right), \tag{2.14}$$

where, in the limit as $\ell \to \infty$, the sum becomes an integral (the spectrum of eigenvalues for the Sturm-Liouville problem becomes continuous); $\Delta k \to 0$ and $k_n \to k$. This leads to the Fourier sine transform pair (both a forward and inverse transform),

$$f(x) = \frac{2}{\pi} \int_0^{\infty} \int_0^{\infty} f(\zeta) \sin(k\zeta) \, \mathrm{d}\zeta \sin(kx) \, \mathrm{d}k, \tag{2.15}$$

which via symmetry can be extended to the more commonly used doubly infinite range. In the limit as $\ell \to \infty$, the number of eigenvalues increases from the countably infinite integers $n = 0, 1, 2, \ldots$ to the uncountably infinite positive real numbers, $0 \leq k < \infty$. This illustrates how the spectrum of eigenvalues for the

standard or periodic Sturm-Liouville problem (e.g., boundary matching along a circle in polar coordinates or an ellipse in elliptical coordinates) is not as *dense* as the spectrum of eigenvalues needed for an infinite interval.

In implementation, the continuous spectrum is approximated discretely (making ℓ large but finite in (2.14)), but with less accuracy than the standard Sturm-Liouville expansion. When expanding boundary conditions on an infinite interval (e.g., expanding the effects of a point source along a 2D Cartesian boundary separating two regions of different materials — see section 3.3), we deal with two infinite quantities: the number of terms in the eigenfunction expansion, N, and the width of the interval, ℓ, over which they are distributed (Boyd, 2000, §17).

2.4 Convolution

Convolution is a special type of superposition, usually applied to the time variable. It is used to create general time behaviors from impulse response functions. Rather than requiring each LT-AEM element to have every possible distinct temporal behavior associated with it, elements are derived for the "unit" impulse case, which can then be readily made into any desired time behavior via convolution.

The Fourier and Laplace transforms both have convolution properties (Churchill, 1972, §17 & 123). Convolution in the time domain becomes simply multiplication in the Laplace domain, therefore LT-AEM allows for separate handling of the temporal, $\bar{g}(p)$, and spatial, $\bar{\Phi}_{\text{imp}}(\mathbf{x})$, behavior of elements. Essentially, space behavior is handled with the AEM (i.e., spatial superposition with boundary matching), while time behavior is handled using Laplace-space convolution.

2.4.1 Duhamel's theorem

Duhamel's theorem states that a general response is the weighted mean of past time behavior, with the weight being the impulse response function (Özişik, 1993,

§5). Duhamel's convolution integral for a general time response, $h(t)$, is

$$h(t) = \int_0^t e(t-\tau)g(\tau)\,\mathrm{d}\tau \tag{2.16}$$

where $e(t-\tau)$ is the impulse response (reversed with respect to the dummy variable of integration, τ), and $g(\tau)$ is the time behavior (see Figure 2.1). The integral

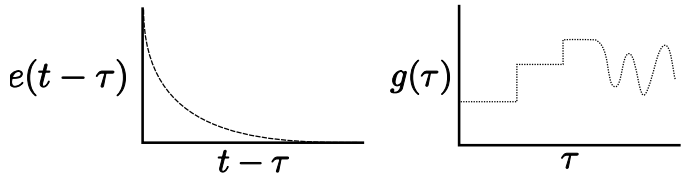

FIGURE 2.1. Impulse response (left) and time behavior (right) functions

is only carried out over $0 < \tau < t$, because the behavior in the future cannot affect the current response. Often we re-define the impulse response as

$$e_0(t-\tau) = \begin{cases} e(t-\tau) & \tau \le t \\ 0 & \tau > t \end{cases} \tag{2.17}$$

making e_0 a causal function (Ben-Menahem and Singh, 2000, §K); then we can extend the upper integration limit to ∞,

$$\int_0^\infty e_0(t-\tau)g(\tau)\,\mathrm{d}\tau = e_0(t) * g(t). \tag{2.18}$$

The Laplace transform of the convolution operator $(*)$ is multiplication of the corresponding Laplace-space image functions,

$$\mathcal{L}\left[e_0(t) * g(t)\right] = \bar{e}_0(p)\bar{g}(p); \tag{2.19}$$

since multiplication in Laplace space is commutative and $\mathcal{L}$ is linear, convolution is also commutative and linear.

2.4.2 Convolution example

The point source (well) solution is illustrated to compare the two methods of performing convolution. In the time domain, the response, $\Phi_{\text{well}}(r,t)$, at a distance r

from a well pumping at the rate $Q(t)$ $[\mathrm{L}^3/\mathrm{T}]$, is found by convolution of the unit well response with $Q(t)$. Using the impulse 2D point source (3D line source) from Carslaw and Jaeger (1959, §10.3), Duhamel's integral for a well with arbitrary time behavior is

$$\begin{aligned}\Phi_{\text{general}}(r,t) &= \Phi_{\text{imp}}(r,t) * Q(t) \\ &= \frac{1}{4\pi}\int_0^t \exp\left(-\frac{r^2}{4(t-\tau)\alpha}\right)\frac{Q(\tau)\,\mathrm{d}\tau}{t-\tau},\end{aligned} \tag{2.20}$$

where the upper limit of integration is kept at t, since without introducing a step function, the impulse solution $\neq 0$ for $\tau > t$. The Laplace transform of (2.20), from tables of Laplace transform pairs, is

$$\bar{\Phi}_{\text{general}}(r,p) = \frac{1}{2\pi}\mathrm{K}_0\left(r\sqrt{\tfrac{p}{\alpha}}\right)\bar{Q}(p), \tag{2.21}$$

where $\mathrm{K}_0(z)$ is a second-kind zero-order modified Bessel function (e.g. McLachlan, 1955, §6). In the case where $Q(t)$ is a constant, the integral in (2.20) can be recognized as an exponential integral, through the change of variables $\xi = r^2/\left[4\alpha(t-\tau)\right]$. This substitution leads to

$$\Phi_{\text{constant}}(r,t) = \frac{Q}{4\pi}\mathrm{E}_1\left(\frac{r^2}{4\alpha t}\right), \tag{2.22}$$

where E_1 is the exponential integral (e.g. Abramowitz and Stegun, 1964, §5). (2.22) is the Theis (1935) solution for drawdown due to a well pumping at a constant rate. Since $\mathcal{L}(c) = c/p$, the solution when $Q(t)$ is a constant is in Laplace space

$$\begin{aligned}\Phi_{\text{general}}(r,t) &= \frac{Q}{2\pi}\mathcal{L}^{-1}\left[\frac{1}{p}\mathrm{K}_0\left(r\sqrt{\tfrac{p}{\alpha}}\right)\right] \\ &= \frac{Q}{2\pi}\frac{1}{2}\int_{\frac{r^2}{4\alpha t}}^{\infty}\frac{e^{-u}}{u}\,\mathrm{d}u,\end{aligned} \tag{2.23}$$

which is found by looking up the inverse transform in a table (e.g. Carslaw and Jaeger, 1959, p.495) or by computing the inverse using Mellin's contour integral (A.4) (e.g. Lee, 1999, §3.2.4). As would be expected, both approaches lead to the exponential integral.

In this example, both the time convolution integral and the Laplace space convolution can be readily evaluated. In more general cases, the convolution integral cannot be evaluated in closed form or in terms of simple functions. Similarly, the inverse Laplace transform is typically unknown, but can be readily evaluated using a numerical inverse Laplace transform.

Utilizing the Laplace transform makes general time behavior in LT-AEM far more flexible, accurate and straightforward, compared to other transient AEM methods. Where transient elements are used directly (Zaadnoordijk and Strack, 1993), each different time behavior (constant in time, pulse in time, etc.) requires deriving a new element or evaluating a new time-domain convolution integral. The Fourier transform approach of Bakker (2004b,c) could potentially use the similar convolution properties of the Fourier transform.

2.4.3 Time behaviors for aquifer tests

While aquifer tests are commonly performed with pulse or step pumping rates, many other pumping schemes are also in use. Slug tests (Hvorslev, 1951; Cooper et al., 1967) use a nearly-instantaneous addition or removal of water from the well as the impulse; they are often used in low-permeability environments or situations where no pump is available. Step tests (i.e., pumping at 3-5 increasing levels) can be used to estimate both aquifer parameters and pumping well efficiency (Jacob, 1947; Rorabaugh, 1953). Hantush (1964a) developed analytic solutions for flow to a well in a confined aquifer pumping at exponentially-, hyperbolically-, and $1/\sqrt{t}$-decaying discharge rates. He characterized these as "uncontrolled" pumping rates, which decayed due to the additional work required to lift water from greater depth as the test proceeded. Black and Kipp (1981) treated sinusoidally-varying pumping rates as a way to increase the diagnostic capacity of an aquifer test. Rasmussen et al. (2003) used this approach, showing how the effects of several pumping wells,

each with its own characteristic amplitude and phase, can be deconvolved from observation data.

All of these different pumping behaviors, as well as arbitrary rates, are simply handled in LT-AEM by multiplying the impulse well solution in the Laplace domain with the Laplace transform of the desired temporal behavior (e.g. Prudnikov et al., 1992) and then inverting the Laplace domain solution analytically or numerically. Additionally, this treatment of general temporal behavior is not restricted to well pumping rates; other boundary conditions or source terms can also be handled in this manner.

2.5 Boundary matching

LT-AEM uses boundary matching to combine solutions, while maintaining the net required boundary condition. Elements are derived using EE, therefore boundaries are curves of constant coordinates; when multiple elements do not share a common coordinate origin, their boundary conditions cannot be handled generally using the EE approach alone. For example, with two non-concentric circles, each circle only appears as a simple expression in its own coordinate system. For the more general case, a Jacobian must be used to express flux in one system in terms of the coordinates of another system (see Appendix B).

2.5.1 Simple illustrative example

Using a cross-sectional "view" of a simplistic well-river combination (ignoring transient effects), Figure 2.2 shows how boundary matching is carried out for a simple system with one active and one passive element. The curve in Figure 2.2A shows the drawdown due to the pumping well (2.22), at first ignoring the effects of the nearby river. The well is a passive element, where Q is the volumetric flowrate

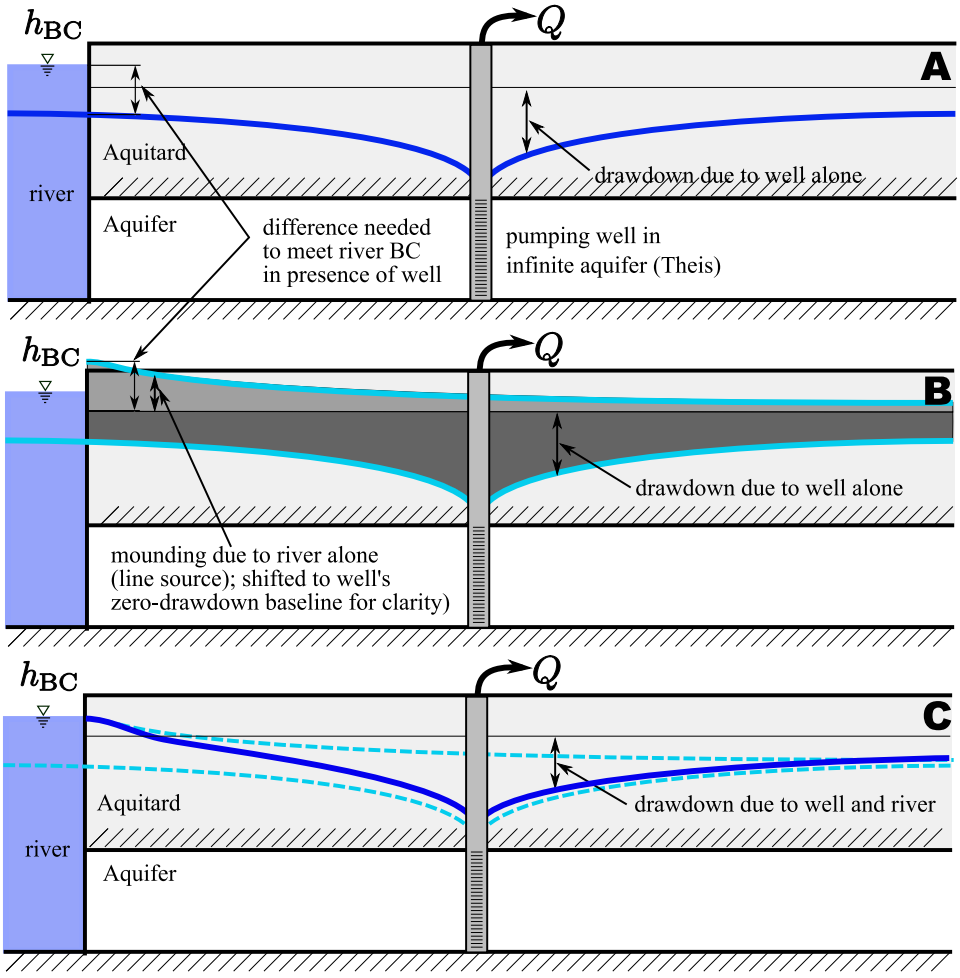

FIGURE 2.2. Conceptual boundary matching example for well and river

leaving the well $[\mathrm{L}^3/\mathrm{T}]$; it is assumed that this constant pumping rate can be maintained no matter how large the drawdown becomes. The river is an active element, where the specified head is h_{BC} $[\mathrm{L}]$; it is assumed there is an adequate source of water in the river to maintain this head.

Because the well is a passive element, the drawdown it creates does not depend on any other elements, only Q and α (aquifer parameters). The river is an active element; its effects depend on h_{BC} and α, but the strength of the element cannot be known without knowledge of the effects that the other elements have at this location. The amount of water that it adds (or removes) from the aquifer is a function

of the amount of head it must "make up" to bring the background conditions up to the specified boundary condition (see top-left of Figures 2.2A and B).

In Figure 2.2B, the effects of both elements are illustrated in the cross-section in terms of areas. The drawdown from the initial state due to the well is the lower (darker) shaded area, while the mounding due to the river accounting for the effects of the well at the river is the upper (lighter) area. The river mounding is shifted up to a common baseline with the well; the areas would otherwise overlap. The background condition at the river (the net effects of other elements at this location) in this case is just the drawdown due to the well at the boundary of the river. Figure 2.2 C shows the results of superimposing these two solutions, which itself is also a solution (due to superposition), and by construction also satisfies the three boundary conditions:

1. Q leaving the aquifer at the well,
2. $h_{\text{well}} + h_{\text{river}} = h_{\text{BC}}$ at river,
3. drawdown=0 at large distance.

This example is additionally complicated by time, represented through the Laplace parameter p. The Laplace parameter lacks an exact physical meaning (see Appendix A), therefore complicating plots. The simple example would be additionally complicated by the presence of multiple active elements, requiring an iterative solution for the head effects at each active element.

2.5.2 Boundary conditions

A circle can be said to cut the 2D plane into two complimentary regions, the interior and exterior (see Figure 2.3). The two domains share a radial coordinate system, centered on the circle. The coordinate system has singularities at $r = 0$ and $r = \infty$, one associated with each element in this case. The singular points

of polar coordinates are related to the fact that the differential element, $r\,\mathrm{d}r\,\mathrm{d}\theta$ (an expression of area), is not finite at these two locations. The differential element in a general curvilinear coordinate system is given in terms of the system's metric coefficients (see Appendix B for metric coefficients of the coordinate systems given in Table 2.1).

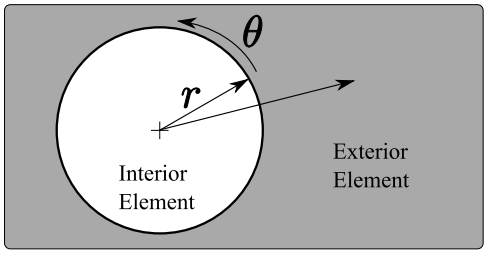

FIGURE 2.3. Interior and exterior circular elements

LT-AEM elements, which themselves are functions of the coordinates, must produce physically plausible solutions, even when coordinates $\to 0$ or ∞. Usually, this condition is satisfied automatically through the proper choice of basis functions.

In polar and elliptical coordinates, the condition that the function be periodic in 2π in the independent variables leads to the eigenvalues for the set of ODEs (§2.3.2); the complete solution for arbitrary BC is the superposition of all the solutions corresponding to every possible eigenvalue. For the radial ODE, only one of the two types of solutions is used based on basis function behavior at the singular points $r = 0$ and ∞. Both solutions can be used in regions without singularities, (e.g., an annulus in polar coordinates) but these are also handled by superimposing two elements.

BC matching is used to determine A_j^k and B_j^k in (2.9); the BC can be Dirichlet, Neumann, or mixed type. Interface BC (i.e., matching or continuity conditions) are posed along boundaries between areas cases where we want a smooth solution and smooth flux across the boundary. A mixed BC along the circumference of an

LT-AEM element is, in its most general form,

$$\xi \nabla \bar{\Phi} \cdot \mathbf{n} + \zeta \bar{\Phi} = \bar{F}(s,p), \tag{2.24}$$

where $\mathbf{n}$ is a unit normal and s is arc length or an angle that parametrizes the boundary. Setting $\xi = 0$ and $\zeta = 1$ leaves a Dirichlet BC, $\bar{F}_{\mathrm{D}}(s,p) = K\bar{h}_{\mathrm{BC}}(s,p)$, the transformed potential along the circumference of the element. With $\zeta = 0$ and $\xi = 1$, (2.24) becomes a Neumann BC where now $\bar{F}_{\mathrm{N}}(s,p) = \nabla\bar{\Phi}_{\mathrm{BC}}(s,p) \cdot \mathbf{n}$ is the transformed specified flux normal to the element boundary.

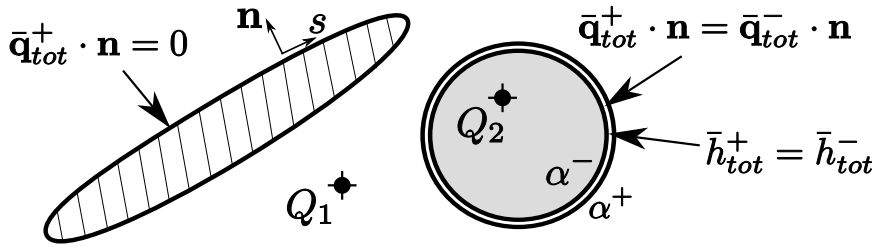

FIGURE 2.4. Example with active no-flow ellipse, passive point sources and active circular matching element with different α inside and out ($+$ and $-$ "parts" of matching element offset for clarity)

A matching BC can be considered to be both an external and internal element at the same physical location (see Figure 2.3 and the double circle in Figure 2.4); each boundary condition is specified in terms of the total ("tot") head due to all visible elements. A Neumann and Dirichlet BC are posed on each side, setting $\bar{F}^+_{\mathrm{N}}(s,p) = \bar{F}^-_{\mathrm{N}}(s,p)$ and $(K^-/K^+)\bar{F}^+_{\mathrm{D}}(s,p) = \bar{F}^-_{\mathrm{D}}(s,p)$. Typically specifying both head and flux boundary conditions overdetermines a diffusion problem, but here the pair only ensures continuity; values are not assigned, only equality between inside and outside. It is noted that mathematically the "inside" and "outside" elements associated with an interface condition can be considered as different elements (having different indices, k), but here they are referred to using the $\pm$ notation, since they are different *sides* of the same element.

Passive element BC are specified in terms of $\bar{\mathbf{q}}^k \cdot \mathbf{n}$ or $\bar{h}^k$ of individual elements,

where

$$\bar{\mathbf{q}} = -\nabla\bar{\Phi} = -K\nabla\bar{h} \tag{2.25}$$

is the Laplace-transformed Darcy flux [L]; they can be combined without iterating via simple superposition. Active element BC (Figure 2.4) are specified in terms of total discharge potential $\left(\bar{\Phi}_{\text{tot}} = \sum_k \bar{\Phi}^k\right)$ or normal flux $\left(\mathbf{n}\cdot\bar{\mathbf{q}}_{\text{tot}} = \sum_k \mathbf{n}\cdot\bar{\mathbf{q}}^k\right)$; if there are at least two active elements, their strengths must be determined simultaneously.

Most elements of interest in LT-AEM are active elements; circles and ellipses which define regions of different aquifer properties or source terms are typically active. A line or point source can be active or passive; if the total flowrate at the well or line is specified, it is passive (like a Theis well). If the total head is specified at the well (like a sump or dewatering pump that is used to keep an excavation dry) the element becomes active, because its strength depends on the surrounding conditions.

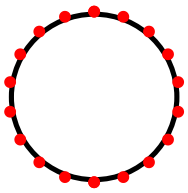

FIGURE 2.5. Matching locations on a circular boundary

To determine active element coefficients, M collocation points are chosen along the matching boundaries (see Figure 2.5), where the $\pm$ sides of an element meet, creating a system of $2M$ equations (M normal flux and M head) and $4N-2$ unknowns (N for even functions, but only $N-1$ for odd ones). Following the AEM overspecification approach of Janković (1997), we choose $2M \geq 4N-2$ and the system of equations is solved in a least-squares sense. Overspecification is considered to produce a smoother solution than the even-determined case $2M = 4N-2$ does, and for the same M, N is smaller (i.e., the solution does not require the

$2M - (4N - 2)$ highest harmonic basis functions). The inclusion of more control points, beyond those needed to make the system evenly determined, is not a great computational cost; these extra points tend to improve the quality of the solution. For these reasons, overspecification is here used in LT-AEM applications.

2.5.3 Detailed boundary matching example

The details regarding boundary matching are introduced using the simple AEM example shown in Figure 2.6; it includes two point sources and nested circles of different hydraulic conductivity.

Head matching Head matching ensures no energy is gained or lost when crossing the boundary (hydraulic head is a measure of energy per unit weight of water) and enforces a "smoothness" in the final solution. It can be expressed generally for each matching element as

$$\bar{h}_{\text{tot}}^{n+}(r_{n0}) = \bar{h}_{\text{tot}}^{n-}(r_{n0}); \tag{2.26}$$

the total heads (due to all contributing elements) immediately interior $(-)$ and exterior $(+)$ to the n^{th} element boundary are equal. The total head is due to the

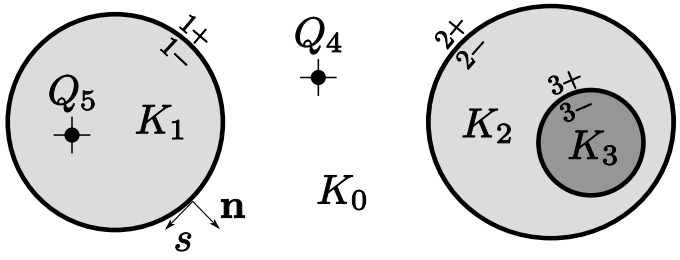

FIGURE 2.6. Example of three active circular elements of different K (background K_0) and two passive point sources, Q_4 and Q_5

current element (n) and all elements in the background of the current element.

Expanding (2.26) in terms of its components and $\bar{\Phi}$, leads to

$$\frac{1}{K_{n+}}\left[\bar{\Phi}^{n+}+\sum_{\substack{k=1\\k\neq n}}^{N_{bg+}}\bar{\Phi}^{k}\right]_{r_{n0}}=\frac{1}{K_{n-}}\left[\bar{\Phi}^{n-}+\sum_{\substack{k=1\\k\neq n}}^{N_{bg-}}\bar{\Phi}^{k}\right]_{r_{n0}}, \tag{2.27}$$

where $N_{bg\pm}$ is the number of elements in the inner and outer background of the element, and r_{n0} indicates all elements in this expression are evaluated on the boundary of element n. For element $2^{\pm}$ in Figure 2.6, element 3^{+} makes up the "inner background", while element 1^{+} and Q_4 are in the "outer background". In Figure 2.7 the hierarchy of elements is illustrated as a tree; background elements include the parent element and all elements that share the same parent (connected by a dashed line in Figure 2.7). Expression 2.27, for head matching on the boundary of element 2 would be

$$\frac{1}{K_0}\left[\bar{\Phi}^{2+}+\bar{\Phi}^{1+}+\bar{\Phi}^{4}\right]_{r_{20}}=\frac{1}{K_2}\left[\bar{\Phi}^{2-}+\bar{\Phi}^{3+}\right]_{r_{20}}, \tag{2.28}$$

where the element number is super-scripted (point sources need no sign). Point source Q_5 and circles $1-$ and $3-$ do not appear in this expression, as they are neither immediately internal nor external to element 2 (see Figure 2.7). This distinction is adopted here to allow regions with different PDEs to be matched; this is a requirement for the modified Helmholtz equation (due to the appearance of the material properties in the PDE), but not for the Laplace equation (the case considered by Strack et al. (1999)), where the material properties only appear in the definition of Φ.

Normal flux matching Flux matching applies to the same set of elements in head matching, but is a statement that mass is not stored or lost at the boundary, since a net difference in mass flux implies mass storage. This is expressed at each matching element as

$$\mathbf{n}_n\cdot\bar{\mathbf{q}}^{+}_{\text{total}}(r_{n0})=\mathbf{n}_n\cdot\bar{\mathbf{q}}^{-}_{\text{total}}(r_{n0}) \tag{2.29}$$

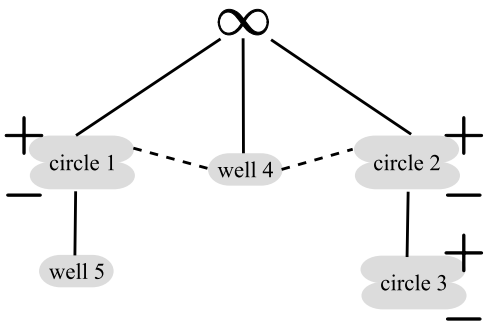

FIGURE 2.7. Tree representation of element hierarchy in Figure 2.6; ∞ represents the background between the elements

where the subscript on the normal indicates the element it is associated with. (2.29) states that the total normal flux across the element boundary is balanced. For Figure 2.6, in terms of $\bar{\Phi}$, the flux balance across element 2 is

$$\left[\frac{\partial\bar{\Phi}^{2+}}{\partial r_2} + \frac{\partial\bar{\Phi}^{1+}}{\partial r_1}J_{r_1r_2} + \frac{1}{r_1}\frac{\partial\bar{\Phi}^{1+}}{\partial\theta_1}J_{\theta_1r_2} + \frac{\partial\bar{\Phi}^{4}}{\partial r_4}J_{r_4r_2}\right]_{r_{20}} = \left[\frac{\partial\bar{\Phi}^{2-}}{\partial r_2} + \frac{\partial\bar{\Phi}^{3+}}{\partial r_3}J_{r_3r_2} + \frac{1}{r_3}\frac{\partial\bar{\Phi}^{3+}}{\partial\theta_3}J_{\theta_3,r_2}\right]_{r_{20}}, \tag{2.30}$$

where subscripts on r and θ indicate the associated element and $J_{\theta_1r_2} = \frac{\partial\theta_1}{\partial x}\frac{\partial x}{\partial r_2} + \frac{\partial\theta_1}{\partial y}\frac{\partial y}{\partial r_2}$ is a Jacobian; each of these coordinate derivatives can be computed explicitly (see Appendix B for details and examples). $\bar{\Phi}$ for each element is defined in terms of a local coordinate system; differentiation with respect to local coordinates (e.g., $\partial\bar{\Phi}^{2+}/\partial r_2$) leads to simple expressions, compared to working in a single global coordinate system everywhere.

2.6 Solution for coefficients

The solution for the coefficients of active elements in an LT-AEM problem can be posed in three ways

- a fixed-point iteration over active elements, each iteration solving a small least-squares problem for the coefficients of a single element;

- a direct least-squares solution for the coefficients of all active elements simultaneously;
- analytical solution for coefficients in certain simple geometries through eigenfunction orthogonality; quadrature can be used to approximate these integrals.

Many AEM problems are solved using the fixed-point iteration; it requires the least amount of the problem to be kept in computer memory at a time. The ready availability of parallelized LAPACK (Anderson et al., 1990) and BLAS (Blackford et al., 2002) linear algebra libraries, makes the direct matrix solution method more feasible and in some cases much faster than the iterative method. Program logic and code size are improved for the direct approach as well.

2.6.1 Fixed-point iteration

When posing multiple active boundary conditions as a fixed-point iteration, only the coefficients of the "current" element are computed, all other unknown coefficients are assumed known. We use the previous example from section 2.5. Starting with element 1 as the current element, head matching one boundary 1 is put into the form

$$\frac{\bar{\Phi}^{1+}(r_{10})}{K_0} - \frac{\bar{\Phi}^{1-}(r_{10})}{K_1} = \frac{\bar{\Phi}^{5}(r_{10})}{K_1} - \frac{1}{K_0}\left[\bar{\Phi}^{2+}(r_{10}) + \bar{\Phi}^{4}(r_{10})\right], \tag{2.31}$$

where the inside and outside coefficients of the current element (1) are on the left side, all passive and background active elements are on the right side. This equation is posed at M evenly-spaced matching locations around the circumference of element 1 ($\frac{2\pi}{M}k; k = 1, 2, \ldots, M$) – see Figure 2.5, in terms of the $4N - 2$ coefficients of element 1 ($2N - 1$ for each side). For example, the $\bar{\Phi}^{1+}$ term in (2.31) can be

expanded using the definitions in terms of the eigenfunction expansions (2.9) into

$$\underbrace{\begin{bmatrix} \xi_0(r_{10})\phi_0(\theta_1)\ldots\xi_{N-1}(r_{10})\phi_{N-1}(\theta_1) \\ \xi_0(r_{10})\phi_0(\theta_2)\ldots\xi_{N-1}(r_{10})\phi_{N-1}(\theta_2) \\ \vdots \\ \xi_0(r_{10})\phi_0(\theta_M)\ldots\xi_{N-1}(r_{10})\phi_{N-1}(\theta_M) \end{bmatrix}}_{\text{even angular functions}} \underbrace{\begin{bmatrix} \xi_1(r_{10})\psi_1(\theta_1)\ldots\xi_{N-1}(r_{10})\psi_{N-1}(\theta_1) \\ \xi_1(r_{10})\psi_1(\theta_2)\ldots\xi_{N-1}(r_{10})\psi_{N-1}(\theta_2) \\ \vdots \\ \xi_1(r_{10})\psi_1(\theta_M)\ldots\xi_{N-1}(r_{10})\psi_{N-1}(\theta_M) \end{bmatrix}}_{\text{odd angular functions}}, \tag{2.32}$$

a $M \times 2N-1$ coefficient matrix, which is multiplied by the coefficient vector

$$\mathbf{x} = [A_0, \ldots, A_{N-1}, B_1, \ldots, B_{N-1}]^T,$$

following the convention of (2.9). The flux matching equation on the same boundary is similarly written

$$\mathbf{n}_1 \cdot \left[\bar{\mathbf{q}}^{1+}(r_{10}) - \bar{\mathbf{q}}^{1-}(r_{10})\right] = \mathbf{n}_1 \cdot \left[\bar{\mathbf{q}}^{5}(r_{10}) - \bar{\mathbf{q}}^{2+}(r_{10}) - \bar{\mathbf{q}}^{4}(r_{10})\right]; \tag{2.33}$$

expressing the flux in terms of derivatives and Jacobians gives

$$\begin{aligned} \left[\frac{\partial\bar{\Phi}^{1+}}{\partial r_1} \; -\frac{\partial\bar{\Phi}^{1-}}{\partial r_1}\right]_{r_{10}} = \\ \left[\frac{\partial\bar{\Phi}^{5}}{\partial r_5}J_{r_5r_1} - \frac{\partial\bar{\Phi}^{2+}}{\partial r_2}J_{r_2r_1} - \frac{1}{r_2}\frac{\partial\bar{\Phi}^{2+}}{\partial\theta_2}J_{\theta_2r_1} - \frac{\partial\bar{\Phi}^{4}}{\partial r_4}J_{r_4r_1}\right]_{r_{10}}. \end{aligned} \tag{2.34}$$

An analogous set of equations is made, with each active element taking the role of the "current" element in turn. In this formulation, 3 small least-squares problems are solved (one for each of the active elements), for each iteration; the background effects (right hand side) are constantly being updated as iterations continue.

In matrix form, (2.31) and (2.34) for element 1 are

$$\begin{aligned} \mathbf{A}\mathbf{x} &= \mathbf{b} \\ \begin{bmatrix} \frac{1}{K_0}\bar{\Phi}^{1+} & -\frac{1}{K_1}\bar{\Phi}^{1-} \\ \frac{\partial\bar{\Phi}^{1+}}{\partial r_1} & -\frac{\partial\bar{\Phi}^{1-}}{\partial r_1} \end{bmatrix} &= \begin{bmatrix} \frac{1}{K_1}\bar{\Phi}^{5} - \frac{1}{K_0}\left(\bar{\Phi}^{2+} + \bar{\Phi}^{4}\right) \\ \frac{\partial\bar{\Phi}^{5}}{\partial r_5}J_{r_5r_1} - \frac{\partial\bar{\Phi}^{2+}}{\partial r_2}J_{r_2r_1} - \frac{1}{r_2}\frac{\partial\bar{\Phi}^{2+}}{\partial\theta_2}J_{\theta_2r_1} - \frac{\partial\bar{\Phi}^{4}}{\partial r_4}J_{r_4r_1} \end{bmatrix} \end{aligned} \tag{2.35}$$

where, for notational simplicity, $\mathbf{A}\mathbf{x}$ is given together on the left hand side in terms of $\bar{\Phi}$. Since everything in $\mathbf{b}$ on the right of (2.35) is assumed constant in the current

iteration, these terms reduce to a vector of length $2M$. $\mathbf{A}$ is a matrix of size $2M \times 4N-2$. Increasing the number of active elements only complicates the calculation of $\mathbf{b}$, and increase the number of iterations required overall, it does not increase the size of each individual $\mathbf{A}$.

The fixed-point iteration described here is equivalent to a block Gauss-Seidel iteration, since computed coefficients are used immediately in the next available calculation (Isaacson and Keller, 1966, §2.4). The iterative approach can be improved slightly using block successive over-relaxation (SOR), where a weighted combination of the current and previous iterations are used to increase convergence; this method is simple to implement, but does not lead to large improvements over the simplistic Gauss-Seidel method.

2.6.2 Direct matrix approach

In the direct formulation we solve for all active elements simultaneously. This significantly increases the size of $\mathbf{A}$, but eliminates the need to iterate. $\mathbf{A}$ used in the fixed-point iteration are the diagonal sub-block elements of the direct method; see the shaded blocks in (2.36). The effects of one active element on another (in $\mathbf{b}$ of (2.35)) become the off-diagonal terms in (2.36). The matching equations for element 1, (2.35), along with the analogous expressions for matching head and flux on elements 2 and 3, becomes the diagonals when the entire problem is given in matrix form, the left-hand side $(\mathbf{Ax})$ is

$$\left[\begin{array}{cc|cc|cc} \frac{\bar{\Phi}^{1+}}{K_0} & -\frac{\bar{\Phi}^{1-}}{K_1} & \frac{\bar{\Phi}^{2+}}{K_0} & 0 & 0 & 0 \\ \mathbf{n}_1\cdot\bar{\mathbf{q}}^{1+} & -\mathbf{n}_1\cdot\bar{\mathbf{q}}^{1-} & -\mathbf{n}_1\cdot\bar{\mathbf{q}}^{2+} & 0 & 0 & 0 \\ \hline \frac{\bar{\Phi}^{1+}}{K_0} & 0 & \frac{\bar{\Phi}^{2+}}{K_0} & -\frac{\bar{\Phi}^{2-}}{K_2} & -\frac{\bar{\Phi}^{3+}}{K_2} & 0 \\ \mathbf{n}_2\cdot\bar{\mathbf{q}}^{1+} & 0 & \mathbf{n}_2\cdot\bar{\mathbf{q}}^{2+} & -\mathbf{n}_2\cdot\bar{\mathbf{q}}^{2-} & -\mathbf{n}_2\cdot\bar{\mathbf{q}}^{3+} & 0 \\ \hline 0 & 0 & 0 & \frac{\bar{\Phi}^{2-}}{K_2} & \frac{\bar{\Phi}^{3+}}{K_2} & -\frac{\bar{\Phi}^{3-}}{K_3} \\ 0 & 0 & 0 & \mathbf{n}_3\cdot\bar{\mathbf{q}}^{2-} & \mathbf{n}_3\cdot\bar{\mathbf{q}}^{3+} & -\mathbf{n}_3\cdot\bar{\mathbf{q}}^{3-} \end{array}\right] \tag{2.36}$$

and the right hand side $(\mathbf{b})$ is

$$\begin{bmatrix} \frac{\bar{\Phi}^5}{K_1} - \frac{\bar{\Phi}^4}{K_0} \\ \hline \mathbf{n}_1 \cdot [\bar{\mathbf{q}}^5 - \bar{\mathbf{q}}^4] \\ \hline -\frac{\bar{\Phi}^4}{K_0} \\ \hline -\mathbf{n}_2 \bar{\mathbf{q}}^4 \\ \hline 0 \\ 0 \end{bmatrix}. \tag{2.37}$$

In (2.36) the off-diagonal flux terms involving two circular elements have both r and θ components, as in (2.34). In the direct matrix form, only passive elements (here wells) and specified BC values appear in $\mathbf{b}$. Each entry in this matrix formulation is itself a smaller $M \times 2N - 1$ matrix, as was the case in (2.35). In this block-matrix formulation, several things become clearer, compared to the iterative formulation:

1. not every element "sees" every other element (Figure 2.7). This is a type of domain decomposition, referred to as *substructuring*;

2. different $\pm$ sides of each matching element can be considered separate entities, appearing as columns in the $\mathbf{A}$ matrix;

3. it is possible to determine the coefficients analytically using orthogonality and numerical integration;

4. other types of iterative methods can be used to solve for $\mathbf{x}$.

The matrix in equation (2.36) is $n2M \times n(4N-2)$, where n is the number of active elements. As more active elements are added the matrix becomes larger. $\mathbf{A}$ is non-symmetric and its sparseness is a function of whether the elements are nested. If all elements are at the same "level", in the same background (same parent in Figure 2.7), then each element is effected by every other element, resulting in $\mathbf{A}$ being full. When an active element appears inside another active element, $\mathbf{A}$ will have some zero off-diagonal entries. Outside their circumscribing element, the inside

elements are not seen; the effects of elements inside it are propagated outside it using the large element's basis functions, often simplifying calculations.

The non-overlapping domain decomposition method known as substructuring (Smith et al., 1996, §4) is commonly applied to gridded problems, but can also be applied to the matrix problem for the generalized Fourier series coefficients posed here. The concept is based on the principle that portions of the domain, which are loosely coupled, can be solved independently or nearly independently (the benefit coming from solving them in parallel). For example, in Figure 2.6 element 2 is the only connection between elements 3 and 1. In cases where many elements are nested inside one larger element, the larger element can be decomposed into its inner and outer contributions. Then these problems can be solved independently and finally re-combined. Quarteroni et al. (2000, §3.9.2) give an illustrative worked example of this approach.

The fixed-point (Gauss-Seidel) iteration is one possibility of solution method for both AEM and LT-AEM (Furman and Neuman, 2003). When the problem is posed in matrix form, (2.36 and 2.37), to allow direct solution, any matrix solution technique that is applicable to over-determined systems could be applied. This includes general iterative techniques, such as bi-conjugate gradient or quasi-minimum residual methods (e.g. Freund and Nachtigal, 1991). The direct method can lead to round-off error in the solution, especially when there is a large contrast in properties between elements. The direct solution can be improved using an iterative approach if high accuracy is desired.

Analytic solution for coefficients When posing the problem in the direct matrix form, we can compute the coefficients analytically, using orthogonality and Cramer's rule. This approach is similar to handling the whole problem using traditional analytic EE techniques; there is no least-squares solution in the boundary-matching problem. The generalized Fourier series coefficients are found via orthogonality

integrals, generally it is only possible to evaluate these integrals in closed form when the active elements share a coordinate (e.g., they are confocal or concentric).

For example, a closed-form solution would be possible for a point source at the center of a circular boundary, a line source at the focus of an elliptical domain, or a layered Cartesian problem. In general, for 2D (see Table 2.1) this includes solutions comprised of both a singular and finite or infinite element of the same coordinate system. Other combinations of geometries typically would not lead to closed-form solutions for the coefficients.

For a system of n unknowns, Cramer's rule requires the evaluation of $n + 1$ determinants of size n (e.g. Householder, 1975, §5). Because of the large computational requirements, this method would be impractical for $n \geq 5$.

Two LT-AEM applications that could capitalize on analytically-derived coefficients include the Post-Widder inverse approach (§5.3.1) or analytic calculation of parameter sensitivities required for an inverse problem (e.g., $\frac{\partial \bar{\Phi}}{\partial K}$ or $\frac{\partial \bar{\Phi}}{\partial S_S}$). Both are possible if analytic (or high accuracy) derivatives can be computed with respect to model parameters or (in the case of the Post-Widder inverse) the Laplace parameter.

Quadrature approach to coefficients Numerical quadrature can be used to extend analytic approach described above beyond simple combinations of concentric elements. In situations where the orthogonality integrals can be posed, but not computed in closed form, numerical quadrature could be applied. The simplest approach would be to uniformly subdivide the 2π boundary, using the the trapezoid rule or Chebyshev quadrature. This would result in a very similar formulation to the least-squares collocation approach, but without the explicitly posing the least squares problem. Boyd (2000, §4.3) posits that the quadrature and collocation approaches are operationally equivalent; they are just different ways of utilizing the function sampling points along the boundary of the element. As an alternative to

using the trapezoid rule or some other method with fixed abscissa, an adaptive integration routine (e.g., QUADPACK, which utilizes Gauss-Kronrod quadrature (Favati et al., 1991)) could be used. Adaptive methods increase the number of sample points where needed to achieve a target error tolerance, allowing the collocation points to be adaptively clustered where they would be needed most (e.g., near singularities where gradients are steeper).

A potential advantage of the quadrature approach is that some integrals that cannot be evaluated in closed form, would be readily evaluated numerically. The difficulty in a numerical integration is proportional to the ability of the function to be fitted with polynomials of some sort. If two active elements are distant from each other, a low-order polynomial approximation may be appropriate and more efficient than utilizing the full set of proper basis functions arising from the standard approach.

As an example, the quadrature approach is illustrated on the first row of (2.36) in the coordinates of element 1. This cannot be computed analytically, due to the fact that the integral of the off-diagonal terms with respect to the angular coordinate of element 1 cannot be evaluated in closed form. Multiplying the first row of (2.36) and (2.37) by the even basis functions of $\bar{\Phi}^{1\pm}$, $\cos m\theta_1$, and integrating over $-\pi < \theta_1 < \pi$, gives the following expression

$$\frac{a_m^{1+}}{K_0} - \frac{a_m^{1-}}{K_1} + \frac{1}{K_0}\int_{-\pi}^{\pi} \cos(m\theta_1)\,\bar{\Phi}^{2+}(r_2,\theta_2)\,\mathrm{d}\theta_1 = \int_{-\pi}^{\pi} \cos(m\theta_1)\left[\frac{\bar{\Phi}^5(r_5)}{K_1} - \frac{\bar{\Phi}^4(r_4)}{K_0}\right]\mathrm{d}\theta_1, \tag{2.38}$$

where the first two integrals were reduced to the m^{th} unknown coefficient using orthogonality, and the rest of the integrals can be evaluated numerically. A similar procedure is performed for the odd basis functions, $\sin n\theta_1$, resulting in an analogous set of equations for b_m^{1+} and b_m^{1-} involving similar integrals.

The other rows of the matrix are handled analogously, with the even and odd

basis functions of each element being multiplied and integrated with all the other terms. Orthogonality of each element's basis functions is used to evaluate the integrals falling on the shaded diagonal blocks in (2.36).

The larger matrix problem for all $n(4N-2)$ coefficients is now broken into N smaller matrix problems, as the orthogonality of the eigenfunctions has been used to decouple the solutions for the different coefficients.

2.6.3 Computation of least-squares solution

In both the fixed-point and direct matrix approaches, least-squares problems will need to be solved numerically for the generalized Fourier series coefficients. For robustness, we take a QR decomposition approach rather than solving the normal equations.

Normal equations The normal equations are conceptually simpler and require fewer operations than QR decomposition, and are therefore commonly used. Beginning with $\mathbf{A}\mathbf{x} = \mathbf{b}$ and pre-multiplying both sides by $\mathbf{A}^T$, we create a Hermitian (and therefore invertible) matrix

$$\mathbf{A}^T\mathbf{A}\mathbf{x} = \mathbf{A}^T\mathbf{b}. \tag{2.39}$$

Pre-multiplying by the inverse of $\mathbf{A}^T\mathbf{A}$ results in an expression for $\mathbf{x}$ often referred to as the *generalized inverse* (Menke, 1984, §4.1),

$$\mathbf{x} = (\mathbf{A}^T\mathbf{A})^{-1}\mathbf{A}^T\mathbf{b}, \tag{2.40}$$

$$= \mathbf{G}^{-g}\mathbf{b}, \tag{2.41}$$

which is the traditional solution to the normal equations. This approach is appealing because after computing $\mathbf{G}^{-g}$ once, it only requires one matrix-vector multiplication to compute $\mathbf{x}$ for each new $\mathbf{b}$. Unfortunately, numerical problems plague this approach. When the square matrix $\mathbf{A}^T\mathbf{A}$ is formed, much of the numerical

detail of $\mathbf{A}$ can be lost (Golub and van Loan, 1996, §5.3.2). To obtain the same accuracy using the generalized inverse as obtained using QR decomposition, a higher working precision must be used in the calculation (Lawson and Hanson, 1974, §19).

QR decomposition The least-squares problem is solved via QR factorization by supposing first that a $\mathbf{Q}$ (a matrix comprised of orthogonal column vectors) has been found such that

$$\mathbf{Q}^T\mathbf{A} = \mathbf{R} = \begin{bmatrix}\mathbf{R}_1 \\ 0\end{bmatrix}, \tag{2.42}$$

where $\mathbf{R}_1$ is upper triangular (Wilkinson, 1965, §9.28). The product of the transposed orthogonal matrix and the right-hand side is decomposed as

$$\mathbf{Q}^T\mathbf{b} = \begin{bmatrix}\mathbf{c} \\ \mathbf{d}\end{bmatrix}, \tag{2.43}$$

where $\mathbf{c}$ is conformal with $\mathbf{R}_1$. The least-squares problem is the minimization of the solution residual, here quantified in terms of a squared matrix norm,

$$||\mathbf{A}\mathbf{x} - \mathbf{b}||_2^2 = ||\mathbf{Q}^T\mathbf{A}\mathbf{x} - \mathbf{Q}^T\mathbf{b}||_2^2, \tag{2.44}$$

$$= ||\mathbf{R}_1\mathbf{x} - \mathbf{c}||_2^2 + ||\mathbf{d}||_2^2, \tag{2.45}$$

where $||\mathbf{x}||_2$ is the Euclidean norm. (2.45) shows that the minimum is found when the first norm $= 0$, therefore $\mathbf{x}$ can be computed from $\mathbf{R}_1\mathbf{x} = \mathbf{c}$ via back-substitution. $||\mathbf{d}||_2^2$ is then the least-squares residual; it is error that cannot be reduced through choice of $\mathbf{x}$. When computing least-squares using the LAPACK routine ZGELSS (Anderson et al., 1990) or equivalently in Matlab using the "backslash" operator (MathWorks, 2007), this is the approach taken. The orthogonal matrix $\mathbf{Q}$ is computed using Householder reflections (e.g. Golub and van Loan, 1996, §5.1.2) to create columns of zeros below the diagonal in $\mathbf{A}$, a numerically stable process. Once $\mathbf{A}$ is made upper triangular, the product of all the individual Householder transformation matrices is $\mathbf{Q}$. An added benefit of the QR decomposition approach is its robustness with respect to degenerate columns in $\mathbf{A}$; $\mathbf{G}^{-g}$ fails to exist for this degeneracy, discussed in section E.3.

2.7 Solution for head or flux

Utilizing the structure of **A** used in the direct matrix solution section (2.6.2), a modified **A** matrix can be created, where the rows correspond to the desired evaluation points, rather than the collocation points along the boundaries of the active elements. Using **x** determined in section 2.6, the head or flux is found through a matrix-vector multiplication. As an example, to compute the head and Cartesian fluxes at a point c in the background (see **x** in Figure 2.8), we construct the following system to determine the effects of the active elements,

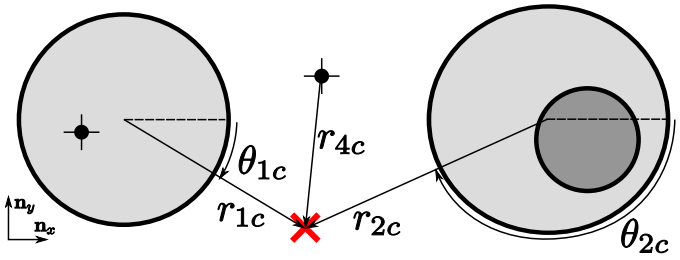

FIGURE 2.8. Geometry of head and flux calculation at c (marked by **x**)

$$\begin{bmatrix} \frac{\bar{\Phi}^{1+}(r_{1c},\theta_{1c})}{K_0} & 0 & \frac{\bar{\Phi}^{2+}(r_{2c},\theta_{2c})}{K_0} & 0 & 0 & 0 \\ \mathbf{n}_x \cdot \bar{\mathbf{q}}^{1+}(r_{1c},\theta_{1c}) & 0 & -\mathbf{n}_x \cdot \bar{\mathbf{q}}^{1+}(r_{2c},\theta_{2c}) & 0 & 0 & 0 \\ \mathbf{n}_y \cdot \bar{\mathbf{q}}^{1+}(r_{1c},\theta_{1c}) & 0 & -\mathbf{n}_y \cdot \bar{\mathbf{q}}^{1+}(r_{2c},\theta_{2c}) & 0 & 0 & 0 \end{bmatrix} \mathbf{x} = \begin{bmatrix} \bar{h}_c \\ q_{xc} \\ q_{yc} \end{bmatrix} \tag{2.46}$$

where the final solution is found by adding on the contribution due to the passive elements. The solution is computed by evaluating the effects of the active elements that can "see" the current calculation point, those elements that do not directly contribute to the solution at the current calculation point have zeros in their columns of (2.46). For circular element $1+$ in (2.46) the calculation point is at the local coordinate (r_{1c}, θ_{1c}), the location of the calculation point in the local coordinates of the element. For the Cartesian fluxes, much of the calculation is shared between the second and third rows, one is projected onto the x-axis, the other onto the y-axis. Obviously, the fluxes could be computed with respect to any desired

coordinate system, but rectangular vector components are typically required by plotting software.

Lastly, the solution is a computed at a vector of values of the Laplace parameter and the time-domain solution is estimated using a numerical inverse Laplace transform algorithm. Several algorithms are discussed in Chapter 5.

Chapter 3
DERIVATION OF ELEMENTS

We cover the derivation of LT-AEM elements for different geometries. Circular, elliptical, and Cartesian 2D coordinates are investigated with general and special case elements derived. 3D elements are explored, to give a feel for the direction this work might proceed.

3.1 Circular elements

In the earliest AEM applications (e.g. Strack and Haitjema, 1981b; Strack, 1989) circles were approximated using polygons of line doublets. Truly circular steady AEM elements were developed by Salisbury (1992) for one or a small number of circles using a complex power series approach, where the trigonometric series are represented in the form of (D.3). Janković (1997) and Barnes and Janković (1999) illustrated the eigenfunction expansion approach, also for the steady-state problem, but showed how it easily extended to numerous circular elements.

Transient circular LT-AEM elements were given by Furman and Neuman (2003) in their LT-AEM proof-of-concept; they are re-derived and extended here in a general framework, illustrating some of the points made for elliptical coordinates in the more familiar polar coordinates, and showing the connection between aquifer test solutions and LT-AEM elements. The solution for a well with a finite radius, with and without wellbore storage is given as a simplified form of an external circular element.

Radial coordinates are defined as $x = r\cos\theta$, $y = r\sin\theta$ with the inverse definitions $r = \sqrt{x^2 + y^2}$ and $\theta = \arctan y/x$. The metric coefficients for standard polar

coordinates are

$$h_r = 1, \qquad h_\theta = r. \tag{3.1}$$

The modified Helmholtz equation (2.3), expressed in circular cylindrical coordinates (Özişik, 1993, §3), is

$$\frac{\partial^2 \bar{\Phi}}{\partial r^2} + \frac{1}{r}\frac{\partial \bar{\Phi}}{\partial r} + \frac{1}{r^2}\frac{\partial^2 \bar{\Phi}}{\partial \theta^2} - \kappa^2 \bar{\Phi} = 0, \tag{3.2}$$

with the condition that $\bar{\Phi}$ is 2π-periodic in θ. By substituting the form $\bar{\Phi}(r,\theta) = B(r)\Theta(\theta)$, this PDE can be separated to the simple harmonic oscillator and modified Bessel ODEs,

$$\frac{\mathrm{d}^2\Theta}{\mathrm{d}\theta^2} + \Theta n^2 = 0, \tag{3.3}$$

$$r\frac{\mathrm{d}}{\mathrm{d}r}\left(\frac{1}{r}\frac{dB}{dr}\right) - \left(\kappa^2 + \frac{n^2}{r^2}\right) B = 0, \tag{3.4}$$

where n is a separation constant. A general solution to (3.3)

$$\Theta_n(\theta) = A\,\cos(n\theta) + C\,\sin(n\theta), \tag{3.5}$$

where $\sin$ and $\cos$ are the eigenfunctions for this problem. The corresponding general solution for (3.4) is

$$B_n(r) = D\,\mathrm{I}_n(r\kappa) + E\,\mathrm{K}_n(r\kappa), \tag{3.6}$$

where I_n and K_n are the first- and second-kind modified Bessel functions (e.g. McLachlan, 1955, §6) and A, C, D, and E are constants. The modified Bessel functions are simply general solutions to (3.4) (not eigenfunctions), taking on a passive role in the calculation. The Bessel functions take on the order (n) dictated by the solution to the periodicity condition associated with (3.3) and their argument is controlled by κ, which includes material properties and the Laplace parameter. The simple harmonic oscillator (3.3) and its solutions (3.5) have no singularities for finite θ. The modified Bessel equation (3.4) has singularities at $r = 0$ and ∞, as do its solutions (3.6) (McLachlan, 1955, p. 185).

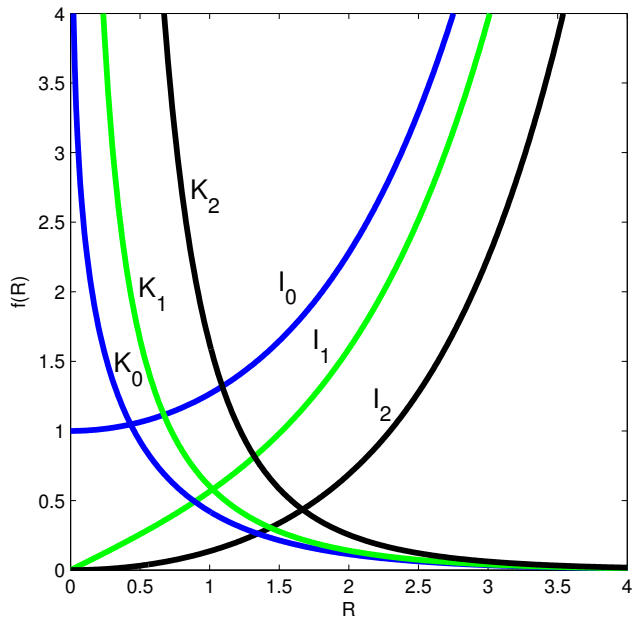

FIGURE 3.1. First- (I_n) and second-kind (K_n) modified Bessel functions of real argument

Enforcing periodicity in θ restricts the separation constant to integer eigenvalues. Recombining the ODE solutions (3.5 and 3.6) and summing over the spectrum of eigenvalues gives general solutions to (3.2) for internal and external elements as

$$\bar{\Phi}_{\mathrm{c}}^{+}(r \geq r_0, \theta) = \sum_{n=0}^{\infty} \mathrm{K}_n(r\kappa) \left(a_n \cos n\theta + b_n \sin n\theta\right), \tag{3.7}$$

$$\bar{\Phi}_{\mathrm{c}}^{-}(r \leq r_0, \theta) = \sum_{n=0}^{\infty} \mathrm{I}_n(r\kappa) \left(c_n \cos n\theta + d_n \sin n\theta\right), \tag{3.8}$$

where a_n, b_n, c_n, and d_n are coefficients to be determined and the radial solutions in (3.7) and (3.8) are chosen based on the fact the solution must remain finite. Normalizing the radial basis functions by their value on the boundary, and truncating

the infinite sum at N terms gives the implemented form of the circular elements as

$$\bar{\Phi}_c^+(r \geq r_0, \theta) \cong \sum_{n=0}^{N-1} \frac{\mathrm{K}_n(r\kappa)}{\mathrm{K}_n(r_0\kappa)} \left(a_n \cos n\theta + b_n \sin n\theta\right), \tag{3.9}$$

$$\bar{\Phi}_c^-(r \leq r_0, \theta) \cong \sum_{n=0}^{N-1} \frac{\mathrm{I}_n(r\kappa)}{\mathrm{I}_n(r_0\kappa)} \left(c_n \cos n\theta + d_n \sin n\theta\right). \tag{3.10}$$

In the LT-AEM formulation used by Furman and Neuman (2004) (which used a fixed-point iteration), the solution inside could be expressed in terms of the solution outside. The simplification is unique to polar coordinates, where the same angular eigenfunctions are used for both interior and exterior elements.

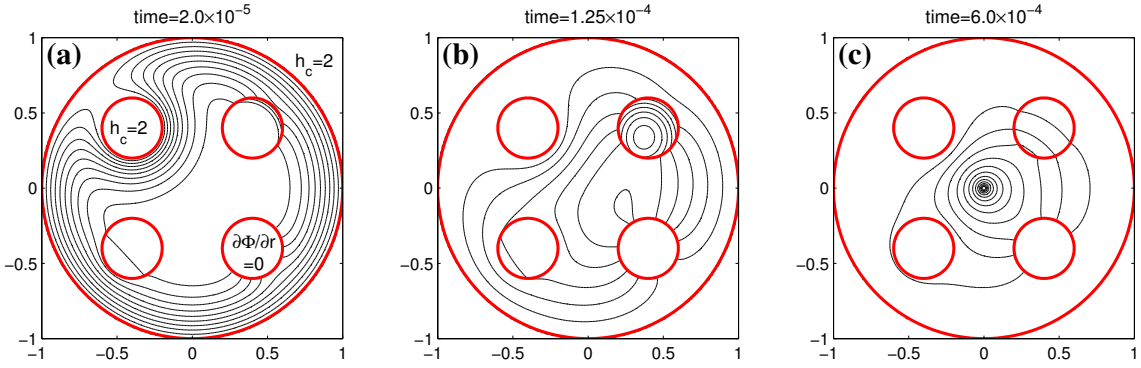

FIGURE 3.2. Contours of head for circular domain with specified head, no-flow, $K > K_{\mathrm{bg}}$, and $K < K_{\mathrm{bg}}$ at three different times. Injection well comes on between b and c

Figure 3.2 is an example of a finite domain using five circular elements and a point source. The outer and upper-left circles are type I BC ($h = 2$), the lower-right circle is a type II BC (no-flow), the lower-left circle is a matching boundary for a region of higher K, and the upper-right circle is a matching boundary for a region of lower K. The initial condition is $h = 1$ everywhere. Panel (a) shows the system at early time, where there are steep gradients around the specified head elements (contour interval = 0.1). Panel (b) shows the system at a later time, when the gradient is flatter across the high-K element, steeper across the low-K element,

and contours are perpendicular to the boundary of the no-flow element. A well begins injecting at $t = 3 \times 10^{-4}$, taking the head in the middle of the domain in panel (c) to levels above those of the specified head boundary conditions.

3.1.1 Well as a circle of small radius (no storage)

A useful simplification of the general circular solutions (3.9) and (3.10) is a circle of small radius. The radius of a well, r_w, is assumed to be small enough that the variation in head across it is negligible. This simplification leads to the finite-radius well source. We begin with the well screen boundary condition of

$$\bar{g}(p)Q = \int_0^{2\pi} \left[r \frac{\partial \bar{\Phi}^+}{\partial r} \right]_{r_w} \mathrm{d}\theta; \tag{3.11}$$

where a general pumping rate is represented by convolution of a general time behavior $g(t)$ and a constant Q, which is $\bar{g}(p)Q$ in Laplace space. Substituting (3.7) into (3.11), we get

$$\frac{\bar{g}(p)Q}{r_w} = \sum_{n=0}^{\infty} \left[\frac{\partial}{\partial r} \mathrm{K}_n(r\kappa) \right]_{r_w} \int_0^{2\pi} \left(a_n \cos n\theta + b_n \sin n\theta \right) \mathrm{d}\theta, \tag{3.12}$$

but due to symmetry only the eigenvalue $n = 0$ survives the integration. Using a recurrence relationship for the derivative of a Bessel function (McLachlan, 1955, p.204), the expression for a_0 is

$$a_0 = \frac{\bar{g}(p)Q}{2\pi r_w} \frac{1}{\mathrm{K}_1(r_w\kappa)}; \tag{3.13}$$

this makes the final expression for the finite-radius well source

$$\bar{\Phi}_{\text{well}}(r) = \bar{g}(p) \frac{Q}{2\pi\kappa r_w} \frac{\mathrm{K}_0(r\kappa)}{\mathrm{K}_1(r_w\kappa)}. \tag{3.14}$$

This solution (for constant Q) was developed by van Everdingen and Hurst (1949) and first given in the hydrology literature by Hantush (1964b). As $r_w \to 0$ it asymptotically simplifies to the Theis (1935) point source solution (2.22) (Lee, 1999,

§4.3.2). Although Theis' point source of infinitesimal radius is commonly used, the finite radius well source is more appropriate when observations are made very close to the pumping well, see Figure 3.3. Capitalizing on the axial symmetry, the plot is in terms of dimensionless time and drawdown

$$t_D = \frac{tK}{S_s r^2}, \qquad s_D = \frac{4\pi(\Phi - \Phi_0)}{Q}. \tag{3.15}$$

Additionally, this more physically realistic solution will be adapted to account for wellbore storage and skin effects in the next section, for which the Theis solution cannot be modified to accommodate.

For $\bar{g}(p) = 1/p$, the solution for the circle of small radius (3.14) is both an LT-AEM element and an analytic solution found in the literature. Passive LT-AEM elements are the simplest type of LT-AEM element, because they usually only have one free parameter (Q in this case). The active element version of (3.14) is found by solving for $\bar{Q} = \bar{g}(p)Q$, where the boundary condition is specified in terms of total head, $\bar{\Phi}_{\text{total}} = \bar{\Phi}_{\text{well}} + \bar{\Phi}_{\text{bg}}$,

$$\bar{Q} = 2\pi\kappa r_w \left(\bar{h}_{\text{BC}} K - \bar{\Phi}_{\text{bg}}\right) \frac{\mathrm{K}_1(r_w\kappa)}{\mathrm{K}_0(r_w\kappa)}. \tag{3.16}$$

Here $\bar{h}_{\text{BC}}$ is the head specified at the well and $\bar{\Phi}_{\text{bg}}$ is the net effect of background elements at the wellscreen (if this is zero, the solution simplifies to an analytic solution for a constant head well). Once $\bar{Q}$ in (3.16) is found, it is substituted into (3.14). Convolution allows arbitrary pumping rates to be assigned to the point source; in this case it is computed in a way to make the head at the well constant in the presence of other elements. This is an example of a well-known analytic solution adapted to be an active LT-AEM element.

If r_w becomes very large (e.g., hand-dug wells or infiltration galleries), both wellbore storage (addressed in the next section) and the variation of the head around the circumference of the well (due to background effects) must be accounted for. The simplification leading to (3.14) cannot be justified, which results

in an expression involving an infinite sum over all the eigenvalues to properly expand the boundary condition at the well. For all the well solutions derived here, we assume minimal change in background effects across the diameter of the well.

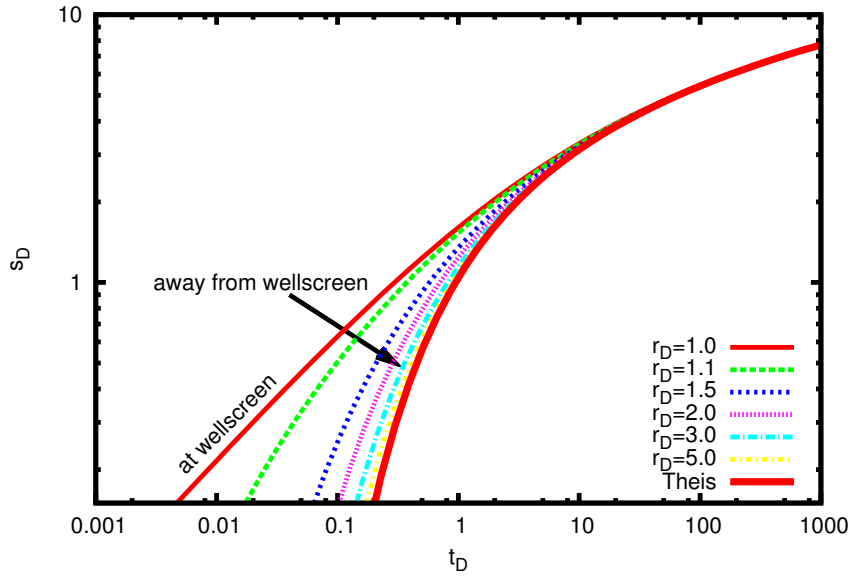

FIGURE 3.3. Finite-radius well solution for a range of $r_D = r/r_w$ values; s_D and t_D are defined in (3.15)

In summary, the most general LT-AEM well solution is (3.9) (i.e, a circle with variable boundary conditions around its circumference); (3.14) is the next most general solution, involving the simplifying assumption that the effects of the well are constant across the well's diameter. Finally, the Laplace space form of the Theis solution (2.22) additionally assumes the wellbore radius itself is insignificant. When $r \geq 5r_w$ (see Figure 3.3) this is a reasonable approximation to the general solution. In most applications, $r_w \leq 30\,\mathrm{cm}$, therefore the effects of the well radius on the solution are only significant within at most $1.5\,\mathrm{m}$ of the well. The finite-radius well solution (in both steady and transient AEM) is often used solely because it avoids the singularity at the well (a problem when computing results onto a grid for contouring), which can occur when the Theis solution is used.

3.1.2 Wellbore storage

For large-diameter pumping wells, especially when aquifer storage is small and observations are made near the pumping well at early time, the effects of wellbore storage can be very significant. Beginning with the finite-radius well solution just derived, these effects can be accounted for, in a manner similar to Papadopulos and Cooper (1967) (who adapted it from the equivalent heat conduction solution of Carslaw and Jaeger (1959, §13.5)), but allowing for matching of elements. The boundary condition is derived from the mass balance for the wellbore (see Figure 3.4), of the form $Q_{\text{in}} - Q_{\text{out}} = \Delta V_{\text{storage}}/\Delta t$,

$$Q_A - Q = C_w \frac{\mathrm{d}s_w}{\mathrm{d}t}, \tag{3.17}$$

where Q_A is the volume flowrate $[\mathrm{L}^3/\mathrm{T}]$ into the well from the aquifer, Q is the volume flowrate leaving the well through the pump, s_w is the drawdown $[\mathrm{L}]$ in the wellbore, and $C_w = \mathrm{d}V_w/\mathrm{d}s_w$ is the coefficient of storage $[\mathrm{L}^2]$ for the wellbore (relating drawdown to change in volume). In open boreholes, $C_w = \pi r_c^2$, where

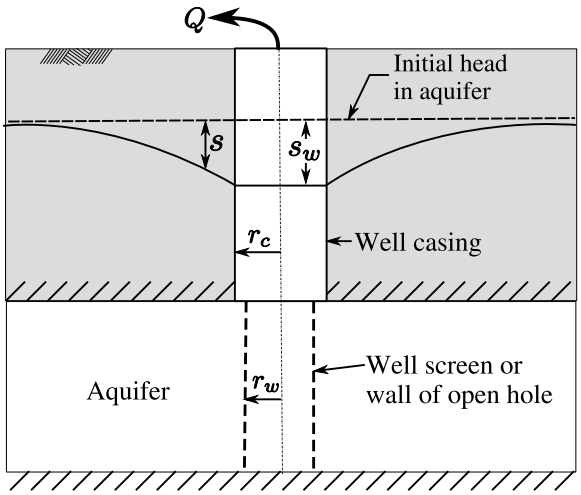

FIGURE 3.4. Large diameter well; adapted from Papadopulos and Cooper (1967)

r_c is the casing radius over the interval where the drawdown of the water table is

taking place. For a pressurized borehole, C_w may need to account for fluid compressibility. Q_A is the total inflow from the aquifer; for an active LT-AEM element this can include the effects of other elements. A general expression for total well inflow is

$$Q_A = \int_0^{2\pi} \left[r \frac{\partial \Phi_{\text{tot}}}{\partial r} \right]_{r_w} \mathrm{d}\theta. \tag{3.18}$$

Assuming that r_w is small enough to ignore the variation in the effects of other elements across the well diameter ($\bar{\Phi}_{\text{tot}}(r_w)$ is constant with respect to θ), (3.17) and (3.18) become

$$2\pi r_w \left[\frac{\partial \Phi_{\text{tot}}}{\partial r} \right]_{r_w} - Q = \frac{\pi r_c^2}{K} \left[\frac{\partial \Phi_{\text{tot}}}{\partial t} \right]_{r_w}, \tag{3.19}$$

after converting drawdown in the wellbore to Φ_{tot} at the well screen. Taking the Laplace transform of (3.19) leads to an inhomogeneous type III boundary condition (2.24) at the well screen,

$$2 \left[\frac{\partial \bar{\Phi}_{\text{tot}}}{\partial r} \right]_{r_w} - \frac{p r_c^2}{K r_w} \bar{\Phi}_{\text{tot}}(r_w) = \frac{\bar{g}(p) Q}{\pi r_w}. \tag{3.20}$$

Here $\bar{\Phi}_{\text{tot}} = \bar{\Phi}_{\text{well}} + \sum \bar{\Phi}_{\text{bg}}$, where $\bar{\Phi}_{\text{well}}$ is (3.14), with $\bar{g}(p) = 1$ and $Q = a_{\text{well}}$ to give an impulse response, with the strength left to be determined. By considering the effects of other elements, a passive well element (3.14) becomes an active one, which must have its coefficient determined at run-time. The solution then becomes

$$\bar{\Phi}_{\text{well}}(r) = \frac{a_{\text{well}}}{2\pi\kappa r_w} \frac{\mathrm{K}_0(r\kappa)}{\mathrm{K}_1(r_w\kappa)}; \tag{3.21}$$

this solution only has one degree of freedom; there is only one eigenvalue. A more general solution could be derived, accounting for the changes in the effects of other elements across the circumference of the well, leading to a general circular element with type III BC of (3.20), but keeping the infinite series of eigenvalues like (3.9).

For a single well (no background elements), the wellbore storage solution has a unit slope on a log-log plot (see Figure 3.5; this figure does not follow the convention of Papadopulos and Cooper (1967), who re-define t_D in terms of r_w), which

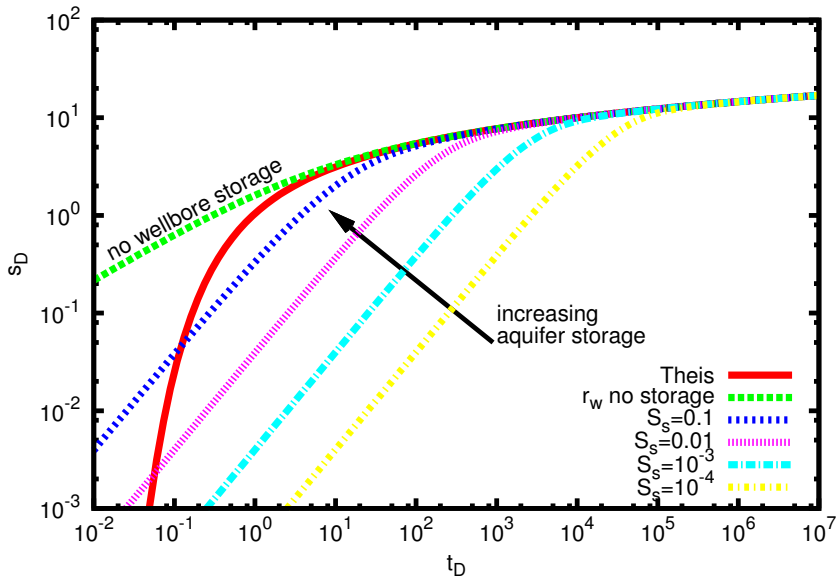

FIGURE 3.5. Drawdown at wellscreen for large-diameter well ($r_c = r_w$); s_D and t_D are defined in (3.15)

is characteristic of drawing water from a finite reservoir (in this case the wellbore). The finite-radius well solution without wellbore storage (3.14) has more drawdown than the point Theis solution (for the same radius from the center of the well), then accounting for the storage of water in the well decreases the observed drawdown. The curves represent different aquifer storage coefficients; if there is more storage available in the aquifer, less must come from the wellbore and therefore the deviation from the Theis solution is smaller. The wellbore storage solution is more useful for aquifer test interpretation than (3.14), because the curves in Figure 3.5 are what would actually be observed in a large-radius pumping well.

Following van Everdingen (1953) (Moench (1984, 1997) in the hydrology literature), an additional skin factor could be added to the formulation of Q_A (3.18) to account for the different permeability associated with a thin under-developed or gravel-packed zone surrounding the wellscreen. This could also be handled using

a small circular LT-AEM element circumscribing the well, to represent the near-well zone more explicitly. This is analogous to the approach taken by Fitts (1991) for steady-state flow to a well in 3D.

3.2 Elliptical elements

Obdam and Veling (1987) and Strack (1989, p. 487) developed steady elliptical elements by conformally mapping the ellipse onto the circle, which had already been solved. Suribhatla et al. (2004) first used the eigenfunction expansion approach to handle many steady elliptical elements.

Transient elliptical elements are derived here using a procedure analogous to that for circles in section 3.1. Bakker (2004a) also derived elliptical AEM elements for the modified Helmholtz equation, in the context of steady flow in a multi-aquifer system. Bakker and Nieber (2004b) and here in Appendix F, elliptical solutions are also derived for the steady linearized unsaturated flow problem. In these applications there is no time dependence, therefore the solutions do not include the parameter p, which becomes large at small time.

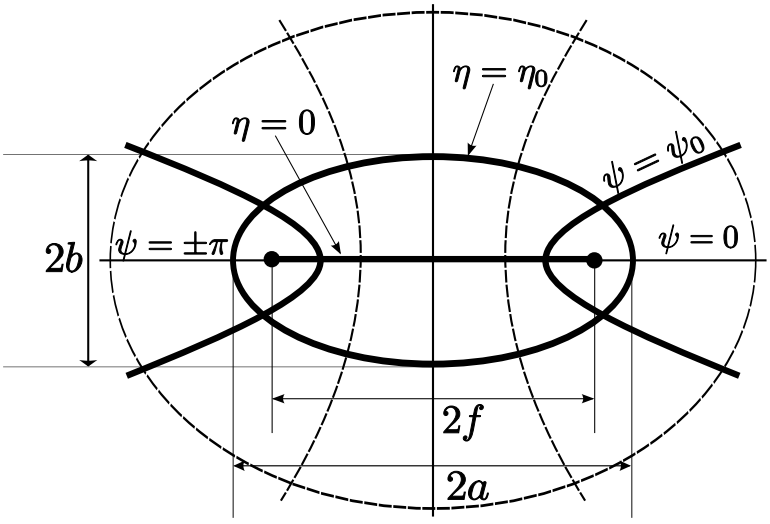

FIGURE 3.6. Components of elliptical coordinates (η, ψ); f, a, and b are semi-focal, -major, and -minor lengths, respectively.

Elliptical coordinates (see Figure 3.6) are defined by

$$x + iy = f\cosh(\eta + i\psi), \tag{3.22}$$

where (η, ψ) are dimensionless elliptical coordinates, and f is the semi-focal length [L]. Equating real and imaginary parts of (3.22) leads to

$$x = f\cosh\eta\cos\psi, \qquad\qquad y = f\sinh\eta\sin\psi. \tag{3.23}$$

These can be used to compute the metric coefficients [L] (see Appendix B),

$$h_\eta = h_\psi = f\sqrt{1/2[\cosh 2\eta - \cos 2\psi]} = f\sqrt{\cosh^2\eta - \cos^2\psi}, \tag{3.24}$$

where the back-transform is $\eta + i\psi = \text{arccosh}\,[(x+iy)/f]$, but the multi-valued complex hyperbolic arc cosine is expressed in terms of a single-valued functions in the form

$$\eta + i\psi = \begin{cases} \ln\left(\frac{x+iy}{f} + \sqrt{\left(\frac{x+iy}{f}\right)^2 - 1}\right) & x > 0 \\ \ln\left(\frac{x+iy}{f} - \sqrt{\left(\frac{x+iy}{f}\right)^2 - 1}\right) & x \leq 0 \end{cases}; \tag{3.25}$$

this convention confines the branch cut to the line between the foci and returns the value corresponding to $\eta > 0$ when $y = 0$.

The modified Helmholtz equation (2.3) in 2D elliptical coordinates (Moon and Spencer, 1961b, p.17) is

$$\frac{2}{f^2\left[\cosh 2\eta - \cos 2\psi\right]}\left[\frac{\partial^2\bar{\Phi}}{\partial\eta^2} + \frac{\partial^2\bar{\Phi}}{\partial\psi^2}\right] - \kappa^2\bar{\Phi} = 0, \tag{3.26}$$

with the condition that $\bar{\Phi}$ is 2π-periodic in ψ. Substituting the form $\bar{\Phi}(\eta,\psi) = H(\eta)\Psi(\psi)$, (3.26) can be separated into the ODEs

$$\frac{\mathrm{d}^2\Psi}{\mathrm{d}\psi^2} + (\omega - 2q\cos 2\psi)\,\Psi = 0, \tag{3.27}$$

$$\frac{\mathrm{d}^2 H}{\mathrm{d}\eta^2} - (\omega - 2q\cosh 2\eta)\,H = 0, \tag{3.28}$$

where ω is a separation constant and $q = -f^2\kappa^2/4$ is the Mathieu parameter. These ODEs are the angular (3.27) and radial (3.28) Mathieu equations. The parameter q is specified through the aquifer properties, element geometry, and p, while the eigenvalues (ω) are determined to make the angular solution periodic (see Appendix E). The solutions to (3.27) and (3.28) are angular and radial Mathieu functions.

3.2.1 Elliptical special functions

Angular Mathieu functions The angular Mathieu equation (3.27) has a general periodic solution, including both even and odd forms,

$$\Psi_n(\psi) = A\,\mathrm{ce}_n(\psi, -q) + B\,\mathrm{se}_n(\psi, -q), \tag{3.29}$$

where A and B are constants and ce_n and se_n are the even (cosine-elliptic) and odd (sine-elliptic) angular Mathieu functions (MF) of order n, argument ψ, and parameter $-q$. The eigenvalues (ω in (3.27) and (3.28)) are different between the even and odd solutions and even and odd orders; this results in four types of angular solutions, described in Table 3.1. Figure 3.7 shows even angular functions for real

function	eigenvalues	major-axis	minor-axis	period
$\mathrm{ce}_{2n}(\psi, -q)$	a_{2n}	symmetric	symmetric	π
$\mathrm{ce}_{2n+1}(\psi, -q)$	b_{2n+1}	symmetric	anti-symmetric	2π
$\mathrm{se}_{2n+1}(\psi, -q)$	a_{2n+1}	anti-symmetric	symmetric	2π
$\mathrm{se}_{2n+2}(\psi, -q)$	b_{2n+2}	anti-symmetric	anti-symmetric	π

TABLE 3.1. Angular Mathieu function types ($q < 0$)

q. For finite ψ and q, (3.27) has no singularities and neither do the angular MF. When $q = 0$ (foreground in Figure 3.7), the functions reduce to their trigonometric counterparts. The zero-order even angular function, $\mathrm{ce}_0(\psi; 0)$, equals $1/\sqrt{2}$ by convention; when $q \neq 0$ it is oscillatory, but it has no zeros. As $|q|$ increases, the functions become more oscillatory, but with the same number of zeros (McLachlan,

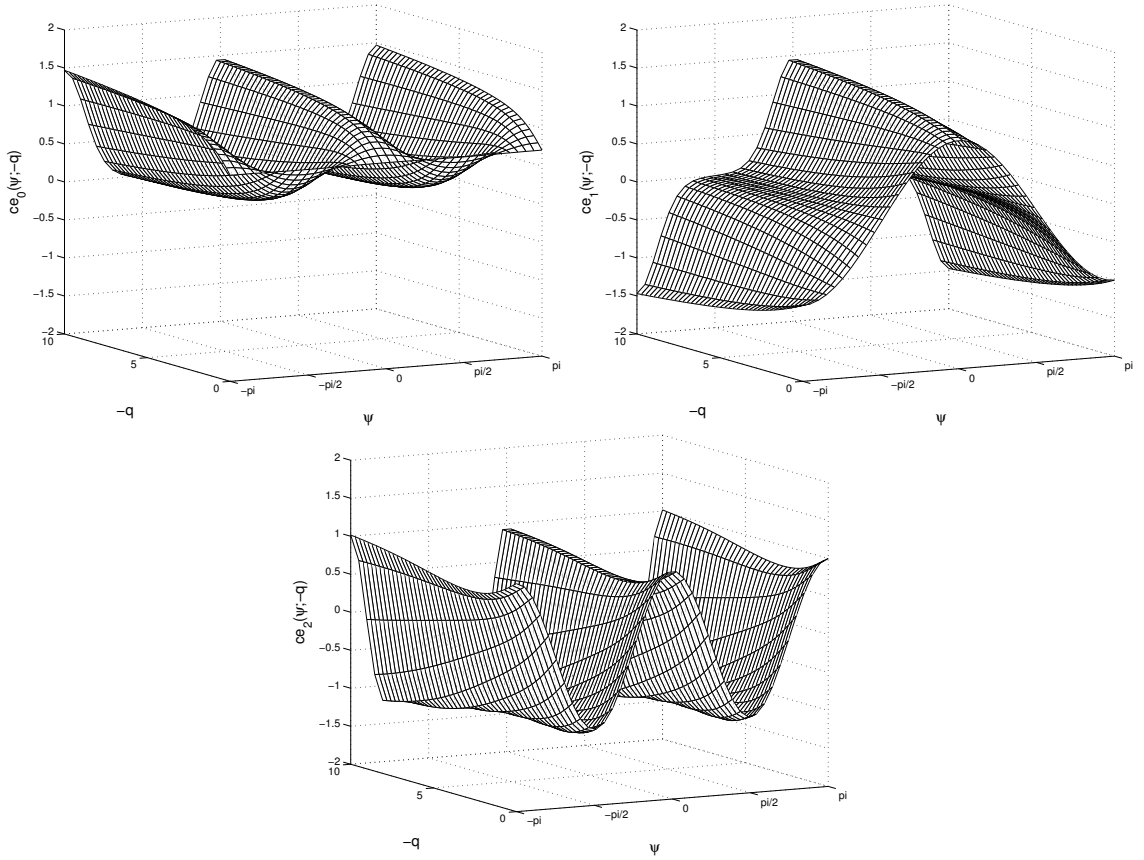

FIGURE 3.7. First three orders of $\mathrm{ce}_n(\psi, -q)$ as functions of both ψ and $-q$

1947, §12); the zeros tend to cluster around $\pm\pi/2$ as $|q| \to \infty$ (as elliptic coordinates approach Cartesian coordinates). Figure 3.8 illustrates the analogous behavior of the odd angular functions, as functions of argument and parameter.

Because $\Psi_n(\psi) = \Psi_n(\psi + 2\pi)$, (3.29) does not include the valid but non-periodic second-kind angular MF; these rarely-used functions are known as $\mathrm{fe}_n(\psi, q)$ and $\mathrm{ge}_n(\psi, q)$ (McLachlan, 1947, §7).

Radial Mathieu functions The radial Mathieu equation (3.28) has a general solution (corresponding to the periodic solution given in (3.29)) of the form

$$H_n(\eta) = C\,\mathrm{Ke}_n(\eta, -q) + D\,\mathrm{Ko}_n(\eta, -q) + E\,\mathrm{Ie}_n(\eta, -q) + F\,\mathrm{Io}_n(\eta, -q). \tag{3.30}$$

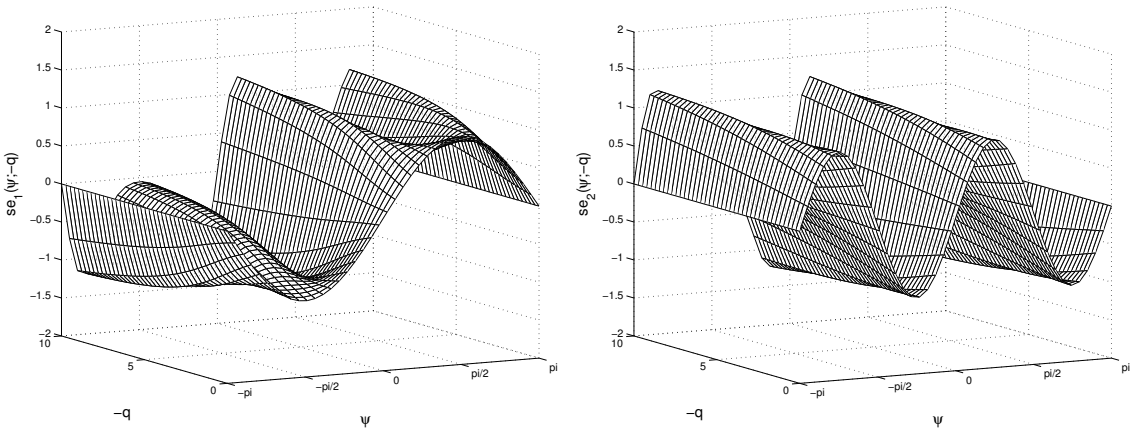

FIGURE 3.8. First two orders of $\mathrm{se}_n(\psi, -q)$ as functions of both ψ and $-q$

where C, D, E, and F are constants, Ie_n and Io_n are even (e) and odd (o) radial MF of the first kind, and Ke_n and Ko_n are the even and odd radial MF of the second kind. All the radial functions in (3.30) are of order n, argument η, and parameter $-q$.

The radial ODE (3.28) has a singularity at $\eta \to \infty$, as does the modified Bessel equation (3.4). But unlike the radial ODE, (3.28) has no singularity at the origin. The first-kind solutions to both the modified Bessel and radial modified Mathieu equations increase exponentially as r and $\eta \to \infty$ (see Figures 3.1 and 3.9). In contrast, when making the transition from circular to elliptical coordinates, the singularity at the origin ($r = 0$) is "spread out" over the line segment $\eta = 0$; the second-kind Mathieu functions become large, but not infinite at the origin, for $q \neq 0$ (see Figure 3.10). Second-kind Bessel functions are singular at $r = 0$ for all integer orders. To aid qualitative comparison with Bessel functions, the radial Mathieu functions are plotted in Figures 3.9 and 3.10, using the physically-based coordinate $\sinh(\eta)$ (Gutiérrez Vega et al., 2003); as $|q|$ increases the first kind solution grows even faster at large distance, while the second kind solution rises slower at the origin, and goes faster to zero as η becomes large.

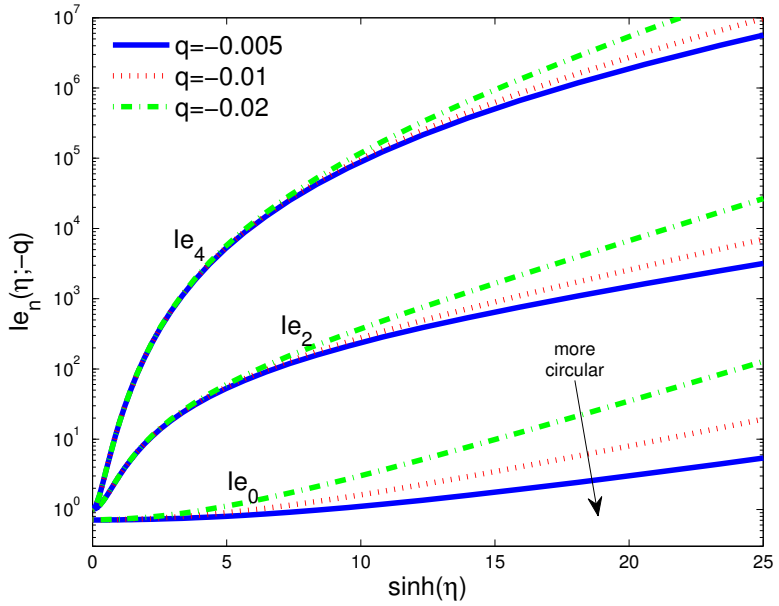

FIGURE 3.9. $\mathrm{Ie}_n(\eta, -q)$ for even n and small values of $-q$. $\mathrm{Io}_n(\eta, -q)$ is similar.

3.2.2 Elliptical PDE solution

When recombining the ODE solutions (3.29 and 3.30) the even/odd cross-products are discarded (since they correspond to different eigenvalues that may only be combined through summation, see Table 3.1), leading to the general solutions of (3.26) for $\Re(q) < 0$

$$\bar{\Phi}_{\mathrm{e}}^{+}(\eta, \psi) = \sum_{n=0}^{\infty} a_n \,\mathrm{Ke}_n(\eta, -q)\,\mathrm{ce}_n(\psi, -q) + \sum_{n=1}^{\infty} b_n \,\mathrm{Ko}_n(\eta, -q)\,\mathrm{se}_n(\psi, -q), \tag{3.31}$$

$$\bar{\Phi}_{\mathrm{e}}^{-}(\eta, \psi) = \sum_{n=0}^{\infty} c_n \,\mathrm{Ie}_n(\eta, -q)\,\mathrm{ce}_n(\psi, -q) + \sum_{n=1}^{\infty} d_n \,\mathrm{Io}_n(\eta, -q)\,\mathrm{se}_n(\psi, -q), \tag{3.32}$$

where a_n, b_n, c_n, and d_n are the coefficients to be determined. Equation 3.31 contains only Ke_n and Ko_n, which are finite as $\eta \to \infty$. Similarly, (3.32) only contains Ie_n and Io_n, which have a continuous value and first derivative across $\eta = 0$ (the focal line). Because $\Re(q) < 0$ these solutions are referred to as modified Mathieu functions, of positive q (analogous to how $\mathrm{I}_n(r)$ and $\mathrm{K}_n(r)$ can be considered mod-

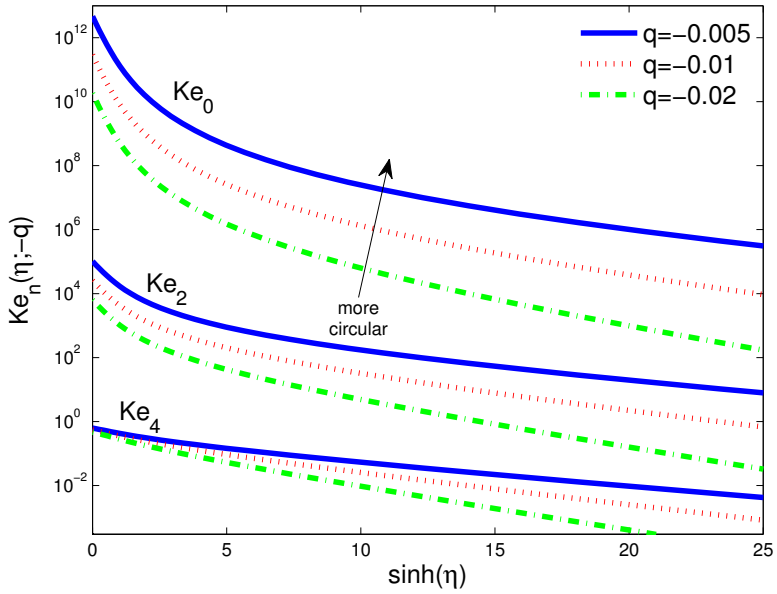

FIGURE 3.10. $\mathrm{Ke}_n(\eta, -q)$ for even n for small values of $-q$. $\mathrm{Ko}_n(\eta, -q)$ is similar.

ified Bessel functions of real argument or related to non-modified Bessel functions of complex argument (e.g. McLachlan, 1955, §6).

To simplify the expression for head matching on the boundary of the ellipse, the radial MF are normalized and the infinite sum is truncated, resulting in

$$\bar{\Phi}_{\mathrm{e}}^{+}(\eta \geq \eta_0, \psi) \cong \sum_{n=0}^{N-1} a_n \frac{\mathrm{Ke}_n(\eta, -q^+)}{\mathrm{Ke}_n(\eta_0, -q^+)} \mathrm{ce}_n(\psi, -q^+) + \sum_{n=1}^{N-1} b_n \frac{\mathrm{Ko}_n(\eta, -q^+)}{\mathrm{Ko}_n(\eta_0, -q^+)} \mathrm{se}_n(\psi, -q^+), \tag{3.33}$$

$$\bar{\Phi}_{\mathrm{e}}^{-}(\eta \leq \eta_0, \psi) \cong \sum_{n=0}^{N-1} c_n \frac{\mathrm{Ie}_n(\eta, -q^-)}{\mathrm{Ie}_n(\eta_0, -q^-)} \mathrm{ce}_n(\psi, -q^-) + \sum_{n=1}^{N-1} d_n \frac{\mathrm{Io}_n(\eta, -q^-)}{\mathrm{Io}_n(\eta_0, -q^-)} \mathrm{se}_n(\psi, -q^-), \tag{3.34}$$

where $\pm$ superscripts on q indicate whether the coefficient involves aquifer parameters from inside $(-)$ or outside $(+)$ the ellipse $\eta = \eta_0$.

The obvious difference between the circular element (3.9) and the elliptical ele-

ment (3.33) is the "even" and "odd" radial functions in elliptical coordinates; radial MF are neither even nor odd, they only share eigenvalues with the even or odd angular MF. A second difference is the appearance of both an argument (η or ψ) and a parameter, $q^{\pm}$, in (3.33) and (3.34). Lastly, both radial and angular MF depend on the coefficients of the PDE (through $q = -[fS_s/(2K)]^2$), while sine and cosine in (3.9) do not, allowing the simplification made by Furman and Neuman (2004) in polar coordinates, but not in elliptical coordinates.

Two contour plots of head illustrating transient effects of a point source and an ellipse of different material properties are shown in Figures 3.11 and 3.12. In Figure 3.11 the head contours are nearly perpendicular to the boundary of the ellipse, although there is a very small component of flow into the ellipse. At $t = 0$, head is zero everywhere; the point source causes mounding in the background surrounding the low-permeability ellipse, but the head remains close to zero inside the ellipse (the steep contours indicate a large gradient, but $K_{\mathrm{e}} = K_{\mathrm{bg}}/1000$, therefore the flux leaving the ellipse is still very small). In the high K ellipse shown in Figure 3.12, the gradient across the ellipse is very flat, due to its high permeability.

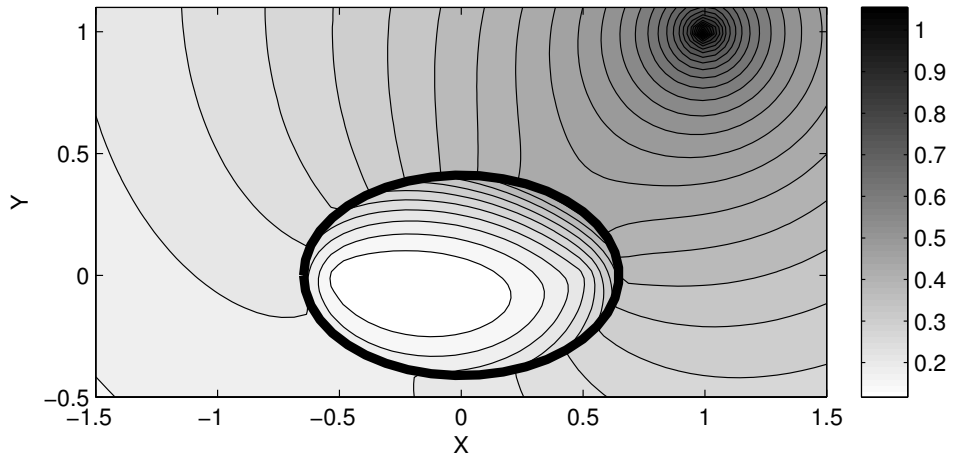

FIGURE 3.11. Head due to a point source near a low permeability ellipse ($K_{\mathrm{e}} = K_{\mathrm{bg}}/1000$)

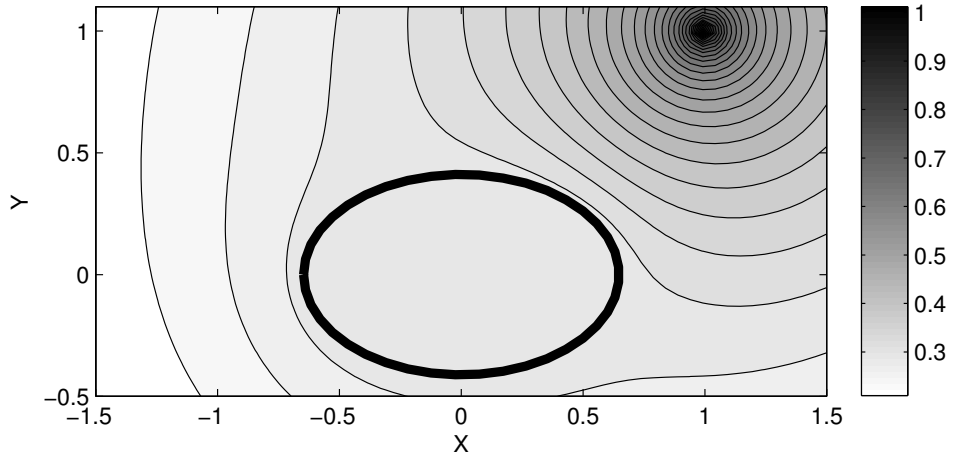

FIGURE 3.12. Head contours due to a point source near a high permeability ellipse ($K_{\mathrm{e}} = 1000 K_{\mathrm{bg}}$)

3.2.3 Specified flux line source

An expression for a line source with a specified spatial distribution of strength (along $y = 0$, from $-f \leq x \leq f$) is obtained from (3.31), using only $\mathrm{ce}_{2n}(\psi, q)$ due to symmetry (see Table 3.1). Normalizing by the radial MF derivative evaluated at $\eta = 0$, $\mathrm{Ke}'_{2n}(0, -q)$, to simplify flux matching, gives

$$\bar{\Phi}_{\text{line}}(\eta, \psi) = \sum_{n=0}^{\infty} \beta_{2n} \, \mathrm{ce}_{2n}(\psi, -q) \, \frac{\mathrm{Ke}_{2n}(\eta, -q)}{\mathrm{Ke}'_{2n}(0, -q)}, \tag{3.35}$$

where β_{2n} are the coefficients to determine. The BC for a specified flux line element in elliptical coordinates is

$$\bar{q}_{\text{BC}}(\psi) = \bar{g}(p) \frac{\lambda}{2f} = -\frac{1}{h_\eta} \frac{\partial \bar{\Phi}_{\text{line}}}{\partial \eta} \bigg|_{\eta = \eta_0}, \tag{3.36}$$

where λ is the constant flowrate $[\mathrm{L}^2/\mathrm{T}]$ for the entire line segment, $2f$ is the length of the line segment, and $\bar{q}_{\text{BC}}(\psi)$ is the normal flux $[\mathrm{L}]$ due to the line source. The metric coefficient (see Appendix B) is required to preserve the correct dimensions.

Differentiating (3.35) with respect to η, evaluating it at $\eta = 0$, and using orthogonality over $0 < \psi < \pi$ gives

$$-\bar{g}(p)\frac{\lambda}{2}\int_0^\pi \sin\psi\,\mathrm{ce}_{2m}^*(\psi,-q)\,\mathrm{d}\psi = \sum_{n=0}^{\infty}\beta_{2n}\int_0^\pi \mathrm{ce}_{2n}(\psi,-q)\,\mathrm{ce}_{2m}^*(\psi,-q)\,\mathrm{d}\psi, \quad (3.37)$$

where $\mathrm{ce}_{2m}(\psi,-q)$ has period π (see Table 3.1). Due to the orthogonality of the angular MF ($*$ is complex conjugate), the integral on the right in (3.37) is 0 for $m \neq n$ and is defined as $\pi/2$ for $m = n$ (McLachlan, 1947, §2.19), reducing the infinite sum to its $(2m)^{th}$ term. The expression for the coefficients is

$$\beta_{2m} = -\bar{g}(p)\frac{\lambda}{\pi}\int_0^\pi \mathrm{ce}_{2m}^*(\psi,-q)\sin\psi\,\mathrm{d}\psi. \quad (3.38)$$

Expanding ce_{2m}^* in terms of its defining infinite cosine series (E.8), and evaluating the resulting integral leaves

$$\beta_{2m} = \bar{g}(p)\frac{2\lambda}{\pi}(-1)^{m+1}\sum_{r=0}^{\infty}(-1)^r\frac{\mathbf{A}_{2r}^{(2m)*}}{1-(2r)^2}, \quad (3.39)$$

where $\mathbf{A}_{2r}^{(2m)}$ are matrices of Mathieu coefficients; their columns are eigenvectors to the angular Mathieu ODE (see Appendix E). The terms in the infinite sum quickly become small as r increases and the largest magnitude terms in $\mathbf{A}_{2r}^{(2m)}$ occur surrounding the diagonal $r \approx m$ (as $q \to 0$, $\mathbf{A}_{2r}^{(2m)}$ becomes a diagonal matrix). Substituting (3.39) back into (3.35) gives the final expression for a constant spatial strength passive line source as

$$\bar{\Phi}_{\text{line}}(\eta,\psi) = \bar{g}(p)\frac{2\lambda}{\pi}\sum_{n=0}^{\infty}(-1)^{n+1}\left[\sum_{r=0}^{\infty}(-1)^r\frac{\mathbf{A}_{2r}^{(2n)*}}{1-(2r)^2}\right]\mathrm{ce}_{2n}(\psi,-q)\,\frac{\mathrm{Ke}_{2n}(\eta,-q)}{\mathrm{Ke}_{2n}'(0,-q)}. \quad (3.40)$$

This formulation of the transient line source is valid for any length line source and can take on different time behaviors through convolution with specific $\bar{g}(p)$. The head distribution due to the constant total flowrate line element expressed in elliptical coordinates is illustrated in Figure 3.13. The line source, expressed as

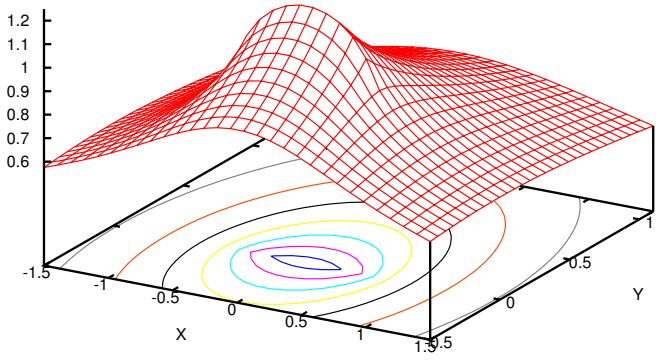

FIGURE 3.13. Head due to specified total flux line source as the ellipse $\eta_0 = 0$

an ellipse of zero radius, is most useful as an active LT-AEM element, where the strength is allowed to vary along the length of the line segment (not simply the constant strength assumed in (3.36)). Analogous to the different point sources discussed in sections 3.1, 3.1.1, and 3.1.2, the elliptical line segment can be assumed to have uniform strength (allowing the coefficients to be computed analytically, as in (3.40)), or can be left more general (3.33). In the more general case, the coefficients of (3.31) are computed at run time (an active element), adjusting to account for the effects of other elements.

3.2.4 Uniform head ellipse

Following a procedure analogous to that above for a flux boundary condition, a passive specified head boundary condition for an elliptical lake or constant head line source is derived. Similarly beginning from (3.31), using only the even-order even functions, but instead normalizing by $\mathrm{Ke}_{2n}(\eta_0, -q)$, gives

$$\bar{\Phi}_{\text{lake}}(\eta \geq \eta_0, \psi) = \sum_{n=0}^{\infty} a_{2n} \mathrm{ce}_{2n}(\psi, -q) \frac{\mathrm{Ke}_{2n}(\eta, -q)}{\mathrm{Ke}_{2n}(\eta_0, -q)}. \tag{3.41}$$

Specifying a constant head at the boundary of the ellipse leaves

$$\bar{\Phi}_{\text{lake}}(\eta \geq \eta_0, \psi) = h_{\text{BC}} K \bar{g}(p) = \sum_{n=0}^{\infty} a_{2n} \mathrm{ce}_{2n}(\psi, -q), \tag{3.42}$$

which can be evaluated for the unknown coefficients using orthogonality of the angular MF. Multiplying by $\mathrm{ce}^*_{2m}(\psi, -q)$ and integrating over $-\pi \leq \psi \leq \pi$, leaves

$$a_{2m} = \frac{h_{\mathrm{BC}} K \bar{g}(p)}{\pi} \int_{-\pi}^{\pi} \mathrm{ce}^*_{2m}(\psi, -q)\, \mathrm{d}\psi. \tag{3.43}$$

The integral can be evaluated by substituting the definition of $\mathrm{ce}^*_{2m}(\psi, -q)$ in terms of its defining cosine series (E.8). This gives

$$a_{2m} = \frac{h_{\mathrm{BC}} K \bar{g}(p)}{\pi} \int_{-\pi}^{\pi} (-1)^m \sum_{r=0}^{\infty} (-1)^r \left[\mathbf{A}^{(2m)}_{2r}\right]^* \cos(2r\psi)\, \mathrm{d}\psi, \tag{3.44}$$

which evaluates to just the $r = 0$ term, leaving only

$$a_{2m} = 2h_{\mathrm{BC}} K \bar{g}(p)(-1)^m \left[\mathbf{A}^{(2m)}_{0}\right]^*. \tag{3.45}$$

Putting (3.45) back into (3.41) gives a passive specified constant head elliptical element (e.g., a lake) as

$$\bar{\Phi}_{\mathrm{lake}}(\eta \geq \eta_0, \psi) = 2h_{\mathrm{BC}} K \bar{g}(p) \sum_{n=0}^{\infty} (-1)^m \left[\mathbf{A}^{(2m)}_{0}\right]^* \mathrm{ce}_{2n}(\psi, -q)\, \frac{\mathrm{Ke}_{2n}(\eta, -q)}{\mathrm{Ke}_{2n}(\eta_0, -q)}. \tag{3.46}$$

A real-variable version of (3.46) was derived by Tranter (1951) for a heat conduction problem. Kucûk and Brigham (1979) applied this solution to flow to a circular well in an anisotropic petroleum reservoir; the circle being distorted into an ellipse by the transformation that rendered the aquifer properties isotropic.

Figure 3.14 shows an example of a line of constant head, simulated using an ellipse with $\eta_0 = 0$. If more than one specified head element is used, (3.46) will not maintain a constant total head; active elements must be used in this case.

3.2.5 Elliptical source in unsaturated media

Appendix F gives the solution for flow from an ellipse due to the boundary condition $h_{\mathrm{BC}} = e^{-a \sin\psi}$ or $h_{\mathrm{BC}} = e^{-b\cos\psi}$; the BC takes this exponential form from the transformations used to linearize Richards' equation. Appendix F is a self-contained manuscript, and therefore has some repetition of definitions and uses

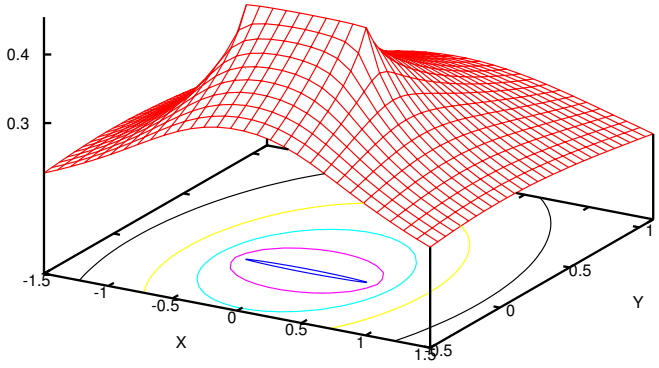

FIGURE 3.14. Head due to constant head line source as the ellipse $\eta_0 = 0$

slightly different conventions in places, because the work is an extension of a circular solution by Philip (1984).

3.3 Cartesian elements

Fitts (1989) modeled steady flow in aquifers using simple potential functions to represent jumps across planes, following an approach detailed by Kellogg (1954, §7). This approach is similar to the method of images (e.g. Lee and Henyey, 1974), which is elegant for some simple geometries, but is not explored fully here.

While 2D Cartesian (i.e., rectangular) coordinates are the most familiar, due to their infinite boundaries the system poses additional complications when used to derive LT-AEM elements by EE. The governing equation (2.3) takes the form

$$\frac{\partial^2 \bar{\Phi}}{\partial x^2} + \frac{\partial^2 \bar{\Phi}}{\partial x^2} - \kappa^2 \bar{\Phi} = 0, \tag{3.47}$$

with the condition that the solution vanishes at $x = \pm\infty$ and $y = \pm\infty$, but no periodicity condition. When separated using $\bar{\Phi}(x, y) = X(x)Y(y)$, (3.47) leads to the two ODEs

$$\frac{\mathrm{d}^2 X}{\mathrm{d}x^2} + n^2 X = 0, \tag{3.48}$$

$$\frac{\mathrm{d}^2 Y}{\mathrm{d}y^2} - (n^2 - \kappa^2) Y = 0, \tag{3.49}$$

where n is a separation constant. In this case, (3.48) is the simple harmonic oscillator and (3.49) is the exponential equation. The general solutions to these ODEs are

$$X(x) = A\,\cos nx + B\,\sin nx, \tag{3.50}$$

$$Y(y) = C\,e^{\sqrt{n^2-\kappa^2}y} + D\,e^{-\sqrt{n^2-\kappa^2}y}, \tag{3.51}$$

where A, B, C, and D are constants. The trigonometric functions in (3.50) are the eigenfunctions, which along with the boundary conditions determine the eigenvalues. For Cartesian coordinates, the ODEs and their solutions have no singularities in the finite plane. The exponential solutions in (3.51) take the passive role in the calculation. Due to the symmetry of Cartesian coordinates, the roles of X and Y can be trivially switched; the choice is made based on the orientation of the matching boundary. If the boundary is parallel to the x-axis, then X should have the eigenfunctions (the simple harmonic oscillator), so that arbitrary boundary conditions can be expanded.

For Cartesian coordinates the eigenvalue spectrum is continuous because the boundary is infinite in length ($-\infty < x < \infty$). The spectrum of eigenvalues behaves quite differently, compared to the standard Sturm Liouville problem (e.g., circular or elliptical boundaries), described in section 2.3.2. Unless the integral (and its back-transformation) can be found using the method of residues or other complex integration techniques, the integral must be approximated asymptotically or as a sum over a large interval.

The approach taken here is to truncate the range to be large but finite, thus retaining the integer eigenvalues and the simplicity that accompanies them. The range is limited to $-W/2 \leq x \leq W/2$, with the condition that $\bar{\Phi}(-W/2, y) = \bar{\Phi}(W/2, y)$ when the boundary is a matching boundary. This assumes that the net effects of other elements is symmetric and centered on the line segment at $x = 0$. This severe limitation is due to the approximate nature of the approach taken here.

A more correct and general approach would involve the entire infinite boundary or, for a simple arrangement of a few elements, the method of images.

Normalizing the interval to 2π and forcing the eigenfunctions to be periodic gives the following eigenvalues and eigenfunctions in x and corresponding passive exponential solutions in y

$$X_n(x) = A_n \cos\left(\frac{2n\pi x}{W}\right) + B_n \sin\left(\frac{2n\pi x}{W}\right), \tag{3.52}$$

$$Y_n(y) = C_n \exp\left[\pm y\sqrt{\left(\frac{2n\pi}{W}\right)^2 - \kappa^2}\right], \tag{3.53}$$

where $n = 1, 2, 3, \ldots$. Since each eigenfunction satisfies the ODE and the boundary conditions at $x = \pm W/2$, any sum of them will also. The coefficients are determined by matching boundary conditions along the boundary parallel to the x-axis.

For Cartesian elements local coordinates are defined so that $y \geq 0$, therefore only the negative exponential is used for all n. This forces the exponentials to automatically satisfy the condition that the effects of the line element die off at large distance (y) from the line.

Recombining the solutions gives the expression for a truncated Cartesian element as

$$\begin{aligned}\bar{\Phi}(|x| \ll W, y \geq 0) = &\sum_{n=0}^{\infty} e^{-y\sqrt{\left(\frac{2n\pi}{W}\right)^2 - \kappa^2}} \\ &\times \left[a_n \cos\left(\frac{2n\pi x}{W}\right) + b_n \sin\left(\frac{2n\pi x}{W}\right)\right].\end{aligned} \tag{3.54}$$

One drawback to these singular Cartesian elements is the requirement that the solution be equal at $x = \pm W/2$.

3.4 Three-dimensional elements

While we do not develop or implement all the details of 3D LT-AEM elements here, some related generalities are discussed. First, to use the EE approach, Helmholtz-

separable 3D coordinates must be identified; the following references list the coordinates with information regarding their solution: Morse and Feshbach (1953, p.655–666), Moon and Spencer (1961b, p.1–48), Ben-Menahem and Singh (2000, p.53), and Arscott and Darai (1981). Geometrically, the 11 3D coordinates in Table 3.2 can be grouped into three categories: cylindrical, rotational and general. Cylindrical coordinates are essentially the 2D coordinates already considered, but extruded in the third dimension. Rotational coordinates come from rotating 2D coordinates about an axis of symmetry. General coordinates cannot be derived from 2D coordinates. Circular cylinder coordinates can be considered either cylindrical (extrude polar coordinates perpendicular to xy-plane) or rotational (rotate Cartesian coordinates about x or y axis).

coordinate system	finite boundary	singular element	infinite boundary	modified Helmholtz special functions
		Cylindrical		
Cartesian	*none*	plane	plane	exponential
circular	*none*	∞ line	circ. tube	mod. Bessel
elliptical	*none*	∞ strip	ellip. tube	mod. Mathieu
parabolic	*none*	half-plane	parabola	Weber
		Rotational		
spherical	sphere	point	cone	sph. Bessel, associated Legendre
prolate spheroidal	spheroid	line segment	hyperboloid	spheroidal wave
oblate spheroidal	spheroid	circ. disc	hyperboloid	spheroidal wave
parabolic	*none*	parabolic disc	paraboloid	Tricomi
		General		
conical	sphere	point	ellip. cone	sph. Bessel, Lamé
ellipsoidal	ellipsoid	ellip. disc	hyperboloids	ellipsoidal wave
paraboloidal	*none*	plane	paraboloids	Whittaker-Hill

TABLE 3.2. Helmholtz-separable 3D coordinate systems (sph. = spherical, mod. = modified, circ. = circular, ellip. = elliptical)

Cylindrical systems appear in both Table 3.2 and Table 2.1, but they behave

differently. In 2D both polar and elliptical coordinates have finite boundaries (the circumferences of the circle or ellipse); these finite 2D curves become infinite 3D surfaces when extruded parallel to the z-axis (perpendicular to the other two dimensions). All the entries in the cylindrical section can also have a plane as an ∞ boundary, but this is only listed under the Cartesian coordinate.

For 3D, the rotational coordinate systems take the role that the cylindrical ones had in 2D; the point, line and circular disc are represented simply as the degenerate spherical, prolate spheroidal (cigar shaped), and oblate spheroidal (discus shaped) coordinate systems, respectively. The main obstacle to overcome for the non-spherical rotational systems is the evaluation of the special functions that arise when separating the modified Helmholtz equation in these systems. Spheroidal wave functions require analogous solution techniques to Mathieu functions. First, an eigenvalue problem is solved to compute valid parameter values, then the functions are evaluated using definitions in terms of infinite series of Associated Legendre and spherical Bessel functions (e.g. Thompson, 1999; Aquino et al., 2002; Li et al., 2002).

The ellipsoidal coordinate system is regarded as the most general 3D system; any of the other 3D systems can be obtained from it by stretching, compressing or translating coordinates (Arscott and Darai, 1981), analogous to how the 2D coordinate systems in Table 2.1 can be derived from the 2D elliptical system. The general coordinate systems are quite esoteric, rarely being used in application for the Helmholtz equation, due to the difficult special functions that arise (Arscott, 1964, §9–10). All 3D coordinate systems (especially rotational and general) have much simpler special functions for the Laplace equation, where they see more application. Applications include steady-state AEM (e.g. Fitts, 1991; Janković and Barnes, 1999; Suribhatla, 2007), gravitational potential (e.g. Kellogg, 1954), and electrostatics (e.g. Hobson, 1931; Moon and Spencer, 1961a; Sten, 2006).

The 3D cylindrical analogs to the 2D coordinate systems utilized already are

briefly discussed, mentioning the special functions which arise and how boundary matching changes between two and three dimensions. Some remarks on the solvability of the coordinate systems in Table 3.2 is given in section E.1, in the context of Mathieu functions.

3.4.1 Cylindrical coordinates

Cylindrical 3D coordinates are conceptually the most straightforward extension of the 2D coordinates already given, because they only have an additional second-order z derivative, otherwise keeping the 2D special functions and adding one additional set, with some slight modifications due to the additional set of eigenvalues. The issues related to the transition of the eigenvalues from the integers to real numbers, as the interval width $\to \infty$ (section 3.3) also applies to the z-dimension in all the cylindrical coordinates.

Circular cylinder The governing equation (2.3) in circular cylinder coordinates (see Figure 3.15) is

$$\frac{\partial^2\bar{\Phi}}{\partial r^2} + \frac{1}{r}\frac{\partial\bar{\Phi}}{\partial r} + \frac{1}{r^2}\frac{\partial^2\bar{\Phi}}{\partial\theta^2} + \frac{\partial^2\bar{\Phi}}{\partial z^2} = \kappa^2\bar{\Phi}, \tag{3.55}$$

with the condition that $\bar{\Phi}$ is 2π-periodic in θ. Substituting the form $\bar{\Phi}(r,\theta,z) = B(r)\Theta(\theta)Z(z)$, this PDE separates into three ODEs (Moon and Spencer, 1961b, p.15),

$$r\frac{\mathrm{d}}{\mathrm{d}r}\left(\frac{1}{r}\frac{dB}{dr}\right) - \left(\kappa^2 + \nu^2 + \frac{n^2}{r^2}\right)B = 0, \tag{3.56}$$

$$\frac{\mathrm{d}^2\Theta}{\mathrm{d}\theta^2} + \Theta n^2 = 0,$$

$$\frac{\mathrm{d}^2 Z}{\mathrm{d}z^2} + Z\nu^2 = 0, \tag{3.57}$$

a slightly different modified Bessel equation (3.4) and two simple harmonic oscillators (SHO). The Bessel equation now involves two separation constants (n and ν) along with the physically-specified parameter, κ). The SHO in terms of Θ is the

same as the 2D case, (3.3), while the SHO in terms of Z involves the the second separation constant, ν. Solutions to these ODEs take the form

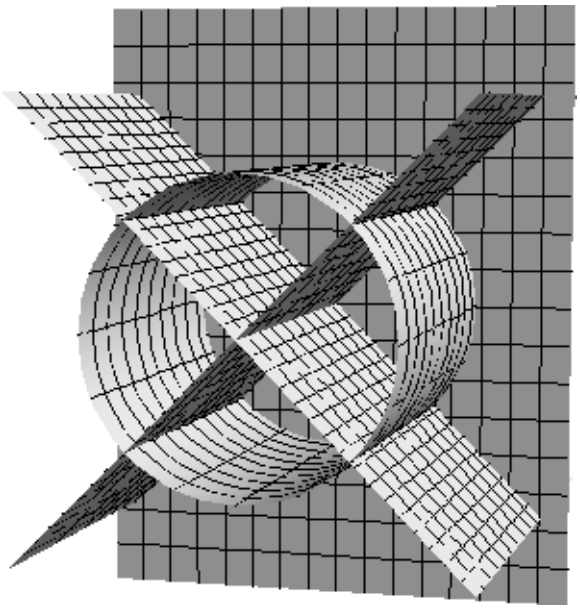

FIGURE 3.15. Surfaces of constant circular cylindrical coordinates; cylinder is $r = 0.6$, rays are $\theta = \pm\frac{\pi}{4}, \pm\frac{3\pi}{4}$, plane is $z = 0.5$.

$$\Theta_n(\theta) = A\,\cos(n\theta) + C\,\sin(n\theta),$$

$$B_{n,\nu}(r) = D\,\mathrm{I}_n(r\sqrt{\nu^2+\kappa^2}) + E\,\mathrm{K}_n(r\sqrt{\nu^2+\kappa^2}), \tag{3.58}$$

$$Z_\nu(z) = F\,\cos(\nu z) + G\,\sin(\nu z), \tag{3.59}$$

where A, C, D, E, F and G are constants. Compared to the 2D case, there is an additional set of eigenvalues to determine; n are controlled by periodicity, $\Theta_n(\theta) = \Theta_n(\theta + 2\pi)$, the ν eigenvalues are determined by the z-coordinate. As an example, the solution inside a circular cylinder (assuming a finite z-interval to ensure integer ν eigenvalues) would take the form

$$\bar{\Phi}^-(r \le r_0, \theta, z_a \le z \le z_b) = \sum_{n=0}^{\infty}\sum_{\nu=0}^{\infty} \mathrm{I}_n(r\beta)\,[a_n\cos(n\theta) + b_n\sin(n\theta)] \times [c_\nu\cos(\nu z) + d_\nu\sin(\nu z)]\,; \tag{3.60}$$

the doubly-infinite sum is characteristic of 3D problems, where multiple eigenvalues are used.

Elliptic cylinder The PDE in elliptic cylinder coordinates (see Figure 3.16) is

$$\frac{2}{f^2\left[\cosh 2\eta - \cos 2\psi\right]}\left[\frac{\partial^2\bar{\Phi}}{\partial\eta^2} + \frac{\partial^2\bar{\Phi}}{\partial\psi^2}\right] + \frac{\partial^2\bar{\Phi}}{\partial z^2} = \kappa^2\bar{\Phi} \tag{3.61}$$

with the condition that $\bar{\Phi}$ is 2π-periodic in ψ. (3.61) can be separated by substituting the form $\bar{\Phi}(\eta,\psi,z) = H(\eta)\Psi(\psi)Z(z)$, leading to the ODEs (Moon and Spencer, 1961b, p.19)

$$\frac{\mathrm{d}^2\Psi}{\mathrm{d}\psi^2} + (\omega - 2\tilde{q}\cos 2\psi)\,\Psi = 0, \tag{3.62}$$

$$\frac{\mathrm{d}^2 H}{\mathrm{d}\eta^2} - (\omega - 2\tilde{q}\cosh 2\eta)\,H = 0, \tag{3.63}$$

$$\frac{\mathrm{d}^2 Z}{\mathrm{d}z^2} + Z(\nu^2 - \kappa^2) = 0, \tag{3.64}$$

where ω is the separation constant associated with periodicity in ψ, $\tilde{q} = -f^2\nu^2/4$ is a Mathieu parameter that no longer involves the physically-determined parameter κ, but instead ν, the second separation constant. The general solutions to these

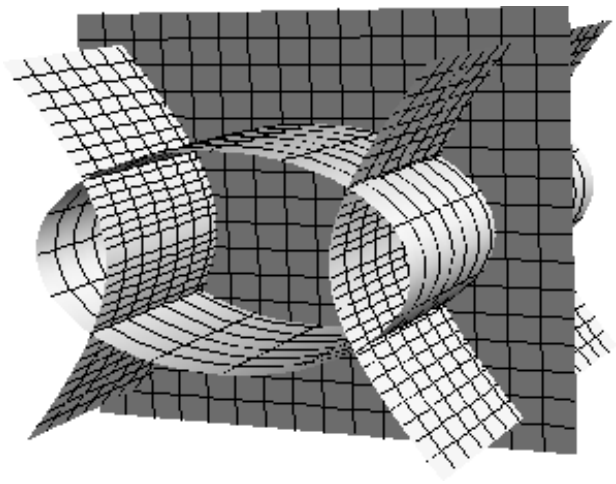

FIGURE 3.16. Surfaces of constant elliptical cylindrical coordinates; $f = 0.75$, cylinder is $\eta = 0.6$, hyperbolas are $\psi = \pm\frac{\pi}{4}, \pm\frac{3\pi}{4}$, plane is $z = 0.5$.

ODEs are

$$\Psi_{n,\nu}(\psi) = A\,\mathrm{ce}_n(\psi;-\tilde{q}) + B\,\mathrm{se}_n(\psi;-\tilde{q}), \tag{3.65}$$

$$H_{n,\nu}(\eta) = C\,\mathrm{Ke}_n(\eta;-\tilde{q}) + D\,\mathrm{Ko}_n(\eta;-\tilde{q}) + E\,\mathrm{Ie}_n(\eta;-\tilde{q}) + F\,\mathrm{Io}_n(\eta;-\tilde{q}), \tag{3.66}$$

$$Z_{n,\nu}(z) = G\,\cos\left(z\sqrt{\nu^2-\kappa^2}\right) + J\,\sin\left(z\sqrt{\nu^2-\kappa^2}\right), \tag{3.67}$$

where the dependence on ν in the two Mathieu solutions (3.65 and 3.66) comes about through the definition of $\tilde{q}$ and A, B, C, D, E, F, G, and J are constants. The Mathieu functions are computed for a given value of the Mathieu coefficient (see Appendix E), which in this case depends on ν, requiring the eigenvalues in the z-direction to be computed first.

3D Cartesian The simplest extension from 2D to 3D coordinates is in Cartesian, where due to the unit metric coefficients, the problem does not change much. The governing equation simply is

$$\frac{\partial^2\bar{\Phi}}{\partial x^2} + \frac{\partial^2\bar{\Phi}}{\partial y^2} + \frac{\partial^2\bar{\Phi}}{\partial z^2} = \kappa^2\bar{\Phi} \tag{3.68}$$

with no periodicity condition. (3.68) is separated into the same ODEs given in section 3.3, but with an additional set of functions and eigenvalues, analogous to those above. The ODEs are

$$\frac{\mathrm{d}^2X}{\mathrm{d}x^2} + n^2X = 0, \tag{3.69}$$

$$\frac{\mathrm{d}^2Y}{\mathrm{d}y^2} + \nu^2Y = 0, \tag{3.70}$$

$$\frac{\mathrm{d}^2Z}{\mathrm{d}z^2} + Z(n^2+\nu^2-\kappa^2) = 0, \tag{3.71}$$

where the X and Y parts of the problem are SHOs (with sines and cosines as solutions) and the Z portion is the exponential equation, with $\pm$ exponentials as solutions. Again, due to the symmetry of Cartesian coordinates, the roles of the eigenfunctions can be switched trivially.

3.4.2 Rotational coordinates

Though spherical coordinates are the only rotational coordinate system in common use, prolate and oblate spheroidal coordinates could be developed to represent the 3D line segment and circular disc as singular elements, using an approach similar to that for 2D elliptical coordinates (see Appendix E).

Spherical coordinates The PDE in spherical coordinates is (Özişik, 1993, §4)

$$\frac{\partial^2\bar{\Phi}}{\partial r^2} + \frac{2}{r}\frac{\partial\bar{\Phi}}{\partial r} + \frac{1}{r^2\sin\theta}\frac{\partial}{\partial\theta}\left[\sin\theta\frac{\partial\bar{\Phi}}{\partial\theta}\right] + \frac{1}{r^2\sin^2\theta}\frac{\partial^2\bar{\Phi}}{\partial\psi^2} = \kappa^2\bar{\Phi} \tag{3.72}$$

with the conditions that $\bar{\Phi}$ is 2π-periodic in ψ and π-periodic in θ. Some representative surfaces in this coordinate system are shown in Figure 3.17; detailed illustrations of this and all other coordinate systems discussed here are found in the physics literature (e.g. Morse and Feshbach, 1953; Moon and Spencer, 1961a,b). Substituting the form $\bar{\Phi}(r,\theta,\phi) = B(r)\Theta(\theta)\Psi(\psi)$ leads to the ODEs

$$\frac{\mathrm{d}^2\Psi}{\mathrm{d}\psi^2} + n^2\Psi = 0, \tag{3.73}$$

$$r\frac{\mathrm{d}}{\mathrm{d}r}\left(\frac{1}{r}\frac{\mathrm{d}B}{\mathrm{d}r}\right) - \left[\kappa^2 + \left(\nu^2 + \frac{1}{2}\right)\frac{1}{r^2}\right]B = 0, \tag{3.74}$$

$$\frac{\mathrm{d}}{\mathrm{d}\theta}\left[\left(1-\theta^2\right)\frac{\mathrm{d}\Theta}{\mathrm{d}\theta}\right] + \left[\nu(\nu+1) - \frac{n^2}{1-\theta^2}\right]\Psi = 0. \tag{3.75}$$

These are the SHO (3.73), modified spherical Bessel (3.74), and associated Legendre (3.75) equations. General solutions to these ODEs are

$$\Psi_n(\psi) = A\,\cos(n\psi) + C\,\sin(n\psi), \tag{3.76}$$

$$B_n(r) = D\,\mathrm{I}_{n+\frac{1}{2}}(\kappa r) + E\,\mathrm{I}_{-(n+\frac{1}{2})}(\kappa r), \tag{3.77}$$

$$\Theta_{n,\nu}(\theta) = F\,\mathrm{P}_\nu^n(\theta) + G\,\mathrm{Q}_\nu^n(\theta), \tag{3.78}$$

where A, C, D, E, F, and G are constants, $\mathrm{P}_\nu^n(\theta)$ and $\mathrm{Q}_\nu^n(\theta)$ are associated Legendre functions (Abramowitz and Stegun, 1964, §8), and $\mathrm{I}_{\pm(n+\frac{1}{2})}$ are the fractional-order modified Bessel functions. Modified spherical Bessel functions of positive

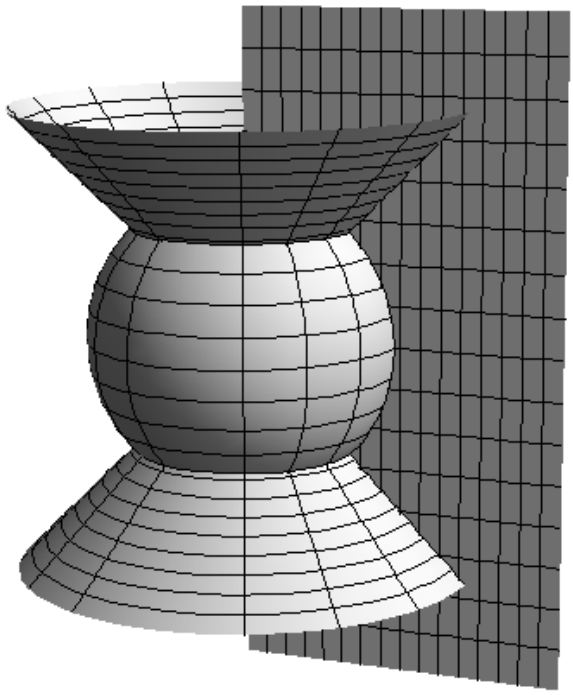

FIGURE 3.17. Surfaces of constant spherical coordinates; sphere is $r = 0.6$, cones are $\theta = \frac{\pi}{4}, \frac{3\pi}{4}$, plane is $\psi = \frac{\pi}{2}$.

fractional order are orthogonal to those of negative fractional order of the same kind; $\mathrm{K}_{n+\frac{1}{2}}$ are possible, but not needed here. There are several other possible separated equations and solutions for spherical coordinates, using simplifications arising from different symmetries (Özişik, 1993).

Spheroidal coordinates The two spheroidal coordinates are obtained from rotating the 2D elliptical coordinate system about its major (prolate) and minor (oblate) axes.

Prolate spheroid In prolate spheroidal coordinates (see Figure 3.18), the degenerate element is a line segment joining the two foci. Fitts (1991) simulated steady-state flow to a 3D line source with this coordinate system. The modified Helmo-

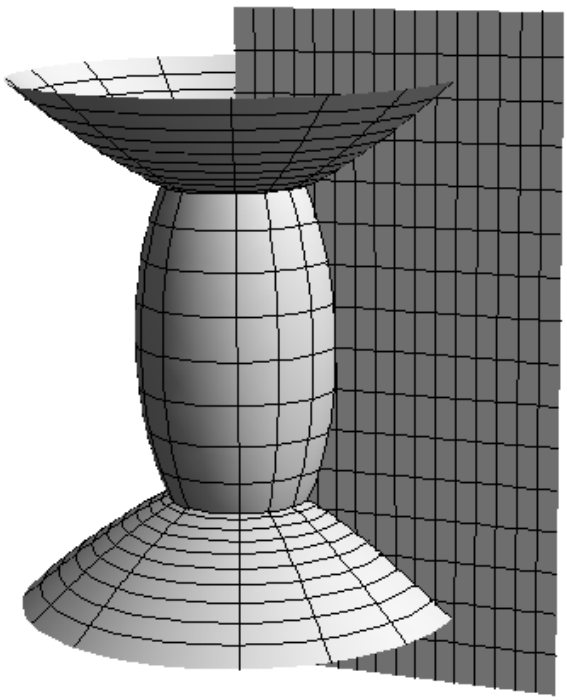

FIGURE 3.18. Surfaces of constant prolate spheroidal coordinates; $f = 0.75$, prolate spheroid is $\eta = 0.5$, hyperboloids of two sheets are $\theta = \frac{\pi}{4}, \frac{3\pi}{4}$, plane is $\psi = \frac{\pi}{2}$.

holtz equation is given as

$$\frac{1}{f^2\left(\sinh^2\eta + \sin^2\theta\right)}\left[\frac{\partial^2\bar{\Phi}}{\partial\eta^2} + \coth\eta\frac{\partial\bar{\Phi}}{\partial\eta} + \frac{\partial^2\bar{\Phi}}{\partial\theta^2} + \cot\theta\frac{\partial\bar{\Phi}}{\partial\theta}\right] + \frac{1}{f^2\sinh^2\eta\sin^2\theta}\frac{\partial^2\bar{\Phi}}{\partial\psi^2} = \kappa^2\bar{\Phi}; \tag{3.79}$$

with the condition that $\bar{\Phi}$ is 2π-periodic in ψ and π-periodic in θ. Substituting the form $\bar{\Phi}(\eta,\theta,\psi) = H(\eta)\Theta(\theta)\Psi(\psi)$ leads to the separated ODEs

$$\frac{\mathrm{d}^2H}{\mathrm{d}\eta^2} + \coth\eta\frac{\mathrm{d}H}{\mathrm{d}\eta} - \left[\kappa^2f^2\sinh^2\eta + n(n+1) + \frac{\nu^2}{\sinh^2\eta}\right]H = 0, \tag{3.80}$$

$$\frac{\mathrm{d}^2\Theta}{\mathrm{d}\theta^2} + \cot\theta\frac{\mathrm{d}\Theta}{\mathrm{d}\theta} - \left[\kappa^2f^2\sin^2\theta - n(n+1) + \frac{\nu^2}{\sin^2\theta}\right]\Theta = 0, \tag{3.81}$$

$$\frac{\mathrm{d}^2\Psi}{\mathrm{d}\psi^2} + \nu^2\Psi = 0. \tag{3.82}$$

Equations (3.80) and (3.81) are forms of the spheroidal wave equation, with solutions analogous to angular and radial Mathieu functions, but comprised of infinite

series of Legendre functions (Chu and Stratton, 1941). (3.82) is the simple harmonic oscillator. These functions and their properties are summarized in Thompson (1999) and Aquino et al. (2002), and given in great detail in Morse and Feshbach (1953), Arscott (1964), and Li et al. (2002).

Oblate spheroid Oblate spheroidal coordinates (see Figure 3.19) have a circular disc as the degenerate element of the system; the two foci of the 2D ellipse form a ring when rotated about the minor axis of the ellipse. A circular hole in a confining

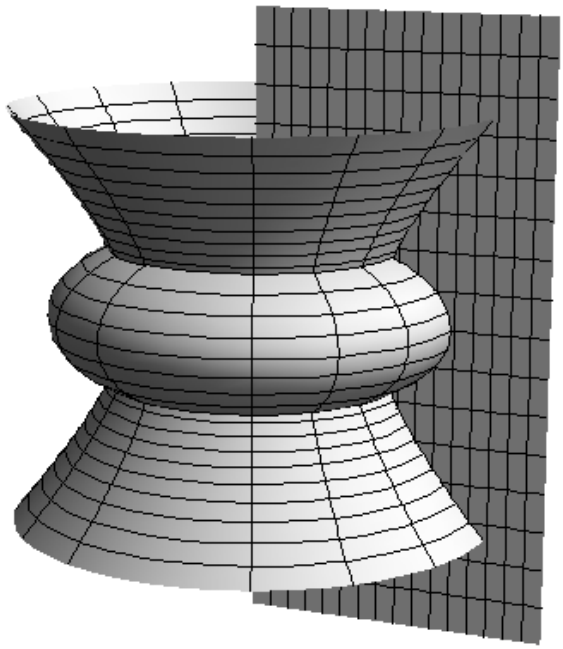

FIGURE 3.19. Surfaces of constant oblate spheroidal coordinates; $f = 0.75$, oblate spheroid is $\eta = 0.5$, hyperboloids of one sheet is $\theta = \frac{\pi}{4}, \frac{3\pi}{4}$, plane is $\psi = \frac{\pi}{2}$.

layer or 3D flow from a circular recharge area could be simulated naturally using this coordinate system. The governing equation is given as

$$\frac{1}{f^2\left(\cosh^2\eta - \sin^2\theta\right)}\left[\frac{\partial^2\bar{\Phi}}{\partial\eta^2} + \tanh\eta\frac{\partial\bar{\Phi}}{\partial\eta} + \frac{\partial^2\bar{\Phi}}{\partial\theta^2} + \cot\theta\frac{\partial\bar{\Phi}}{\partial\theta}\right] + \frac{1}{f^2\cosh^2\eta\sin^2\theta}\frac{\partial^2\bar{\Phi}}{\partial\psi^2} = \kappa^2\bar{\Phi}, \tag{3.83}$$

which has the same periodicity as (3.79) and the two systems are clearly very similar; more specifically, one can go from one to the other by transformations of the form $f = if$ and $\eta = i\eta$. Similarly substituting the separated form leads to the following ODEs

$$\frac{\mathrm{d}^2 H}{\mathrm{d}\eta^2} + \tanh\eta \frac{\mathrm{d}H}{\mathrm{d}\eta} - \left[\kappa^2 f^2 \cosh^2\eta + n(n+1) - \frac{\nu^2}{\cosh^2\eta}\right] H = 0, \tag{3.84}$$

$$\frac{\mathrm{d}^2 \Theta}{\mathrm{d}\theta^2} + \cot\theta \frac{\mathrm{d}\Theta}{\mathrm{d}\theta} + \left[\kappa^2 f^2 \sin^2\theta + n(n+1) - \frac{\nu^2}{\sin^2\theta}\right] \Theta = 0, \tag{3.85}$$

$$\frac{\mathrm{d}^2 \Psi}{\mathrm{d}\psi^2} + \nu^2 \Psi = 0, \tag{3.86}$$

which have analogous solutions as the prolate spheroidal coordinate system.

3.4.3 3D summary

As avenues for extending LT-AEM to 3D problems, cylindrical and spherical geometries would be conceptually straightforward. Spheroidal (prolate and oblate) coordinates would be useful geometries to implement (the line segment and circular plate are degenerate elements in these systems), but requiring development of solutions analogous to that done for Mathieu functions here (see Appendix E). Cylindrical coordinates may have the simplest special functions, but their infinite boundaries lead to continuous eigenvalue problems, rather than discrete (integer) eigenvalues, and therefore one must either deal with convergence issues due to truncating or intersecting boundaries or deal with integrals over the continuous eigenvalues. The parabolic and general coordinate systems do not appear to be readily solvable or useful for the modified Helmholtz equation in hydrologic problems.

Chapter 4
DISTRIBUTED SOURCES

Source terms often arise because a process is not explicitly simulated, therefore it must be represented as a lumped or distributed source. Sources may arise because we ignore the details of a physical, chemical, or biological process, representing the net effect as a source term. Additionally, a source can be used to account for an entire spatial dimension; boundary conditions with respect to a dimension not simulated lead to distributed sources.

Both fluid transfer between matrix and continuum (i.e., dual-domain behavior) and the effects that inertia have on the momentum balance (i.e., Darcy's law) are distributed sources arising from truly distributed physical processes.

In 2D, distributed sources also arise from boundary conditions that cannot be handled due to the lack of an explicit third dimension. Surface recharge, delayed yield from the water table, and leakage from adjoining layers are all boundary conditions along the top or bottom of an aquifer; in 2D they become distributed area sources. Though 3D representations are more physically realistic, often 2D approximations are adequate or all that are feasible to solve. Most of the source terms considered here are of the later sort; they would not carry over to a 3D LT-AEM problem.

Elements that represent finite areas or are associated with the entire domain can be governed by PDEs that differ from (2.3) either simply by material properties (which changes the definition of κ) or the presence of distributed source terms. The LT-AEM sources dealt with here are all linear and can either come from a homogeneous (a source linear in $\bar{\Phi}$; non-linear sources could also lead to a homogeneous PDE, but cannot be handled by LT-AEM) or inhomogeneous PDE (a Poisson

term). Homogeneous LT-AEM source terms are dealt with using the EE solutions derived in Chapter 3, since (2.3) contains a term linear in $\bar{\Phi}$; additional terms can be thought of as simply changing the definition of κ^2. Inhomogeneous source terms (including Φ_0 in (2.2)) must be expressed in terms of a particular solution, requiring a modified approach.

4.1 Inhomogeneous sources

2D area sources (e.g., circles, ellipses, or the entire domain) can be used to represent recharge (precipitation and infiltration) or discharge (evapotranspiration), where the source term is not proportional to aquifer head or drawdown. For steady AEM problems this leads to the Poisson equation (e.g. Haitjema and Kelson, 1996; Bakker, 1998), for transient flow problems it leads to a Poisson term in the modified Helmholtz equation (e.g., the initial condition in (2.2)). Kuhlman and Neuman (2006) showed that an impulse area source, applied at $t = 0$, can be used to represent a non-zero initial condition.

4.1.1 Decomposition of potential

Adapting the method outlined by Strack (1989, §37) for steady-state analytic elements, specified area flux elements are derived in Laplace space by decomposing $\bar{\Phi}$ into homogeneous and particular solutions, separately considering $\bar{\Phi}_p$ inside and outside of an area,

$$\nabla^2 \bar{\Phi}_p - \kappa^2 \bar{\Phi}_p = \bar{\gamma}(\mathbf{x}, p) \qquad \text{inside,} \tag{4.1}$$

$$\nabla^2 \bar{\Phi}_p - \kappa^2 \bar{\Phi}_p = 0 \qquad \text{outside,} \tag{4.2}$$

where $\bar{\gamma}$ is the strength of the area flux that, in general, can be a function of both space and time. The PDE used inside the area element has the same form as the Laplace transformed diffusion equation, before the simplification of zero initial

condition (2.2), with $\bar{\gamma} = -\Phi_0/\alpha$. The total discharge potential is defined as a sum of two functions,

$$\bar{\Phi} = \bar{\Phi}_p + \bar{\Phi}_h, \tag{4.3}$$

where $\bar{\Phi}_h$ is the homogeneous solution for which elements were derived in Chapter 3. $\bar{\Phi}_p$ is identically zero outside the element, and satisfies the above PDE inside; it is any particular (inhomogeneous) solution. The combination of these two functions is used to make $\bar{\Phi}$ match correctly at element boundaries (there may be a jump in $\bar{\Phi}_{\text{total}}$ if there is a change in K).

To ensure continuity in h, the jump in $\bar{\Phi}_h$ across the circumference of the circle is proportional to the jump in $\bar{\Phi}_p$,

$$\frac{\bar{\Phi}_p}{K^-} = \frac{\bar{\Phi}_h^+}{K^+} - \frac{\bar{\Phi}_h^-}{K^-}. \tag{4.4}$$

The homogeneous solution $\bar{\Phi}_h^{\pm}$ is the total discharge potential due to all participating elements ($\bar{\Phi}_h^{\pm} = \bar{\Phi}^{k\pm} + \sum \bar{\Phi}_{\text{bg}}^{\pm}$). The modified form of the head matching condition (2.27) for element n with a passive area flux is

$$\frac{1}{K^+}\left[\bar{\Phi}^{n+} + \sum_{\substack{k=1\\k\neq n}}^{N_{bg+}} \bar{\Phi}^k\right]_{r_0} = \frac{1}{K^-}\left[\bar{\Phi}^{n-} + \bar{\Phi}_p + \sum_{\substack{k=1\\k\neq n}}^{N_{bg-}} \bar{\Phi}^k\right]_{r_0} \tag{4.5}$$

similarly, the modified form of the normal flux matching condition (2.29) would be

$$\mathbf{n}\cdot\left[\bar{\mathbf{q}}^{n+} + \sum_{\substack{k=1\\k\neq n}}^{N_{bg+}} \bar{\mathbf{q}}^{k+}\right]_{r_0} = \mathbf{n}\cdot\left[\bar{\mathbf{q}}^{n-} + \bar{\mathbf{q}}_p + \sum_{\substack{k=1\\k\neq n}}^{N_{bg+}} \bar{\mathbf{q}}^{k+}\right]_{r_0} \tag{4.6}$$

Particular solutions can be found using several approaches; for some simpler distributions the particular solution may be found by inspection. The simplest nontrivial form which $\bar{\Phi}_p^-$ can take, so that $\bar{\Phi}$ still satisfies (4.2), is that of a recharge rate which is constant in space but variable in time. The particular solution for constant areal flux is simply

$$\bar{\Phi}_p = -\bar{g}(p)\frac{\bar{\gamma}}{\kappa^2}, \tag{4.7}$$

where $\bar{\gamma}$ is a constant source strength, and $\bar{g}(p)$ represents the area source time variability. In this simple case, since $\bar{\Phi}_p$ is constant in space, the modified normal flux matching (4.6) reverts to its original form ($\bar{\Phi}_p$ does not contribute to normal flux), and only the head matching equation must be modified.

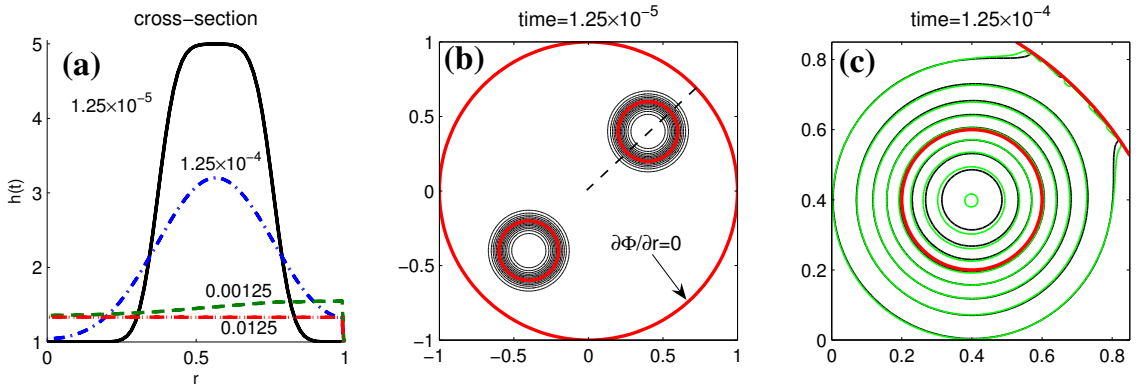

FIGURE 4.1. Non-zero initial condition in two circular regions; cross-section (a) located on dashed line in (b); (c) contours from both LT-AEM and MODFLOW.

Figure 4.1 illustrates a constant non-zero initial condition applied over a circular sub-area of a finite circular domain with an outer no-flow boundary. Panel (a) is a cross-sectional radial slice through the domain, illustrated as a dotted line in panel (b). Panel (c) shows a comparison between MODFLOW (McDonald and Harbaugh, 1988) and LT-AEM in the upper right quadrant of panel (a), corresponding to the second curve in panel (a); the contours are essentially identical.

The general time variability term, $\bar{g}(p)$, in (4.7) makes this relatively simple solution quite flexible. For example, barometric pressure or tidal fluctuations can be decomposed into key sinusoidal components, then loaded directly onto the aquifer using (4.7) with $\bar{g}(p)$ composed of a superposition of several Laplace-transformed sinusoids. For barometric fluctuations, a thick vadose zone can also be accounted for by exponentially dampening the sinusoidal components, to account the non-instantaneous flow of air through the subsurface (Weeks, 1979). Accurate accounting for observations of these fluctuations in open boreholes requires applying a

corresponding loading condition at the wellbore.

When more complex particular solutions are needed, they can be derived using the variation of parameters method, which integrates two known solutions to the homogeneous problem, which could be eigenfunctions (Morse and Feshbach, 1953, p.529). Lastly, Strack and Janković (1999) developed an area source for the Laplace equation in a general functional form, to allow matching quite arbitrary 2D distributions of Poisson terms.

4.2 Homogeneous sources

Homogeneous distributed source terms arise from effects that are proportional to head or drawdown in the aquifer. For example, transient leakage from adjacent aquitards (§ 4.2.1), delayed yield in unconfined systems (§ 4.2.3), and dual domain behavior (e.g. Moench, 1984) all lead to homogeneous source terms that can be handled with the same techniques LT-AEM uses to handle transient effects.

In the AEM literature, Bakker and Strack (2003) arrived at the Helmholtz equation by considering steady multi-aquifer flow. Bakker and Nieber (2004a) also reached this governing equation by from linearizing steady unsaturated flow. Furman and Neuman (2003), Bakker (2004c), and this dissertation also arrive at the Helmholtz equation from applying an integral transform to the diffusion equation. de Glee (1930) solved the problem of steady flow to a well in a leaky aquifer, resulting in a solution of the form $\mathrm{K}_0(r)$, the fundamental solution for the Helmholtz equation. Although the modified Helmholtz equation is typically not considered one of the fundamental equations of groundwater flow, it arises in numerous situations where source terms in homogeneous PDEs are considered. The methodology used here to solve the transient flow problem can easily be extended to handle these other terms, with little or no change to the solution methodology, presented in Chapter 2.

4.2.1 Leaky aquifer source term

An example of a 2D homogeneous source term is leakage from an adjacent unpumped aquitard, following the approach of Hantush (1960) (see Figure 4.2).

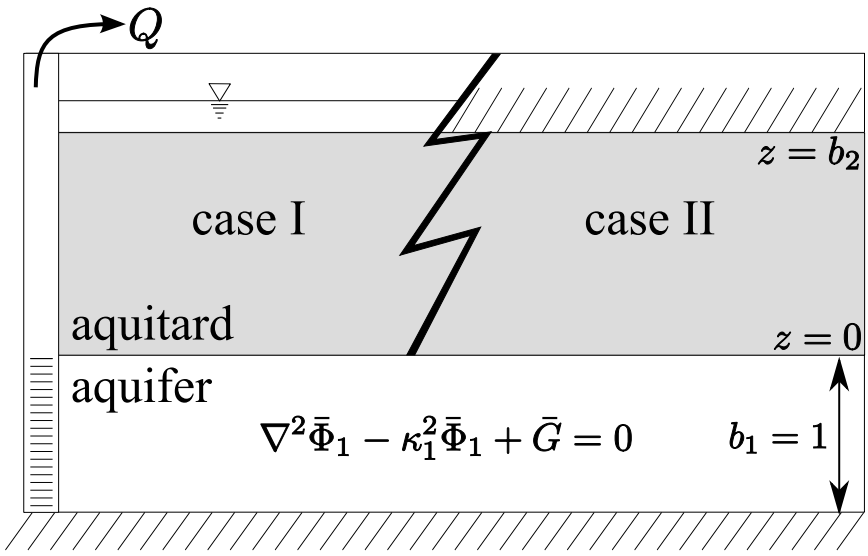

FIGURE 4.2. Leaky system conceptual diagram

Beginning again with (2.1) but keeping the source term, G, when converting to Φ and taking the Laplace transform; the aquifer flow equation with a distributed source is

$$\nabla^2\bar{\Phi}_1 - \kappa_1^2\bar{\Phi}_1 + \bar{G} = 0, \tag{4.8}$$

where variables with subscript 1 pertain to the aquifer and 2 or 3 will relate to an adjacent aquitard. Assuming vertical flow in the overlying aquitard (common when $K_1 \gg K_2$), the flow equation in the aquitard simplifies to the ODE

$$\frac{\mathrm{d}^2\bar{\Phi}_2}{\mathrm{d}z^2} - \kappa_2^2\bar{\Phi}_2 = 0, \tag{4.9}$$

assuming a zero initial condition in the aquitard. Head matching at the aquifer-aquitard interface ($z = 0$) gives the condition

$$\bar{\Phi}_2(z = 0) = K_2\bar{\Phi}_1(\mathbf{x})/K_1, \tag{4.10}$$

where the aquifer PDE is 2D (x and y) and the aquitard ODE (z) is 1D, being orthogonal to the aquifer problem; a different aquitard ODE is posed at each $\mathbf{x}$ location. At the far side of the aquitard ($z = b_2$) there is a no-drawdown condition, $\bar{\Phi}_2 = 0$ (see case I of Figure 4.2). The solution to (4.9) that satisfies both of these conditions is

$$\bar{\Phi}_2(z) = \frac{K_2 \bar{\Phi}_1}{K_1} \left[\cosh \kappa_2 z - \coth \kappa_2 b_2 \, \sinh \kappa_2 z\right]. \tag{4.11}$$

Differentiating (4.11) and evaluating it at $z = 0$ gives the vertical flux from the aquitard at the interface,

$$\bar{G} = \frac{1}{b_1} \left[\frac{\partial \bar{\Phi}_2}{\partial z}\right]_{z=0}. \tag{4.12}$$

Substituting this into (4.8), the aquifer flow PDE becomes

$$\nabla^2 \bar{\Phi}_1 - \left[\kappa_1^2 + \kappa_2 \frac{K_2}{b_1 K_1} \coth \kappa_2 b_2\right] \bar{\Phi}_1 = 0. \tag{4.13}$$

This PDE can be solved using the same elements from Chapter 3, because the effects of the neighboring aquitard contributes the second terms in brackets in (4.13), which is a constant, and therefore only redefines κ^2 in (2.3). Since the aquitard ODE is linear with homogeneous initial and boundary conditions, superposition is valid.

Exploiting the axial symmetry in this case, Figure 4.3 shows dimensionless results; see definitions in equation (3.15). The curve labeled $E_1(t_D/4)$ represents the non-leaky Theis (1935) solution (2.22), shown for comparison. Less drawdown is seen in the leaky aquifer, because the leaky layers supply water to the aquifer at a rate proportional to the level of drawdown.

A similar procedure can be used to develop leaky source elements with different upper aquitard BC; the PDE for a no-flow BC at $z = b_2$ is (case II, the upwardly-deviating curves in Figure 4.3)

$$\nabla^2 \bar{\Phi}_1 - \left[\kappa_1^2 + \kappa_2 \frac{K_2}{b_1 K_1} \tanh \kappa_2 b_2\right] \bar{\Phi}_1 = 0. \tag{4.14}$$

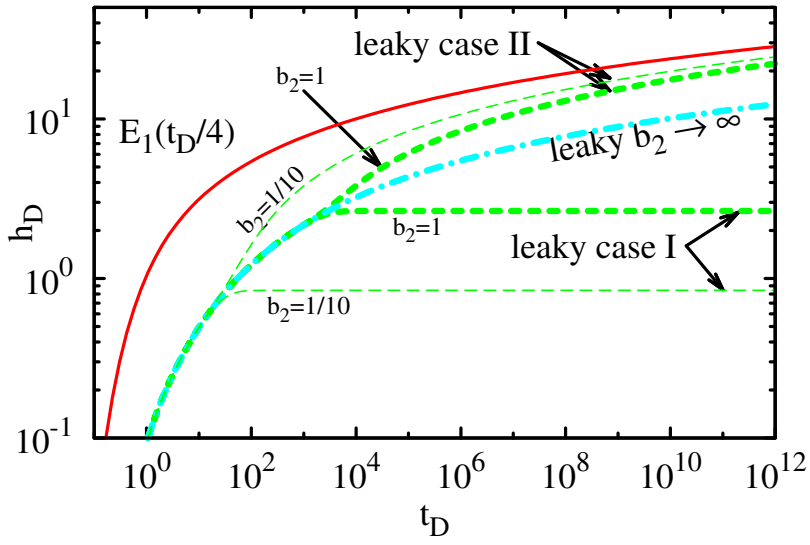

FIGURE 4.3. Leaky response at $r = 1$ due to point source, comparing results for different aquitard BC and b_2 with the non-leaky E_1 solution; $S_{s2}/S_{s1} = 100$, $K_1/K_2 = 5$.

Case II is limited by the assumption of vertical flow in the aquitard to early-time flow. Significant horizontal gradients will develop once drawdown has reached the upper boundary (Malama et al., 2007), which this simplified model cannot properly account for.

For the case $b_2 \to \infty$, $\coth \kappa_2 b_2$ in (4.13) and $\tanh \kappa_2 b_2$ in (4.14) both simplify to unity (the middle leaky curve in Figure 4.3), and the PDE then becomes

$$\nabla^2 \bar{\Phi}_1 - \left[\kappa_1^2 + \kappa_2 \frac{K_2}{b_1 K_1} \right] \bar{\Phi}_1 = 0. \tag{4.15}$$

The effects of the boundary condition at $z = b_2$ are only observed at later time when the three curves separate (the thin curves in Figure 4.3 represent an aquitard $1/10$ as thick as the heavy curves, they deviate at an earlier time). The effects of two aquitards (above and below) can also be included, as done by Hantush (1960). For example, the PDE for a system consisting of a type I aquitard above (layer 2)

and a type II aquitard below (layer 3) is

$$\nabla^2\bar{\Phi}_1 - \left[\kappa_1^2 + \kappa_2\frac{K_2}{b_1K_1}\coth\kappa_2 b_2 - \kappa_3\frac{K_3}{b_1K_1}\tanh\kappa_3 b_3\right]\bar{\Phi}_1 = 0. \tag{4.16}$$

This model produces homogeneous source terms in the aquifer PDE for aquitards which are immediately adjacent to the main aquifer. Using the model of Hantush (1960), four or more layer system do not produce solutions which simply depend on the drawdown in the main aquifer. Multi-aquifer systems are addressed in a more general manner in section 4.2.2.

The finite wellbore (3.14) and wellbore storage (3.20) type wells can just as easily be solved for this type of problem. Moench (1985) developed a leaky solution for large-diameter wells, not unlike the single-well solution developed here. A major advantage of the LT-AEM approach is that these elements may be combined, using boundary matching to solve more complex geometries.

Leaky source examples The leaky PDE (e.g., (4.13), (4.14), or (4.15)) could be solved for the entire domain, as was done in Figure 4.3 for a pumping well in an infinite aquifer, the leaky PDE can be confined to a region bounded by circles or ellipses, or the complementary infinite domain with circular or elliptical regions cut from it. The boundary matching approach used here is what allows different PDEs to be solved in different regions; superposition of solutions to different PDEs is not allowed.

Figures 4.4 and 4.5 show a situation where a well is pumping from a confined aquifer, but there are six "holes" in the confining layer, separating the confined aquifer from another, unpumped aquifer. The two aquifers are initially in equilibrium with each other (there is no leakage), but as the main aquifer is pumped, leakage occurs through the six holes, assuming the rest of the aquitard is impermeable. Figure 4.6 illustrates that this spatially-distributed leakage falls between the confined behavior and fully-leaky behaviors, as would be expected. The geometry

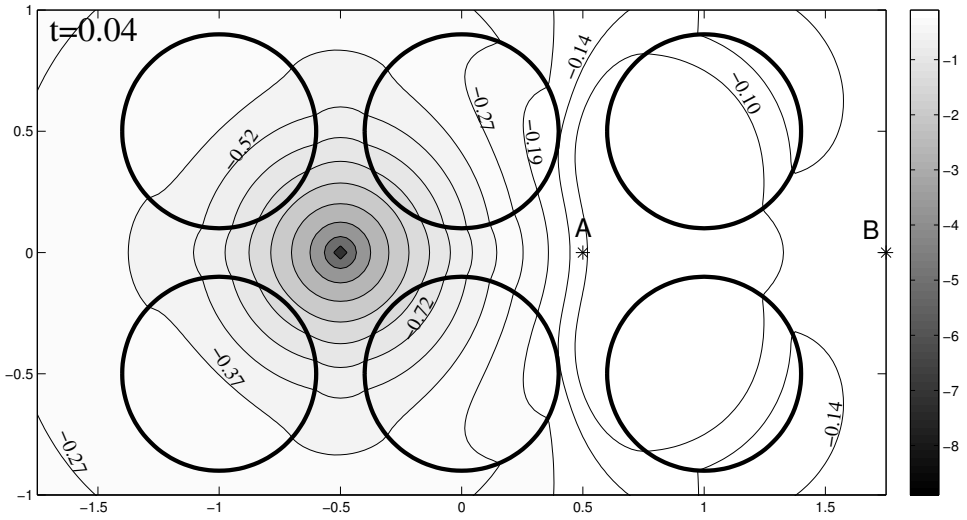

FIGURE 4.4. Contours of head due to a point source in a system of leaky (type I) circles in a confined aquifer, at $t = 0.04$

of the leaky circles causes the drawdown at point A to be less than point B (except at very late time); despite the fact that A is closer, B is not surrounded by leaky sources. For comparison, the sources for the uniformly leaky case are solid lower lines.

Figure 4.7 shows drawdown due to all three types of leaky systems at two observation locations relative to a specified total flowrate line source (3.40) located at $-0.75 \leq x \leq 0.75$, $y = 0$. The line source could be used to model the effects of a river on an aquifer with a leaky aquitard immediately below it. At larger distance the time-drawdown plot for the line source more closely resembles the same plot for the point source solution in Figure 4.3. In this example, $K/K_2 = 1000$, $S/S_2 = 0.001$, $b_2 = b = 1$. The effects that the different parameters and aquitard boundary conditions have on the drawdown due to a line source in a leaky aquifer is analogous to the response due to a point source. One significant difference between the two is that the drawdown at the line source $(\eta = 0; -f \leq x \leq f, y = 0)$ is finite, while drawdown at a point source $(r = 0)$ is not.

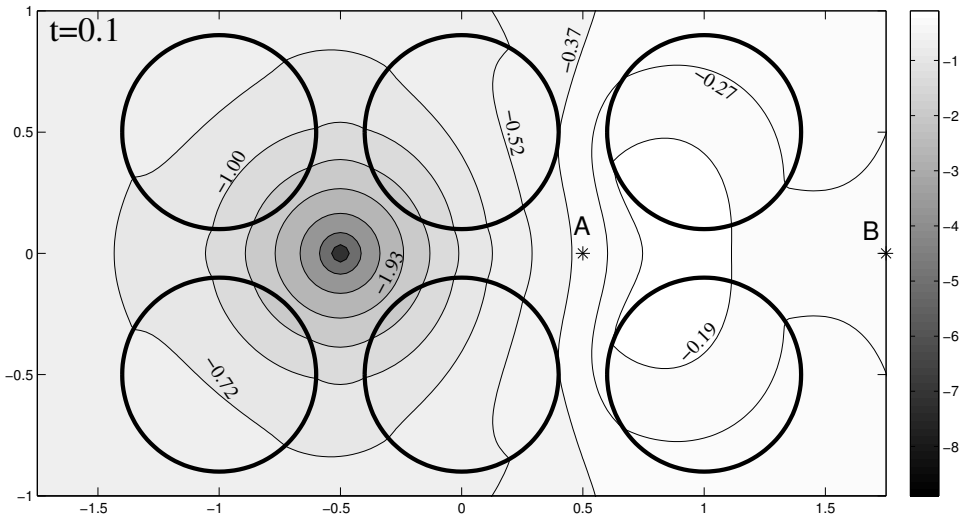

FIGURE 4.5. Contours of head due to a point source in a system of leaky (type I) circles in a confined aquifer, at $t = 0.1$

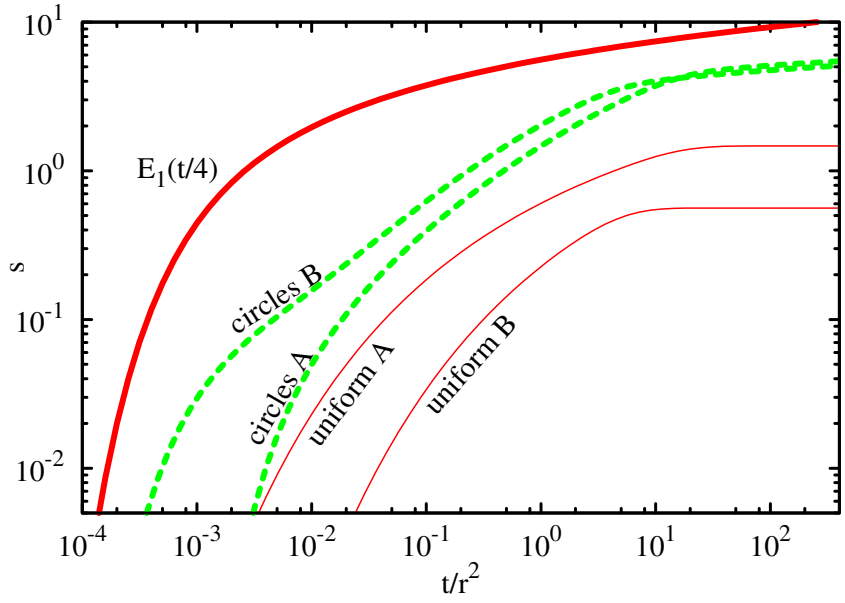

FIGURE 4.6. Drawdown through time at points A and B in Figures 4.4 and 4.5. Uniform curves represent the leaky solution of Hantush (1960).

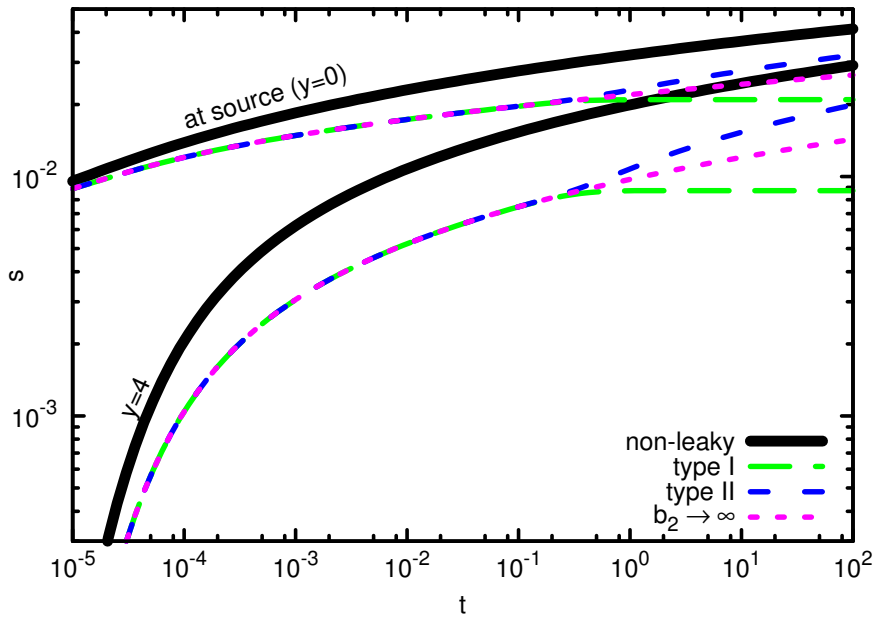

FIGURE 4.7. Drawdown due to line source in leaky aquifer at 2 observation locations; on the source ($x = 0$, $y = 0$) and away from the source ($x = 0$, $y = 4$)

4.2.2 Layered system solution

Transient multi-aquifer systems have been considered by Neuman and Witherspoon (1969), Hemker and Maas (1987), Li and Neuman (2007), and Malama et al. (2008). We follow the general transient matrix formulation of Hemker and Maas (1987) and Maas (1987), but we do not limit the solution to radial flow to a single well in the multi-layer system as they did. The matrix formulation (Maas, 1986) is valid for any number of layers (even $n \to \infty$); the boundary conditions at the top and bottom of the system (see Figure 4.8) are later imposed on the general solution. The multi-aquifer transient problem does not result in a homogeneous governing equation in terms of a single potential. Despite this difference, this material is presented in this chapter because the matrix techniques used here do result in an system of uncoupled equations for a modified potential; each uncoupled aquifer then behaves like the other homogeneous sources described in this chapter. The final solution is found through a matrix-vector product back-transformation.

Extending the aquifer-aquitard system of section 4.2.1 to n aquifers and $n+1$ aquitards (see Figure 4.8) is relatively straightforward, resulting in a matrix equation for $\bar{\Phi}_i$ and $\bar{\Phi}'_i$, the discharge potential in the i^{th} aquifer and aquitard respectively.

Similar to the leaky problem, flow in aquifers is assumed to be 2D (horizontal x, y), while flow in aquitards is assumed 1D (vertical z). The governing equation in the i^{th} aquifer is

$$\nabla^2 \bar{\Phi}_i - \kappa_i^2 \bar{\Phi}_i + \bar{G}_{i\uparrow} - \bar{G}_{i\downarrow} = 0, \tag{4.17}$$

where the source terms due to the aquitards above ($\uparrow$) and below ($\downarrow$) aquifer i are

$$\bar{G}_{i\uparrow} = \frac{1}{b_i} \frac{\partial \bar{\Phi}'_i}{\partial z_i}\bigg|_{z_i=0}, \tag{4.18}$$

$$\bar{G}_{i\downarrow} = \frac{1}{b_i} \frac{\partial \bar{\Phi}'_{i+1}}{\partial z_{i+1}}\bigg|_{z_{i+1}=b'_{i+1}}; \tag{4.19}$$

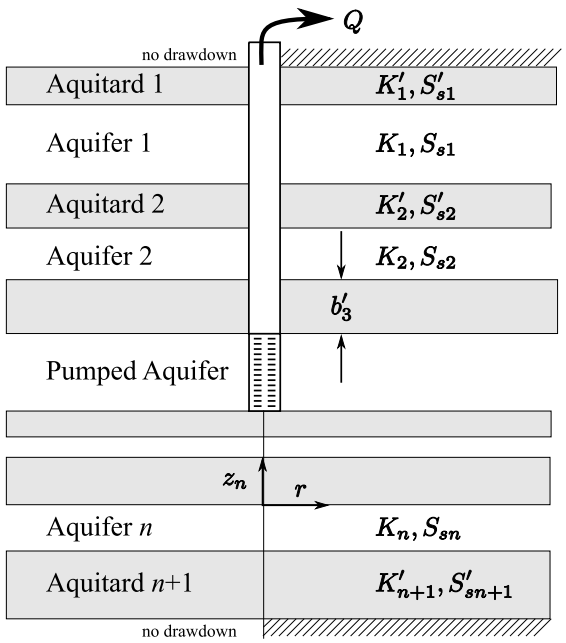

FIGURE 4.8. Schematic of layered system, after Hemker and Maas (1987)

primed quantities are related to aquitards, unprimed ones are related to aquifers. Since the aquifers have no z-coordinate, unprimed z_i is the local coordinate across the aquitards $(0 \leq z_i \leq b'_i)$. 1D flow in the i^{th} aquitard is given by the ODE

$$\frac{\mathrm{d}^2\bar{\Phi}'_i}{\mathrm{d}z_i^2} - \kappa_i'^2\bar{\Phi}'_i = 0, \tag{4.20}$$

with a general solution of the form

$$\bar{\Phi}'_i(z,p) = \beta'_i \cosh z_i\kappa'_i + \delta'_i \sinh z_i\kappa'_i, \tag{4.21}$$

where β' and δ' are coefficients to be determined from boundary conditions at the boundaries between aquifers and aquitards.

Up to this point, the development is identical to that for the leaky problem, but generalized to multiple aquifers. In the leaky system, simple boundary conditions were applied at the far side of the adjoining aquitard (no drawdown or no flow), resulting in simple solutions to (4.21) and therefore simple source terms (4.18 and 4.19). The leaky solutions only depended on the drawdown in the pumped aquifer.

By considering the head in the other aquifers to be a dependent variable, a system of equations for potentials in all the layers must be solved simultaneously.

Performing head matching at the top and bottom of each aquitard to determine the coefficients β'_i and δ'_i in (4.21), and taking the derivative of (4.21) to determine the vertical flux at the aquifer/aquitard interface leads to

$$\bar{G}_{i\uparrow} = \frac{K'_i\kappa'_i}{b_i K_{i-1}\sinh\left(\kappa'_i b'_i\right)}\bar{\Phi}_{i-1} - \frac{K'_i\kappa'_i\coth\left(\kappa'_i b'_i\right)}{b_i K_i}\bar{\Phi}_i, \tag{4.22}$$

$$\bar{G}_{i\downarrow} = \frac{K'_{i+1}\kappa'_{i+1}\coth\left(\kappa'_{i+1} b'_{i+1}\right)}{b_i K_{i+1}}\bar{\Phi}_{i+1} - \frac{K'_{i+1}\kappa'_{i+1}}{b_i K_i\sinh\left(\kappa'_{i+1} b'_{i+1}\right)}\bar{\Phi}_i; \tag{4.23}$$

substituting these into (4.17) and expressing the problem in matrix form leads to

$$\nabla^2\bar{\mathbf{\Phi}} - \mathbf{A}\bar{\mathbf{\Phi}} = \mathbf{0} \tag{4.24}$$

where $\mathbf{A}$ is a tridiagonal matrix that accounts for the leaky source terms (4.22 and 4.23) that include the effects of adjacent aquifers and transient effects of the current aquifer (second term in (4.17)) and $\bar{\mathbf{\Phi}}$ is a vector of the discharge potentials in all the aquifers. A characteristic section of $\mathbf{A}$ is

$$\begin{bmatrix} \ddots & \ddots & \ddots & & & & \\ 0 & A_{i-1,i-2} & A_{i-1,i-1} & A_{i-1,i} & 0 & \dots & \dots \\ \dots & 0 & A_{i,i-1} & A_{i,i} & A_{i,i+1} & 0 & \dots \\ \dots & \dots & 0 & A_{i+1,i} & A_{i+1,i+1} & A_{i+1,i+2} & 0 \\ & & & & \ddots & \ddots & \ddots \end{bmatrix} \tag{4.25}$$

where the terms in row i of (4.25) are

$$A_{i,i-1} = -\frac{K'_i\kappa'_i}{b_i K_{i-1}}\operatorname{csch}\left(\kappa'_i b'_i\right), \tag{4.26}$$

$$A_{i,i} = \frac{K'_i\kappa'_i}{b_i K_i}\coth\left(\kappa'_i b'_i\right) + \frac{K'_{i+1}\kappa'_{i+1}}{b_i K_i}\operatorname{csch}\left(\kappa'_{i+1} b'_{i+1}\right) + \kappa_i^2, \tag{4.27}$$

$$A_{i,i+1} = -\frac{K'_{i+1}\kappa'_{i+1}}{b_i K_{i+1}}\coth\left(\kappa'_{i+1} b'_{i+1}\right). \tag{4.28}$$

The approach taken here is to decouple the aquifers by substituting the eigenvalues and eigenvectors of $\mathbf{A}$. This allows their solution to be computed using the

standard scalar techniques already given. For a problem with 5 or more aquifers this leads to a numerical solution; this limitation is related to the fact that there is no algebraic solution to the roots of a polynomial of higher than fourth order. This numerical-only solution could be considered to degrade the elegance of the otherwise analytic (in Laplace space) LT-AEM. The approach is useful though, because it extends 2D LT-AEM to multi-aquifer systems that would otherwise need to be handled using 3D models.

Substituting $\mathbf{A} = \mathbf{S}\boldsymbol{\Lambda}\mathbf{S}^{-1}$ into (4.24), gives

$$\nabla^2\bar{\boldsymbol{\Phi}} - \mathbf{S}\boldsymbol{\Lambda}\mathbf{S}^{-1}\bar{\boldsymbol{\Phi}} = \mathbf{0} \tag{4.29}$$

where $\mathbf{S}$ is an orthogonal matrix (that is guaranteed to have an inverse) composed of the eigenvectors of $\mathbf{A}$ arranged as columns and $\boldsymbol{\Lambda}$ is a diagonal matrix of the corresponding eigenvalues of $\mathbf{A}$ (e.g. Strang, 1988, §5.2). Pre-multiplying both sides of (4.29) by $\mathbf{S}^{-1}$ and defining the new potential $\bar{\boldsymbol{\Psi}} = \mathbf{S}^{-1}\bar{\boldsymbol{\Phi}}$ leaves

$$\nabla^2\bar{\boldsymbol{\Psi}} - \boldsymbol{\Lambda}\bar{\boldsymbol{\Psi}} = \mathbf{0}, \tag{4.30}$$

which is a set of n uncoupled modified Helmholtz equations, because $\boldsymbol{\Lambda}$ is a diagonal matrix of eigenvalues,

$$\begin{aligned} \nabla^2\bar{\Psi}_1 - \lambda_1\bar{\Psi}_1 &= 0 \\ \nabla^2\bar{\Psi}_2 - \lambda_2\bar{\Psi}_2 &= 0 \\ &\vdots \end{aligned} \tag{4.31}$$

Once the eigenvalues of $\mathbf{A}$ are computed, the solution for $\bar{\Psi}_i$ in each layer can be computed independently, then they are converted back through the matrix-matrix multiplication

$$\bar{\boldsymbol{\Phi}} = \mathbf{S}\bar{\boldsymbol{\Psi}} = \mathbf{S}\mathbf{S}^{-1}\bar{\boldsymbol{\Phi}} = \mathbf{I}\bar{\boldsymbol{\Phi}}, \tag{4.32}$$

where $\mathbf{I}$ is the identity matrix.

The approach of Hemker and Maas (1987) only considers aquifer that "communicate" through leaky layers between them, this always leads to a tridiagonal $\mathbf{A}$. The same eigensolution decoupling technique used here could be applied to multi-aquifer systems with other possible inter-aquifer connections (e.g., unpumped wells screened across multiple aquifers) or completely different physical arrangements. These alternative connections between aquifers would lead to off-diagonal $\mathbf{A}$ terms, but the approach would remain unchanged.

The solution presented by Hemker and Maas (1987) was for radially symmetric flow to a well, but any of the LT-AEM elements derived in Chapter 3 could be applied to this system of equations, even different source terms (e.g., surface recharge or the unconfined source considered in section 4.2.3) or elements (e.g., line source on surface, point sources in some of the aquifers below) in the different aquifers of the system. Due to linearity, superposition of compatible systems is valid (i.e., layers have zero initial conditions and the same properties in each layer). Bakker and Strack (2003), Bakker (2004a), and Bakker (2006) have developed similar AEM solutions to multi-layer problems for steady-state flow.

System boundary conditions simply redefine the first and last rows of $\mathbf{A}$, as were done for the leaky case. No-drawdown (left half of Figure 4.8) or no-flow (right half) conditions may be specified at the top of aquitard 1, or the bottom or aquitard n. The thickness of the extremal aquitards may also be made very large, with similar simplifications to (4.15).

4.2.3 Boulton's delayed yield source term

Boulton's delayed yield solution (1954) is an empirically-derived model of the effects that delayed yield has on flow in 2D aquifers. Herrera et al. (1978) showed that while the general 2D integro-differential model for an unconfined aquifer is approximate at very small time and small radial distances from a pumping well, it

can be used successfully elsewhere. Herrera et al. (1978) give a generalized form of Boulton's equation for flow in the aquifer as

$$K\nabla^2\Phi = S_s\frac{\partial\Phi}{\partial t} + S_y\int_0^t \left.\frac{\partial\Phi}{\partial t}\right|_{t=\tau} \mathcal{B}(r, t-\tau)\,\mathrm{d}\tau, \tag{4.33}$$

where S_y is dimensionless specific yield and $\mathcal{B}(r, t-\tau)$ is a convolution kernel; for simplicity Boulton chose $\mathcal{B}(t-\tau) = \tilde{\alpha}e^{-\tilde{\alpha}(t-\tau)}$. The fitting parameter $\tilde{\alpha}$, $[\mathrm{T}^{-1}]$, does not have direct physical meaning. To produce a solution that depends on physical parameters, Herrera et al. (1978) used a more complex convolution kernel,

$$\mathcal{B}(t-\tau) = 2\sum_{n=1}^{\infty}\frac{\gamma_n}{\rho_n^2 - 1 + \sigma^2}e^{-\gamma_n(t-\tau)}, \tag{4.34}$$

where $\sigma = \sqrt{S_s/S_y}$, $\gamma_n = K_z\rho_n^2/(bS_y)$, K_z is vertical aquifer hydraulic conductivity, b is aquifer thickness and ρ_n are roots of the transcendental equation

$$\rho_n = \tan(\rho_n\sigma)\left(\frac{1}{\sigma} - \sigma\right). \tag{4.35}$$

Equation 4.33 is (2.3) with an extra time convolution term of the form (2.18), which is equivalently multiplication of the image functions in Laplace space (§ 2.4). Both kernels have transforms of the type $\mathcal{L}\{\mathcal{B}(t-\tau)\} = \xi/(\xi+p)$. Assuming a zero initial condition, the transformed flow PDE for Boulton's (1954) kernel is

$$\nabla^2\bar{\Phi} - \left[\kappa^2 + \frac{S_y p}{K}\frac{\tilde{\alpha}}{\tilde{\alpha}+p}\right]\bar{\Phi} = 0. \tag{4.36}$$

Analogously, the transformed PDE using the kernel of Herrera et al. (1978) is

$$\nabla^2\bar{\Phi} - \left[\kappa^2 + \frac{2S_y p}{K}\sum_{n=1}^{\infty}\frac{\gamma_n}{(\rho_n^2 - 1 + \sigma^2)(\gamma_n + p)}\right]\bar{\Phi} = 0. \tag{4.37}$$

Either Boulton's empirical $\tilde{\alpha}$ can be equated with physical parameters by comparing it to the form of (4.34), or the more complex kernel of Herrera et al. (1978) with physically-based parameters can be used. (4.34) gives a more realistic solution at small time, but involves solving for the roots of a non-linear equation and a poorly-converging infinite series. The simplest approximation (when $S_s = 0$, $\rho_1^2 = 3$ and

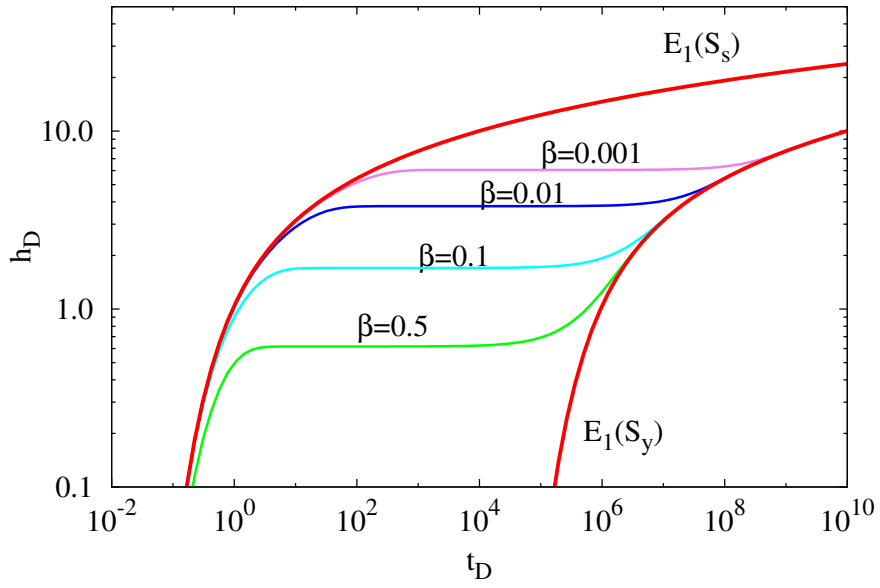

FIGURE 4.9. Drawdown due to a point sources (3.14) for Boulton's unconfined PDEs at $r = 1$ through time

$\rho^2_{n\neq 1} = 0$) leads to the correspondence $\tilde{\alpha} = 3K_z/(S_y b)$. In Figure 4.9 $r = b = 1$, therefore $\beta = r^2 K_z/(Kb^2)$ is proportional to the aquifer anisotropy ratio.

The delayed yield source term can also be applied to the line element (ellipse with $\eta_0 = 0$), potentially representing a horizontal well or a recharging river (ignoring the non-linear effects of the vadose zone). In Figure 4.10 the curve of drawdown observed at $x = 0$, $y = 0$ (on the line source $y = 0$, $-0.75 \leq x \leq 0.75$) shows the most drawdown and is the least shaped like the curves for an unconfined point source (see Figure 4.9) due to the geometry of the source. As the observation point moves away from the line (as y increases), the geometry effects becomes smaller; at large distance, we expect the line and point sources to behave similarly. Note that in contrast to the point source, which produces infinite drawdown at $r = 0$, the line source produces finite drawdown at $\eta = 0$ ($y = 0$ in Figure 4.10).

For comparison with the point source shown in Figure 4.9, Figure 4.11 illustrates a confined line source using S_S (the upper curve), one using S_y (lower curve),

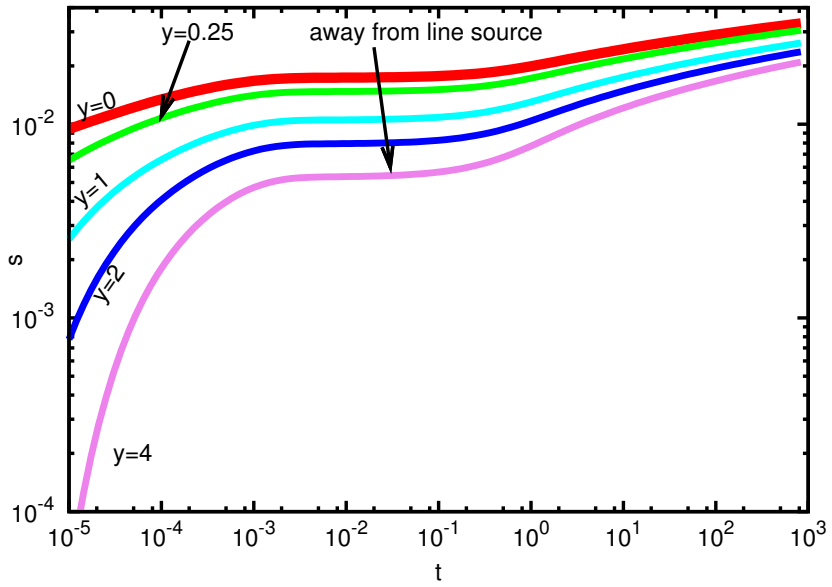

FIGURE 4.10. Drawdown through time due to a line source ($f = 0.75$, $S_y = 0.25$, $S_s = 5 \times 10^{-4}$, $\beta = 1/100$, $x = 0$)

and the unconfined line source. Different values of β represent different K_z in the aquifer; aside from the source geometry, the solution is identical to the unconfined point source.

Boulton's model is used here for the unconfined flow problem to illustrate how an integro-differential equation with time convolution can be handled using LT-AEM techniques, rather than to advocate its use as the most physically realistic model of unconfined aquifer flow.

The leaky (§ 4.2.1) and unconfined solutions can be combined. For a well in a shallow unconfined aquifer, with a leaky aquitard below; the governing flow equation would be

$$\nabla^2 \bar{\Phi} - \left[\kappa^2 + \kappa_2 \frac{K_2}{b_1 K_1} + \frac{2 S_y p}{K_1} \sum_{n=1}^{\infty} \frac{\gamma_n}{(\rho_n^2 - 1 + \sigma^2)(\gamma_n + p)} \right] \bar{\Phi} = 0. \tag{4.38}$$

using the leaky (4.15) and unconfined (4.37) solutions already given. This illustrates the ease with which new solutions may be constructed in Laplace space,

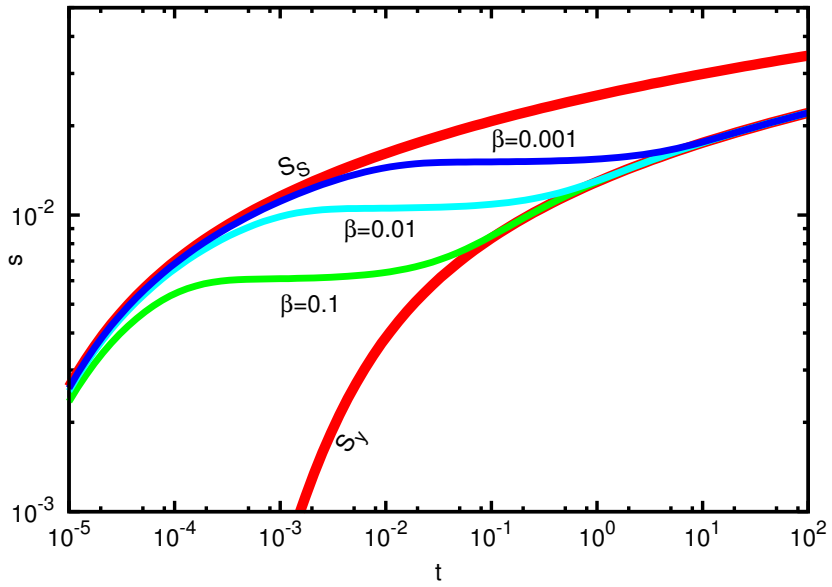

FIGURE 4.11. Drawdown through time due to a line source for different values of β ($y = 1$), comparing with early and late confined line sources.

allowed by the flexibility of the numerical inverse transform. This type of arrangement (2D unconfined aquifer flow, 1D aquitard flow) has been recently investigated by Zlotnik and Zhan (2005), a special case of the more general 3D flow solution of Malama et al. (2007).

4.2.4 Source term from Darcy's law

Higher-order time derivatives in the governing time-domain PDE can also add a homogeneous source term to the transformed PDE. For example, consider the more complete transient form of Darcy's law, averaged from or based on analogy with the Navier-Stokes equations (Bear, 1988, §4.7), given as

$$\mathbf{q} = -\left(\nabla\Phi + \tau\frac{\partial \mathbf{q}}{\partial t}\right), \tag{4.39}$$

where τ is a relaxation parameter [T] that is very small, therefore the $\mathbf{q}$ time derivative term is usually neglected. Löfqvist and Rehbinder (1993) define $\tau = K/(ng)$,

where n is dimensionless porosity and g is the acceleration due to gravity $[\mathrm{L/T^2}]$. Nield and Bejan (2006, §1.5) contend that $\tau = \rho \mathbf{c}_a$, where ρ is the fluid density and $\mathbf{c}_a$ is the *acceleration coefficient tensor* that depends on the geometry of the largest pores. While details related to the physical significance of τ may be under contention, in general it is believed to be related to the amount of time it takes for the system to become diffusion-dominated.

Applying the Laplace transform to (4.39) gives

$$\bar{\mathbf{q}} = -\left[\nabla\bar{\Phi} + \tau\left(p\bar{\mathbf{q}} - \mathbf{q}_0\right)\right] \tag{4.40}$$

where $\mathbf{q}_0$ is the initial flux condition. Assuming this is zero, solving for $\bar{\mathbf{q}}$, and incorporating this into the Laplace-transformed mass balance expression

$$-\nabla\cdot\bar{\mathbf{q}} = \frac{p}{\alpha}\bar{\Phi}p \tag{4.41}$$

leads to the governing flow equation that incorporates the additional transient effects,

$$\nabla\cdot\left[\frac{1}{1+\tau p}\nabla\bar{\Phi}\right] - \kappa^2\bar{\Phi} = 0. \tag{4.42}$$

This PDE can be written as

$$\nabla^2\bar{\Phi} - \kappa^2\left[1+\tau p\right]\bar{\Phi} = 0, \tag{4.43}$$

which is again of similar form to (2.3), (but with p^2 in the wave number, representing $\partial^2/\partial t^2$) allowing its ready solution with existing LT-AEM techniques (see Figure 4.12). (4.43) in the time domain is

$$\nabla^2\Phi = \frac{S_s}{K}\left[\frac{\partial\Phi}{\partial t} + \tau\frac{\partial^2\Phi}{\partial t^2}\right], \tag{4.44}$$

which is the damped wave equation. The diffusion equation is a simplified form of (4.44) (as $\tau \rightarrow 0$). For problems governed by the wave equation, pulses always propagate at finite speed (e.g., see steep leading edge of s surface in Figure 4.12b), while the diffusion equation allows changes to propagate at infinite

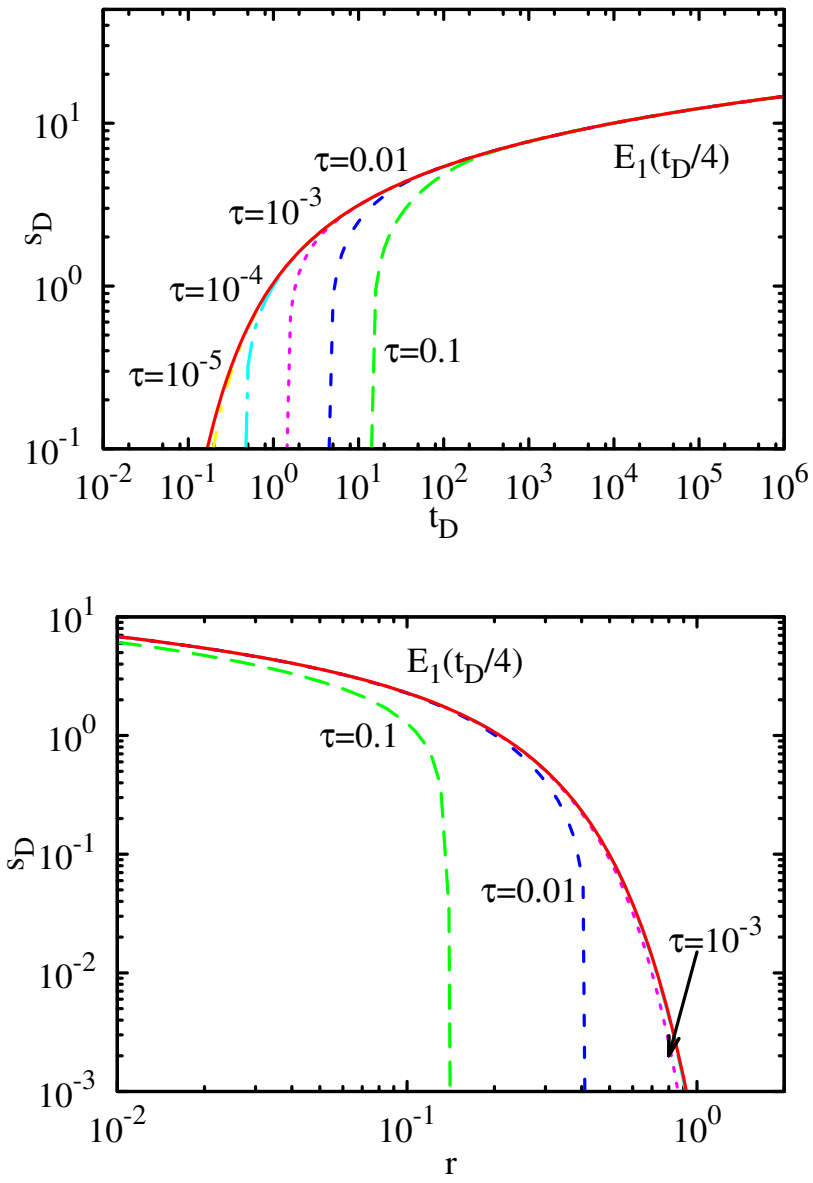

FIGURE 4.12. (a) Time drawdown at $r = 1$ and (b) distance drawdown at $t = 0.01$ for finite radius point source ((3.14), $r_w = 0.01$) considering inertia effects.

speed (Vásquez, 2007); although the changes are infinitesimally small, and hence tolerated. In the time domain, τ is attached to a $\partial^2\Phi/\partial t^2$ term, which only becomes significant when there are rapid transient changes (Löfqvist and Rehbinder, 1993). The effect of not considering this "inertia" term, in situations where it may be sig-

nificant (e.g., the gravel-packed region surrounding a pumping well), may lead to slight over-estimation of storage parameters using diffusion (see Figure 4.12a).

Chapter 5
NUMERICAL INVERSE LAPLACE TRANSFORM

Analytic techniques for evaluating Mellin's integral (A.4), including the method of residues, are very problem-specific and may only yield a solution in the form of an integral or a slowly converging infinite series; using a numerical $\mathcal{L}^{-1}$ allows flexibility and generality (Cohen, 2007).

For all numerical inverse Laplace transform algorithms, a vector of image function values are computed for required values of p, then the object function is approximated from this vector. Furman and Neuman (2003) utilized the doubly-accelerated Fourier series method of de Hoog et al. (1982); the current LT-AEM implementation can also utilize other algorithms: Post-Widder (Widder, 1946), Weeks (Weeks, 1966), and Chebyshev (Piessens, 1972). A solution is considered more robust if it is computed using two different methods yielding similar results (Davies and Martin, 1979).

5.1 General algorithm

For LT-AEM, an ideal inverse transform method accurately inverts $\Phi(\mathbf{x}, t)$ for as wide a range of t as possible, using the fewest evaluations of $\bar{\Phi}(\mathbf{x}, p)$. In LT-AEM, the vast majority of computational time is spent computing $\bar{\Phi}(\mathbf{x}, p)$, so an $\mathcal{L}^{-1}$ algorithm which is slower and more complicated to implement, but makes very efficient use of the image function evaluations would be more efficient overall. Published numerical surveys of $\mathcal{L}^{-1}$ algorithms by Davies and Martin (1979) and Duffy (1993) have not broken the effort required for the inverse transform into these two contributions. Most published inverse Laplace transform routines call the image function (here an entire Laplace-space AEM model) as a subroutine, not

taking advantage of the spatial relationships between calculation locations (each point in the domain is solved independently). While more general, this behavior could lead to incorrect recommendations as to the optimum inverse algorithm for applications with a spatial structure. For LT-AEM problems, we found the Fourier series methods (most of its many variants) converge fastest, are least sensitive to auxiliary parameters, and are able to transform $\Phi(\mathbf{x}, t)$ across at least a log-cycle of t using the vector of $\bar{\Phi}(\mathbf{x}, p)$ associated with the largest time in that decade.

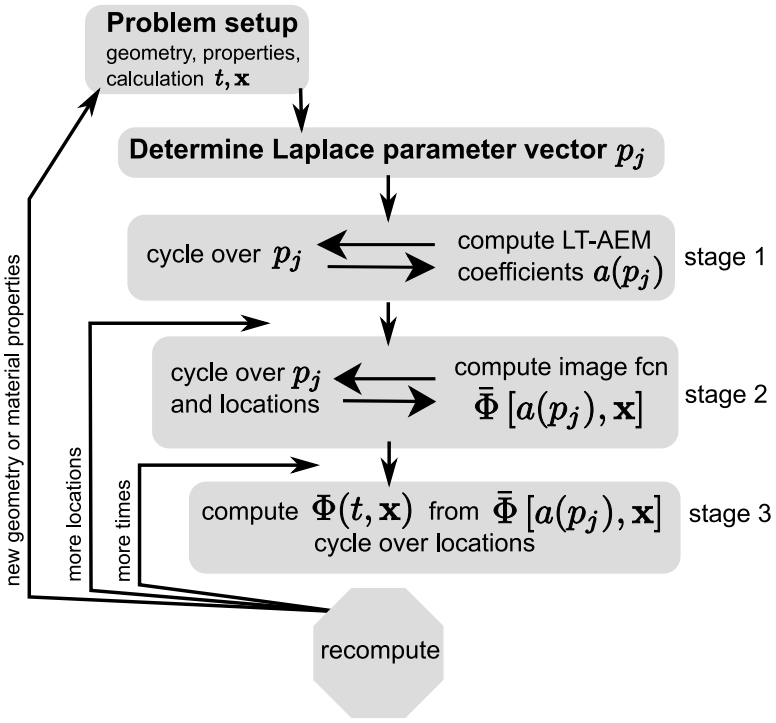

FIGURE 5.1. Numerical inverse Laplace transform flowchart

Figure 5.1 illustrates the flow of an LT-AEM calculation. The required values of the Laplace parameter, p, are determined at the beginning of the calculation; this approach optimizes efficiency of the routine, but makes it difficult to incorporate adaptive algorithms, which determine their p values as required during the calculation.

LT-AEM itself is a two-step process (stages 1 and 2), step 1 being independent

of the locations where the solution is required (unlike the single step finite element method). The image function is computed for each required value of p and at each desired space location, then these results are passed to the numerical inverse Laplace transform algorithm as a matrix.

The arrows on the left of Figure 5.1 indicate what steps can be skipped in a re-calculation, depending on what new information is required. If more $\Phi(t, \mathbf{x})$ are required at new times (which are in the same log cycle of time as previous times – not requiring new values of p), but locations where the solution is already computed, the results of the LT-AEM model need not be re-computed; only stage 3 requires re-calculation. If the solution is required at new locations (and potentially new times but only those that reuse the same p values), then the LT-AEM solution can be recomputed using the existing coefficients, requiring going back to re-compute stages 2 and 3. Finally, if the solution is desired for new problem geometry, parameters or times that vary by more than a log cycle from existing times, the entire problem must be re-computed, since new values of p are required in every step of the process.

5.2 Parallelization

All numerical inverse transform algorithms allow for parallel LT-AEM implementation, since p is a parameter (no time marching). Each $\bar{\Phi}(\mathbf{x}, p)$ can be computed independently on a different slave processor, then the inverse LT algorithm assembles $\Phi(\mathbf{x}, t)$ on a master processor (calculation of the $\mathcal{L}^{-1}$ takes an insignificant amount of time compared to the calculation of the required $\bar{\Phi}(\mathbf{x}, p)$). This *coarse-grained* parallelization is simple to implement and usually results in a nearly ideal improvement in speed (i.e., n processors $\approx$ n times faster) (Davies and Crann, 2002), in contrast to more complicated (and less successful) schemes needed to parallelize the solution of time-marching methods, where large amounts of infor-

mation must be shared between processors.

Simple threaded parallelization (as opposed to message passing parallelization) can be achieved using OpenMP (LLNL, 2008). OpenMP is not a library to be added at link-time, but rather it requires a compiler that can create special threaded executables from the OpenMP source statements. The GNU project produces a free Fortran90 compiler with OpenMP support (FSF, 2008). OpenMP creates one executable, requiring a multi-processor computer to run it in parallel, but can be almost trivially added to existing Fortran code through special comments surrounding loops in the code which should be parallelized. This allows OpenMP code to be compiled either serially or threaded, changing from one to the other just by changing compiler options.

Simple parallelization of the LT-AEM has been performed on two levels. First a parallel BLAS library (TACC, 2008) is used for matrix computations, requiring no changes to the code, only linking with the GotoBLAS library. Secondly, OpenMP is used to distribute the calculation of the matching coefficients for each value of p to different threads. With the recent proliferation of multi-processor desktop computers, this approach is effective and much simpler than message-passing schemes (e.g., MPI (Hempel, 1994)) needed for communication over a network between computers on a cluster.

5.3 Specific methods

There are many numerical $\mathcal{L}^{-1}$ algorithms; most of them can be broadly classified into those that approximate (A.4) using quadrature (e.g. de Hoog et al., 1982) and those that approximate $\bar{\Phi}(\mathbf{x}, p)$ using basis functions that have analytic inverse transforms (e.g. Piessens, 1972; Weeks, 1966).

Three classes of numerical $\mathcal{L}^{-1}$ algorithms which have historically proven useful in hydrology and specifically in LT-AEM are discussed in more detail in the

following sections. Numerical comparison of results for a few representative LT-AEM elements is given at the end of the chapter.

5.3.1 Post-Widder

The Post-Widder inversion expression (Widder, 1946), can either be considered an alternative definition of the inverse Laplace transform, or it can be considered of the functional approximation form. The approximation in Laplace space is a Taylor series in the image function (equivalent to a power series in t of the object function – see Appendix A). The method is defined as a limit of a sequence, $\Phi(t) = \lim_{n\to\infty} \Phi_n(t)$; each term in the sequence is defined as

$$\Phi_n(t) = \frac{(-1)^n}{n!} p^{n+1} \frac{\partial^n \bar{\Phi}(p)}{\partial p^n}, \qquad p = \frac{n+1}{t}, \tag{5.1}$$

where the required values of p directly depend on the desired value of t. The Stehfest (1970) algorithm is a numerical approximation of (5.1), using finite differences to replace the derivative and acceleration of the sequence $\{f_n(t)\}_0^\infty$ with Salzer summation. The Stehfest algorithm is

$$\Phi(t) \approx \frac{\ln 2}{t} \sum_{k=1}^{N} V_k \, \bar{\Phi}\left(k \frac{\ln 2}{t}\right), \tag{5.2}$$

where the V_k coefficients are independent of $\bar{\Phi}(p)$. The V_k only depend on the total number of terms, N (which must be even); they are given by

$$V_k = (-1)^{\frac{N}{2}+k} \sum_{j=\frac{j+1}{2}}^{\min(j,\frac{N}{2})} \frac{j^{\frac{N}{2}}(2j)!}{(\frac{N}{2}-j)!\, j!\, (j-1)!\, (k-j)!\, (2j-k)!}. \tag{5.3}$$

The Stehfest algorithm has seen application in hydrology (e.g. Moench and Ogata, 1981, 1984; Hemker and Maas, 1987; Lee, 1999), because it only requires real p values and is algorithmically simple. The V_k coefficients can be computed once and stored as constants. Unfortunately, V_k quickly become very large and the terms

oscillate in sign as k increases, making the optimum N a function of the working precision of the computer. For double precision, $N = 16$ is considered optimum; larger N suffer from severe cancellation. The algorithm is not designed to handle functions with step changes or oscillations in t, unless N is very high.

Abate and Valkò (2003) showed that the Stehfest algorithm can be accurately applied in an arbitrary precision environment, such as Mathematica (Wolfram Research, 2007) or MPF90 (Bailey, 1995), where V_k can be computed accurately for large N. The downfall of this approach is that the entire LT-AEM model must also be implemented in arbitrary precision, which is usually impossible or very expensive. Philosophically, the arbitrary precision approach is also inelegant, since it requires brute numerical precision to achieve what can easily be done using complex double precision in other methods.

When the image function is available in closed form, (5.1) may be evaluated directly. For general LT-AEM problems, where the generalized Fourier series coefficients are computed from a least-squares problem, analytically computing $\partial/\partial p$ is typically not possible.

In the cases where coefficients may be computed analytically (passive or simple active elements), this method may be applied. An example of this is given using the impulse point source, which has the image function

$$\bar{\Phi}_{\mathrm{pt}}(r,p) = \frac{Q}{2\pi}\mathrm{K}_0\left(r\sqrt{\frac{p}{\alpha}}\right), \tag{5.4}$$

corresponds to the object function

$$\Phi_{\mathrm{pt}}(r,t) = \frac{Q}{4\pi t}\exp\left[-\frac{r^2}{4t\alpha}\right], \tag{5.5}$$

which is used to evaluate the error of the following numerical results. Convolution of (5.4) with $1/p$ gives the traditional Theis (1935) solution (see example section 2.4.2).

Applying (5.1) to (5.4) results in an unusually simple expression, because of the recurrence relationships that exist for Bessel function derivatives (McLachlan,

1955, p.204). The Post-Widder expression can be simplified to the form

$$\Phi_n(r,t) = \frac{Q}{2\pi p}\frac{p^{n+1}}{n!}\frac{r^n \mathrm{K}_n\left(r\sqrt{\frac{p}{\alpha}}\right)}{2^n(\alpha p)^{n/2}}, \qquad p = \frac{n+1}{t}. \tag{5.6}$$

For $\alpha = 1$, $r = 0.1$, $Q = 1$, and $t = 0.25$, values of the errors committed in estimating $\Phi_n(r,t)$ are listed in Table 5.1. Although the Post-Widder solution itself is only accurate for very large values of n, the series can be accelerated to achieve higher accuracy. Aitken's δ^2-process (Antia, 2002, §6.2) is used because it only requires three adjacent terms of the series. Stehfest (1970) utilized Salzer summation (requiring the $1 - N$ series) in his numerical approach.

A benefit of the Post-Widder approach, when it can be applied, is the solution only requires *one term* for the non-accelerated Post-Widder solution, or three terms for the δ^2-process accelerated solution (there is no $n = 1, 2$ in Table 5.1). Higher-order derivatives for some functions may be ill-defined, may not have convenient recurrence relationships, or may be more involved to compute than Bessel functions.

n	error $\lvert\Phi_n - \Phi(t)\rvert$	accelerated error $\lvert\delta^2[\Phi_n] - \Phi(t)\rvert$
3	9.668686 $\times 10^{-3}$	1.722383 $\times 10^{-5}$
4	6.503074 $\times 10^{-3}$	1.174752 $\times 10^{-5}$
5	4.893049 $\times 10^{-3}$	8.153614 $\times 10^{-6}$
6	3.920859 $\times 10^{-3}$	5.810009 $\times 10^{-6}$
7	3.270615 $\times 10^{-3}$	4.295339 $\times 10^{-6}$
8	2.805238 $\times 10^{-3}$	3.286391 $\times 10^{-6}$
9	2.455745 $\times 10^{-3}$	2.588455 $\times 10^{-6}$
10	2.183659 $\times 10^{-3}$	2.088368 $\times 10^{-6}$
20	1.035797 $\times 10^{-3}$	5.067141 $\times 10^{-7}$
30	6.788946 $\times 10^{-4}$	2.222317 $\times 10^{-7}$
40	5.049138 $\times 10^{-4}$	1.241183 $\times 10^{-7}$
50	4.019141 $\times 10^{-4}$	7.908633 $\times 10^{-8}$

TABLE 5.1. Error in with Post-Widder approximation to $\mathcal{L}^{-1}$; n is the order of the term, not the total number of terms used.

For most solutions, numerical evaluation of the Post-Widder formula is un-

wieldy. For certain geometries, if the functional form is easily manipulable (potentially using a computer algebra system), this method may be feasible. Other, more sophisticated acceleration schemes may be utilized to further improve convergence of this simple approach, in these situations.

The Post-Widder inverse is presented here to illustrate a method that capitalizes on the analytic solutions that can sometimes be derived in Laplace space for groundwater flow problems. This is an example of a benefit due to the elegance that arises when working with analytic or semi-analytic solutions; a gridded numerical method could also be posed in Laplace space, but it would be impossible to compute derivatives (aside from finite difference approximations to the derivatives) of the gridded solution with respect to the Laplace parameter.

5.3.2 Schapery

The method of Schapery (1962) is different from the other methods considered here, since it only approximates the deviation of $f(t)$ from a corresponding steady-state solution. This obviously requires a steady solution, which does not always exist (e.g., $\sin(t)$ has no steady value). It is typically easier to reformulate and solve the Laplace equation, than to attempt to solve the modified Helmholtz equation for $t \to \infty$ (i.e., as $p \to 0$). The deviation is expanded in terms of decaying exponential basis functions — a simple but potentially ill-posed approach (Lanczos, 1956, §4.23); the method is given as

$$f(t) = f_s + \sum_{i=1}^{M} a_i e^{-p_i t} \tag{5.7}$$

where the steady-state or reference solution f_s is assumed to exist, and a_i is a vector of constants to be determined. Applying (A.1) to (5.7) gives

$$\bar{f}(p_j) = \frac{f_s}{p_j} + \sum_{i=1}^{M} \frac{a_i}{p_i + p_j} \quad j = 1, 2, \ldots, M. \tag{5.8}$$

M values of p_j are picked (typically a geometric series) which cover the "important fluctuations" in $\bar{f}(p)$; after setting $p_i = p_j$ the a_i coefficients can be determined as the solution to a matrix problem. Posing (5.8) as $P_{ij}a_i = \left(\bar{f}(p_j) - f_s/p_j\right)$, the matrix to invert becomes

$$P_{ij} = \begin{bmatrix} (p_1 + p_1)^{-1} & (p_1 + p_2)^{-1} & \dots & (p_1 + p_M)^{-1} \\ (p_2 + p_1)^{-1} & (p_2 + p_2)^{-1} & \dots & (p_2 + p_M)^{-1} \\ \vdots & \vdots & \ddots & \vdots \\ (p_M + p_1)^{-1} & (p_M + p_2)^{-1} & \dots & (p_M + p_M)^{-1} \end{bmatrix} \tag{5.9}$$

The matrix P_{ij} does not depend on $\bar{f}(p)$, so it only needs to be inverted once for a choice of p_j, with the resulting a_i coming from a matrix-vector multiplication with the calculated $\bar{f}(p)$ and f_s.

This method also only requires real computation and historically has seen some use (e.g. Liggett and Liu, 1983; Hemker and Maas, 1987), but has two main drawbacks. It requires an additional steady-state or reference solution and no theory is presented to indicate an optimal way to pick p_j. A geometric series is suggested, but Liggett and Liu (1983, p.177) note that some trial and error is required. This method is briefly mentioned due to show its different approach and for historical completeness.

5.3.3 Fourier series

The Fourier series approach for approximating (A.4) was initially made into a usable algorithm by Dubner and Abate (1968), it was first accelerated by Crump (1976), and the method was further improved by de Hoog et al. (1982), among others. There have been many different modifications and extensions to the basic Fourier series approach, because it is a generally robust numerical inverse Laplace transform method (Davies and Martin, 1979).

The method is based upon the connection between the Mellin integral and the Fourier transform. Following Churchill (1972, §66), this begins by expanding (A.4)

into real and imaginary parts ($p = \sigma + i\omega$, where σ is fixed), giving

$$\Phi(t) = \frac{e^{\sigma t}}{2\pi} \int_{\sigma_0 - i\infty}^{\sigma_0 + i\infty} e^{i\omega t} \bar{\Phi}(\sigma + i\omega)\, \mathrm{d}\omega. \tag{5.10}$$

This complex contour integral along a contour parallel to the imaginary axis can be broken into two real improper integrals,

$$\Phi(t) = \frac{e^{\sigma t}}{2\pi} \left[\int_{-\infty}^{0} e^{i\omega t} \bar{\Phi}(\sigma + i\omega)\, \mathrm{d}\omega + \int_{0}^{\infty} e^{i\omega t} \bar{\Phi}(\sigma + i\omega)\, \mathrm{d}\omega \right]. \tag{5.11}$$

By the change of variables $\omega = -\omega$ in the first integral, the two integrals can be combined as

$$\Phi(t) = \frac{e^{\sigma t}}{2\pi} \int_{0}^{\infty} \left[e^{-i\omega t} \bar{\Phi}(\sigma - i\omega) + e^{i\omega t} \bar{\Phi}(\sigma + i\omega) \right] \mathrm{d}\omega, \tag{5.12}$$

where the integrand is of the form $[f(z)]^* + f(z) = 2\Re[f(z)]$. The two functions in the integrand of (5.12) are conjugates of each other, $\left[e^{i\omega t} \bar{\Phi}(\sigma + i\omega)\right]^* = e^{-i\omega t} \bar{\Phi}(\sigma - i\omega)$, because $\bar{\Phi}(p^*) = \bar{\Phi}^*(p)$, rather than the more general form $\left[\bar{\Phi}(p)\right]^* = \bar{\Phi}^*(p^*)$ (Milne-Thompson, 1996, §5.14). The simpler conjugation rule comes from conjugating both sides of (5.10); a real function of real argument equals its conjugate, therefore the integrand must equal its conjugate (of conjugate argument). The integrand of (5.12) then becomes

$$2\Re\left\{ (\cos\omega t + i \sin\omega t) \left[\Re\left(\bar{\Phi}\right) + i\Im\left(\bar{\Phi}\right) \right] \right\}; \tag{5.13}$$

multiplying out all four terms in (5.13) and only keeping the real part puts (5.12) into the form

$$\Phi(t) = \frac{e^{\sigma t}}{\pi} \int_{0}^{\infty} \left\{ \Re\left[\bar{\Phi}(p)\right] \cos\omega t - \Im\left[\bar{\Phi}(p)\right] \sin\omega t \right\} \mathrm{d}\omega, \tag{5.14}$$

which is a Fourier series approximation of the object function, $\Phi(t)$, in terms of the image function $\bar{\Phi}(p)$. As with most Fourier series approximations, the function can be expanded equivalently in terms of a Fourier sine, cosine, or complex

exponential series. These three equivalent forms are

$$\Phi(t) = \frac{e^{\sigma t}}{\pi} \int_0^\infty \Re\left[\bar{\Phi}(p)\right] \cos \omega t \, \mathrm{d}\omega, \tag{5.15}$$

$$= -\frac{e^{\sigma t}}{\pi} \int_0^\infty \Im\left[\bar{\Phi}(p)\right] \sin \omega t \, \mathrm{d}\omega, \tag{5.16}$$

$$= \frac{e^{\sigma t}}{\pi} \Re\left(\int_0^\infty e^{i\omega t} \bar{\Phi}(\sigma + i\omega) \, \mathrm{d}\omega \right), \tag{5.17}$$

where (5.15) is a Fourier cosine transform of the time-domain solution, (5.16) is a Fourier sine transform and (5.17) is the real portion of a complex Fourier transform.

Although all 3 of these analytic representations of $\Phi(t)$ are equivalent (e.g., Dubner and Abate (1968) used (5.15), while de Hoog et al. (1982) used (5.17)), when evaluating (5.14) numerically with the trapezoid rule, Durbin (1973) showed that using (5.17) leads to the smallest discretization error. Wynn (1966) found that in general it is profitable to utilize the complex exponential Fourier series form over the simpler trigonometric form, when applying nonlinear series acceleration; we simply discard the unneeded imaginary component at the end. The trapezoid rule approximation to (5.17) is

$$\Phi(t) = \frac{e^{\sigma t}}{T} {\sum_{k=0}^{2M}}' \Re\left[\bar{\Phi}\left(\sigma + \frac{i\pi k}{T} \right) \exp\left(\frac{i\pi t}{T} \right) \right], \tag{5.18}$$

where T is a scaling parameter (often set to $2t_{max}$) and the prime indicates that the $k = 0$ and $2M$ terms in the summation are halved. The values of p required for the method (the argument to $\bar{\Phi}$) do not functionally depend on the time being inverted. Equation 5.18 is the non-accelerated Fourier series inverse algorithm, and is of little practical use in this form, requiring thousands of evaluations of $\bar{\Phi}(p)$ for many types of functions (Crump, 1976); there are several methods to accelerate this summation.

Richardson extrapolation can be used to estimate the limit as the integration step size $\to 0$, one way of accelerating the convergence of (5.18). This technique

is often referred to as Romberg integration (e.g. Antia, 2002, §6.2); it is very effective for smooth functions with bounded derivatives. Here we are guaranteed this, based on the definition of the Laplace transform; all singularities are left of the Bromwich contour.

The ϵ-algorithm of Wynn (1966) can be used to increase convergence of the trapezoid rule (5.18); this was the approach taken by Crump (1976) in the first accelerated form of this method, and is illustrated by Antia (2002, §9.8). In their widely-used version of this method, de Hoog et al. (1982) utilized a Padé approximation (rational polynomials) with an analytic expression for the remainder of the truncated series (which they termed *double-acceleration*). Homeier (1993) developed a more generalized non-linear transformation which performs better than the ϵ-algorithm, but is more unstable near singularities. Oleksy (1996) developed an initial transformation using trigonometric identities, which is applied before acceleration and leads to increased convergence near singularities. Sakurai (2004) applied a variant of Euler summation to (5.18) to optimally accelerate the Fourier series solution in the presence of singularities.

Any of these acceleration methods can be used to make the Fourier series approach a robust and efficient numerical inversion method for most $\Phi(t)$, but the non-linear acceleration can cause numerical dispersion in some convective problems. Morales-Casique and Neuman (2008) describe difficulties in reproducing pure advection, caused by the non-linear acceleration of Gibbs' phenomena near sharp fronts. Brio et al. (2005) feel this shortcoming of the otherwise very robust Fourier series approach is reason enough to use the Möbius-based methods, which do not use or benefit from non-linear acceleration. For diffusion problems, non-linear acceleration does not pose such a great threat.

5.3.4 Möbius mapping

The numerical inverse transform algorithms based upon the Möbius transform fall into the category of methods which expand the image function in terms of basis functions that have analytic inverse transforms. Several different versions of this approach (using Legendre, Chebyshev, and Laguerre polynomials) are discussed in an early book by Lanczos (1956, §4.23–31); we discuss here the two most successful of these, in their modern implementations.

Since, by definition, the image function is analytic in the right half of the p-plane (see shaded area in left portion of Figure 5.2), the Möbius (i.e., bilinear) transform can advantageously be used to map this region into the unit circle (see Strack, 1989, §30; Needham, 1997, §3); following the convention of Davies (2002, §19), this is given as

$$z = \frac{p - a - b}{p - a + b}, \qquad a > \sigma_0, \qquad b > 0, \tag{5.19}$$

where z is the mapped complex variable and a and b are auxiliary parameters. The plane $\Re(p) > a \mapsto |z| \leq 1$, with the line $\Re(p) = a \mapsto |z| = 1$ (see dotted line A in Figure 5.2) and the real line ($0 < \Re(p) < \infty$, $\Im(p) = 0$) is mapped to the diameter of the circle, $-1 < \Re(z) < 1$, $\Im(z) = 0$ (see dashed line B Figure 5.2). As is evident in the Möbius inverse transform,

$$p - a + b = \frac{2b}{1 - z}, \tag{5.20}$$

the point $p = \infty$ is mapped to $z = +1$, requiring all image functions to be analytic as a function of $1/p$ at infinity, to ensure convergence at this point on the circumference of the unit circle.

The inversion algorithms attributed to Weeks (1966) and Piessens (1972) use this approach, largely the same but utilizing different basis functions. The Weeks method uses Laguerre polynomials for complex z (on the unit circle, A), while

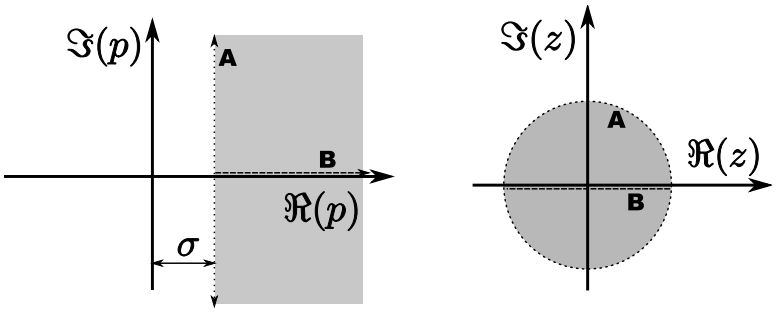

FIGURE 5.2. Möbius transformation between p (left) and z planes (right)

Piessen's method uses Chebyshev polynomials for real z (on the diameter of the unit circle, B). These methods are similar, and share a common theoretical framework (though they were developed independently). Both methods expand the mapped image function $\bar{\Phi}(p)$ in basis functions that have analytic inverse transforms, allowing more rigorous error analysis and very different convergence properties than the Fourier series approach.

When the singularities of $\bar{\Phi}(p)$ are known, a and b can be chosen to allow any values of $\Phi(t)$ to be computed from a single set of image function evaluations. Unfortunately, due to the mapping, the Möbius methods are quite sensitive to the values of the auxiliary parameters (a and b), sometimes completely diverging for non-optimal parameter values. Despite these shortcomings, these methods are a potentially useful alternative in some LT-AEM applications, especially simulation of advection. This approach would be useful where interest lies only in one type of element and time behavior, and therefore we can afford to make an in-depth analysis of the optimum a and b values.

Weeks method The time-domain solution, using Weeks' basis functions is

$$\Phi(t) = e^{(a-b)t} \sum_{n=0}^{N} a_n \mathrm{L}_n(2bt), \tag{5.21}$$

where $\mathrm{L}_n(x)$ is an n^{th} order Laguerre polynomial (e.g. Andrews, 1998, §5.3) and a_n are coefficients to determine. The Laplace transform of (5.21), in terms of z, is

$$\mathcal{L}\left[\Phi(t)\right] = \bar{\Phi}(p) = \left(\frac{1-z}{2b}\right) \sum_{n=0}^{N} a_n z^n, \tag{5.22}$$

which is a power series expansion of the image function (the mapped image function is guaranteed to be analytic inside the unit circle). The simple form of (5.22) is what has lead many to call the Weeks algorithm the most "natural" inverse transform method (Davies, 2002). The coefficients can be determined from integrating $\bar{\Phi}(z)$ on the unit circle using the midpoint rule (designed to not sample the point $z = 1$, which corresponds to $p = \infty$),

$$a_n = \frac{1}{M} \sum_{j=1}^{M} \Psi\left(e^{2i\theta_{j-1/2}}\right) e^{-2in\theta_{j-1/2}} \tag{5.23}$$

where $\theta_k = k\pi/M$. The function $\Psi(z)$ is the conformally-mapped image function; it is given by

$$\Psi(z) = \frac{b}{1-z}\, \bar{\Phi}\left(\frac{2b}{1-z} + a - b\right). \tag{5.24}$$

Weeks originally suggested that $a = 1/t_{max}$ and $b = 2N/t_{max}$, where t_{max} is the maximum time needed to be transformed. While the values of p required by $\bar{\Phi}(p)$ do not functionally depend on the time being inverted, the optimal parameter values do. Without information about the location of singularities in $\bar{\Phi}(p)$ ($\mapsto |z| > 1$) the most successful optimization is a 2-parameter search in the Laplace plane; this requires many evaluations of $\bar{\Phi}(p)$. Weideman (1999) proposes some optimization schemes for determining parameter values for a given problem, but his techniques are quite expensive, often requiring hundreds of evaluations of $\bar{\Phi}(p)$ to estimate optimum parameters.

Chebyshev method Since the method is similar to Weeks' method, the discussion here is minimal. The time domain solution is given as

$$\Phi(t) = e^{(a-b)t} {\sum_{n=0}^{N-1}}' a_n \, {}_2F_2(-n, n; \tfrac{1}{2}, 1; bt) \tag{5.25}$$

where ${}_2F_2$ is a generalized hypergeometric function (e.g. Andrews, 1998, §11), which for the given argument and parameters is just a polynomial. The Laplace transform of (5.25) is

$$\Phi(p + a - b) = \frac{1}{p} {\sum_{n=0}^{N-1}}' a_n \mathrm{T}_n \left(1 - \frac{2b}{p}\right), \tag{5.26}$$

where $\mathrm{T}_n(x)$ is an n^{th}-order Chebyshev polynomial (e.g. Andrews, 1998, §5.4.2). The coefficients are evaluated using Chebyshev quadrature along the line $-1 < z < 1$, resulting in

$$a_n = \frac{2}{N} \sum_{k=0}^{N-1} \Psi\left(\cos\frac{\pi(k+1/2)}{N}\right) \cos\frac{n\pi(k+1/2)}{N}, \tag{5.27}$$

with $\Psi(z)$ defined in (5.24).

Recurrence relationships for functions For both Möbius methods, the basis functions are most stably computed from recurrence relationships, as severe cancellation occurs when evaluating them directly from their published definitions for large n. Davies (2002, §19) gives general stable expressions for these functions; they are listed here in a simplified form. The two-term recurrence relationship for the Laguerre polynomials (required in (5.21)) is

$$n\mathrm{L}_n(x) = (2n - 1 - x)\mathrm{L}_{n-1}(x) - (n-1)\mathrm{L}_{n-2}(x) \quad n = 3, 4, 5, \ldots \tag{5.28}$$

The stable three-term recurrence relationship for the generalized hypergeometric functions (required in (5.25)), listed briefly as $\phi_n(x)$, is

$$\phi_n(x) = (A_n + B_n x)\phi_{n-1} + (C_n + D_n x)\phi_{n-2} + E_n\phi_{n-3} \quad n = 4, 5, 6, \ldots \tag{5.29}$$

which is completed using the following simplified expressions for A_n–E_n

$$A_n = \frac{3n^2 - 8n + 3}{(n-2)n} \qquad B_n = -\frac{4}{n} \qquad C_n = -\frac{3n^2 - 10n + 6}{(n-2)n} \tag{5.30}$$
$$D_n = -\frac{4(n-1)}{(n-2)n} \qquad E_n = -\frac{(n-1)(3-n)}{(n-2)n}$$

with the recurrence relationships seeded using the first few values of n, given in Table 5.2.

n	$\mathrm{L}_n(x)$	${}_2F_2(-n, n; \frac{1}{2}, 1, x)$
0	1	1
1	$1 - x$	$1 - 2x$
2	$1 - 2x + \frac{x^2}{2}$	$1 - 8x + 4x^2$
3	$1 - 3x + \frac{3}{2}x^2 - \frac{x^3}{6}$	$1 - 18x + 24x^2 - \frac{16x^3}{3}$
4	$1 - 4x + 3x^2 - \frac{2}{3}x^3 + \frac{x^4}{24}$	$1 - 32x + 80x^2 - \frac{128x^3}{3} + \frac{16x^4}{3}$

TABLE 5.2. Basis functions for Möbius mapping methods

Chapter 6
LT-AEM INVERSE APPLICATIONS

This chapter is comprised of two LT-AEM inverse-modeling applications. The first uses the parameter estimation code PEST (Doherty, 2007) to estimate aquifer properties using data from one of several unpublished aquifer tests conducted at a field site in Boise, Idaho (Barrash et al., 2006). In the first of three LT-AEM models used to interpret the tests, aquifer parameters are assumed homogeneous; using PEST, the model parameters were adjusted to best fit the observed head. After introducing two circular regions of different aquifer parameters, the model is re-calibrated to better fit drawdown at two observation wells. For comparison, the first homogeneous model with a confined governing equation is used to illustrate the effects the unconfined behavior have on the solution.

The second inverse modeling application is a synthetic forward model that uses a Markov chain Monte Carlo inverse method (Vrugt et al., 2003b) to estimate the location of 4 circular elements with K different from the background, when the aquifer parameters are assumed known.

6.1 Boise aquifer test

The aquifer test was performed in a shallow unconfined aquifer (Figure 6.1, see Barrash et al. (2006) for photomap of field site). The test was a dipole of two wells (well C5 pumping on the west side of the group, well C2 injecting on the east side) for a pumping duration of 280 minutes, with 200 minutes of recovery. The pumping rate was approximately $4.3\,\mathrm{L/sec}$ ($68\,\mathrm{gpm}$) throughout the test for both pumping and injection. Observations were made at 13 monitoring wells and the two pumping/injection wells using pressure transducers and a datalogger. Well

coordinates are given in Table 6.1; all wells are assumed to fully penetrate the $5\,\mathrm{m}$ thick unconfined aquifer.

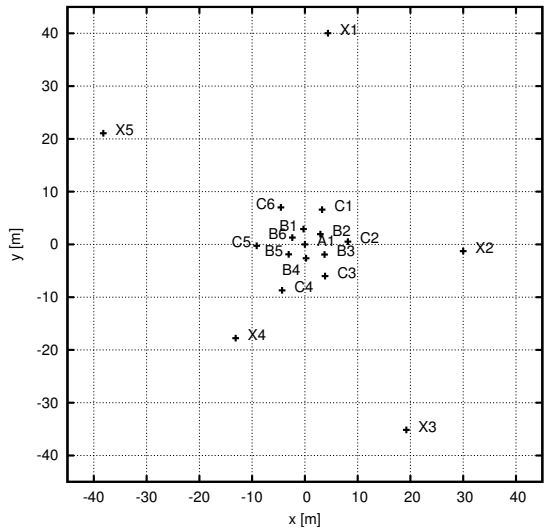

FIGURE 6.1. Boise Hydrogeophysics Research Site well locations; see Barrash et al. (2006) for photomap of site.

6.1.1 LT-AEM model

Due to an apparently irregular initial head surface at the beginning of the test, the analysis was performed using drawdown from a baseline condition, averaged over observations made during the hour before pumping began. It was observed that the data recover to a common non-zero level of drawdown; Barrash et al. (2006) indicates the trees surrounding the site have an observable evapotranspiration signal, varying sinusoidally by a few millimeters, with a period of 24 hours.

The observed drawdown was reproduced using a solution with an unconfined source term (see model in §4.2.3). Drawdown observed in the pumping and injection wells was observed to be influenced by a skin effect (Barrash et al., 2006), which only affects those observations made in the pumping/injection wells. We circumscribed two circular matching elements around a point pumping well to

well	x $[m]$	y $[m]$
A1	0.00	0.00
B1	-0.27	2.92
B2	2.94	1.94
B3	3.72	-1.92
B4	0.23	-2.64
B5	-3.08	-1.89
B6	-2.38	1.30
C1	3.26	6.59
C2	8.14	0.52
C3	3.82	-6.01
C4	-4.33	-8.72
C5	-9.13	-0.26
C6	-4.56	7.01
X2	30.02	-1.28
X4	-13.12	-17.78

TABLE 6.1. BHRS well locations

simulate the effects of wellbore storage a skin effect. The inner $10.2\,\mathrm{cm}$-diameter circle (corresponding to the diameter of the well casing), was assigned a unit specific storage $S_S = 1$ and very large permeability ($K = 250\,\mathrm{cm/sec}$), while the outer circle has a $12.7\,\mathrm{cm}$ diameter. The annulus between the two circles was assigned a very low specific storage (i.e., approximately steady-state – common in wellbore skin solutions); its permeability was a free parameter.

The parameters that were estimated from the data included aquifer properties for the homogeneous domain, K, S_s, K_z, S_y, and the permeability of the skin at both the pumping and injection well.

6.1.2 Homogeneous model results

As a first estimate, a homogeneous LT-AEM model was used to fit the observed head data. Barrash et al. (2006) have characterized the site as being relatively homogeneous, based on single-well pumping tests. Two of the observation wells (X2 and X4) did not fit particularly well at intermediate time (see Figure 6.4), po-

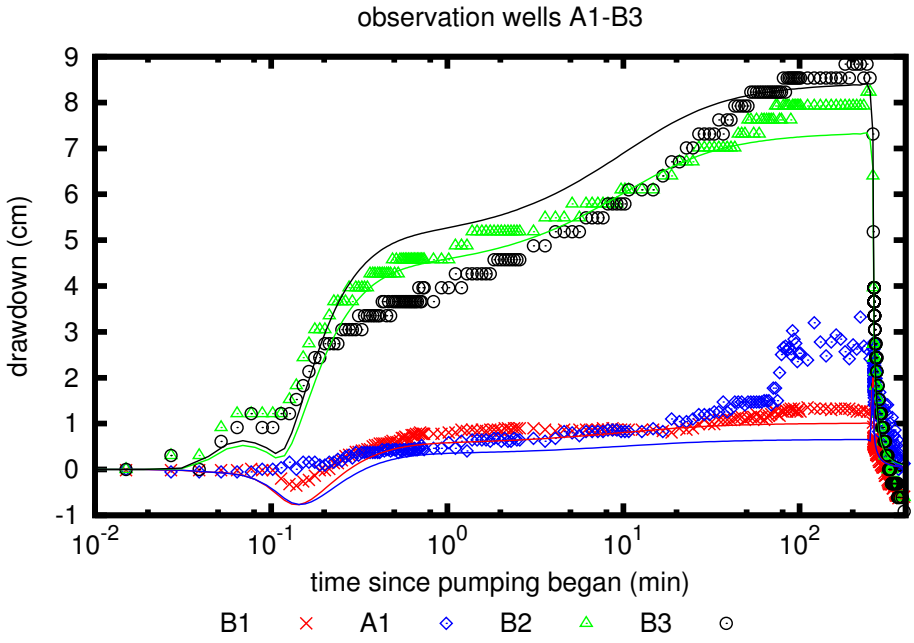

FIGURE 6.2. LT-AEM model (lines) and observed data (points) for observation group 1

tentially due to some heterogeneity or anisotropy in the domain, which is not explained by the homogeneous LT-AEM model used here. The aquifer properties

			95% confidence interval	
parameter	units	estimated	lower limit	upper limit
K	cm/sec	4.844	4.828	4.860
S_s	–	0.002688	0.002497	0.002893
S_y	–	0.07317	0.07287	0.07346
K_z	cm/sec	0.03341	0.03185	0.03504
$K_{\text{skin}}^{\text{pump}}$	cm/sec	0.02964	0.02956	0.02972
$K_{\text{skin}}^{\text{inj}}$	cm/sec	0.1264	0.1142	0.1398

TABLE 6.2. Results of parameter estimation for homogeneous model

estimate here are physically reasonable for an unconsolidated fluvial deposit, as is observed at the Boise site.

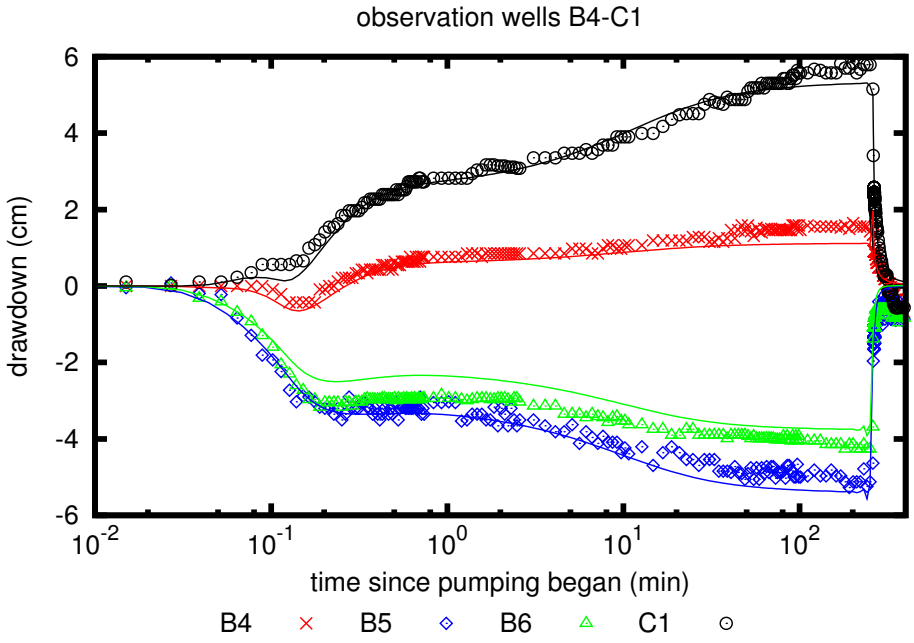

FIGURE 6.3. LT-AEM model (lines) and observed data (points) for observation group 2

6.1.3 Inhomogeneous model results

Two circular inhomogeneities were introduced, each surrounding one of the wells X2 or X4 (see Figure 6.6), where the unconfined aquifer properties (K_z and S_y) were allowed to vary independently from those in the background aquifer (the confined aquifer properties were kept constant everywhere). A second set of parameters was then estimated using PEST and the same observations, based on the results of some preliminary "hand calibration" testing. The (x_c, y_c) locations of the centers of the two circles $(-15\text{m}, 25\text{m})$, $(42\text{m}, -6\text{m})$ and radii of the two circles (17m each) were not included in the estimation process. The K_z in the circular regions was estimated to be about two orders of magnitude lower than the background (see Table 6.3), which was found to have the largest effect on fitting the intermediate-time observations at wells X2 and X4 (compare the fit in Figures 6.4 and 6.7; the plots for the other observation wells were not repeated as they are largely unaffected by

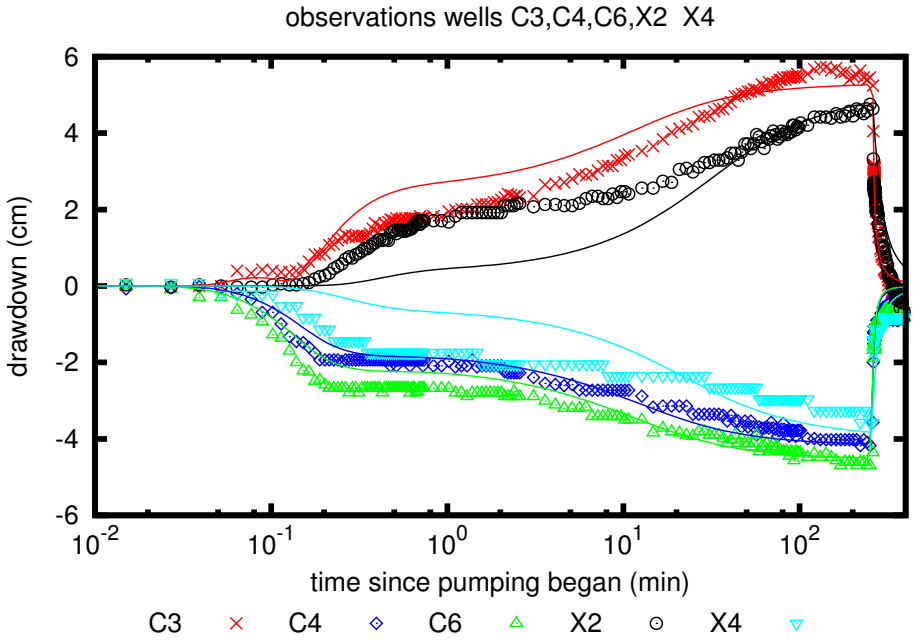

FIGURE 6.4. LT-AEM model (lines) and observed data (points) for observation group 3

			95% confidence interval	
parameter	units	estimated	lower limit	upper limit
K	cm/sec	5.068	5.042	5.093
S_s	–	0.002061	0.0018467	0.002301
S_y	–	0.07317	0.07288	0.07346
K_z	cm/sec	0.03837	0.03709	0.03969
K_z^{X2}	cm/sec	0.0009003	0.0001038	0.007812
K_z^{X4}	cm/sec	0.0003497	3.905×10^{-5}	0.003132
S_y^{X2}	cm/sec	1.060×10^{-7}	2.343×10^{-8}	4.796×10^{-7}
S_y^{X4}	cm/sec	1.542×10^{-6}	3.429×10^{-7}	6.935×10^{-6}

TABLE 6.3. Results of parameter estimation for inhomogeneous model

the two circular inhomogeneities). Decreasing K_z, while maintaining the aquifer thickness, has the effect of decreasing β in Figure 4.9. Smaller β values correspond to models that predict results with increased drawdown at intermediate times; this behavior is like that observed at wells X2 and X4 in Figure 6.4 for the homogeneous solution. The S_y estimated for the two circular regions was estimated to be

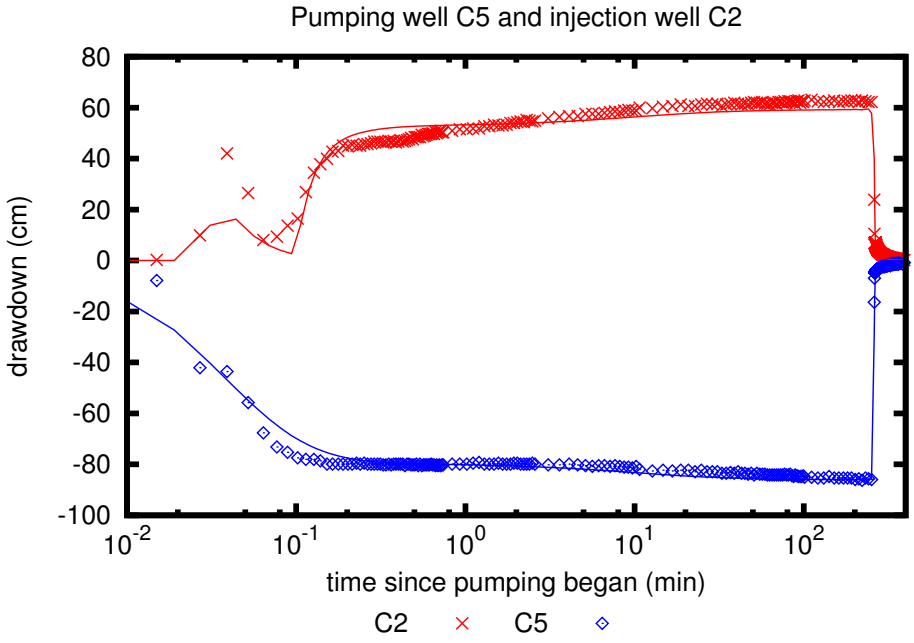

FIGURE 6.5. LT-AEM model (lines) and observed data (points) for pumping and injection wells

un-physically small (smaller than confined storage). This in combination with the low K_z values points to the explanation that the aquifer is behaving more confined (essentially no delayed yield) near these wells. This might be attributed to some clay layers near the top of the aquifer, but without field observations this is pure speculation. The aquifer properties for the rest of the aquifer were estimated to be approximately the same as for the homogeneous case, because the fit of the model to the data elsewhere was good

6.1.4 Unconfined vs confined

As an exercise, the original homogeneous results given in the previous section were recomputed with only a confined model (no S_y and K_z) for comparison.

Comparing the results in Figures 6.8–6.11 to those for the unconfined case in Figures 6.2–6.5, it is clear that the unconfined behavior is required to reproduce

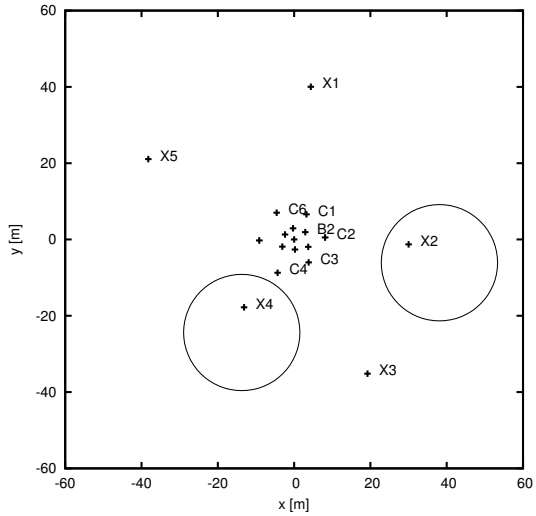

FIGURE 6.6. Well locations and circular inhomogeneous regions

the "two-hump" behavior observed in many of the observation wells (especially wells B2 and B3 in Figure 6.8). The early-time and late-time data match the confined model well, but the intermediate-time data clearly do not. The matches at the pumping wells (see Figure 6.11) only show slight deviations from the data, illustrating that the wellbore storage and skin effects have a larger observable impact on drawdown there than the delayed yield from the aquifer.

Interestingly, wells X2 and X4 (see Figure 6.10), that were determined in the previous section to have very small delayed yield in the circular regions surrounding the wells, do not fit well with the "confined everywhere" model presented here. Unconfined effects are visible in the data, but not to the same extent as seen in the other wells. One possible manner to explain this observed difference is through heterogeneous distribution of unconfined properties.

LT-AEM can be used to first match an aquifer test or similar data set using a homogeneous solution with only a few parameters, similar to an analytic solution. If desired, more complexity can be added by introducing regions of different aquifer properties or source terms. This allows flexibility not commonly found in a tran-

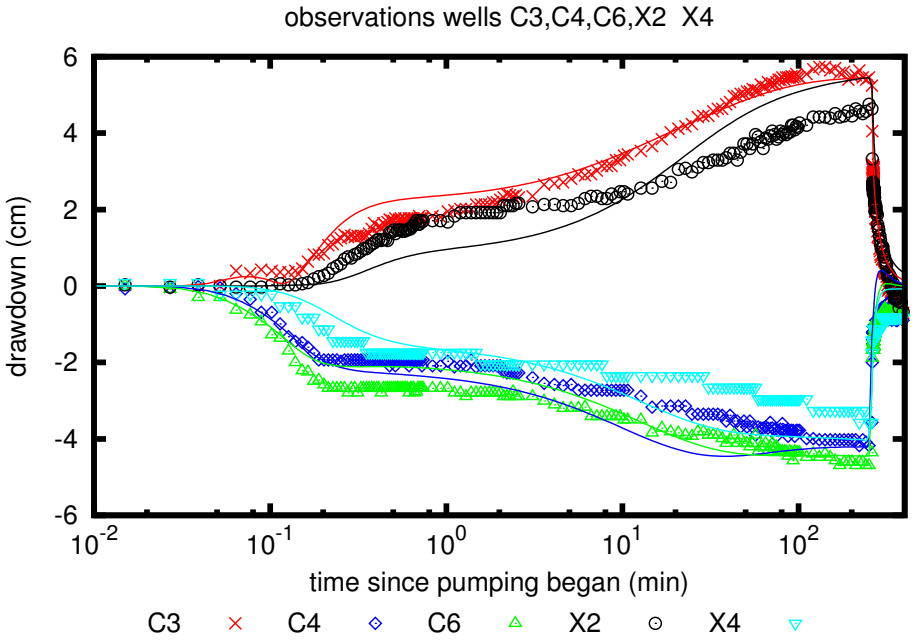

FIGURE 6.7. Inhomogeneous LT-AEM model with 2 circles (lines) and observed data (points) for observation group 3

sient analytic solution, without requiring the hydrologist to switch from the first simple solution to a more flexible (but completely different) gridded flow model.

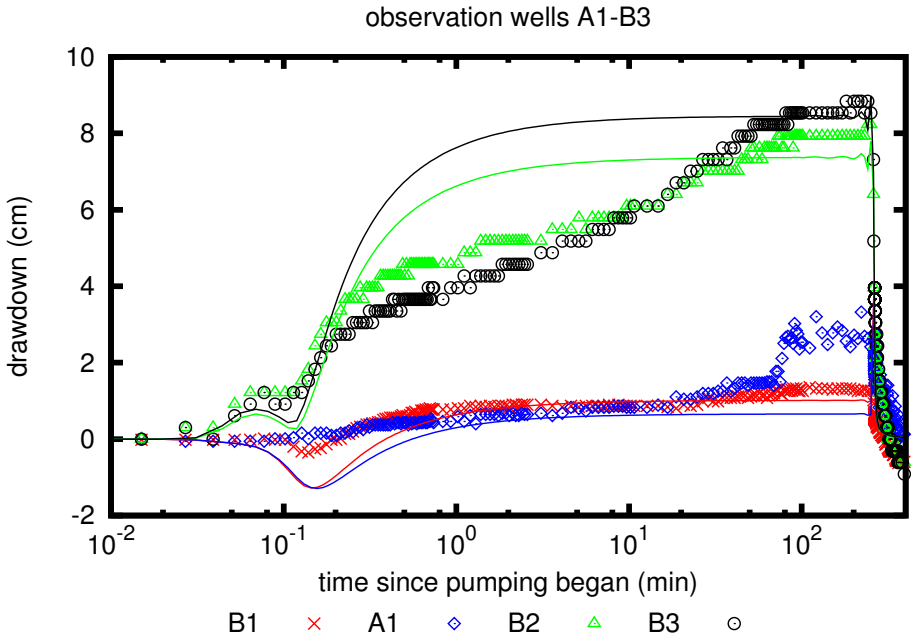

FIGURE 6.8. Confined LT-AEM model (lines) and observed data (points) for observation group 1

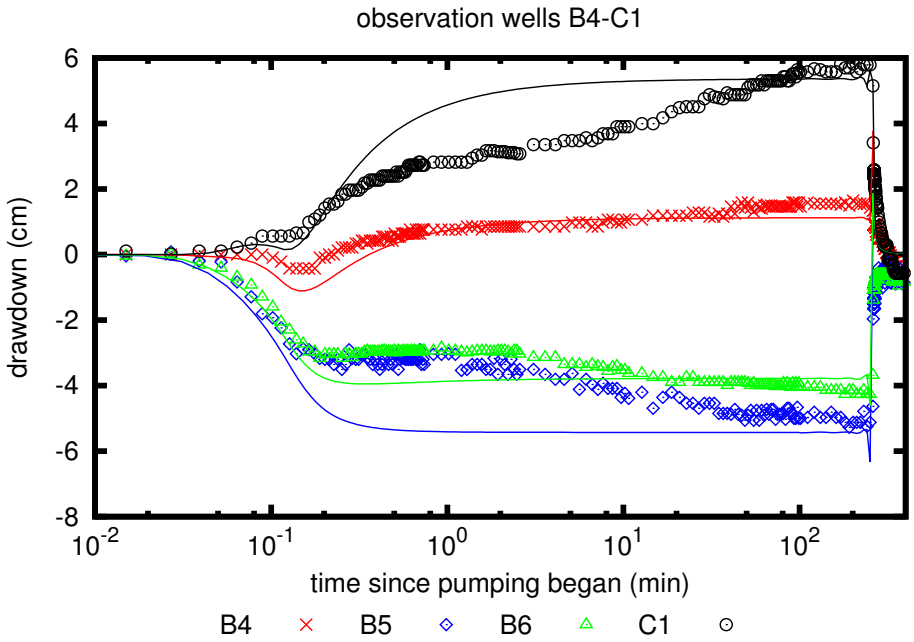

FIGURE 6.9. Confined LT-AEM model (lines) and observed data (points) for observation group 2

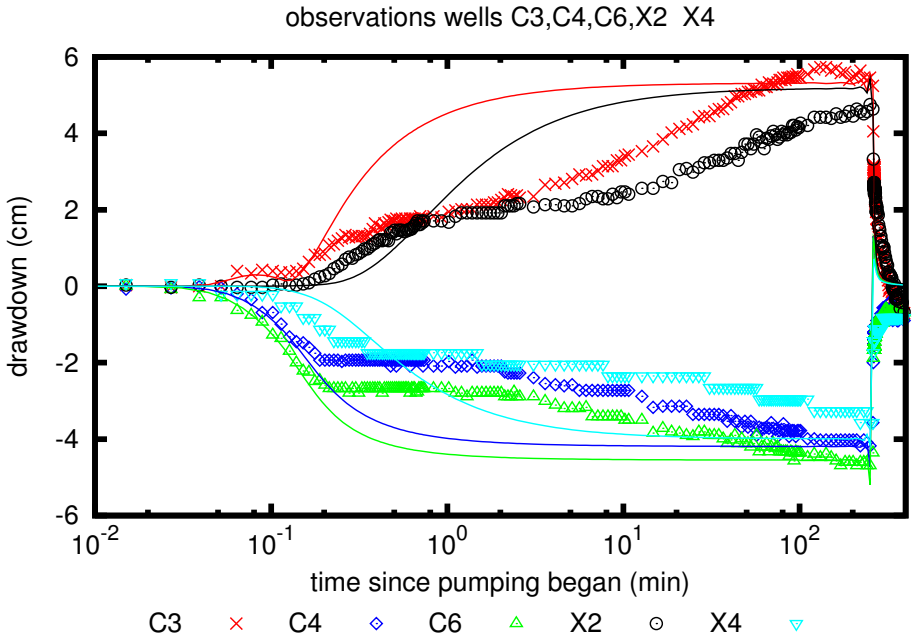

FIGURE 6.10. Confined LT-AEM model (lines) and observed data (points) for observation group 3

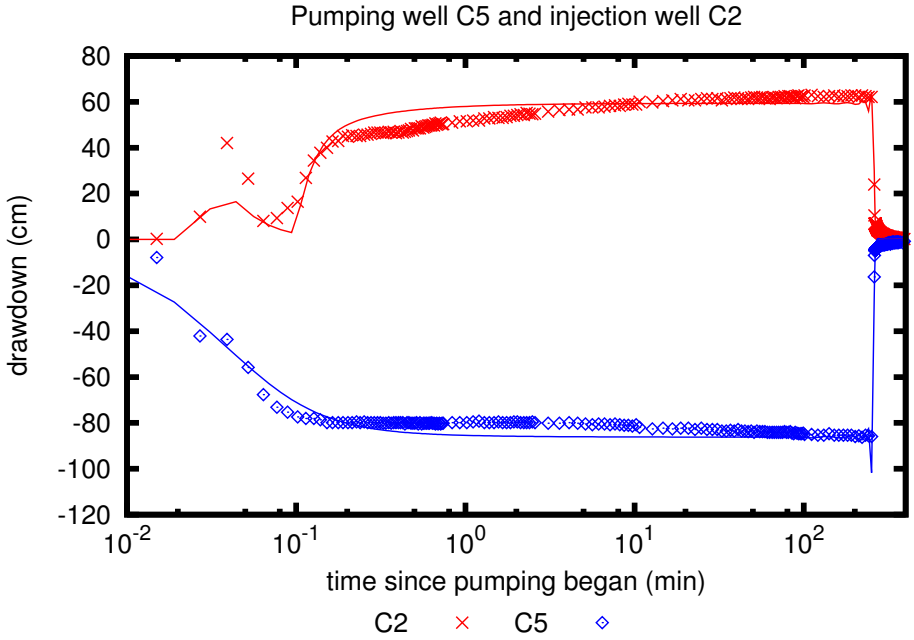

FIGURE 6.11. Confined LT-AEM model (lines) and observed data (points) for pumping and injection wells

6.2 Synthetic inverse problem

A synthetic problem was created to facilitate the exploration of different possible avenues for inverse modeling with LT-AEM, compared to the more traditional use of PEST in the previous section. In this synthetic inverse problem it is assumed we know the aquifer properties of the background and circular elements, but the location of the circular elements is unknown. Tiedman et al. (1995) studied an analogous synthetic problem related to steady-state flow in the presence of discrete high permeability fracture zones, using a BEM forward model.

6.2.1 Synthetic problem description

Heads were sampled through time at 9 observation locations (stars in Figure 6.12), then corrupted with unbiased Gaussian noise ($\sigma = 0.0025$); the input data for the inverse model are plotted in Figure 6.13. The LT-AEM model was fit to the data using the Markov chain Monte Carlo inverse model SCEM-UA (Vrugt et al., 2003b) to estimate the location of the 4 circular elements. Each of the 4 circular elements have the same $K_c = 100K_{\text{bg}}$ but different known radii; S_S is uniform across the background and all 4 circular elements.

6.2.2 SCEM inverse approach

The shuffled complex evolution Metropolis algorithm (SCEM-UA) takes a different approach compared to search-based inverse methods (e.g., PEST); its goal is to estimate the probability density associated with the parameters of the model (from which the optimum parameters can be obtained). SCEM does not require an initial parameter guess, only ranges over which the parameters will be sampled and an initial distribution to sample them from.

There were 8 total parameters to estimate; x- and y-coordinates for each of the 4 the circle centers. SCEM was provided with ranges $-5 \leq x \leq 5$ and $-5 \leq y \leq 5$,

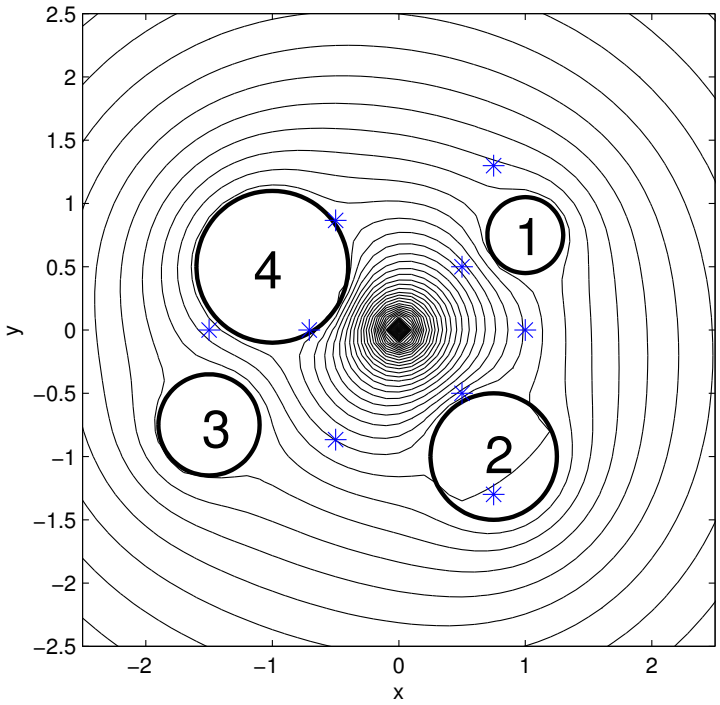

FIGURE 6.12. Synthetic problem geometry, observation locations, and characteristic drawdown contours. $K_c = 100K_{\text{bg}}$

along with a uniform probability distribution (essentially non-informative prior information). SCEM begins with an initial sampling phase (here 10,000 iterations), where the whole 8-dimensional parameter space is sampled to develop an initial estimate of the multi-dimensional density function associated with the parameters. After the sampling phase, the parameters are refined until the total number of forward model runs are completed (here 50,000). Figures 6.14–6.17 show the parameter estimates for iterations 10,001 through 50,000 (i.e., not including the initial sampling phase) as an image with the scaled *a posteriori* density function associated with the 4 element locations.

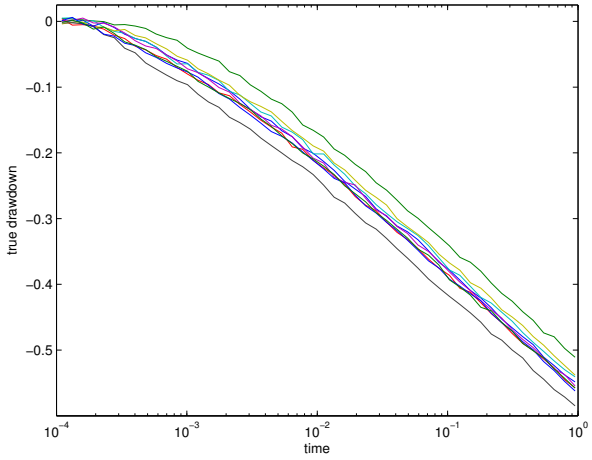

FIGURE 6.13. Synthetic noise-corrupted data used in inversion

6.2.3 SCEM results

In this synthetic example there were four circular elements, each with a distinct radius ($r_1 = 0.3$, $r_2 = 0.5$, $r_3 = 0.4$, $r_4 = 0.6$) and a common known hydraulic conductivity. The results are shown as relative density in Figures 6.14–6.17 for the location of each circle independently. Each image illustrates the probability distribution associated with 2 parameters, the x and y location of the center of the circle (and the radius associated with that circle as well).

Using only 4 observation locations, either in the arrangement shown in Figure 6.14 or that rotated by $\pi/4$ in Figure 6.15, the parameters were not determined correctly or uniquely. The arrows indicate where each predicted circle should actually be located, diffuse areas of gray indicate a poorly-defined solution, while distinct black circles indicate a well-defined solution. It is clear that just because the SCEM inverse model locates a circle with great certainty, it can be incorrect, due to a lack of adequate information in the observed drawdown.

Using 8 observation locations (the first two groups of observations used together), the inverse model successfully locates circle 2 and circle 4, see Figure 6.16.

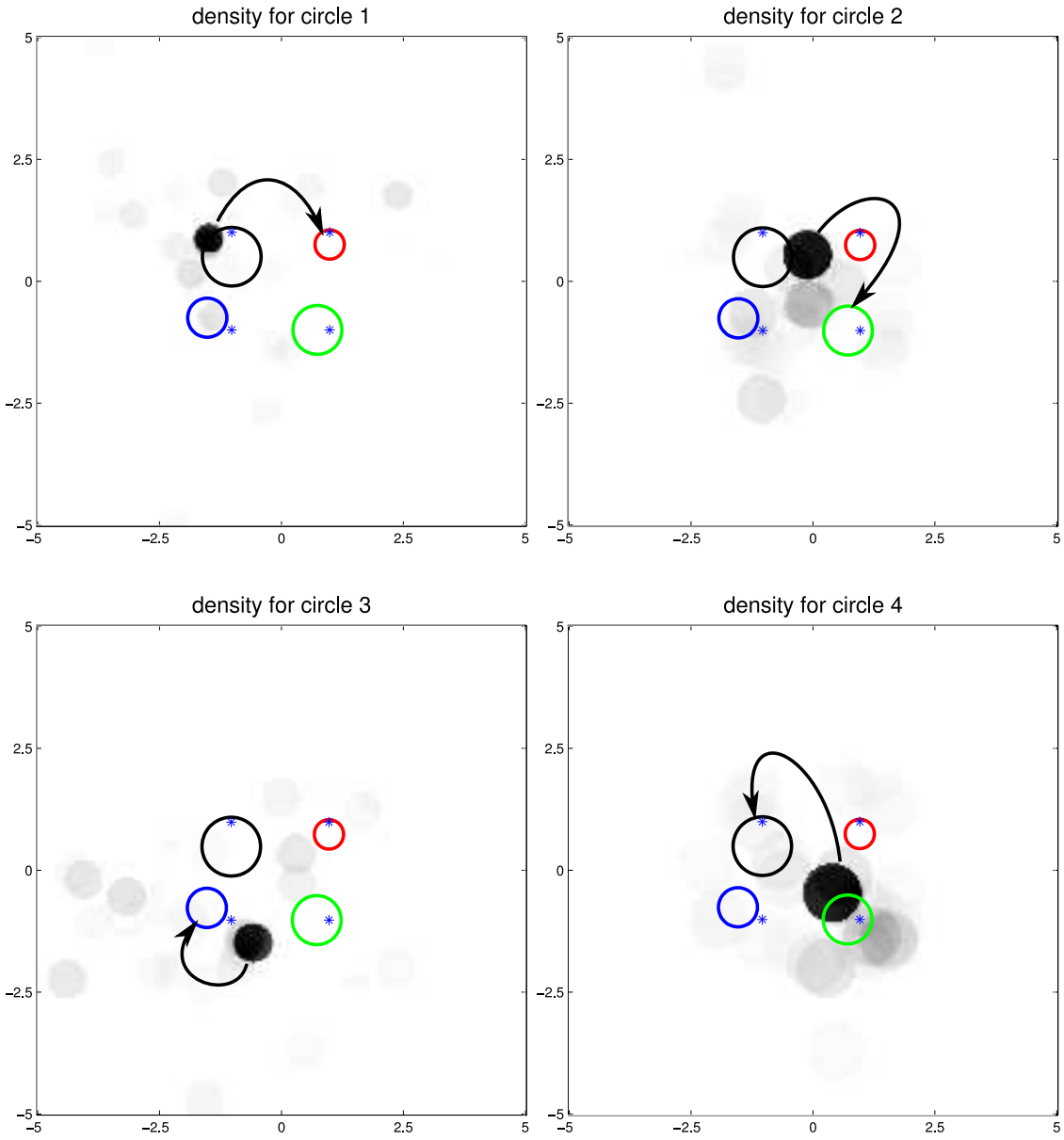

FIGURE 6.14. SCEM results showing true circle locations, SCEM-estimated locations and 4 observation points (stars). Grayscale image represents scaled density, black is highest probability.

Circle 1 is located incorrectly, and with low certainty (see the two gray circles in the upper right). The poor performance with respect to circle 3 could be attributed to the fact that none of the observation locations are very close to the true location of

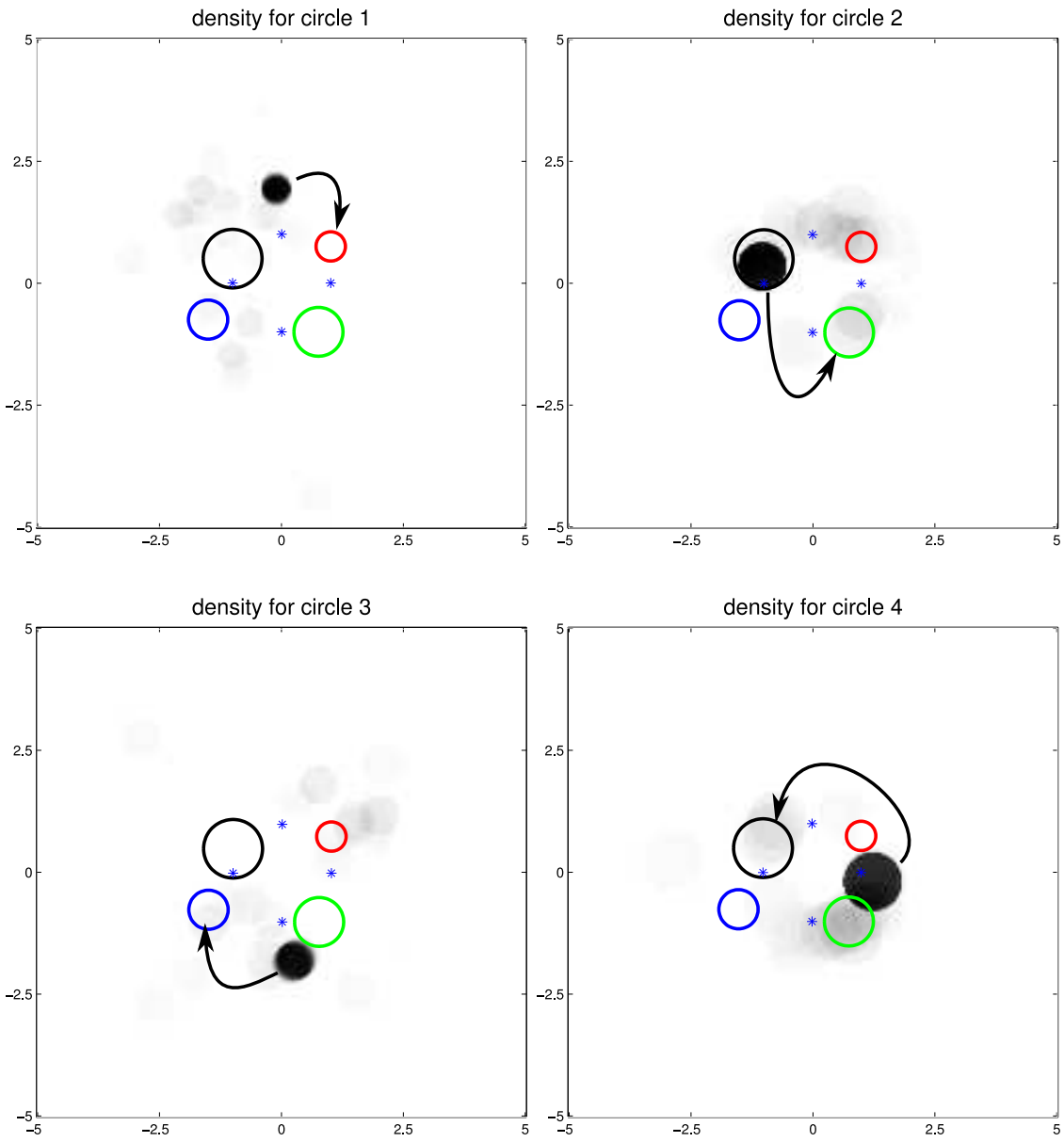

FIGURE 6.15. SCEM results showing true circle locations, SCEM-estimated locations and 4 alternate observation points (stars). Grayscale image represents scaled density, black is highest probability.

this circle. Circle 1 is the smallest of the 4, and therefore makes the smallest impact on the observed drawdown, likely leading to its mis-placement.

Finally, using 16 observations (an entirely different group of observations, with

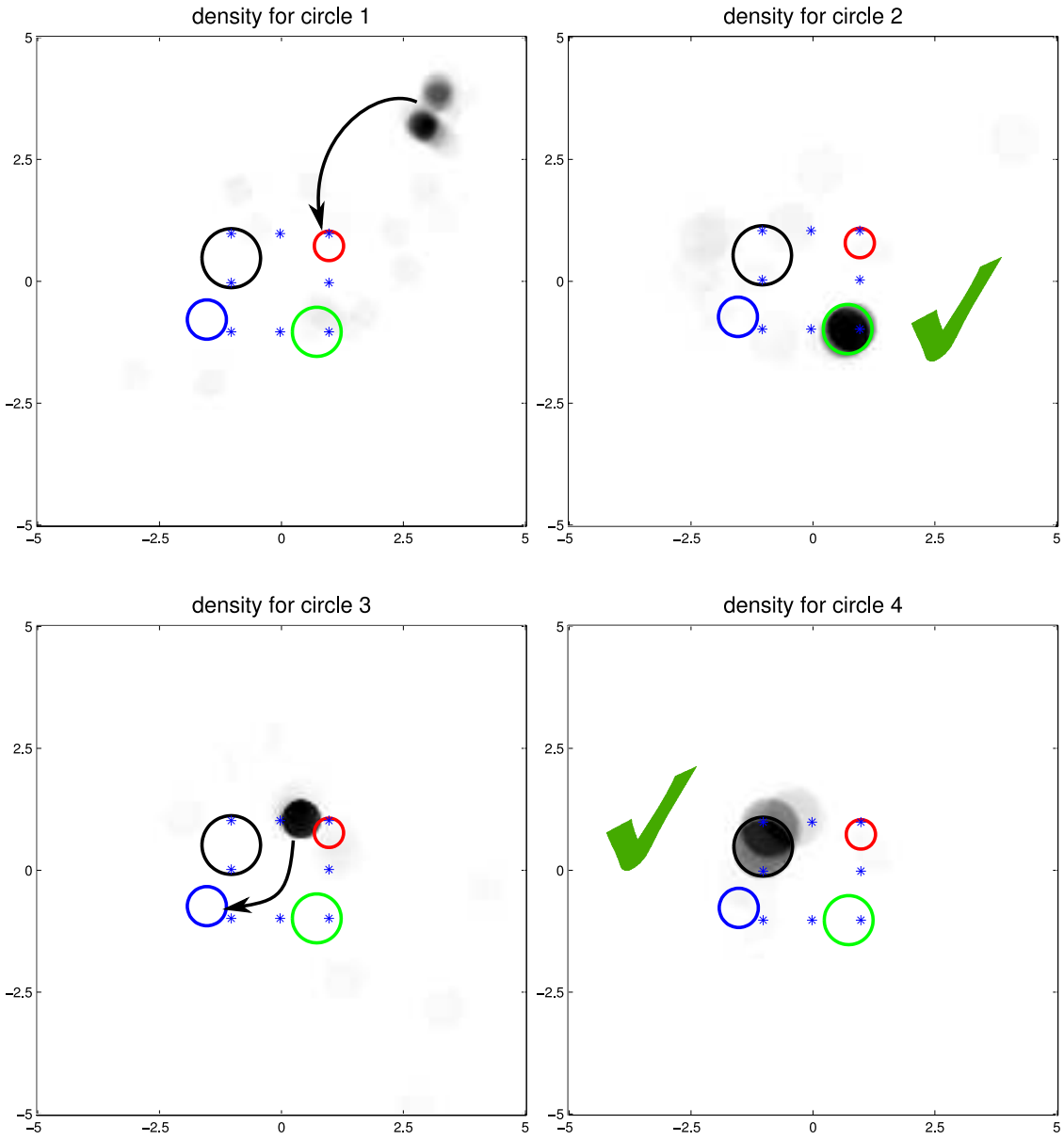

FIGURE 6.16. SCEM results showing true circle locations, SCEM-estimated locations and 8 observation points (stars). Grayscale image represents scaled density, black is highest probability.

no overlap with the previous figures), SCEM locates all of the circles correctly with great certainty, see Figure 6.17. With this arrangement of observation locations, each true circle location is either surrounded by observations points or one of the

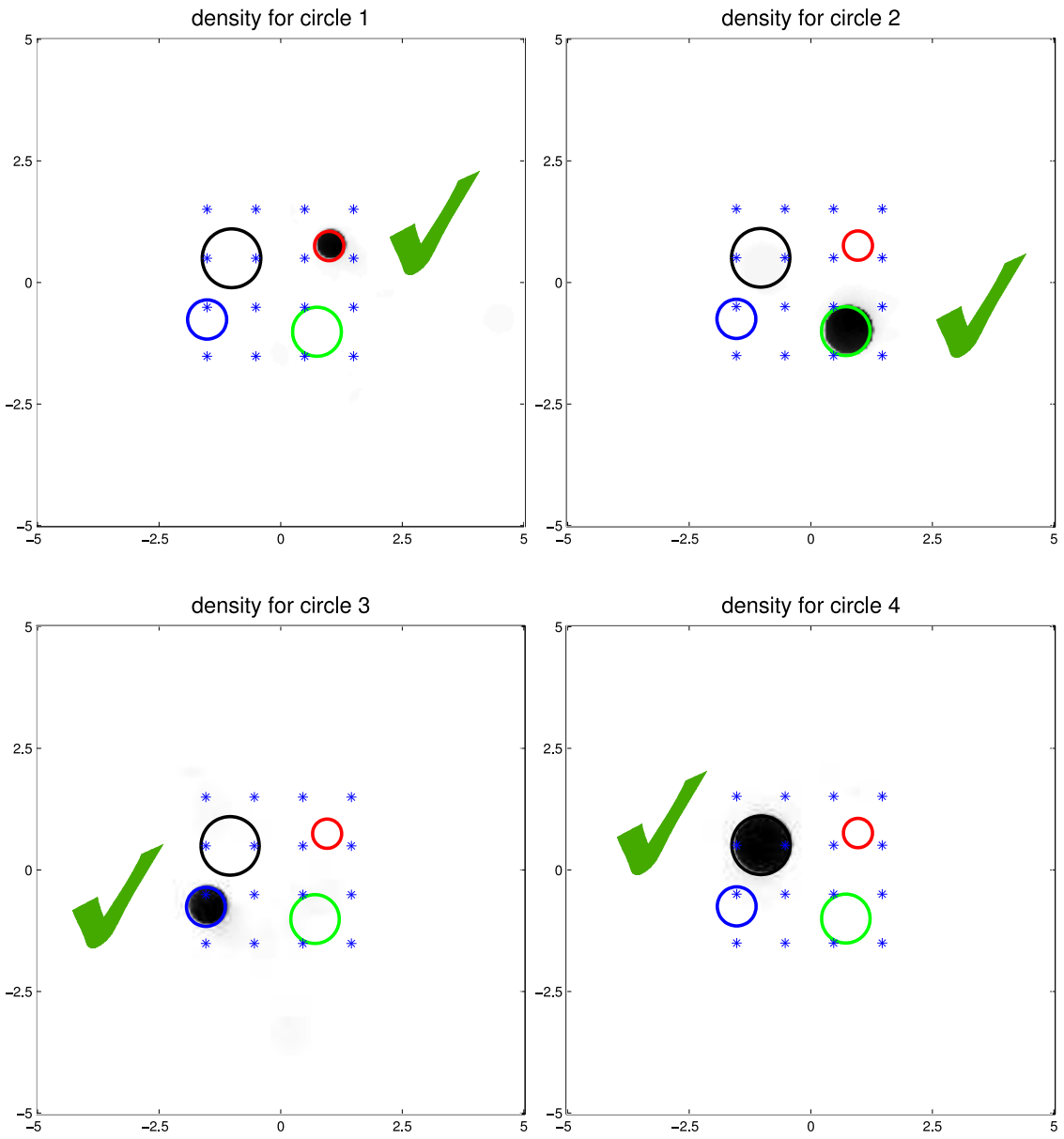

FIGURE 6.17. SCEM results showing true circle locations, SCEM-estimated locations and 16 observation points (stars). Grayscale image represents scaled density, black is highest probability.

observation points falls within the circle.

Qualitative comparisons We investigated the effects of more or less data noise, observations over fewer or more logcycles of time, more or less contrast in the elements

compared to the background, and more or less observation locations on the ability of SCEM-UA to correctly locate the circles. Using only early time data (50 observations over 2 rather than 4 logcycles of time) resulted in a very poor fit, with at best only one of the circles being located at all. The results with un-corrupted data are better, as would be expected; likewise, more noise ($\sigma = 0.1$) lead to poorer results than those shown here.

SCEM applications SCEM has seen numerous applications in surface water (Vrugt et al., 2003a), and soil geophysical (Heimovaara et al., 2004; Huisman et al., 2004) models where the forward models are simple and efficient and they can easily be run many thousands of times. LT-AEM is efficient enough (each forward model run used here took < 4 seconds) that semi-analytic transient solutions for non-homogeneous groundwater flow problems can also be solved using the Markov chain Monte Carlo approach.

This example was performed to illustrate a different approach to the inverse problem compared to gridded forward models. In most forward models the model grid is assumed *a priori*, but the parameters are allowed to vary in some manner across the domain. The difference between using a fixed simulation grid and "moving" elements could be likened to the difference between Eulerian and Lagrangian coordinates. Analytic models of subsurface flow would be well-suited to Monte Carlo parameter estimation techniques, except they usually do not have many degrees of freedom and cannot simulate flow problems of general interest. LT-AEM allows the efficient and elegant analytic solution to be applied to more general geometries and transient behaviors.

Chapter 7
CONCLUSIONS

The Laplace transform analytic element method (LT-AEM) lies somewhere between analytic solutions and gridded models in both flexibility and accuracy; it provides much of the elegance of analytic solutions to a broader set of geometries. The use of the Laplace transform gives flexible analytic temporal behavior, while retaining the benefits of the analytic element method (AEM).

LT-AEM and AEM Although conceptually LT-AEM is an application of AEM to (2.3), operationally, the methods are quite different in several key ways. Since the modified Helmholtz equation (2.3) contains the Laplace parameter p which generally takes on complex values during numerical Laplace transform (LT) inversion (see Appendix A), the differential equations have complex arguments or parameters. Although some numerical inverse LT algorithms only require real values of p (see Chapter 5), they are usually less successful at inverting general time behaviors (Davies, 2002), unless the calculations are performed using arbitrary precision (Abate and Valkò, 2003).

Steady AEM solves Laplace's equation, $\nabla^2\Phi = 0$, where the aquifer properties do not appear directly in the governing equation (only in the definition of discharge potential, Φ), thus allowing direct superposition of solutions across regions of different aquifer properties. Helmholtz's equation does not allow this simplification since $\kappa^2 = pS_s/K$ appears in the governing flow equation, therefore the approach given in section 2.5 must be used, unless aquifer properties and source terms are uniform everywhere.

Steady 2D AEM often utilizes complex potential formulation, $\Omega = \Phi + i\Psi$ (where Ψ is a streamfunction). In LT-AEM both $\bar{\Phi}$ and $\bar{\Psi}$ are themselves complex

due to p, hence this convention is not applicable. If a numerical inverse Laplace transform algorithm requiring only real p were used, expressions for the conjugate potentials (analogous to the Cauchy-Riemann equations for Laplace's equation) can be utilized (Duffin, 1971). Conformal mapping (Strack, 1989, §29–33) is a commonly used AEM technique for extending solutions of $\nabla^2\Omega = 0$ to new geometries. Although potentially applicable to the Helmholtz equation (Schinzinger and Laura, 2003, §5.7), the method loses its elegance, compared to Laplace's equation, due to the appearance of extra terms (the original and mapped functions do not satisfy the same governing equation).

For steady flow the streamfunction Ψ coincides with particle traces, but in transient problems streamlines and particle pathlines are generally different and the transient problem requires a time integration to compute pathlines.

For steady 2D AEM, an important distinction is made between elements which have an effect at "infinity" (e.g., the 2D Green's function $-\ln(r)$) and those which do not (e.g., circular elements $\sum_{n=0}^{\infty} r^{-n}(a_n \cos n\theta + b_n \sin n\theta)$), corresponding to functions of Ω with and without a branch cut (Strack, 1989). LT-AEM elements are either bounded or derived assuming no effect at ∞, which simplifies derivation and implementation. In the limit as $t \to \infty$ and therefore $p \to 0$ (reducing (2.3) to Laplace's equation), these elements *would* have effects at infinite distance, but only in this limit. Therefore, in LT-AEM there are no branch cuts to consider or far-field fixed heads that must be set to obtain a solution, as are required for several common elements in 2D steady-state AEM.

Lastly, as discussed in Chapter 4, LT-AEM can handle certain distributed source terms more easily than methods derived for $\nabla^2\Phi = 0$, since the effects of transient storage can itself be considered a source term in (2.3). The LT-AEM solution techniques given here can readily be used to solve governing equations with additional source terms, higher order time derivatives or convolution integrals. Leakance and transient effects must be dealt with approximately (Strack, 2006) or using inflexi-

ble area sources (Zaadnoordijk and Strack, 1993) in traditional AEM for the Laplace equation, but are handled simply and precisely in LT-AEM.

LT-AEM theory We extended the introductory LT-AEM work of Furman and Neuman (2003) under a more general light and introduced additional circular elements which illustrate the usefulness of LT-AEM to aquifer test interpretation. The save approach was used for elliptical LT-AEM elements, which are the most general 2D coordinate system where the modified Helmholtz equation can be solved via eigenfunction expansion (EE). For a few geometries eigenfunction expansion is an powerful and elegant method for deriving LT-AEM elements. Two limitations of the EE approach have been encountered in this work; first the effort associated with calculation and implementation of the special functions that arise, often for complex argument or parameter. Secondly, the geometries associated with EE are limited; creating elements from intersecting elements (e.g., a "cluster of grapes" element that is the union of several circular elements) leads to some significant convergence issues. These issues were noticed by Janković (1997) for steady circular elements.

More general geometries can be approached using numerical approximation techniques borrowed from BEM, traditional AEM, and the spectral element literature. As noted in the discussion on 3D EE (§3.4), due to the very involved special functions that arise as solutions to the differential equations in some geometries, these approximate approaches may be more appropriate.

The LT-AEM methodology (EE + numerical inverse Laplace transform) was used to solve the leaky, unconfined, multi-layer, and damped-wave flow problems. These exemplify how LT-AEM can be extended to more general aquifer test analysis scenarios; dual porosity may be similar handled. Analyzing transient multi-source aquifer tests including inhomogeneities, finite leaky layers, nearby boundaries and rivers would previously have been done using a finite difference

or finite element model, but now they can be addressed with the LT-AEM.

Gibbs' phenomena (§D.2.3) arise when we truncate a Fourier series (or generalized Fourier series). For LT-AEM these can manifest themselves in two independent ways. When utilizing the Fourier series approach to the numerical inverse Laplace transform (§5.3.3) the inverted solution will have "wiggles" in time, due to incomplete resolution of the image function with the defining Fourier series. The EE approach taken by here for the LT-AEM also can suffer from Gibbs' phenomena in space, when a discontinuous or singular boundary condition is expanded. These two expressions of Gibbs' phenomena are independent; temporal fluctuations tend to manifest themselves across the portion of space effected by the temporally-variable element, and spatial fluctuations tend to manifest at all times (especially early and late where p takes on extreme values).

Elegance The elegance of both the AEM and LT-AEM have been mentioned at several points in the previous discussions. An analytic solution can be considered elegant because it concisely embodies one or more relationships about the process being modeled. Some understanding can be gleaned without actually computing a numerical solution. In steady AEM the elements themselves are analytic solutions, therefore carrying over much of this elegance to the method. The numerical boundary matching step, used to compute the coefficients of active elements, could be said to weaken the elegance of the overall result. The resulting AEM solution is very accurate and *resembles* an analytic solution, but the flexibility of the boundary matching approach is in some part exchanged for elegance in the final solution.

Extending this to the LT-AEM, which additionally utilizes a numerical inverse Laplace transform on top AEM boundary matching, the elegance could be considered to be even further degraded. This further loss of elegance is traded for the temporal flexibility that the numerical inverse transform gives the problem. As discussed in section 2.6.2, the coefficients can be found analytically for some very

special geometries. These analytic expressions, though limited, increase the elegance and diagnostic capacity of the method. To obtain a truly analytic solution for LT-AEM, these coefficients would also need to have analytic inverse Laplace transforms (i.e., closed form expressions for the solution depending only on aquifer parameters and geometry). When possible, this approach is essentially deriving an analytic solution from an LT-AEM solution.

The AEM or LT-AEM will therefore never have all the elegance of an analytic solution, but the flexibility obtained in exchange for this can be considered a fair trade. These methods do produce solutions that have the *appearance* of an analytic solution, which can be argued is a form of elegance in itself.

Examples The examples given throughout Chapters 3 and 4, as well as the inverse applications in Chapter 6 illustrate the potential usefulness of LT-AEM for interpreting aquifer tests; delivering a flexibility not found in standard analytic aquifer flow solutions, and an accuracy and elegance greater than that found in gridded numerical approaches. The flexibility and applicability of LT-AEM can be increase through extension of LT-AEM to 3D flow, elements with anisotropic K, the inclusion of transient particle tracking, the addition of more aquifer test related elements (e.g., elements with wellbore storage or a skin layer), and the addition of approximate elements.

While the nomenclature and examples used here are specific to hydrogeology, LT-AEM would be useful for the solution of heat conduction, neutron scattering and other diffusion-dominated processes. The extension to the damped-wave problem also shows that LT-AEM has the ability to solve additional problems which can be transformed into the modified Helmholtz equation using the Laplace transform, which includes other non-diffusion processes.

Future directions The most obvious extension of 2D LT-AEM is to three dimensions. Using the EE approach given here, there are several coordinate systems that would produce useful and tractable results (spherical, spheroidal, and cylindrical). Other approaches, analogous to those used in steady AEM and BEM, including Green's function integration and Chebyshev function approximation, could also be used to develop additional elements, for geometries where the EE approach is not feasible.

Another possible LT-AEM extension would be the solution of transport problems. A particle tracing or method of characteristics approach could be taken, using the results from the existing LT-AEM in its present form. The LT-AEM approach might also be applied to solve the governing advection dispersion equation in Laplace space, although this does not result in the modified Helmholtz equation considered here without significantly restricting simplifications (e.g., unidirectional flow allowing non-linear transformations analogous to those used in Appendix F).

The LT-AEM could be coupled with gridded numerical approaches (e.g., finite elements or finite difference), to quite naturally supply external boundary conditions. Since the analytic solutions used as elements in LT-AEM readily extend to infinity, this could be coupled with a local and potentially non-linear gridded flow or transport model, taking advantage of the strengths of each approach.

Appendix A

LAPLACE TRANSFORM

A.1 Forward transform

The Laplace transform of a function of space and time, $f(\mathbf{x}, t)$, is defined for $t \geq 0$ as

$$\mathcal{L}\{f(\mathbf{x}, t)\} = \bar{f}(\mathbf{x}, p) = \int_0^\infty f(\mathbf{x}, t) e^{-pt} \, \mathrm{d}t, \tag{A.1}$$

where p is the generally complex Laplace parameter, and the over-bar indicates a transformed time-dependent variable. The transformed function, $\bar{f}(\mathbf{x}, p)$, is called the *image* of the *object* function, $f(\mathbf{x}, t)$.

Time, represented by the real variable $0 \leq t < \infty$, is transformed into a parameter p with $\Re(p) > 0$; valid for the right half of the complex plane. Theoretically, each value of t is related to the entire complex p plane, except at very small and very large times, where the two are inversely related.

A brief list of useful pairs of image and object functions are given in Table A.2; many more transform pairs can be found in reference books, the most modern and comprehensive being Prudnikov et al. (1992).

The region of convergence for both (A.1) and the image function is illustrated in Figure A.1 as the gray region extending to the right of the dashed line, the axis of convergence. The axis is specified by σ_0, the abscissa of convergence (Lepage, 1980, §10.4). The abscissa of convergence is important in numerical Laplace transform inversion routines, as all singularities in the image function lie to the left of it. A few example values are given in Table A.1, which indicates where the image functions relating to these object functions have their rightmost singularities.

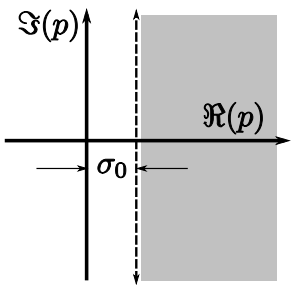

FIGURE A.1. Region of convergence of Laplace image function in p-plane

$f(t)$	σ_0
e^{kt}	k
$\sin t$	0
1	0
e^{-kt}	$-k$
$1 - H(t-1)$	$-\infty$

TABLE A.1. Abscissa of convergence for simple time functions

A.1.1 Two-sided Laplace transform

Two standard (one-sided) Laplace transforms can be connected to form the bilateral or two-sided Laplace transform (Poularikas, 1996, §5.8)

$$\mathcal{L}_2\left[f(\mathbf{x},t)\right] = \int_{-\infty}^{\infty} f(\mathbf{x},t)e^{-pt}\,\mathrm{d}t = \int_0^{\infty} f(\mathbf{x},t)e^{-pt}\,\mathrm{d}t + \int_0^{\infty} f(\mathbf{x},-t)e^{pt}\,\mathrm{d}t, \qquad \text{(A.2)}$$

where this integral converges if both one-sided Laplace transforms converge. The argument of the second integral is *folded* with respect to the integration variable, flipping the sense of the convergence (it now converges to the *left* of its abscissa of convergence). The overlapping region of convergence for the two integrals is illustrated in Figure A.2; the standard Laplace integral (on the left in (A.2)) has its convergence region to the right (associated with σ_{01}), while the folded Laplace integral (on the right of (A.2)) converges on the left of the p-domain (associated with σ_{02}). The overlap region (cross-hatched in Figure A.2) is the region of convergence for the dual-sided Laplace transform.

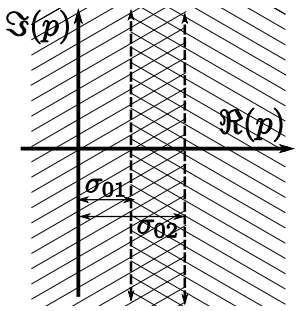

FIGURE A.2. Regions of convergence for dual-sided Laplace transform in p-plane

A.1.2 Fourier transform

The two-sided Laplace transform and its region of convergence can be related to the Fourier transform (Churchill, 1972, §131), defined by

$$F(\omega) = \int_{-\infty}^{\infty} f(x) e^{-2\pi i x \omega} \, \mathrm{d}\omega, \tag{A.3}$$

when $p = 2\pi i x$ (the factor i is related to the rotation of one region of convergence with respect to the other – compare Figures A.2 and A.3). The domain of convergence for the Fourier transform is also related to the singularities of the image function; Figure A.3 shows it is a strip along the real axis in the ω-plane. Boyd (2000, §2.10) heuristically proves how the width of the region of convergence, ρ_0, is related to the convergence of the analogous Fourier series. Section D.2 illustrates how the convergence of a Fourier series is degraded by discontinuities in the function or its derivatives. With the Fourier transform, an object function with discontinuities or discontinuous derivatives has a vanishingly small strip of convergence $\rho_0 \to 0$; a function must be infinitely smooth for $\rho_0 \to \infty$.

This comparison between Fourier and Laplace transforms mathematically illustrates why using the Laplace transform is superior to using a Fourier transform in time (as was done by Bakker (2004c)). First, the one-sided Laplace transform is able to handle discontinuous time functions. This improved ability comes about partially because of the increased region of convergence of the object function, al-

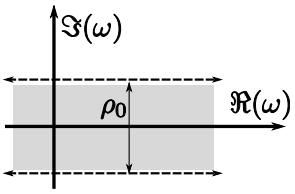

FIGURE A.3. Region of convergence for Fourier transform in ω-plane

lowing different methods for inverting the object function (e.g., the different methods of numerical Laplace transform inversion discussed in Chapter 5). Secondly, when the Laplace transform is modified to handle both positive and negative time (A.2), its domain of convergence is greatly restricted (similar to the Fourier transform). With the hydrologic problems dealt with here, defining the problem for $t \geq 0$ only is an advantage, leading to better convergence of the resulting solution.

A.2 Inverse transform

The inverse LT is defined as the Mellin contour integral (McLachlan, 1953, §8), which can be derived from the Fourier transform, is given as

$$\mathcal{L}^{-1}\left\{\bar{f}(\mathbf{x},p)\right\} = f(\mathbf{x},t) = \frac{1}{i2\pi}\int_{\sigma_0-i\infty}^{\sigma_0+i\infty} \bar{f}(\mathbf{x},p)e^{pt}\,\mathrm{d}p. \tag{A.4}$$

A common strategy for evaluating this integral is to deform the contour into a large half circle of radius $R \to \infty$ (the Bromwich contour), enclosing all the singularities (Churchill, 1972, §71–74). If the singularities of the image function are poles, the solution can be found using the method of residues; if any of the singularities are branch points, the Bromwich contour must be deformed to accommodate them. The strategy and details behind the evaluation of (A.4), for problems arising in hydrology applications, are found in Lee (1999, §3.2).

It is difficult to come up with both necessary and sufficient conditions that ensure any arbitrary $\bar{f}(\mathbf{x},p)$ has a corresponding physical $f(\mathbf{x},t)$ (Lepage, 1980, §12.8). A criteria that is appropriate for the work presented here is the numerical stability

and existence of the numerical inverse Laplace transform (see Chapter 5); some additional forms may be valid but they would have little physical significance to the current problem. For well-behaved $\bar{f}(\mathbf{x}, p)$, there is a physically unique $f(\mathbf{x}, t)$ (excluding discontinuous points where the function may differ – i.e., Lerch's theorem). If the true solution is discontinuous in time at $t = \tau$, the inverse transform of the image function converges to the average value at that point,

$$f(\tau) = \frac{1}{2}\left[f(\tau - \epsilon) + f(\tau + \epsilon)\right], \tag{A.5}$$

where $\epsilon \to 0$. This mathematical detail comes up when trying to evaluate an inverse Laplace transform at $t = 0$. The function is defined to be zero for $t < 0$ and if it is non-zero for $t \geq 0$; the solution will converge to $f(t = 0^+)/2$. Most numerical inverse Laplace transform algorithms also have unrelated problems with evaluating functions at or very close to $t = 0$, because this point essentially corresponds to $p \to \infty$, which causes difficulties when evaluated on a computer with finite precision. The Möbius methods often handle this point best of the numerical inverse algorithms discussed in Chapter 5.

A.3 General properties

The properties of Laplace transforms, which make them useful for solving differential equations, are the simplicity of calculus operations in Laplace space. Using integration by parts on (A.1), derivatives with respect to time can be seen to be equivalent to multiplication by p (with an assumption of zero initial condition). Integration with respect to time is likewise division by p. Analogously, taking a derivative of (A.4) with respect to p shows how multiplication by powers of $-t$ in the time domain corresponds to differentiation in Laplace space. An alternating sign power series in t can be related to a Taylor series in p.

A.4 Some time behaviors

Some time behaviors that are potentially useful for hydrology applications (i.e., behavior of pumping wells) are given in Table A.2. Except for $\cos(kt)$, these func-

	const	step on	pulse from τ_1 to τ_2	steps (k wide)	cosine
$f(t)$	c	$H(t-\tau)$	$H(t-\tau_1)-H(t-\tau_2)$	$\sum H(t-k)$	$\cos(kt)$
$\bar{f}(p)$	$1/p$	$e^{-\tau p}/p$	$(e^{-\tau p}-e^{-2\tau p})/p^2$	$1/(p-pe^{-kp})$	$p/(p^2+k^2)$

TABLE A.2. Useful LT-AEM time functions

tions are all discontinuous in time. The ability of the Laplace transform to handle discontinuous time functions is both a benefit and a potential weakness for numerical inversion of the resulting image function, as discontinuous functions are the most difficult types of functions to invert accurately. Step-like functions, with continuous derivatives can be used in place of the unit step, but translating this time behavior to a non-zero time involves using the shift operator, $e^{-\tau p}$, which itself has a step behavior.

Appendix B

VECTOR COORDINATE CHANGE

A detailed treatment of vectors in different coordinate systems is found in Morse and Feshbach (1953, §1.3) or Chou and Pagano (1992, §12), the required portions of this theory needed to compute useful Jacobians for projecting flux from one coordinate system to another are given here, with an example of a transform given.

B.1 Metric coefficients

A coordinate system is defined by its metric coefficients; they are fundamentally defined in terms of the length element,

$$\mathrm{d}s^2 = \mathrm{d}x^2 + \mathrm{d}y^2 + \mathrm{d}z^2 = \sum_n h_n^2 \xi_n^2, \tag{B.1}$$

where h_n is the scale factor (i.e., metric coefficient) for the general coordinate ξ_n. Cartesian coordinates conveniently have unit scale factors and constant unit vectors; the scale of the coordinates is invariant with position. Table B.1 gives the metric coefficients for the 2D coordinate systems used in this work. Metric coefficients for 3D coordinates (Table 3.2) are quite lengthy for some of the coordinates, and can be found in Moon and Spencer (1961b).

	ξ_1	h_1	ξ_2	h_2
Cartesian	x	1	y	1
polar	r	1	θ	r
elliptical	η	$f\sqrt{\cosh^2\eta - \cos^2\psi}$	ψ	$f\sqrt{\cosh^2\eta - \cos^2\psi}$
parabolic	u	$\sqrt{u^2+v^2}$	v	$\sqrt{u^2+v^2}$

TABLE B.1. Metric coefficients for Helmholtz-separable coordinate systems

B.2 Vector transformation

The fundamental definition of how vectors transform from one coordinate system to another is

$$F'_n = \sum_m \gamma_{mn} F_m, \tag{B.2}$$

where F_n is the n^{th} component of the vector $\mathbf{F}$, the primed component is in the new coordinate system, the unprimed component in the old system, and γ is a direction cosine. The γ can be defined equivalently in either of the following ways

$$\frac{h_m}{h'_n}\frac{\partial \xi_m}{\partial \xi'_n} = \gamma_{mn} = \frac{h'_n}{h_m}\frac{\partial \xi'_n}{\partial \xi_m}. \tag{B.3}$$

The alternate definitions are useful, since sometimes a derivative with respect to the old coordinate system is much simpler to compute than with respect the new one.

B.3 Example transformation

As an example, a conversion of the flux from a polar coordinate system, to an elliptical coordinate system is given in detail. This could be used to project the flux vector due to a circular element onto the normal to the boundary of an elliptical element, which is required to preserve normal flux continuity. The circular element has local coordinates (r, θ), while the elliptical element has local coordinates (η, ψ); as an intermediate step, the transformation goes through the global Cartesian coordinates.

A vector, $\mathbf{F}$, which is the negative gradient of a scalar, ϕ, in an arbitrary coordinate system is

$$\mathbf{F} = \sum_n F_n \mathbf{e}_{\xi_n} = -\nabla\phi = -\sum_n \frac{1}{h_{\xi_n}}\frac{\partial \phi}{\partial \xi_n}\mathbf{e}_{\xi_n}. \tag{B.4}$$

where $\mathbf{e}_{\xi_1}$ is the unit vector in the ξ_1 direction.

Flux in the local coordinate for the circular element is given as

$$\overset{c}{\mathbf{q}} = -\left[\frac{1}{h_r}\frac{\partial\overset{c}{\bar{\Phi}}}{\partial r}\mathbf{e}_r + \frac{1}{h_\theta}\frac{\partial\overset{c}{\bar{\Phi}}}{\partial\theta}\mathbf{e}_\theta\right], \tag{B.5}$$

where the overset character indicates which element the flux or potential is for. (B.5) simplifies to

$$\overset{c}{\mathbf{q}} = -\left[\frac{\partial\overset{c}{\bar{\Phi}}}{\partial r}\mathbf{e}_r + \frac{1}{r}\frac{\partial\overset{c}{\bar{\Phi}}}{\partial\theta}\mathbf{e}_\theta\right]. \tag{B.6}$$

Flux in the local coordinate for the ellipse is

$$\overset{e}{\mathbf{q}} = -\left[\frac{1}{h_\eta}\frac{\partial\overset{e}{\bar{\Phi}}}{\partial\eta}\mathbf{e}_\eta + \frac{1}{h_\psi}\frac{\partial\overset{e}{\bar{\Phi}}}{\partial\psi}\mathbf{e}_\psi\right], \tag{B.7}$$

which simplifies to

$$\overset{e}{\mathbf{q}} = \frac{-1}{f\sqrt{\cosh^2\eta - \cos^2\psi}}\left[\frac{\partial\overset{e}{\bar{\Phi}}}{\partial\eta}\mathbf{e}_\eta + \frac{\partial\overset{e}{\bar{\Phi}}}{\partial\psi}\mathbf{e}_\psi\right]. \tag{B.8}$$

For flux matching on the boundary of the ellipse, the flux effects of the circular element (both radial and angular components) are needed, but expressed in terms of the elliptical element's radial coordinate, η (the normal to the elliptical boundary). Using the transformation definition (B.2), $\overset{c}{q}_\eta$ can be defined first in terms of Cartesian coordinates as

$$\overset{c}{q}_\eta = \gamma_{\eta x}\overset{c}{q}_x + \gamma_{\eta y}\overset{c}{q}_y, \tag{B.9}$$

then each of the Cartesian flux components can be defined in terms of the polar coordinates of the circular element as

$$\begin{aligned}\overset{c}{q}_x &= \gamma_{xr}\overset{c}{q}_r + \gamma_{x\theta}\overset{c}{q}_\theta,\\ \overset{c}{q}_y &= \gamma_{yr}\overset{c}{q}_r + \gamma_{y\theta}\overset{c}{q}_\theta,\end{aligned} \tag{B.10}$$

Substituting (B.10) into (B.9), gives

$$\overset{c}{q}_\eta = \left[\gamma_{\eta x}\gamma_{xr} + \gamma_{\eta y}\gamma_{yr}\right]\overset{c}{q}_r + \left[\gamma_{\eta x}\gamma_{x\theta} + \gamma_{\eta y}\gamma_{y\theta}\right]\overset{c}{q}_\theta, \tag{B.11}$$

which becomes the following, after substituting the definitions of the direction cosines (B.3),

$$\begin{aligned} \overset{c}{q}_\eta = &\left[\left(\frac{h_x}{h_\eta}\frac{\partial x}{\partial \eta}\right)\left(\frac{h_x}{h_r}\frac{\partial x}{\partial r}\right)+\left(\frac{h_y}{h_\eta}\frac{\partial y}{\partial \eta}\right)\left(\frac{h_y}{h_r}\frac{\partial y}{\partial r}\right)\right]\overset{c}{q}_r \\ &+\left[\left(\frac{h_x}{h_\eta}\frac{\partial x}{\partial \eta}\right)\left(\frac{h_x}{h_\theta}\frac{\partial x}{\partial \theta}\right)+\left(\frac{h_y}{h_\eta}\frac{\partial y}{\partial \eta}\right)\left(\frac{h_y}{h_\theta}\frac{\partial y}{\partial \theta}\right)\right]\overset{c}{q}_\theta. \end{aligned} \tag{B.12}$$

This simplifies to

$$\overset{c}{q}_\eta = \frac{1}{h_\eta}\left\{\left[\frac{\partial x}{\partial \eta}\frac{\partial x}{\partial r}+\frac{\partial y}{\partial \eta}\frac{\partial y}{\partial r}\right]\overset{c}{q}_r+\left[\frac{\partial x}{\partial \eta}\frac{1}{r}\frac{\partial x}{\partial \theta}+\frac{\partial y}{\partial \eta}\frac{1}{r}\frac{\partial y}{\partial \theta}\right]\overset{c}{q}_\theta\right\}. \tag{B.13}$$

Derivatives of the coordinates required above are computed from definitions:

$$\begin{aligned} &\frac{\partial x}{\partial \eta} = f\sinh\eta\cos\psi; && \frac{\partial y}{\partial \eta} = f\cosh\eta\sin\psi; \\ &\frac{\partial x}{\partial r} = \cos\theta; && \frac{\partial y}{\partial r} = \sin\theta; \\ &\frac{\partial x}{\partial \theta} = -r\sin\theta; && \frac{\partial y}{\partial \theta} = r\cos\theta; \end{aligned} \tag{B.14}$$

This finally gives the expression for flux with respect to the radial coordinate of the ellipse, due to a circular element as

$$\begin{aligned} \overset{c}{q}_\eta = &\frac{f}{h_\eta}\big\{\left[\sinh\eta\cos\psi\cos\theta+\cosh\eta\sin\psi\sin\theta\right]\overset{c}{q}_r \\ &-\left[\sinh\eta\cos\psi\sin\theta-\cosh\eta\sin\psi\cos\theta\right]\overset{c}{q}_\theta\big\}, \end{aligned} \tag{B.15}$$

which is entirely in terms of the coordinates where the derivatives are being evaluated. For the case of flux matching on the boundary of the ellipse, the M matching points along the boundary all have the same $\eta = \eta_0$ value, they have a range of $-\pi < \psi \leq \pi$, and the polar coordinates are these matching points, in terms of the local coordinates of the circle (which depends on the translation and rotation of the two local coordinate systems with respect to the global Cartesian system).

The definitions of flux as the gradient of potential can also be inserted into the

definition, which makes the expression

$$\frac{1}{h_\eta}\frac{\partial \overset{c}{\bar{\Phi}}}{\partial \eta} = \frac{f}{h_\eta}\left\{ \left[\sinh\eta\cos\psi\cos\theta + \cosh\eta\sin\psi\sin\theta\right]\frac{\partial \overset{c}{\bar{\Phi}}}{\partial r} - \left[\sinh\eta\cos\psi\sin\theta - \cosh\eta\sin\psi\cos\theta\right]\frac{1}{r}\frac{\partial \overset{c}{\bar{\Phi}}}{\partial \theta}\right\}, \tag{B.16}$$

but the metric coefficients associated with the radial flux for the ellipse (LHS), would cancel with a similar metric coefficient, which accompanies the normal flux term on the inside of the ellipse, and is evaluated at the same location.

Appendix C
LT-AEM AND METHOD OF WEIGHTED RESIDUALS

The method of weighted residuals (MWR) is introduced to illustrate how AEM and LT-AEM fit within this framework. Quite generally, in MWR the free parameters associated with some test or basis functions are chosen so that the residual associated with the solution is made to in some average sense.

C.1 MWR derivation

Following the outline presented in Finlayson (1972, §1), a general MWR solution is posed for the 2D modified Helmholtz equation (2.3) with type I boundary conditions. First, the solution is expanded in a set of complete orthogonal basis functions,

$$\bar{\Phi}(\mathbf{x}, p) \approx \sum_{i=1}^{N} c_i(p)\phi_i(\mathbf{x}, p), \tag{C.1}$$

where ϕ_i are known basis functions, c_i are constants to determine, and the relation is approximate because the series is truncated at N terms. Unless the trial functions are analytic solutions to the problem (satisfying both the PDE and boundary conditions exactly), they will produce a residual, R, which must be minimized. The residual is computed by substituting (C.1) into governing equation (2.3),

$$R_D(c_i, \mathbf{x}, p) = \sum_i \left[\nabla^2\phi_i(\mathbf{x}, p) - \kappa^2\phi_i(\mathbf{x}, p)\right] c_i(p), \tag{C.2}$$

and the boundary conditions

$$R_B(c_i, s, p) = \sum_i c_i(p)\phi_i(\mathbf{x}(s), p) - \bar{\Phi}_{\text{BC}}(s, p), \tag{C.3}$$

where s parametrizes the boundary (e.g., arc length or angle), and $\bar{\Phi}_{\text{BC}}$ is a specified potential boundary condition (BC). The total residual is the sum of the domain and

boundary residuals, $R = R_B + R_D$. Type II BC, sometimes referred to as *natural* BC, arise naturally when posing the PDE in integral form, through use of Gauss' divergence theorem, and therefore do not need special consideration. Type I BC are handled here separately from the PDE; type III BC would be handled similar to the manner in which type I BC are illustrated here.

The weighted integral of the residuals over the domain is forced to zero,

$$\int_\Omega w_j R_{Di}\,\mathrm{d}A + \int_\Gamma w_j R_{Bi}\,\mathrm{d}\Gamma = 0 \tag{C.4}$$

where w_j is a general weight function (to be chosen later), Ω represents the interior of the domain, Γ the domain boundary (see Figure C.1), and A is the domain area.

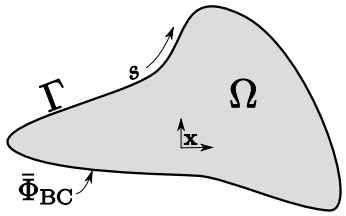

FIGURE C.1. Notation used for MWR problem

Substituting the definition of the residuals (C.2 and C.3) into (C.4) gives

$$\sum_i c_i \int_\Omega w_j \left[\nabla^2\phi_i - \kappa^2\phi_i\right]\,\mathrm{d}A + \sum_i \int_\Gamma w_j \left[c_i\phi_i(s) - \bar{\Phi}_{\mathrm{BC}}(s)\right]\,\mathrm{d}s = 0. \tag{C.5}$$

This can be rearranged as

$$\sum_i \left\{\int_\Omega w_j \left[\nabla^2\phi_i - \kappa^2\phi_i\right]\,\mathrm{d}A + \int_\Gamma w_j\phi_i(s)\,\mathrm{d}s\right\} c_i = \int_\Gamma w_j\bar{\Phi}_{\mathrm{BC}}(s)\,\mathrm{d}s \tag{C.6}$$

which then can be written compactly in matrix form as $A_{ij}c_i = b_j$. In theory, the A_{ij} matrix could be inverted to find the coefficients, c_i, once the basis and weighting functions are known and the integrals are evaluated.

The MWR as outlined above is very broad and inclusive; different choices for the weight and basis functions result in different numerical methods as special cases.

C.2 Choice of basis function

There are three choices for the basis functions, ϕ_i, based on how they affect R_D and R_B;

- **interior:** basis functions satisfy BC, but not PDE ($R_B \equiv 0$),
- **mixed:** basis functions don't satisfy either BC or PDE,
- **boundary:** basis function satisfy PDE, but not BC ($R_D \equiv 0$).

AEM, LT-AEM and the boundary element method use boundary-type basis functions, while the spectral element method, and finite element methods basis functions come from the mixed or interior class. In boundary methods, the residual is identically zero throughout the interior of the domain. The total residual reduces to just R_B, which in 2D is a line integral along the domain boundary; only the second integral in (C.5) is non-zero.

C.3 Choice of weight function

The collocation boundary matching approach can be fit into this MWR framework by picking $\ell = 1, 2, \ldots, M$ points along the boundary, defining the weight function as

$$w_j(s_\ell) = \delta(s - s_\ell) \tag{C.7}$$

which is illustrated in Figure C.2. Due to the properties of the δ-function, the integral is reduced to the value of the boundary residual at the collocation points. The total residual for a method using boundary-type basis functions, becomes the sum of these errors,

$$\sum_{\ell=1}^{M} \sum_{i=1}^{N} \left[c_i \phi_i(s_\ell) - \bar{\Phi}_{\text{BC}}(s_\ell) \right] = 0. \tag{C.8}$$

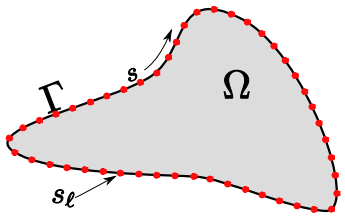

FIGURE C.2. Use of weight function to discretize boundary

For example, when the element is a circle and $\phi_n(s_\ell) = \cos(n\theta_\ell)$ this expression becomes a trigonometric interpolation of the specified boundary condition (Lanczos, 1956, §4.11).

A different choice of weighting function can also incorporate the least-squares (overspecification) collocation approach introduced to the AEM community by Janković (1997), mentioned as an alternative approach by Boyd (2000, §3.1), and previously known in the MWR community. The history of this approach is recounted by Finlayson (1972, p.27); it dates back to 1964 in nuclear reactor engineering. If the weighting function is chosen as

$$w_j(s_\ell) = \frac{\partial R_j}{\partial c_j}\delta(s - s_\ell) \tag{C.9}$$

the integral along the boundary becomes

$$\sum_{\ell=1}^{M}\sum_{i=1}^{N}\left[c_i\phi_i(s_\ell) - \bar{\Phi}_{\text{BC}}(s_\ell)\right]^2 = 0. \tag{C.10}$$

due to the linearity of the residual to c_j. This is the classic least-squares collocation problem, posed in the framework of the MWR. This is the formulation for one active element, but as discussed in section 2.6, the method can be readily extended to any number of active elements simultaneously using a direct approach.

While this taxonomic discussion does not change the way in which LT-AEM problems are posed or solved in practice, it does put LT-AEM in its place among the many numerical methods that fall under the MWR umbrella.

Appendix D
EIGENFUNCTION EXPANSION

The relevant theoretical foundation of eigenfunction expansion (EE) is given here, as it applies to LT-AEM. While often considered an "elementary" technique for solving PDEs, it is the most geometrical and intuitive PDE solution method. In general, solutions for a PDE and its associated boundary conditions can be found using

- eigenfunction expansion (separation of variables);
- Green's functions (integration of fundamental solutions);
- variational methods (integral approach using weak form of PDE).

The Green's function and variational approaches work for arbitrarily-shaped domains, but result in integrals that often can only be evaluable in closed form for simple geometries. The variational approach is one of the foundations for the Trefftz boundary element (Qin, 2000) and finite element methods (Hughes, 2000). Finite elements can equivalently be considered a special case of the MWR solution in Appendix C. The direct BEM (Brebbia et al., 1984) and AEM approach of Strack (1989, 2003) are based upon a Green's function solution. The LT-AEM approach taken here uses eigenfunction expansion.

In general, successful EE depends on meeting the following conditions, paraphrased from Gustafson (1999):

1. the domain can be described in some coordinate system so that the boundaries consist of constant curves in that coordinate system;
2. the PDE is separable into ODEs corresponding to coordinate variables;

3. the resulting ODEs are solvable (by means of special functions).

Gustafson (1999) also includes a qualification that the domain be bounded, but this condition can often be relaxed, given the proper coordinate system and boundary condition at infinity. This point was operationally addressed in the section on LT-AEM boundary conditions (section 2.5.2).

Separation of variables is believed to have been first used by Daniel Bernoulli in 1753 for the taut string problem (Jeffreys and Jeffreys, 1972, p.436). The functions comprising the Generalized Fourier series are orthogonal and form a separable Hilbert space (infinite dimensional) solution (MacCluer, 2004, §6). The modern Hilbert space approach can be used to justify the existence of the separation of variables solution on more rigorous grounds, but is not pursued here.

D.1 Generalized Fourier series

The Fourier series approach posits that any piecewise-smooth function can be approximated using trigonometric functions over a periodic domain (e.g., $f(\theta) = f(\theta + 2\pi)$). Finite, non-periodic regions can be mapped onto periodic ones, resulting in Chebyshev polynomials, which extends the approach to additional domains. The expansion of a PDE solution in terms of Fourier or equivalent Chebyshev functions is the foundation of the spectral element method (SEM).

For SEM, Boyd (2000, §1.6) argues that one should always use Chebyshev polynomials or Fourier series, due to their simplicity, rather than the potentially "exotic" basis functions that may satisfy the ODEs in some coordinate systems (e.g., elliptic and parabolic). This viewpoint is held by many engineers and modelers, because the trigonometric basis functions do so well in most situations, and typically they are unfamiliar with coordinate systems beyond Cartesian and polar. In support of using the appropriate eigenfunction expansions, rather than blindly using Fourier series everywhere, Gustafson (1999) contends:

> "One might ask, why solve all these special classes of ODEs resulting from separation of variables, why not just expand everything in terms of the trigonometric functions and hope for the best? One can indeed adopt the latter viewpoint in many cases, accepting the resulting 'approximate' solutions given by the partial sums of the Fourier trigonometric expansion. But those solutions are not as good as those resulting from the natural expansion functions, the error may be harder to determine, and the 'physically correct' fit has been lost."

Morse and Feshbach (1953, §6.3) illustrate how the convergence of any proper set of eigenfunctions is the same as a Fourier series expansion of the same function; they prove that the expansion of any continuous function in eigenfunctions converges or diverges at any point as the related Fourier series converges or diverges at that point. Since a large body of theory has been developed to prove the convergence and summability of Fourier series under a broad range of conditions (e.g. Lanczos, 1966; Torchinsky, 2004); these proofs then also apply to eigenfunction expansions, earning them the title *generalized Fourier series*.

Reasons for using trigonometric and Chebyshev series, rather than the proper generalized eigenfunctions, include familiarity, ease of implementation, and the existence of the fast Fourier transform (FFT). While some generalized "fast" eigenfunction transforms do exist for special functions with a 3-term recurrence relationship (Orszag, 1986), they are not as efficient as the venerable FFT. Although many engineers will go to great lengths to apply fast transforms, in LT-AEM and other boundary approaches, these types of fast transforms do not have the huge impact they do in SEM and other interior methods. The fast transforms only show large gains when $N \geq 10,000$ (Boyd, 2000, §10). In fact, Orszag (1986) states that the largest fraction of the total improvement in solving problems using EE and fast transforms comes from separating the coordinates (e.g., making the boundary a

circle, where r is a constant). The speedup from using a fast transform to evaluate the eigenfunctions (even FFT) is secondary.

A disadvantage for using the proper eigenfunctions that satisfy the PDE comes from the complex-valued Laplace parameter. Since the parameter appears explicitly in the governing equation as $\kappa = \sqrt{p/\alpha}$, any set of eigenfunctions which satisfies this PDE will likewise incorporate κ into their definition, requiring the special functions to be evaluated for complex argument or parameter. Most special functions take on very different behavior for complex argument. When utilizing interior-type basis functions (like SEM, finite difference or finite element — see §C.2 for interior/exterior definitions), the basis functions need not be complex-valued; only the coefficients need to be complex. This advantage is balanced by the fact that interior methods require matching at both boundary and domain points, effectively increasing the dimensionality of the numerical problem, making fast transforms more necessary.

Eigenfunctions are as powerful as Fourier series and more importantly they are the natural basis functions that automatically satisfy the PDE (and therefore make good candidates for boundary methods like LT-AEM). It then seems that this approach is very useful for LT-AEM. More general and potentially approximate approaches for deriving elements (e.g., integration of Greens' functions or interior basis function methods) should be taken only when these methods fail.

D.2 Convergence of Fourier series

In LT-AEM, issues related to the convergence of Fourier series arise in two places. First they arise in the convergence of the series of spatial basis functions that comprise the LT-AEM elements themselves, since the elements are generalized Fourier series. Secondly, they can arise in the convergence of the inverse Laplace transform methods, since the Fourier series approach is an effective strategy for solving the

numerical inverse Laplace transform. While the discussion here is mostly centered around the first point, the Laplace transform inversion discussion in Chapter 5 benefits as well.

For infinitely smooth functions (functions with continuous derivatives of every order), a Fourier series expansion is said to have exponential or spectral convergence (Boyd, 2000, §2.4). This means the magnitude of the coefficients decrease faster than $1/n^k$ for any finite k. This is the ideal case, any flaws in the function or its derivatives will degrade the rate of convergence.

D.2.1 Singularities

Darboux's principle states that both the domain and rate of convergence for a power series is controlled by the location and strength of the gravest singularity (Boyd, 2000, §2.6). Singularities include poles, fractional powers, logs and discontinuities in the function or its derivatives. For AEM, point sources are typically not located directly on boundaries between regions, so functional discontinuities are the main concern. While it is possible to locate singularities on boundaries between regions, this would result in a potentially divergent, or at least very slowly-converging eigenfunction series. In practice the singularity could be moved off the boundary line by a small amount, greatly reducing the strength of the discontinuity in the function to be expanded, but giving essentially the same solution.

While Darboux's principle is related to the convergence of a power series, it is equally valid for Fourier series, since they can be recast as complex power series. For example, an infinite trigonometric series can be equivalently expressed in the

following forms

$$f(x) = \sum_{n=0}^{\infty} a_n \cos nx + \sum_{n=1}^{\infty} b_n \sin nx \tag{D.1}$$

$$= \sum_{n=-\infty}^{\infty} c_n e^{inx} \tag{D.2}$$

$$= \sum_{n=0}^{\infty} c_n z^n + \sum_{n=1}^{\infty} c_{-n} z^{-n} \tag{D.3}$$

where $c_{\pm n} = \frac{1}{2}\left(a_{\pm n} \mp i b_{\pm n}\right)$ and $z = \exp(ix)$. Equation (D.3) is a power series style representation of the function, heavily utilized in older steady AEM solutions (e.g. Strack, 1989; Salisbury, 1992). A benefit of working with the trigonometric form (D.1), rather than the more compact power series form (D.3) is the ease of handling of even- or odd-symmetric boundary conditions.

Integral expressions for the Fourier series coefficients in (D.1) are derived using orthogonality of the sines and cosines

$$\int_{-\pi}^{\pi} \sin n\theta \sin m\theta \, \mathrm{d}\theta = \int_{-\pi}^{\pi} \cos n\theta \cos m\theta \, \mathrm{d}\theta = \pi \delta_{nm} \tag{D.4}$$

where δ is the Kronecker delta. The coefficients are found by multiplying by either $\cos m\theta$ or $\sin m\theta$, then integrating over the domain ($-\pi \leq x \leq \pi$), giving

$$a_n = \frac{1}{\pi} \int_{-\pi}^{\pi} f(\theta) \cos n\theta \, \mathrm{d}\theta \tag{D.5}$$

$$b_n = \frac{1}{\pi} \int_{-\pi}^{\pi} f(\theta) \sin n\theta \, \mathrm{d}\theta \tag{D.6}$$

These integral representations for the coefficients can be used to determine their leading behavior for large n. Integration by parts is a common technique for deriving asymptotic behavior when the method is appropriate (Bender and Orszag, 1999); applied to (D.5) it yields

$$a_n = \frac{1}{\pi} \left\{ \left[\frac{f(\theta)}{n} \sin(n\theta) \right]_{-\pi}^{\pi} - \frac{1}{n} \int_{-\pi}^{\pi} f'(\theta) \sin(n\theta) \, \mathrm{d}\theta \right\}. \tag{D.7}$$

Using parts again on the remaining integral in (D.7) gives

$$a_n = \frac{1}{\pi}\left\{\left[\frac{f(\theta)}{n}\sin(n\theta)\right]_{-\pi}^{\pi} + \left[\frac{f'(\theta)}{n^2}\cos(n\theta)\right]_{-\pi}^{\pi} - \frac{1}{n^2}\int_{-\pi}^{\pi} f''(\theta)\cos(n\theta)\,\mathrm{d}\theta\right\}. \quad \text{(D.8)}$$

The sine term falls out due to the boundary conditions, as $n \to \infty$ the second term is most significant, since higher derivatives of $f(\theta)$ are presumably small, and not a function of n; this leaves

$$a_n \sim \frac{(-1)^n}{\pi n^2}\left[f'(\pi) - f'(-\pi)\right]. \quad \text{(D.9)}$$

Analogous analysis for the sine coefficients (D.6) leads to

$$b_n = \frac{1}{\pi}\left\{\left[\frac{f(\theta)}{n}\cos(n\theta)\right]_{-\pi}^{\pi} + \left[\frac{f'(\theta)}{n^2}\sin(n\theta)\right]_{-\pi}^{\pi} - \frac{1}{n^2}\int_{-\pi}^{\pi} f''(\theta)\sin(n\theta)\,\mathrm{d}\theta\right\}, \quad \text{(D.10)}$$

which, for large n, behaves as

$$b_n \sim \frac{(-1)^n}{\pi n}\left[f(\pi) - f(-\pi)\right]. \quad \text{(D.11)}$$

For any general $f(\theta)$, the sine coefficients in (D.11) decay in magnitude as $\mathcal{O}(1/n)$, but if $f(\theta)$ is smooth the cancellation in the $f(\pi) - f(-\pi)$ term suppresses this leading behavior. Going back to (D.10) and performing parts again, we see the next most significant b_n term would be $\mathcal{O}(1/n^3)$, while the remaining cosine coefficients are $\mathcal{O}(1/n^2)$; if the first derivative is also smooth, then the next sine term dominates. Based on this analysis we would then expect convergence of the coefficients to be at least $\mathcal{O}(1/n^2)$ for smooth functions, and $\mathcal{O}(1/n^3)$ for functions with smooth head and flux (with respect to θ). Continuing this process, we can see how an infinitely smooth function would have coefficients that converge faster than $1/n^k$, for any finite k, which is spectral convergence (Boyd, 2000). To generalize the previous discussion, a single discontinuity can always be shifted to the location $\theta = \pm\pi$, and a region with multiple discontinuities can be broken into piecewise-smooth regions with each mapped onto the $-\pi \leq \theta \leq \pi$ interval.

D.2.2 Fourier series residual

Given a general infinite Fourier series, (D.1), and the partial sum of the first N Fourier terms, $f_N(x)$, the truncation error in the finite Fourier expansion,

$$R_N = |f(x) - f_N(x)|, \tag{D.12}$$

is bounded by the sum of all neglected coefficients,

$$R_N \leq \sum_{n=N+1}^{\infty} \left[|a_n| + |b_n|\right], \tag{D.13}$$

since the trigonometric functions have an absolute value ≤ 1. For large n, the coefficients of an infinitely smooth Fourier series decay exponentially, therefore the truncation error is on the order of the size of the last term retained,

$$R_N \sim \mathcal{O}(|a_N|) \sim \mathcal{O}(|b_N|). \qquad \text{spectral} \tag{D.14}$$

For the case where the function is not smooth, convergence will be sub-spectral (or sub-geometric); low-order algebraic convergence (worst-case) leads a residual term of larger order (Boyd, 2000, §2.12),

$$R_N \sim \mathcal{O}(N|a_N|) \sim \mathcal{O}(N|b_N|) \qquad \text{algebraic} \tag{D.15}$$

where $|a_N|$ must be smaller, therefore requiring more terms, to achieve the same residual compared to the spectrally-convergent case, because the infinite sum of truncated Fourier series coefficients is not dominated solely by the first neglected term.

D.2.3 Gibbs' phenomenon

The type of singularity which is of most concern to LT-AEM problems is a discontinuity, which leads to slower algebraic convergence. This poor convergence was first explained by Gibbs (1898), where a truncated Fourier series systematically

over- and under-shoots a jump by $\approx \pm 9\%$ of the jump value. As N increases, the width of the overshoot region becomes smaller, but the amplitude of the over- and under-shoot does not.

There are several strategies for improving poor convergence in cases where Gibb's effect is problematic; popular tactics include series transformation and acceleration (Oleksy, 1996), the use of smoothing factors to dampen high-frequency oscillations (Lanczos, 1966), or simply ignoring the problem and using a very large number of terms (confining the error to a very small region). When using the large N "brute force" approach, care must be exercised. When manipulating series that are exhibiting Gibb's oscillations, the integral of such a series will certainly exist, but derivatives may not (Morse and Feshbach, 1953, §6.3). Smoothing factors can both reduce the high-frequency oscillations associated with Gibb's phenomenon and increase the convergence of the trigonometric series. For a truncated Fourier series, the Lanczos σ factors simply modify the existing coefficients,

$$f_N(x) = \sum_{n=0}^{N-1} \sigma_n a_n \cos nx + \sum_{n=1}^{N-1} \sigma_n b_n \sin nx \tag{D.16}$$

where the σ factors come from the "sinc" function used in digital signal processing (Smith, 1999, p. 212). The σ-factors are analogous to taking a moving average of the function, before expanding it in a Fourier series Lanczos (1956, §4.10). The σ-factors and sinc function are defined as

$$\sigma_k(N) = \frac{\sin(k\pi/N)}{k\pi/N}, \tag{D.17}$$

using this $\sigma_0 = 1$ and $\sigma_N \to 0$; higher frequency harmonics are damped. These frequencies would normally be damped by still higher frequency terms that have not been included, due to truncation of the series. While the σ terms do not eliminate Gibb's phenomenon, they reduce it from $\approx \pm 8.95\%$ to $\approx \pm 1.19\%$ of the jump discontinuity magnitude (Lanczos, 1956). Other trigonometric smoothing coefficients similar to this one, utilized in the SEM literature, are given by Canuto et al. (2006).

In his PhD dissertation, Janković (1997) implemented intersecting steady circular AEM elements, which were discontinuous in θ. He declared them to be largely unusable, since a very large number of terms (thousands) were required to keep the overshoot confined to a small region. He did not attempt to use smoothing factors or series transformations to improve the convergence of the series.

The only place in eigenfunction expansion, where Gibb's phenomena have arisen, has been in expansion of discontinuous boundary conditions. For example, using an active circular element with $\Phi(r_0, 0 \leq \theta < \pi) = 1$ and $\Phi(r_0, -\pi \leq \theta < 0) = 0$ would have convergence issues at $\theta = 0$ and $\pm\pi$. These issues were not extensively investigated, since this type of boundary condition was considered non-physical. This type of boundary does arise when intersecting elements (as described above); for circular elements the Lanczos σ-factors or series transformation and acceleration techniques of Oleksy (1996) would lead to improvements. For elliptical elements there is less theory regarding the acceleration of convergence of these series, but similar approaches can be taken.

Appendix E
MATHIEU FUNCTIONS

We introduce the properties of Mathieu functions (MF) needed for the applications demonstrated in section 3.2. The angular MF follow the original (British mathematical) naming convention introduced by Whittaker (1912), which draws on the analogy to trigonometric functions. For the radial MF the newer (American physics) naming convention is used (e.g. Stratton, 1941; Chu and Stratton, 1941; Morse and Feshbach, 1953), which draws on the analogy between Bessel and Mathieu functions. This hybrid nomenclature is common, but not universal. See Gutiérrez Vega et al. (2003) and Abramowitz and Stegun (1964, §20) for tables listing equivalences between the different common naming conventions that exist in the MF literature.

For the Helmholtz equation in elliptical coordinates, Mathieu functions are the proper eigenfunctions, which are discussed in the section on generalized Fourier series D.1; Arscott (1964, §3.9.1) has some specific discussion and lists additional references related to proofs on the convergence of series of Mathieu functions.

E.1 Higher special functions

The ODEs that arise when performing separation of variables on the Helmholtz equation lead to various special functions (see Table 3.2), including Mathieu functions. These coordinate systems and special functions can be categorized by their singularities (e.g. Ince, 1956; Moon and Spencer, 1961b; Arscott, 1981). Cartesian, spherical and circular cylindrical are the simplest three coordinates, corresponding to the three in most common use. These simpler coordinate systems can be derived from a general coordinate system with three regular singularities (Morse

and Feshbach, 1953, §5), by moving the singularities to 0 or ∞ and, if required, moving two of them together (a confluence of singularities). This three-singularity coordinate system is solved most generally by hypergeometric functions; exponential, Bessel, and Legendre functions are all special cases of hypergeometric functions (Andrews, 1998, §9–12). Hypergeometric functions can always be put into a two-term recurrence, which essentially means the functions turn a second-order differential equation into a first-order difference equation. This is one of the fundamental reasons there are so many "nice" relationships involving Bessel functions and their derivatives (e.g. Watson, 1944; McLachlan, 1955).

The rest of the coordinates systems (rotational, except spherical, and general) and their associated special functions in Table 3.2 do not conform to this three-singularity model (Arscott, 1981). The ODEs that arise from performing separation of variables on the Helmholtz equation in these more general coordinate systems (except for ellipsoidal coordinates) are simplifications of the Heun equation, which has four regular singularities (Ronveaux, 1995, §1). Solutions to this equation have three-term recurrences; a second-order differential equation is transformed into a second-order difference equation. While usable, this three-term recurrence is not the big improvement seen with the two-term recurrence arising from the hypergeometric equation.

The point being made is that Mathieu functions are more complicated than Bessel functions; they do not share most of the nice properties of Bessel functions. The general and rotational (except spherical) coordinate systems appearing in Table 3.2 are on par with, or more difficult than, elliptic coordinates (most certainly with fewer references and publications). This is seen as a limitation of the eigenfunction expansion approach for developing LT-AEM elements. In these cases a simpler Fourier or Chebyshev series approach (Boyd, 2000) may be worth the extra effort and inelegance required to implement it.

E.2 Matrix formulation

To compute MF of complex argument, the matrix formulation of the eigenvalue problem is used (Chaos-Cador and Ley-Koo, 2002; Stamnes and Spjelkavik, 1995). Because of their required periodicity, the angular MF can be expanded in either odd or even Fourier series; general expressions for the solutions are therefore of the form

$$C_n(\psi) = \sum_{r=0}^{\infty} A_r \cos r\psi, \tag{E.1}$$

$$S_n(\psi) = \sum_{r=1}^{\infty} B_r \sin r\psi. \tag{E.2}$$

Putting these expressions into the angular Mathieu equation leads to the following four (even and odd coefficients are independent) recurrence relationships for the Mathieu coefficients (McLachlan, 1947, §3.10)

$$\begin{aligned} aA_0 - qA_2 &= 0 \\ (a-4)A_2 - q(2A_0 + A_4) &= 0 \\ (a-j^2)A_j - q(A_{j+2} + A_{j-2}) &= 0 \qquad j = 4, 6, 8, \ldots \end{aligned} \tag{E.3}$$

$$\begin{aligned} (a-1)A_1 - q(A_1 + A_3) &= 0 \\ (a-j^2)A_j - q(A_{j+2} + A_{j-2}) &= 0 \qquad j = 3, 5, 7, \ldots \end{aligned} \tag{E.4}$$

$$\begin{aligned} (b-4)B_2 - qB_4 &= 0 \\ (b-j^2)B_j - q(B_{j+2} + B_{j-2}) &= 0 \qquad j = 2, 4, 6, \ldots \end{aligned} \tag{E.5}$$

$$\begin{aligned} (b-1)B_1 - q(B_3 - B_1) &= 0 \\ (b-j^2)B_j - q(B_{j+2} + B_{j-2}) &= 0 \qquad j = 3, 5, 7, \ldots \end{aligned} \tag{E.6}$$

where a and b are the traditional names for the separation constant in Mathieu's equation (Mathieu characteristic numbers), for the even and odd solutions, respectively (see Table 3.1). These recurrence relationships can be put into to the form of infinite tri-diagonal matrices minus a constant on the diagonal, multiplied by a vector of Mathieu coefficients, which is the form of an eigenvalue problem. For example, the even-indexed even coefficients (E.3) can be expressed in matrix form as

$$\left\{ \begin{bmatrix} 0 & q & & \cdots & \cdots & \cdots \\ 2q & 4 & q & & & \\ & q & 16 & q & & \\ \vdots & & & \ddots & & \\ \vdots & & & q & [2(M-2)]^2 & q \\ & & & & q & [2(M-1)]^2 \end{bmatrix} - a\mathbf{I} \right\} \begin{bmatrix} A_0 \\ A_2 \\ A_4 \\ \vdots \\ A_{2(M-2)} \\ A_{2(M-1)} \end{bmatrix} = \mathbf{0} \quad \text{(E.7)}$$

where the infinite recursion is truncated at M terms, and there would be similar matrix expressions for the other three recurrence relationships. A non-degenerate square matrix of rank M has M eigenvalues, for each eigenvalue there is an eigenvector. This matrix problem is readily and accurately solved with LAPACK routine ZGEEV (Anderson et al., 1990). When q is real, the matrix can be made symmetric, and the solution can be found more efficiently using Cholesky factorization. For complex q, the matrix would need to be Hermitian to be made similarly efficient (not possible in the current application).

It is also clear in matrix form, that when $q \to 0$ the matrix becomes diagonal; the eigenvalues of a diagonal matrix are simply the values on the diagonal, which are integers. The MF each reduce to only one of the harmonics in (E.1), indicating how MF degenerate to sine or cosine.

Blanch and Clemm (1969) give an example of the traditional continued fraction approach applied to the complex Mathieu parameter case, which is potentially more efficient than the matrix method, but requires an initial guess and is only valid for small Mathieu parameter, $|q| \leq 4n$, with asymptotic relationships

required for larger q (e.g. Alhargan, 2000a; Hunter and Guerrieri, 1981; Arscott, 1964). The matrix used to compute the eigenvectors is a truncated infinite matrix; the size of the matrix required is proportional to the highest order of MF needed, the accuracy desired, and $|q|$ (Delft Numerical Analysis Group, 1973); we find N+20 terms is adequate in most cases (where N is the highest order of MF needed).

E.3 Double points

When the Mathieu parameter takes on complex values (because complex p are required for $\mathcal{L}^{-1}$), the eigenvalues become complex, and in the case of the angular Mathieu equation, pairs of eigenvalues (and their associated eigenvectors) degenerate at isolated branch points (i.e., double points) in the complex q plane. Figure E.1 illustrates the double points in a portion of the first quadrant; $a(q)$ and $b(q)$ for the other quadrants can be found through symmetries (Hunter and Guerrieri, 1981) (a_{2n+1} and b_{2n+1} switch across the imaginary axis).

As given in Table 3.1, $a_{n,m}$ is the m^{th} degenerate eigenvalues for $\mathrm{ce}_n(\psi, q)$ and $b_{n,m}$ the same for $\mathrm{se}_n(\psi, q)$). The complex coordinates of the double points in Figure E.1 are tabulated in Blanch and Clemm (1969) and their calculation is discussed in Hunter and Guerrieri (1981). When q becomes complex and approaches one of the double points shown in Figure E.1, two different eigenvalues approach one another; e.g., at the value of $q_D \approx 63 + 20i$, labeled $a_{9,11}$, $\mathrm{ce}_9(\psi; q_D)$ and $\mathrm{ce}_{11}(\psi; q_D)$ are no longer orthogonal.

This eigenvalue degeneracy results in the occasional pair of eigenvectors being less than orthogonal, depending on the value of q (numerically, the eigenvectors aren't likely to be *exactly* degenerate). This behavior is not a problem for the overall convergence of the solution when a more general least-squares solution (e.g., LAPACK routine ZGELSS) is used, which can accommodate this occasional degener-

acy (see least-squares discussion in section 2.6.3). All numerical $\mathcal{L}^{-1}$ methods use $\bar{\Phi}(\mathbf{x}, p)$ for a vector of p values to compute a single time-domain solution. An entry in this vector may coincide with a double point of Mathieu's equation, shown in Figure E.1, but because this degeneracy only affects a pair of the N eigenvectors at one (or possibly two) of the values of p, it is not critical to the overall performance of the method.

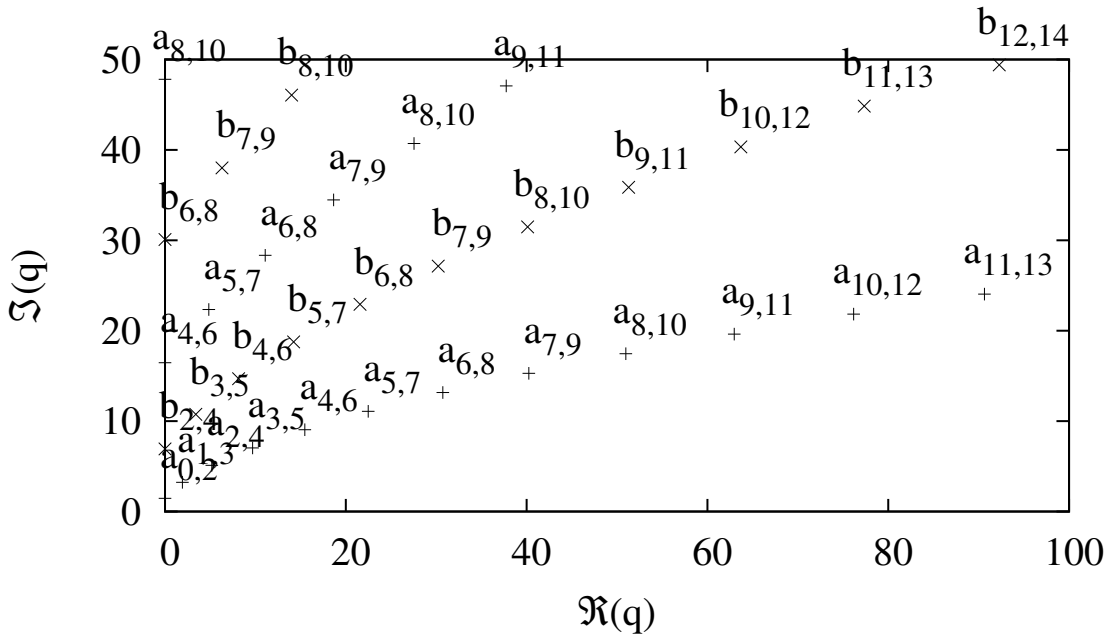

FIGURE E.1. Double points of Mathieu's equation (3.27), where the eigenvalues associated with two eigenfunctions merge.

E.4 Definitions

E.4.1 Angular Mathieu functions

Angular MF are evaluated from their definitions in terms of infinite sine and cosine series (second kind non-period angular MF are not useful in our application), for $\Re(q) < 0$ (which arises due to the sign on κ^2 in the governing Yukawa or modified Helmholtz equation) they are (McLachlan, 1947, §2.18):

$$\mathrm{ce}_{2n}(\psi, -q) = (-1)^n \sum_{r=0}^{\infty} (-1)^r \mathbf{A}_{2r}^{(2n)} \cos[2r\psi], \tag{E.8}$$

$$\mathrm{ce}_{2n+1}(\psi, -q) = (-1)^n \sum_{r=0}^{\infty} (-1)^r \mathbf{B}_{2r+1}^{(2n+1)} \cos[(2r+1)\psi], \tag{E.9}$$

$$\mathrm{se}_{2n+1}(\psi, -q) = (-1)^n \sum_{r=0}^{\infty} (-1)^r \mathbf{A}_{2r+1}^{(2n+1)} \sin[(2r+1)\psi], \tag{E.10}$$

$$\mathrm{se}_{2n+2}(\psi, -q) = (-1)^n \sum_{r=0}^{\infty} (-1)^r \mathbf{B}_{2r+2}^{(2n+2)} \sin[(2r+2)\psi], \tag{E.11}$$

where $\mathbf{A}_r^{(n)}$ and $\mathbf{B}_r^{(n)}$ are matrices of Mathieu coefficients, corresponding to the a_n and b_n eigenvalues (both functions of q); the r terms of each comprise the eigenvectors associated with the n^{th} eigenvalue that provides a periodic solution to angular Mathieu equation. Even order ($2n$ and $2n+2$) MF are π periodic, while odd order MF are 2π periodic, see Table 3.1 for symmetries of the angular MF.

E.4.2 Mathieu coefficients

Because eigenvectors only define a direction, their length must be normalized according to a standard. An extension of the normalization proposed by Goldstein (1927) is used, since it is readily generalized to the complex case and it produces angular MF of approximately unit size and constant amplitude for the entire range of ψ (LAPACK subroutine ZGEEV returns this scaling, additionally scaling the

largest element to be real). The Mathieu coefficients are normalized by

$$\int_{-\pi}^{\pi} \mathrm{ce}_n(\psi,-q)\,\mathrm{ce}_n^*(\psi,q)\,\mathrm{d}\psi = \pi \tag{E.12}$$

$$\int_{-\pi}^{\pi} \mathrm{se}_n(\psi,-q)\,\mathrm{se}_n^*(\psi,q)\,\mathrm{d}\psi = \pi \tag{E.13}$$

where $*$ is complex conjugate, so the MF degenerate to trigonometric functions as $q \to 0$. These integrals specify that the angular MF have the same root mean squared value as the trigonometric functions, $1/\sqrt{2}$, and this quantity is not a function of q. All of the eigenvectors are normalized to unit length (which leaves the sign ambiguous), except the coefficients of $\mathrm{ce}_{2n}(\psi,-q)$, the first entry in the eigenvector is weighted twice,

$$2\mathbf{A}_0^0\left(\mathbf{A}_0^0\right)^* + \sum_{r=1}^{\infty} \mathbf{A}_{2r}^{2n}\left(\mathbf{A}_{2r}^{2n}\right)^* = 1. \tag{E.14}$$

The sign of the eigenvectors is set so that the real portion of the diagonal elements positive; this allows the Mathieu functions to naturally degenerate to their corresponding trigonometric functions as $q \to 0$.

Alternate normalizations Morse and Feshbach (1953, p.1409) are in common use (Alhargan, 2000a), but lead to large values of the angular MF for large values of q, and do not readily generalize to complex q.

E.4.3 Radial Mathieu functions

Radial MF are best defined in terms of Bessel function product series (convergent for all η); the most appropriate definitions are given below. These definitions are for $\Re(q) < 0$, explicitly indicated by the negative on q on the left hand side. The effects of changing the sign of q from the standard definition are accounted for by the change of variables $\tilde{z} = \frac{\pi}{2} - z$, then the "non-negative" value for q is used when it appears on the right hand side of the definitions below. The radial MF are

defined as (McLachlan, 1947, §13.30)

$$\mathrm{Ie}_{2n}(\eta,-q)=\frac{(-1)^n p_{2n}}{\left[\mathbf{A}_0^{(2n)}\right]^2}\sum_{r=0}^{\infty}(-1)^r\mathbf{A}_{2r}^{(2n)}\mathrm{I}_r(v_1)\mathrm{I}_r(v_2), \tag{E.15}$$

$$\mathrm{Ie}_{2n+1}(\eta,-q)=\frac{(-1)^n s_{2n+1}}{\sqrt{q}\left[\mathbf{B}_1^{(2n+1)}\right]^2}\sum_{r=0}^{\infty}(-1)^r\mathbf{B}_{2r+1}^{(2n+1)}\left[\mathrm{I}_r(v_1)\mathrm{I}_{r+1}(v_2)+\mathrm{I}_{r+1}(v_1)\mathrm{I}_r(v_2)\right], \tag{E.16}$$

$$\mathrm{Io}_{2n+1}(\eta,-q)=\frac{(-1)^{n+1} p_{2n+1}}{\sqrt{q}\left[\mathbf{A}_1^{(2n+1)}\right]^2}\sum_{r=0}^{\infty}(-1)^r\mathbf{A}_{2r+1}^{(2n+1)}\left[\mathrm{I}_r(v_1)\mathrm{I}_{r+1}(v_2)-\mathrm{I}_{r+1}(v_1)\mathrm{I}_r(v_2)\right], \tag{E.17}$$

$$\mathrm{Io}_{2n+2}(\eta,-q)=\frac{(-1)^{n+1} s_{2n+2}}{q\left[\mathbf{B}_2^{(2n+2)}\right]^2}\sum_{r=0}^{\infty}(-1)^r\mathbf{B}_{2r+2}^{(2n+2)}\left[\mathrm{I}_r(v_1)\mathrm{I}_{r+2}(v_2)-\mathrm{I}_{r+2}(v_1)\mathrm{I}_r(v_2)\right], \tag{E.18}$$

where $v_1=\sqrt{q}e^{-\eta}$ and $v_2=\sqrt{q}e^{+\eta}$ and the angular MF identities used above are

$$p_{2n}=\mathrm{ce}_{2n}(0,q)\,\mathrm{ce}_{2n}\left(\tfrac{\pi}{2};q\right), \qquad p_{2n+1}=\mathrm{ce}_{2n+1}(0,q)\,\mathrm{ce}'_{2n+1}\left(\tfrac{\pi}{2};q\right), \tag{E.19}$$

$$s_{2n+2}=\mathrm{se}'_{2n+2}(0,q)\,\mathrm{se}'_{2n+2}\left(\tfrac{\pi}{2};q\right), \qquad s_{2n+1}=\mathrm{se}'_{2n+1}(0,q)\,\mathrm{se}_{2n+1}\left(\tfrac{\pi}{2};q\right). \tag{E.20}$$

The second kind Bessel function product series are

$$\mathrm{Ke}_{2n}(\eta,-q)=\frac{(-1)^n p_{2n}}{\pi\left[\mathbf{A}_0^{(2n)}\right]^2}\sum_{r=0}^{\infty}\mathbf{A}_{2r}^{(2n)}\mathrm{I}_r(v_1)\mathrm{K}_r(v_2), \tag{E.21}$$

$$\mathrm{Ke}_{2n+1}(\eta,-q)=\frac{(-1)^n s_{2n+1}}{\pi\sqrt{q}\left[\mathbf{B}_1^{(2n+1)}\right]^2}\sum_{r=0}^{\infty}\mathbf{B}_{2r+1}^{(2n+1)}\left[\mathrm{I}_r(v_1)\mathrm{K}_{r+1}(v_2)-\mathrm{I}_{r+1}(v_1)\mathrm{K}_r(v_2)\right], \tag{E.22}$$

$$\mathrm{Ko}_{2n+1}(\eta,-q)=\frac{(-1)^{n+1} p_{2n+1}}{\pi\sqrt{q}\left[\mathbf{A}_1^{(2n+1)}\right]^2}\sum_{r=0}^{\infty}\mathbf{A}_{2r+1}^{(2n+1)}\left[\mathrm{I}_r(v_1)\mathrm{K}_{r+1}(v_2)+\mathrm{I}_{r+1}(v_1)\mathrm{K}_r(v_2)\right], \tag{E.23}$$

$$\mathrm{Ko}_{2n+2}(\eta,-q)=\frac{(-1)^{n+1} s_{2n+2}}{\pi q\left[\mathbf{B}_2^{(2n+2)}\right]^2}\sum_{r=0}^{\infty}\mathbf{B}_{2r+2}^{(2n+2)}\left[\mathrm{I}_r(v_1)\mathrm{K}_{r+2}(v_2)-\mathrm{I}_{r+2}(v_1)\mathrm{K}_r(v_2)\right]. \tag{E.24}$$

Abramowitz and Stegun (1964) and Gutiérrez Vega et al. (2003) have tables relating the radial Mathieu functions' various names found in different publications. Derivatives of MF are found by applying the derivative to the definitions; no simple recurrence relationships exist (see discussion in section E.1).

Appendix F

QUASILINEAR INFILTRATION FROM AN ELLIPTICAL CAVITY

F.1 Introduction

A solution for flow from a long elliptic cylinder cavity is given in two-dimensional elliptical coordinates for the quasilinear (Philip, 1968) form of the steady unsaturated flow equation (Richards, 1931) in a homogeneous porous medium. The solution is an extension of one by Philip (1984) for flow from a circular cylinder cavity.

The approach taken here is to expand the linearized potential in the natural eigenfunctions that arise in elliptical coordinates. This technique has been utilized extensively in the physics literature (e.g., Stratton (1941, §6.12), Chu and Stratton (1941), Morse and Feshbach (1953, p.1407–1432), Moon and Spencer (1961a), Arscott (1964), and Kleinermann et al. (2002)), but the solution derived here for the current problem's boundary conditions is new.

Unsaturated porous media flow, specifically infiltration, is a very non-linear process that is often solved numerically with finite element codes such as HYDRUS (e.g., Skaggs et al. (2004)). Analytic solutions to infiltration problems, restricted as they may be, often deliver more insightful results due to their simplicity. They give solutions with fewer potentially complicating auxiliary parameters. Pullan (1990) reviews the history of the quasilinear solution methodology and compares numerous approaches for solving the linearized Richards equation.

In the context of predicting furrow infiltration, Rawls et al. (1990) compared steady infiltration solutions for 1, 2, and 3 dimensions, using the 2D point source solution of Philip (1968) in the comparison. The solution derived here for an el-

liptical shape is more realistically furrow-shaped; ellipses have the capability of simulating the geometry associated with either wide or deep cavities and strips, rather than simple point approximations. Warrick et al. (2007) and Warrick and Lazarovitch (2007) discuss the impacts that dimensionality and "edge effects" have on infiltration from strips and parabolic-shaped furrows.

The elliptical solution derived here can represent the geometry of a strip or furrow explicitly, although without surface or water table boundary effects. It is a free-space solution, since it is valid at large distance. A dry far-field condition is assumed, resulting in no-flow far away from the ellipse. Including the effects of the land surface (potentially intersecting the ellipse) would require imposing a no-flow boundary condition. This homogeneous type II boundary condition would become an inhomogeneous type III boundary condition after applying the required non-linear transformations (Wooding, 1968). A solution for flow from an elliptical cavity that accounted for this boundary condition would most likely be approximate in nature (e.g., a linearized AEM or gridded numerical solution). An alternative approach would be to use the integral expression of Lomen and Warrick (1978, eq.5) (with $D = 0$, and no dependence on Y or T) to include the effects of a horizontal evaporative or no-flow boundary. Similarly, Philip (1989) and Warrick (2003, p.276) indicate how a water table condition can be accounted for with a free-space solution. Using the solution derived here in these integral relationships leads to integral expressions that cannot be evaluated in closed form for general values of the coordinates.

Bakker and Nieber (2004b) applied the analytic element method to the quasi-linear flow equation for the problem of uniform vertical flow through ellipses of different material properties. Their approach is quite general, but to obtain a solution for multiple elements involves performing two nested iterations. A non-linear boundary-matching iteration is nested within an outer iteration that accounts for the effects elements have on one another. In the analysis presented here, no itera-

tions are required to compute the solution, outside of those potentially needed to compute the required Mathieu functions (also needed for the AEM solution).

Mathieu functions arise as solutions to the modified Helmholtz equation in elliptic-cylinder coordinates (Morse and Feshbach (1953, p.562), Moon and Spencer (1961b), Arscott and Darai (1981), and Ben-Menahem and Singh (2000, p.53)). We use a modern matrix eigenvector approach (Stamnes and Spjelkavik, 1995; Chaos-Cador and Ley-Koo, 2002), allowing all the required functions and coefficients to be computed using any combination of widely available eigensolution (e.g., Matlab (MathWorks, 2007) or LAPACK (Golub and van Loan, 1996)) and Bessel function routines.

F.2 Governing equation

F.2.1 Quasilinear flow equation

The steady-state unsaturated porous media flow equation (Richards, 1931) is

$$\widehat{\nabla} \cdot \Big(K(h) \widehat{\nabla} h \Big) = \frac{\partial K}{\partial z}, \tag{F.1}$$

where $\widehat{\nabla}$ is the 2D spatial derivative operator, $K(h)$ is hydraulic conductivity $[L/T]$, a non-linear function of pressure head, h $[L]$. Flow is driven by gradients in hydraulic head, $\Phi = h - z$, the sum of pressure and elevation heads (z positive downwards). Hats indicate the differential operators are dimensional. The Kirchhoff transformation (Klute, 1952) is used to linearize (F.1); it is

$$\Theta(h) = \int_{-\infty}^{h} K(u)\, \mathrm{d}u, \tag{F.2}$$

where u is a dummy variable and Θ is matric flux potential $[L^2/T]$. Applying (F.2) and setting $K(-\infty) = 0$, (F.1) becomes

$$\widehat{\nabla}^2 \Theta = \frac{1}{K} \frac{\mathrm{d}K}{\mathrm{d}h} \frac{\partial \Theta}{\partial z}. \tag{F.3}$$

The Gardner (1958) exponential hydraulic conductivity distribution is used to simplify (F.3) further, by assuming the convenient relationship

$$K(h) = K_0 e^{\alpha h}, \tag{F.4}$$

where $h < 0$ for unsaturated flow, α is the sorptive number $[1/L]$ (related to pore size) and K_0 is K at saturation. Using (F.4), the flow equation becomes

$$\widehat{\nabla}^2 \Theta = \alpha \frac{\partial \Theta}{\partial z}, \tag{F.5}$$

which is the quasilinear form of Richards' equation, first extensively studied by Philip (1968). Pullan (1990) summarizes the benefits and limitations related to the quasilinear approximation.

F.2.2 Elliptical geometry

A long elliptical pipe is represented as a surface of constant elliptical radius in two-dimensional elliptic cylinder coordinates, where the variation along the length of the pipe is assumed negligible. For a horizontal ellipse, the major axis is parallel to the land surface (x-axis) and the positive z-axis points down (see Figure F.1). The elliptical angular coordinate starts at the positive x-axis and increases clockwise, $0 \leq \psi \leq 2\pi$. The Cartesian coordinates (x, z) $[L]$ for the horizontal ellipse are defined in terms of the dimensionless elliptical coordinates (η, ψ) by

$$x = f \cosh(\eta) \cos(\psi), \qquad z = f \sinh(\eta) \sin(\psi), \tag{F.6}$$

where f is the semi-focal distance $[L]$. The boundary of the cylinder is defined as $\eta = \eta_0$. The narrow dimension of the ellipse is twice the semi-minor axis, $b = f \sinh(\eta_0)$, while the wide dimension is twice the semi-major axis, $a = f \cosh(\eta_0)$. The eccentricity of the ellipse is a dimensionless quantity,

$$e = \sqrt{1 - \frac{b^2}{a^2}}, \tag{F.7}$$

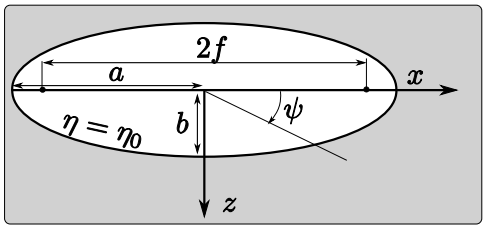

FIGURE F.1. Elliptical cutout geometry and coordinate convention. η and ψ are the elliptical radial and angular coordinates; a, b, and f are the semi-major, -minor, and -focal lengths, respectively.

equivalently given as $f = ea$, that ranges from 0 (circle) to 1 (line segment joining the foci). The pair (a, e) completely specifies the geometry of the problem; a is a measure of the size of the cavity, while e is related to its shape. There are other combinations of parameters that can equivalently specify the problem, for example specifying (f, η_0) or (a, b) is also possible. These other pairs of parameters, while valid, have less physical meaning; they must be kept in a specified ratio to preserve the size or shape of the problem, which comes naturally for the (a, e) combination. Four ellipses, used in later examples, with $a = 1$ and different values of e are plotted for comparison in Figure F.2, with their properties listed in Table F.1. Ellipses with $e < 0.5$ appear to be circles, unless the two are plotted next to each other for comparison.

$e = f$	η_0	b	c
0	∞	1	2π
0.5	1.317	0.866	5.870
0.9	0.467	0.436	4.697
1	0	0	4

TABLE F.1. Parameters for ellipses in Figure F.2; $a = 1$

The circumference of the ellipse, c $[L]$, cannot be evaluated exactly in closed form; it is defined by an elliptic integral, but can be approximated using one of several formulas. We use the simple YNOT expression (Maertens and Rousseau,

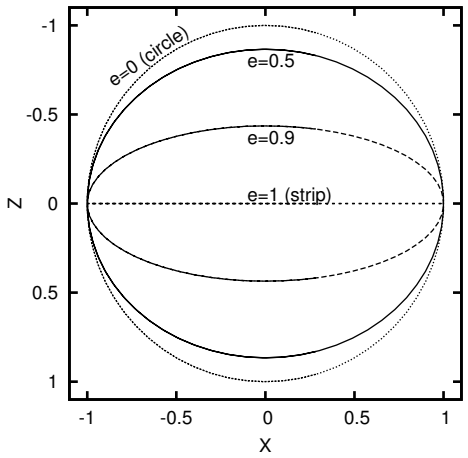

FIGURE F.2. Comparison of ellipses with $a = 1$ and $e = [0, 0.5, 0.9, 1]$. See Table F.1 for corresponding elliptical coordinates.

2000)

$$c \approx 4\sqrt[y]{a^y + b^y}, \tag{F.8}$$

where $y = \ln(2)/\ln\left(\frac{\pi}{2}\right)$ and the error in the approximation is at most 0.4%.

F.2.3 Non-dimensionalizing

Because of the problem's homogeneity, it can be made dimensionless with respect to the sorptive number of the porous medium. Dimensionless lengths are defined as

$$\frac{A}{a} = \frac{B}{b} = \frac{F}{f} = \frac{C}{c} = \frac{X}{x} = \frac{Z}{z} = \frac{\alpha}{2}, \tag{F.9}$$

where capital letters are dimensionless versions of lower-case variables. The matric flux potential is non-dimensionalized by

$$\vartheta = \frac{\Theta}{\Theta_0}. \tag{F.10}$$

where $\Theta_0 = \Theta(\eta_0)$. The boundary condition on the ellipse is specified pressure head or moisture potential (h is a constant and Φ is proportional to $-z$ on the

boundary),

$$h(\eta_0) = h_0 \tag{F.11}$$

while for simplicity, the far-field boundary condition is no-flow,

$$h(\eta \to \infty) = -\infty, \qquad \Theta[h(\eta \to \infty)] = 0. \tag{F.12}$$

The linearized flow equation (F.5) written in dimensionless form is

$$\nabla^2 \vartheta = 2\frac{\partial \vartheta}{\partial Z} \tag{F.13}$$

with corresponding dimensionless boundary conditions of

$$\vartheta(\eta_0, \psi) = 1, \qquad \vartheta(\eta \to \infty) \to 0. \tag{F.14}$$

To eliminate the Z derivative we make an exponential substitution (Wooding, 1968),

$$\vartheta = He^Z, \tag{F.15}$$

which reduces (F.13) to the Yukawa (Duffin, 1971) or modified Helmholtz equation,

$$\nabla^2 H = H, \tag{F.16}$$

subject to the boundary conditions

$$H(\eta_0, \psi) = e^{-F\sinh(\eta_0)\sin(\psi)} = e^{-B\sin(\psi)}, \tag{F.17}$$

$$H(\eta \to \infty) = He^{F\sinh(\eta)\sin(\psi)} \to 0, \tag{F.18}$$

in terms of the elliptical coordinates. Specifying the boundary condition on the ellipse as constant Φ rather than constant h results in the condition $H(\eta_0, \psi) = \exp[B\sin(\psi)]$, but leads to positive h, which the quasilinear governing equation cannot accommodate.

The dimensionless moisture potential, $\mathbf{\Psi}$, and hydraulic head, $\mathbf{\Phi}$, are defined and related to ϑ by

$$\mathbf{\Psi} = \frac{h}{h - h_0} = \tfrac{1}{2}\ln(\vartheta), \qquad \mathbf{\Phi} = \frac{\Phi}{\Phi - h_0} = \tfrac{1}{2}\ln(\vartheta) - Z, \tag{F.19}$$

where we take $h_0 = 0$ for simplicity.

F.3 Solution via separation of variables

The dimensionless modified Helmholtz equation (F.16) in elliptical coordinates (Moon and Spencer, 1961b, p.17) is

$$\frac{2}{F^2\left[\cosh(2\eta)-\cos(2\psi)\right]}\left(\frac{\partial^2 H}{\partial\eta^2}+\frac{\partial^2 H}{\partial\psi^2}\right)=H. \tag{F.20}$$

We perform separation of variables by substituting $H(\eta,\psi)=R(\eta)Y(\psi)$, dividing by H, separating everything dependent on η from terms dependent on ψ, then setting both quantities equal to the separation constant, λ. The results are simplified into the form of Mathieu's differential equations,

$$\frac{\mathrm{d}^2 R}{\mathrm{d}\eta^2}=R\left(2q\cosh(2\eta)+\lambda\right), \tag{F.21}$$

$$\frac{\mathrm{d}^2 Y}{\mathrm{d}\psi^2}=-Y\left(2q\cos(2\psi)+\lambda\right). \tag{F.22}$$

These are the radial (F.21) and angular (F.22) modified Mathieu equations (McLachlan, 1947). Here, λ is an eigenvalue chosen to make the angular solution, $Y(\psi)$, periodic for the specified value of the Mathieu parameter, $q=-F^2/4$. A negative is used in the definition of q to put the equations into standard form. The solutions to equations (F.21) and (F.22) are radial and angular modified Mathieu functions; see Gutiérrez Vega et al. (2003) and Bakker and Nieber (2004b) for characteristic functional plots. The periodic solution to (F.22) and the corresponding free-space solution to (F.21) is

$$Y(\psi)=a_0\mathrm{ce}_0(\psi;-q)+\sum_{n=1}^{\infty}a_n\mathrm{ce}_n(\psi;-q)+b_n\mathrm{se}_n(\psi;-q), \tag{F.23}$$

$$R(\eta)=c_0\mathrm{Ke}_0(\eta;-q)+\sum_{n=1}^{\infty}c_n\mathrm{Ke}_n(\eta;-q)+d_n\mathrm{Ko}_n(\eta;-q), \tag{F.24}$$

where a_n, b_n, c_n, and d_n are coefficients to determine and $\mathrm{ce}_n(\psi,-q)$ and $\mathrm{se}_n(\psi,-q)$ are the even and odd, n^{th}-order, first-kind angular Mathieu functions of argument

ψ and parameter $-q$. Historically, they were referred to as *cosine-elliptic* and *sine-elliptic*, based on how they degenerate to trigonometric functions as $q \to 0$ (see Appendix A for definitions). Similarly, $\mathrm{Ke}_n(\eta, -q)$ and $\mathrm{Ko}_n(\eta, -q)$ are the even and odd, n^{th}-order, second-kind radial Mathieu functions of argument η and parameter $-q$. Radial Mathieu functions are analogous to modified Bessel functions, degenerating to them as $q \to 0$.

There are additional solutions to (F.21) and (F.22) not needed for the solution of (F.20), including the non-periodic second-kind angular Mathieu functions and the first-kind radial Mathieu functions (analogous to I Bessel functions) that grow exponentially as $\eta \to \infty$. Modified Mathieu functions are by convention associated with $q < 0$, but non-modified Mathieu functions can equivalently be used. This equivalence is analogous to that between Bessel functions of imaginary argument and modified Bessel functions of real argument.

The product of the solutions to the Mathieu equations is a solution to (F.20), namely

$$H(\eta \geq \eta_0, \psi) = \sum_{n=0}^{\infty} \beta_n \frac{\mathrm{Ke}_n(\eta, -q)}{\mathrm{Ke}_n(\eta_0, -q)} \mathrm{ce}_n(\psi, -q) + \sum_{n=1}^{\infty} \gamma_n \frac{\mathrm{Ko}_n(\eta, -q)}{\mathrm{Ko}_n(\eta_0; -q)} \mathrm{se}_n(\psi; -q) \quad \text{(F.25)}$$

where β_n and γ_n are coefficients to determine and the radial Mathieu functions are normalized by their value on the boundary of the ellipse. Expression (F.25) simplifies to a generalized Fourier series expansion in the natural eigenfunctions of the system (Churchill, 1972, §9) at $\eta = \eta_0$,

$$H_0(\eta_0, \psi) = \beta_0 \mathrm{ce}_0(\psi; -q) + \sum_{n=1}^{\infty} \beta_n \mathrm{ce}_n(\psi; -q) + \gamma_n \mathrm{se}_n(\psi; -q). \quad \text{(F.26)}$$

F.3.1 Determination of coefficients

The orthogonality of the angular Mathieu functions is derived from the orthogonality of their sine and cosine components (see McLachlan (1947) §2.19), which

is

$$\int_0^{2\pi} \mathrm{ce}_n(\psi, q)\mathrm{se}_m(\psi, q)\,\mathrm{d}\psi = 0 \tag{F.27}$$

for any integer m, n. The orthogonality of the Mathieu functions then is

$$\int_0^{2\pi} \mathrm{se}_n(\psi, q)\mathrm{se}_m(\psi, q)\,\mathrm{d}\psi = \int_0^{2\pi} \mathrm{ce}_n(\psi, q)\mathrm{ce}_m(\psi, q)\,\mathrm{d}\psi = \pi\delta_{nm} \tag{F.28}$$

where δ_{nm} is the Kronecker delta and the two Mathieu functions share the same real q. Multiplying (F.26) by each angular Mathieu function and integrating over the domain, integral expressions for the coefficients are

$$\beta_n = \frac{1}{\pi}\int_0^{2\pi} H_0(\eta_0, \psi)\mathrm{ce}_n(\psi, -q)\,\mathrm{d}\psi, \tag{F.29}$$

$$\gamma_n = \frac{1}{\pi}\int_0^{2\pi} H_0(\eta_0, \psi)\mathrm{se}_n(\psi, -q)\,\mathrm{d}\psi. \tag{F.30}$$

Equation (F.31) is expanded using (F.17) and the definition of the modified angular Mathieu functions (F.61–F.62) resulting in

$$\beta_{2n} = \frac{(-1)^n}{\pi}\sum_{r=0}^{\infty}(-1)^r \mathbf{A}_{2r}^{(2n)} \int_0^{2\pi} e^{-B\sin(\psi)}\cos(2r\psi)\,\mathrm{d}\psi, \tag{F.31}$$

$$\beta_{2n+1} = \frac{(-1)^n}{\pi}\sum_{r=0}^{\infty}(-1)^r \mathbf{B}_{2r+1}^{(2n+1)} \int_0^{2\pi} e^{-B\sin(\psi)}\cos\left[(2r+1)\psi\right]\,\mathrm{d}\psi. \tag{F.32}$$

Using an integral definition for the modified Bessel function of the first kind (Watson, 1944, §6.22), a phase shift of $\pi/2$, and a trigonometric identity, (F.31) simplifies to

$$\beta_{2n} = 2(-1)^n \sum_{r=0}^{\infty} \mathbf{A}_{2r}^{(2n)} \mathrm{I}_{2r}(B), \tag{F.33}$$

while (F.32) is zero for all integer r, based on symmetry. This infinite sum of I Bessel functions (F.33) is equivalent to one of several definitions of the first-kind radial Mathieu functions (F.68), further simplifying the coefficient expression to

$$\beta_{2n} = 2p_{2n}\mathrm{Ie}_{2n}(\eta_0; -q), \tag{F.34}$$

where $p_{2n} = \mathbf{A}_0^{(2n)} / \mathrm{ce}_{2n}\left(\frac{\pi}{2}; q\right)$ is a normalization constant and the argument of the I Bessel functions in (F.68) is $\omega = \mathrm{arcsinh}(B/F)$, which is simply $\omega = \eta_0$. Similarly, the coefficients of the odd functions become

$$\gamma_{2n+1} = \frac{(-1)^n}{\pi} \sum_{r=0}^{\infty} (-1)^r \mathbf{A}_{2r+1}^{(2n+1)} \int_0^{2\pi} e^{-B\sin(\psi)} \sin\left[(2r+1)\psi\right] \, \mathrm{d}\psi \tag{F.35}$$

$$= 2(-1)^{n+1} \sum_{r=0}^{\infty} \mathbf{A}_{2r+1}^{(2n+1)} \mathrm{I}_{2r+1}(B), \tag{F.36}$$

$$= 2p_{2n+1} \mathrm{Io}_{2n+1}(\eta_0, -q) \tag{F.37}$$

where due to symmetry the integral involving se_{2n+2} is zero for all integer r, and $p_{2n+1} = \sqrt{q}\mathbf{A}_1^{(2n+1)} / \mathrm{ce}'_{2n+1}\left(\frac{\pi}{2}; q\right)$, with the prime indicating differentiation with respect to the argument.

Using (F.34) and (F.36), the solution for H from a horizontal ellipse is

$$H(\eta \geq \eta_0, \psi) \cong 2 \sum_{n=0}^{N-1} p_{2n} \mathrm{Ie}_{2n}(\eta_0, -q) \mathrm{ce}_{2n}(\psi, -q) \frac{\mathrm{Ke}_{2n}(\eta, -q)}{\mathrm{Ke}_{2n}(\eta_0, -q)} + p_{2n+1} \mathrm{Io}_{2n+1}(\eta_0, -q) \mathrm{se}_{2n+1}(\psi, -q) \frac{\mathrm{Ko}_{2n+1}(\eta, -q)}{\mathrm{Ko}_{2n+1}(\eta_0, -q)}. \tag{F.38}$$

The approximation comes from truncating the infinite sum at $2N-1$ terms. The first kind radial Mathieu functions can be evaluated using their identity as an infinite series of I Bessel functions of argument B, given in (F.33) and (F.36). These Bessel functions have the same argument and therefore they can all be computed recursively from the two values $\mathrm{I}_0(B)$ and $\mathrm{I}_1(B)$ using a backwards recurrence relationship (Press et al., 2007, §5.4.1), as is done in most available Bessel function libraries.

F.3.2 Limiting cases

Circular As the ellipse becomes a circle, $[A, B] \to R_0$, the dimensionless circular radius. In this limit $q \to 0$, then the eigenvector matrices, $\mathbf{A}_{2r}^{(2n)}$ and $\mathbf{A}_{2r+1}^{(2n+1)}$, become purely diagonal (see Appendix B); each angular Mathieu function is comprised

of only one harmonic ($n = r$). Therefore, the coefficients in r reduce to a single term, $\mathrm{I}_{2n}(B)$. The angular Mathieu functions become trigonometric functions and both the odd and even radial Mathieu functions become modified Bessel functions. The elliptical solution uses both even and odd angular (and corresponding radial) functions due to the symmetry associated with the chosen coordinate convention.

The circular cylinder solution of Philip (1984) can readily be re-derived for the coordinate system given in Figure F.1; this results in a circular solution that corresponds to the degeneration of (F.38) as $e \to 0$,

$$H(R \geq R_0, \phi) \cong \frac{\mathrm{K}_0(R)}{\mathrm{K}_0(R_0)}\mathrm{I}_0(R_0) + 2\sum_{n=1}^{N-1}(-1)^n \frac{\mathrm{K}_{2n}(R)}{\mathrm{K}_{2n}(R_0)}\mathrm{I}_{2n}(R_0)\cos(2n\phi) - 2\sum_{m=0}^{N-1}(-1)^m \frac{\mathrm{K}_{2m+1}(R)}{\mathrm{K}_{2m+1}(R_0)}\mathrm{I}_{2m+1}(R_0)\sin\left[(2m+1)\phi\right], \tag{F.39}$$

where the $\cos(0)$ term is halved, K_n is the second-kind modified Bessel function, $R = r\alpha/2$ is the dimensionless radius, and ϕ is the angle (following the same convention as ψ in Figure F.1, which is shifted $\pi/2$ from that used by Philip). The integrals involving the odd orders cosine and the even orders of sine are zero by symmetry for all integer values of n.

Numerically, (F.38) is ill-behaved as $e \to 0$. The Mathieu functions do asymptotically become Bessel functions, but for $e \leq 0.01$ the solution is more efficiently and accurately approximated with (F.39).

Strip In the other limiting case, as the elliptical cylinder degenerates to a ribbon or strip ($e = 1, \eta_0 = 0$, and $B = 0$), the $\mathrm{I}_r(B)$ coefficients all become zero except $\mathrm{I}_0(0) = 1$, leaving

$$H(\eta \geq 0, \psi) \cong 2\sum_{n=0}^{N-1}(-1)^n \mathbf{A}_0^{(2n)}\mathrm{ce}_{2n}(\psi, -q)\frac{\mathrm{Ke}_{2n}(\eta, -q)}{\mathrm{Ke}_{2n}(0, -q)}, \tag{F.40}$$

which is the same form given by Tranter (1951) and used by Kucûk and Brigham (1979) for the case of constant specified potential along an ellipse (not restricted to

$\eta_0 = 0$ in their cases). When $B = 0$, the boundary condition on the ellipse (F.17) becomes constant, since there is no z-variation across the strip. Numerically, (F.40) is well-behaved, as the radial Mathieu functions can be evaluated at $\eta = 0$ without problems.

F.3.3 Modification for vertically oriented ellipse

Since the modified Helmholtz equation (F.16) is symmetric with respect to x and z, the boundary conditions and back-transformation functions can be changed, leading to the analogous solution for a vertically oriented ellipse (see Figure F.3). The boundary condition for a vertical ellipse in terms of dimensionless matric flux potential, analogous to (F.14), are

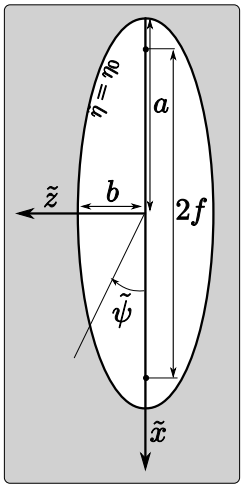

FIGURE F.3. Elliptical cutout geometry and coordinate convention for vertically-oriented ellipse

$$\tilde{\vartheta}(\eta_0, \tilde{\psi}) = 1, \qquad \tilde{H}_0(\eta_0, \tilde{\psi}) = e^{-A\cos(\tilde{\psi})}, \tag{F.41}$$

where a tilde indicates the variable is related to the vertically-oriented ellipse; the far-field boundary condition remains unchanged. This boundary condition leads

to modified expressions for the coefficients

$$\begin{aligned}
\tilde{\beta}_{2n} &= \frac{(-1)^n}{\pi}\sum_{r=0}^{\infty}(-1)^r \mathbf{A}_{2r}^{(2n)} \int_0^{2\pi} e^{-A\cos(\tilde{\psi})}\cos(2r\tilde{\psi})\,\mathrm{d}\tilde{\psi} \\
&= 2(-1)^n \sum_{r=0}^{\infty}(-1)^r \mathbf{A}_{2r}^{(2n)} \mathrm{I}_{2r}(A), \qquad \text{(F.42)} \\
&= 2s_{2n}\mathrm{Ie}_{2n}(\eta_0, -q), \\
\tilde{\beta}_{2n+1} &= \frac{(-1)^n}{\pi}\sum_{r=0}^{\infty}(-1)^r \mathbf{B}_{2r+1}^{(2n+1)} \int_0^{2\pi} e^{-A\cos(\tilde{\psi})}\cos\left[(2r+1)\tilde{\psi}\right]\,\mathrm{d}\tilde{\psi} \\
&= 2(-1)^{n+1} \sum_{r=0}^{\infty}(-1)^r \mathbf{B}_{2r+1}^{(2n+1)} \mathrm{I}_{2r+1}(A), \qquad \text{(F.43)} \\
&= -2s_{2n+1}\mathrm{Ie}_{2n+1}(\eta_0, -q)
\end{aligned}$$

where symmetry results in the integrals involving se_n being zero for all integer values of r, $s_{2n} = \mathbf{A}_0^{(2n)}/\mathrm{ce}_{2n}\,(0;q)$ and $s_{2n+1} = \sqrt{q}\mathbf{B}_1^{(2n+1)}/\mathrm{se}'_{2n+1}(0,q)$. The solution for $\tilde{H}$, analogous to (F.38), is

$$\tilde{H}(\tilde{\eta} \geq \eta_0, \tilde{\psi}) \cong 2\sum_{n=0}^{N-1}(-1)^n s_n \mathrm{Ie}_n(\eta_0, -q)\mathrm{ce}_n(\tilde{\psi}, -q)\frac{\mathrm{Ke}_n(\tilde{\eta}, -q)}{\mathrm{Ke}_n(\eta_0, -q)}, \qquad \text{(F.44)}$$

which is very analogous in form to equation 27 of Philip (1984).

This solution is then back-transformed to dimensionless Cartesian coordinates using the modified definitions

$$\tilde{\vartheta} = \tilde{H}e^{\tilde{X}}, \qquad \tilde{X} = F\cosh(\tilde{\eta})\cos(\tilde{\psi}), \qquad \tilde{Z} = F\sinh(\tilde{\eta})\sin(\tilde{\psi}), \qquad \text{(F.45)}$$

where $\tilde{X}$ points downward (see Figure F.3). The dimensionless potentials are

$$\tilde{\mathbf{\Psi}} = \frac{\tilde{h}}{\tilde{h} - h_0} = \frac{1}{2}\ln(\tilde{\vartheta}), \qquad \tilde{\mathbf{\Phi}} = \frac{\tilde{\Phi}}{\tilde{\Phi} - h_0} = \frac{1}{2}\ln(\tilde{\vartheta}) - \tilde{X}. \qquad \text{(F.46)}$$

The vertically-oriented solution (F.44) does not simplify in the limiting case $\eta_0 = 0$, due to its orientation; the source always has a boundary condition which varies with $\tilde{X}$.

F.4 Darcy flux along elliptical circumference

To determine the total flowrate, $\widehat{Q}\ [L^3/T]$, and the average flux, $\overline{v}\ [L/T]$, across the elliptical surface, the flux on the boundary of the ellipse is found, beginning with the dimensional form of Darcy's law,

$$\mathbf{v} = -K(h)\widehat{\nabla}\Phi, \tag{F.47}$$

where $\mathbf{v}$ is the Darcy flux $[L/T]$. Expressing the gradient operator in elliptical coordinates (Moon and Spencer, 1961b) makes (F.47)

$$\mathbf{v} = \frac{-K(h)}{f\sqrt{\frac{1}{2}(\cosh(2\eta) - \cos(2\psi))}}\left(\frac{\partial\Phi}{\partial\eta}\mathbf{e}_\eta + \frac{\partial\Phi}{\partial\psi}\mathbf{e}_\psi\right), \tag{F.48}$$

where $\mathbf{e}$ is a unit vector. For the horizontal ellipse, we substitute the definition of hydraulic head in elliptical coorindates $\Phi = h - f\sinh(\eta)\sin(\psi)$, using the notation $\xi(\eta,\psi) = \sqrt{\frac{1}{2}(\cosh(2\eta) - \cos(2\psi))}$, and taking the dot product with $\mathbf{e}_\eta$ leads to the following for the radial (η) component of the flux

$$\mathbf{v}\cdot\mathbf{e}_\eta = \frac{K(h)}{f\xi(\eta,\psi)}\left[f\cosh(\eta)\sin(\psi) - \frac{\partial h}{\partial\eta}\right]. \tag{F.49}$$

Evaluating (F.49) at $\eta = \eta_0$, applying the Kirchhoff transformation (F.2), using the Gardner exponential model, and non-dimensionalizing the flux leads to

$$V_0 = \frac{1}{F\xi(\eta_0,\psi)}\left\{2\sin(\psi) - \left[\frac{\partial\vartheta}{\partial\eta}\right]_{\eta_0}\right\}, \tag{F.50}$$

where $V_0 = 2\mathbf{v}(\eta_0)\cdot\mathbf{e}_\eta/(\Theta_0\alpha)$ and the subscript zero indicating the fluxes are evaluated on the boundary of the ellipse. The derivative in (F.50) can be expanded using the product rule as

$$\left[\frac{\partial\vartheta}{\partial\eta}\right]_{\eta_0} = e^{B\sin(\psi)}\left\{\left[\frac{\partial H}{\partial\eta}\right]_{\eta_0} + A\sin(\psi)H(\eta_0)\right\}, \tag{F.51}$$

where H and its radial derivative are computed from (F.38).

F.4.1 Average normal flux

Multiplying by the dimensionless metric coefficient $F\xi(\eta_0, \psi)$, the integral of (F.50) over $0 \leq \psi \leq 2\pi$ represents the weighted average dimensionless normal flux across the boundary of the ellipse, $\overline{V}_0$. The metric coefficient is necessary in elliptical coordinates, due to the non-constant nature of the metric coefficients which define the coordinate system (Morse and Feshbach, 1953, §1.3); i.e., lines of constant ψ are spaced closer together near $\psi \in [0, \pi, 2\pi]$. The dimensionless average normal flux integral is found using the integral relationships from (F.31) and (F.36), along with the following integral relations

$$\begin{aligned}\int_0^{2\pi} e^{B\sin(\psi)}\sin(\psi)\mathrm{ce}_{2n}(\psi,-q)\,\mathrm{d}\psi &= 2\pi(-1)^n\sum_{r=0}^{\infty}\mathbf{A}_{2r}^{(2n)}\mathrm{I}'_{2r}(B),\\ &= 2\pi p_{2n}\mathrm{Ie}'_{2n}(\eta_0,-q), \qquad \text{(F.52)}\\ \int_0^{2\pi} e^{B\sin(\psi)}\sin(\psi)\mathrm{se}_{2n+1}(\psi,-q)\,\mathrm{d}\psi &= 2\pi(-1)^n\sum_{r=0}^{\infty}\mathbf{A}_{2r+1}^{(2n+1)}\mathrm{I}'_{2r+1}(B),\\ &= 2\pi p_{2n+1}\mathrm{Io}'_{2n+1}(\eta_0,-q), \qquad \text{(F.53)}\end{aligned}$$

which can be found using trigonometric product identities (Abramowitz and Stegun, 1964, eq. 4.3.31 – 4.3.33), the Bessel function derivative recurrence relationship $2\mathrm{I}'_n(z) = \mathrm{I}_{n-1}(z) + \mathrm{I}_{n+1}(z)$, and definitions of the first-kind radial Mathieu functions (see Appendix A). Combining these, the expression for the average normal flux at the boundary of the ellipse is found to be

$$\begin{aligned}\overline{V}_0 \cong -4\pi\sum_{n=0}^{N-1}&\left[p_{2n}\mathrm{Ie}_{2n}(\eta_0,-q)\right]^2\frac{\mathrm{Ke}'_{2n}(\eta_0,-q)}{\mathrm{Ke}_{2n}(\eta_0,-q)}\\ &+\left[p_{2n+1}\mathrm{Io}_{2n+1}(\eta_0,-q)\right]^2\frac{\mathrm{Ko}'_{2n+1}(\eta_0,-q)}{\mathrm{Ko}_{2n+1}(\eta_0,-q)} \qquad \text{(F.54)}\\ &-A\mathrm{Ie}_{2n}(\eta_0,-q)\mathrm{Ie}'_{2n}(z,-q)\\ &-Ap_{2n+1}^2\mathrm{Io}_{2n+1}(\eta_0,-q)\mathrm{Io}'_{2n+1}(z,-q).\end{aligned}$$

The total flowrate is $Q = \overline{V}_0 C$, where C is the dimensionless circumference of the ellipse, given by (F.8) and (F.9).

When $B = 0$ and $\eta_0 = 0$, the average flux due to the strip source (F.54) simplifies to

$$\overline{V}_0(\eta_0 = 0) \cong -4\pi \sum_{n=0}^{N-1} \left[\mathbf{A}_0^{(2n)}\right]^2 \frac{\mathrm{Ke}'_{2n}(0,-q)}{\mathrm{Ke}_{2n}(0,-q)}. \tag{F.55}$$

For the strip, the circumference is $4F$ and $\xi(0,\psi) = |\sin(\psi)|$.

F.4.2 Normal flux for vertical ellipse

Beginning again with (F.48), but instead substituting $\tilde{\Phi} = \tilde{h} - f\cosh(\tilde{\eta})\cos(\tilde{\psi})$, the expression for the dimensionless normal flux to the boundary for the vertical ellipse, analogous to (F.50), becomes

$$\tilde{V}_0 = \frac{1}{F\xi(\eta_0,\tilde{\psi})} \left\{ 2\cos(\tilde{\psi}) - \left[\frac{\partial\tilde{\vartheta}}{\partial\tilde{\eta}}\right]_{\eta_0} \right\}, \tag{F.56}$$

where the derivative in (F.56) is, analogous to (F.51), expanded as

$$\left[\frac{\partial\tilde{\vartheta}}{\partial\tilde{\eta}}\right]_{\eta_0} = e^{A\cos(\tilde{\psi})} \left\{ \left[\frac{\partial\tilde{H}}{\partial\tilde{\eta}}\right]_{\eta_0} + B\cos(\tilde{\psi})\tilde{H}(\eta_0) \right\}. \tag{F.57}$$

Following a similar procedure, the average flux on the vertically-oriented ellipse is

$$\begin{aligned} \widetilde{\overline{V}}_0 \cong & -4\pi \sum_{n=0}^{N-1} \left[s_n \mathrm{Ie}_n(\eta_0,-q)\right]^2 \frac{\mathrm{Ke}'_n(\eta_0,-q)}{\mathrm{Ke}_n(\eta_0,-q)} \\ & -Bs_n^2 \mathrm{Ie}_n(\eta_0,-q)\mathrm{Ie}'_n(w,-q), \end{aligned} \tag{F.58}$$

with the following simplification for a strip source,

$$\widetilde{\overline{V}}_0(\eta_0 = 0) \cong -4\pi \sum_{n=0}^{N} \left[s_n \mathrm{Ie}_n(\eta_0,-q)\right]^2 \frac{\mathrm{Ke}'_n(0,-q)}{\mathrm{Ke}_n(0,-q)}. \tag{F.59}$$

F.5 Results and comparisons

Plots of dimensionless hydraulic head, $\mathbf{\Phi}$, and moisture potential, $\mathbf{\Psi}$, contours for the case of an horizontal elliptical-shaped source are given in Figure F.4 for $e = 0.9$,

similar contours for the degenerate case of a line segment ($e = 1$) are given in Figure F.5, while contours for the nearly-circular case ($e = 0.01$) are presented in Figure F.6. The difference between the circular and elliptical cases when $e = 0.01$ and $A = R = 1.0$ is less than 1.5×10^{-5} units of dimensionless moisture potential. Above the cutout ($Z < -B$), the circular solution is slightly larger, and slightly smaller below.

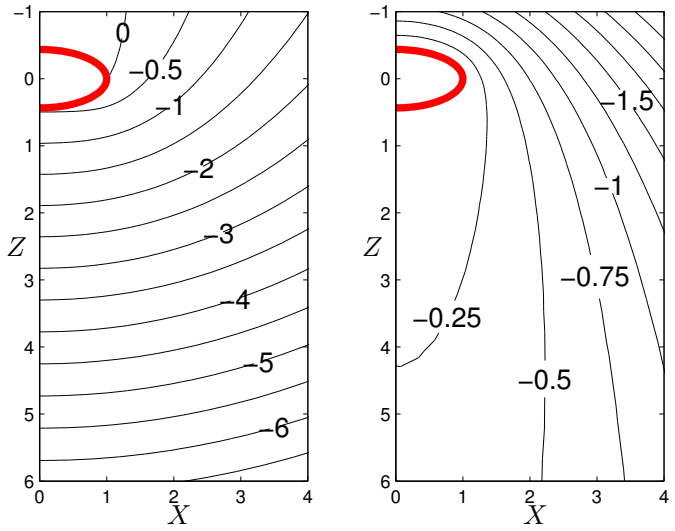

FIGURE F.4. Contours of dimensionless hydraulic head, $\mathbf{\Phi}$, (left) and moisture potential, $\mathbf{\Psi}$, (right) for horizontal ellipse ($A = 1.0$, $e = 0.9$)

For the horizontal strip source (Figure F.5), the specified h boundary condition is a constant (like Tranter (1951) and Kucûk and Brigham (1979)), because the entire element has the same elevation, $z = 0$. For both the elliptical- (Figure F.4) and circular-shaped (Figure F.6) cavities, the variation in $\mathbf{\Phi}$ along the boundary of the source can be seen in the contours.

Analogously, for vertical ellipses, Figures F.7 and F.8 show contours of $\tilde{\mathbf{\Phi}}$ and $\tilde{\mathbf{\Psi}}$ for the elliptical and slit cases respectively. Unlike the horizontal ellipse, the solution for the degenerate slit (the line segment $-1 \leq \tilde{X} \leq 1$) does not simplify the boundary condition.

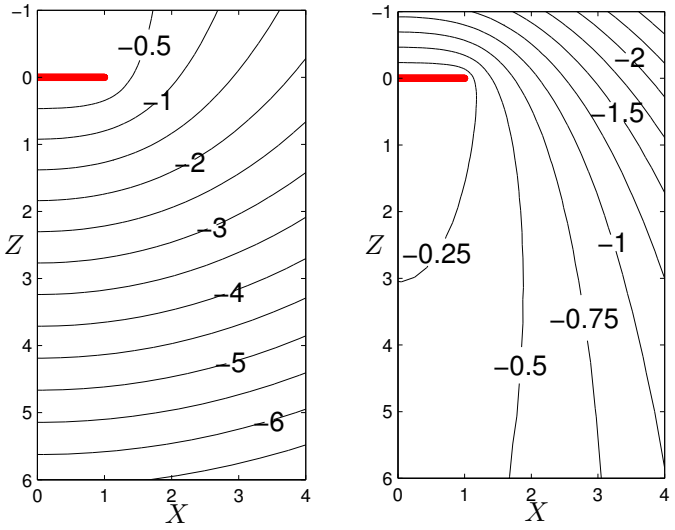

FIGURE F.5. Contours of dimensionless hydraulic head, $\mathbf{\Phi}$, (left) and moisture potential, $\mathbf{\Psi}$, (right) head for horizontal strip ($A = 1.0$, $e = 1.0$)

For plotting contour maps, such as Figures F.4–F.8, a great deal of effort can be saved if the solution is computed on a "separated" elliptical mesh (Orszag, 1986). The angular Mathieu functions are computed for a vector of ψ and the radial Mathieu functions are computed for a vector of η, then they are combined in an outer-product sense. Many plotting programs can accommodate a non-Cartesian mesh, facilitating the use of this strategy. The dimensionless flowrate, $Q = C\overline{V}_0$, is plotted on semi-log and log-log scales in Figure F.9 for ranges of dimensionless semi-width, A, and eccentricity, e. For a given size, there is more water flowing from the circular cavity due to the greater surface area normal to flow. A horizontal ellipse (solid lines) deviates less from the circular solution (highest dash-dot line) than an equivalent vertical ellipse (dotted lines). This can also be seen comparing the location of the -0.25 $\mathbf{\Psi}$ contour in Figures F.4–F.8; the vertical strip is smallest, while the circular cutout is largest. For ellipses where $e \leq 0.5$ the difference between the flowrate for the circular and elliptical cases is small; this is expected, based on their similar shapes (Figure F.2).

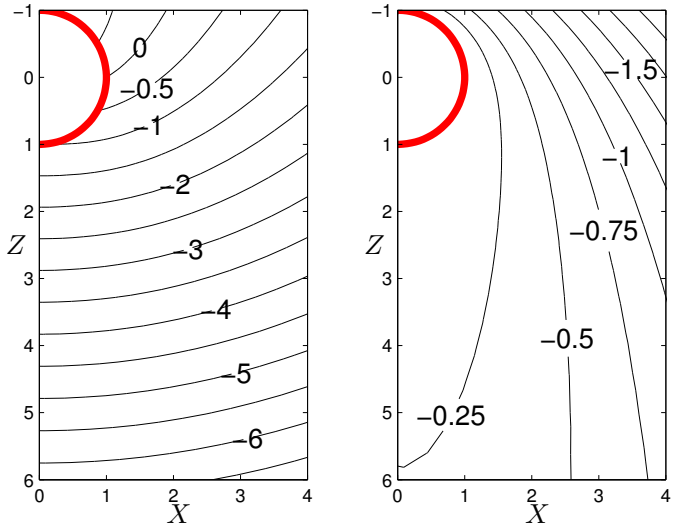

FIGURE F.6. Contours of dimensionless hydraulic head,$\mathbf{\Phi}$, (left) and moisture potential, $\mathbf{\Psi}$, (right) for nearly circular ellipse ($A = 1.0$, $e = 0.01$)

Second-degree rational polynomials were fitted in a least-squares sense; the error in the approximation is illustrated in Figure F.10, with the coefficients of the polynomials given in Table F.2. The polynomial regression is performed in log-log space, where the curves take the form

$$\log_{10}\left[Q(A)\right] = \frac{c_0 + c_1 \log_{10}(A) + c_2 \left[\log_{10}(A)\right]^2}{1 + c_3 \log_{10}(A)}. \tag{F.60}$$

	circular	horizontal ellipse			vertical ellipse		
e	0	1	0.9	0.5	1	0.9	0.5
c_0	1.7054	1.2021	1.3975	1.6344	1.0991	1.3364	1.6199
c_1	2.3638	2.1901	2.2727	2.3411	2.1291	2.3231	2.3636
c_2	-0.2747	-0.8789	-0.5527	-0.3298	-0.7294	-0.3172	-0.2678
c_3	-0.1700	-0.4488	-0.2977	-0.1951	-0.3603	-0.1813	-0.1651

TABLE F.2. Rational polynomial regression coefficients for $Q(A)$ in (F.60)

The distribution of V_0 along the boundary of the ellipse, as a function of ψ, for different values of A, is given in Figures F.11 and F.12 for the horizontal and vertical

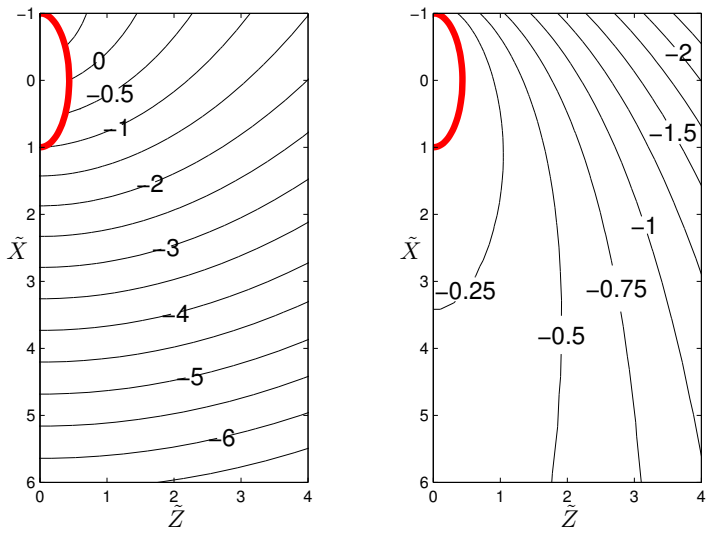

FIGURE F.7. Contours of dimensionless hydraulic head, $\tilde{\mathbf{\Phi}}$, (left) and moisture potential, $\tilde{\mathbf{\Psi}}$, (right) for vertical ellipse ($A = 1.0$, $e = 0.9$)

cases, respectively. For the larger cavity, the variation of flux along the circumference of the cavity is greater, due to the boundary condition that is a function of the vertical coordinate.

F.6 Summary

We derived a 2D solution in elliptic-cylinder coordinates for Richards' equation, illustrating its degeneration to the strip and circular cases. Infinite series expressions for the flowrate and flux from the elliptical cutout were also derived. The solutions are in terms of the eigenfunctions for elliptical coordinates, which themselves can be computed from infinite series of the eigenfunctions for polar coordinates.

Although the solutions developed herein are for free space, they represents strip and furrow geometries more realistically than the widely used point (Philip, 1968) or circular (Philip, 1984) solutions. To incorporate boundary conditions on horizontal surfaces, approximate boundary-matching techniques must be used

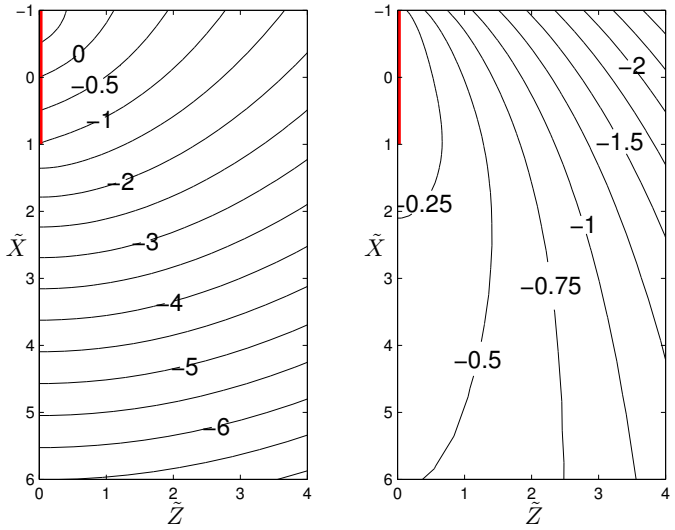

FIGURE F.8. Contours of dimensionless hydraulic head, $\tilde{\mathbf{\Phi}}$, (left) and moisture potential, $\tilde{\mathbf{\Psi}}$, (right) for vertical strip ($A = 1.0$, $e = 1.0$)

(e.g., those used by Bakker and Nieber (2004b)). The general solution (F.25) is in the form of an AEM solution, but the final forms (F.38 or F.44) only have two free parameters beyond the geometry (α and h_0); flexible AEM elements commonly have many more. Analytic solutions usually have fewer free parameters than elements in AEM do, but this is what makes them simpler to use.

A short Matlab script which computes the required Mathieu functions and evaluates the dimensionless potentials and fluxes is available from the corresponding author upon request.

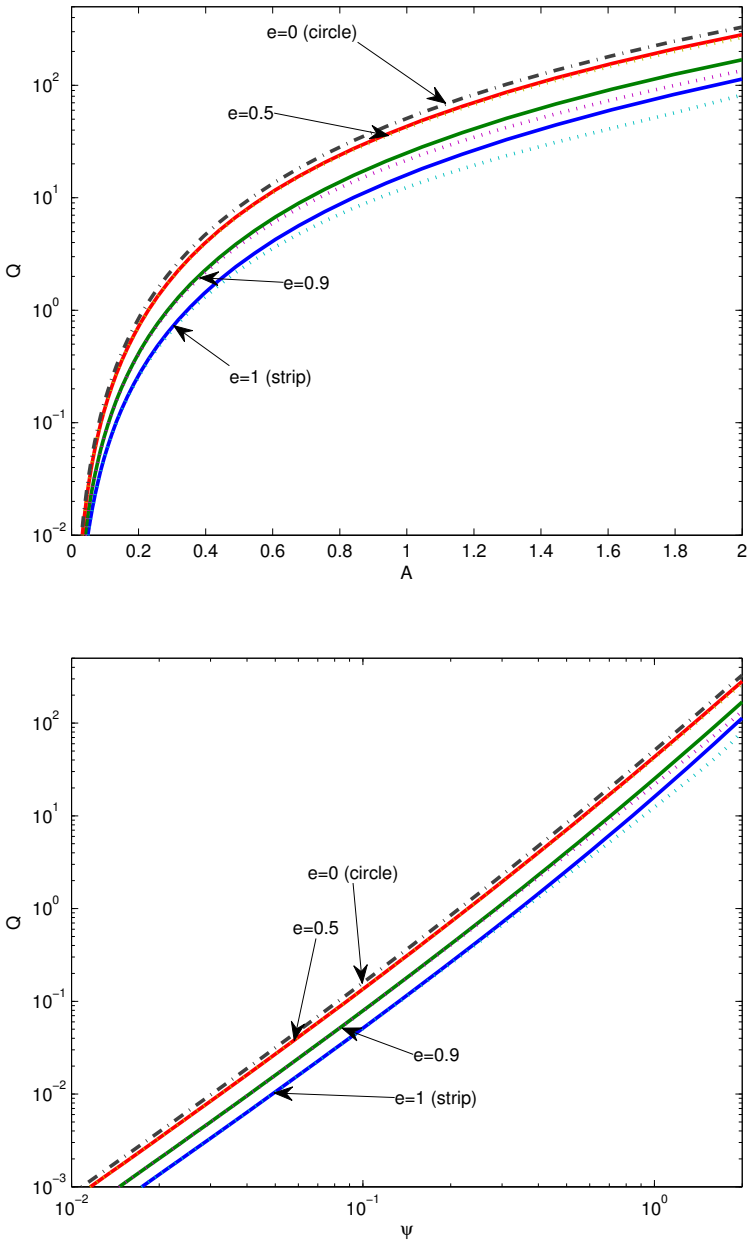

FIGURE F.9. Linear-log and log-log plots of dimensionless flowrate, $Q = C\overline{V}_0$, as a function of size (A) and shape (e) of the horizontal (solid lines) and vertical (dotted lines) cavities. Limiting circular case is dash-dot line.

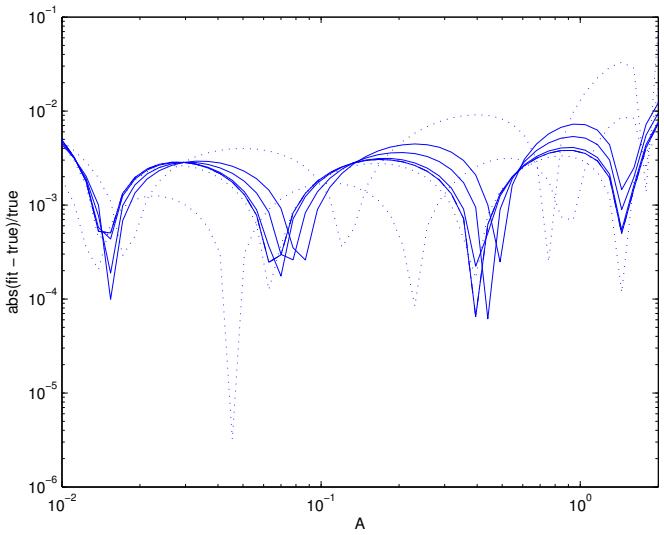

FIGURE F.10. Relative error in least-squares rational polynomial regression for dimensionless flowrate, Q, for the horizontal (solid lines) or vertical (dotted lines) elliptical and circular (dash-dot line) cavities.

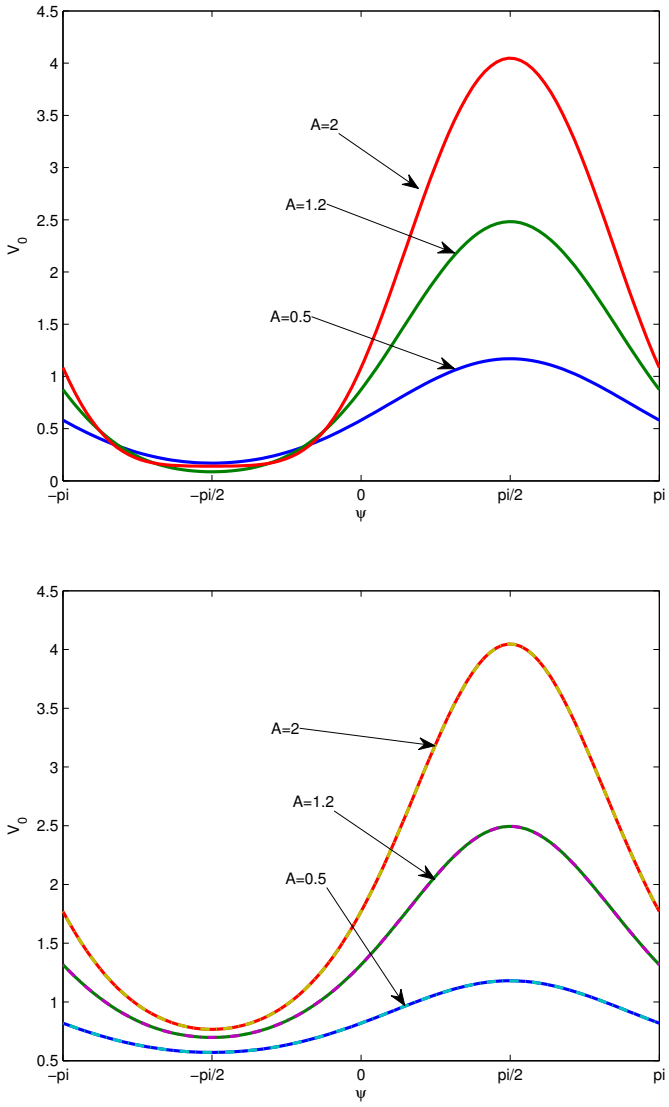

FIGURE F.11. Distribution of dimensionless normal flux, V_0, as a function of angle, ψ, for horizontal strip (left, $e = 1$) and horizontal near circular (right, $e = 0.01$) cases (true circular solution shown as dash-dot line, nearly coincident with elliptical solution)

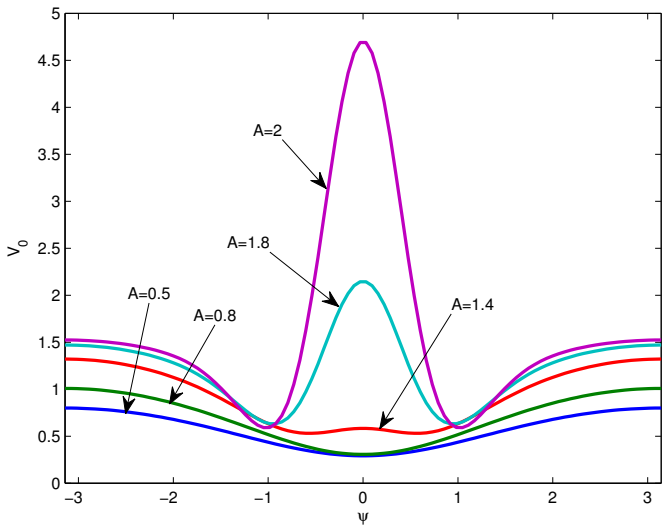

FIGURE F.12. Distribution of dimensionless normal flux, V_0, as a function of angle, ψ, for vertical strip ($e = 1$)

F.7 Appendix F1

The modified angular Mathieu functions are defined as infinite series of trigonometric functions (see McLachlan (1947, §2.18)),

$$\mathrm{ce}_{2n}(\psi,-q) = (-1)^n \sum_{r=0}^{\infty}(-1)^r \mathbf{A}_{2r}^{(2n)} \cos[2r\psi], \tag{F.61}$$

$$\mathrm{ce}_{2n+1}(\psi,-q) = (-1)^n \sum_{r=0}^{\infty}(-1)^r \mathbf{B}_{2r+1}^{(2n+1)} \cos[(2r+1)\psi], \tag{F.62}$$

$$\mathrm{se}_{2n+1}(\psi,-q) = (-1)^n \sum_{r=0}^{\infty}(-1)^r \mathbf{A}_{2r+1}^{(2n+1)} \sin[(2r+1)\psi], \tag{F.63}$$

$$\mathrm{se}_{2n+2}(\psi,-q) = (-1)^n \sum_{r=0}^{\infty}(-1)^r \mathbf{B}_{2r+2}^{(2n+2)} \sin[(2r+2)\psi], \tag{F.64}$$

where $\mathbf{A}_r^{(n)}$ and $\mathbf{B}_r^{(n)}$ are matrices of the Mathieu coefficients (eigenvectors for each eigenvalue λ_n), they are the generalized Fourier series coefficients representing the Mathieu functions; see Appendix B. The integer n is related to the number of zeros the function has on the $0 \leq \psi < 2\pi$ interval. The even-ordered functions have period π, while the odd-order functions have period 2π. The symmetry of these functions with respect to the major and minor axes of the ellipse are listed in Table F.3, from McLachlan (1947, §16.12).

	major	minor
ce_{2n}	even	even
ce_{2n+1}	even	odd
se_{2n+1}	odd	even
se_{2n+2}	odd	odd

TABLE F.3. Symmetry of angular Mathieu functions about the axes of an ellipse.

The radial modified Mathieu functions of the second kind are used as solutions to the radial Mathieu equation (F.21) and are only evaluated in ratios of functions of the same kind and order, allowing them to be simplified from their definitions

in terms of Bessel function product series (McLachlan, 1947, §13.30),

$$\mathrm{Ke}_{2n}(\eta,-q)=D_n\sum_{r=0}^{\infty}\mathbf{A}_{2r}^{(2n)}\mathrm{I}_r(v_1)\mathrm{K}_r(v_2), \tag{F.65}$$

$$\mathrm{Ke}_{2n+1}(\eta,-q)=D_n\sum_{r=0}^{\infty}\mathbf{B}_{2r+1}^{(2n+1)}\left[\mathrm{I}_r(v_1)\mathrm{K}_{r+1}(v_2)-\mathrm{I}_{r+1}(v_1)\mathrm{K}_r(v_2)\right], \tag{F.66}$$

$$\mathrm{Ko}_{2n+1}(\eta,-q)=D_n\sum_{r=0}^{\infty}\mathbf{A}_{2r+1}^{(2n+1)}\left[\mathrm{I}_r(v_1)\mathrm{K}_{r+1}(v_2)+\mathrm{I}_{r+1}(v_1)\mathrm{K}_r(v_2)\right], \tag{F.67}$$

where D_n is a normalization constant (not all the same) that is only a function of the order, $v_1=\sqrt{q}e^{-\eta}$, $v_2=\sqrt{q}e^{\eta}$, and the eigenvectors $\mathbf{A}_r^{(n)}$ and $\mathbf{B}_r^{(n)}$ are the same used in the angular Mathieu function definitions. The normalization constants can be found in McLachlan (1947, p.368).

The integral expressions evaluate to radial Mathieu functions of the first kind, when they are given in one of their several equivalent solutions in terms of Bessel function series (McLachlan, 1947, §8.30)

$$\mathrm{Ie}_{2n}(\omega,-q)=(-1)^n\frac{\mathrm{ce}_{2n}\left(\frac{\pi}{2};q\right)}{\mathbf{A}_0^{(2n)}}\sum_{r=0}^{\infty}\mathbf{A}_{2r}^{(2n)}\mathrm{I}_{2r}\left[2\sqrt{q}\sinh(\omega)\right] \tag{F.68}$$

$$\mathrm{Ie}_{2n}(\omega,-q)=(-1)^n\frac{\mathrm{ce}_{2n}(0,q)}{\mathbf{A}_0^{(2n)}}\sum_{r=0}^{\infty}(-1)^r\mathbf{A}_{2r}^{(2n)}\mathrm{I}_{2r}\left[2\sqrt{q}\cosh(\omega)\right] \tag{F.69}$$

$$\mathrm{Ie}_{2n+1}(\omega,-q)=(-1)^n\frac{\mathrm{se}'_{2n+1}(0,q)}{\sqrt{q}\mathbf{B}_1^{(2n+1)}}\sum_{r=0}^{\infty}(-1)^r\mathbf{B}_{2r+1}^{(2n+1)}\mathrm{I}_{2r+1}\left[2\sqrt{q}\cosh(\omega)\right] \tag{F.70}$$

$$\mathrm{Io}_{2n+1}(\omega,-q)=(-1)^{n+1}\frac{\mathrm{ce}'_{2n+1}\left(\frac{\pi}{2};q\right)}{\sqrt{q}\mathbf{A}_1^{(2n+1)}}\sum_{r=0}^{\infty}\mathbf{A}_{2r+1}^{(2n+1)}\mathrm{I}_{2r+1}\left[2\sqrt{q}\sinh(\omega)\right] \tag{F.71}$$

In general, radial Mathieu functions can be expressed in terms of infinite sums of hyperbolic trigonometric functions, Bessel functions with hyperbolic trigonometric arguments (F.68–F.71), or series of products of Bessel functions (F.65–F.67). The series of Bessel function products have the widest and fastest convergence (Gutiérrez Vega et al., 2003), and are therefore the most utilized; in the current case the alternate definitions are only used for simplifying the infinite sums of Bessel functions.

F.8 Appendix F2

Alhargan (2000b) has published C++ routines for evaluating Mathieu functions based on the more efficient but less widely applicable continued fraction expansion method. These routines utilize a different normalization scheme than (F.28) and are only valid for small Mathieu parameter ($q \leq 4n$). To evaluate (F.38) or (F.44) it is straightforward to use the more general matrix formulation with available matrix solution software (Chaos-Cador and Ley-Koo, 2002), which is valid for any q, even negative or complex values.

The matrices for which the eigenvalues are computed are derived from the 3-term recurrence relationship obtained by substituting the Mathieu function definitions (F.61–F.64) into the angular Mathieu equation (F.22); the details of the process can be found in Green and Michaelson (1965) or Delft Numerical Analysis Group (1973). The main and off-diagonals of the infinite matrices, from which the eigenvalues and eigenvectors are computed, are

$$\mathrm{Aev} = \begin{bmatrix} 0 & 4 & 16 & \dots & (2r)^2 & \dots \\ \sqrt{2}q & q & q & \dots & q & \dots \end{bmatrix}, \tag{F.72}$$

$$\mathrm{Aod} = \begin{bmatrix} 1-q & 9 & 25 & \dots & (2r+1)^2 & \dots \\ q & q & q & \dots & q & \dots \end{bmatrix}, \tag{F.73}$$

$$\mathrm{Bod} = \begin{bmatrix} 1+q & 9 & 25 & \dots & (2r+1)^2 & \dots \\ q & q & q & \dots & q & \dots \end{bmatrix}, \tag{F.74}$$

where $\mathbf{A}_{2r}^{(2n)}$ is the matrix of eigenvectors from the symmetric tri-diagonal matrix composed of the diagonal (first row) and the off-diagonals (second row) of Aev. Similarly, Aod leads to $\mathbf{A}_{2r+1}^{(2n+1)}$ and Bod leads to $\mathbf{B}_{2r+1}^{(2n+1)}$; $\mathbf{B}_{2r+2}^{(2n+2)}$ are not needed for the current problem.

The matrices (F.72–F.74) and the eigenvector matrices derived that are from them $\mathbf{A}_r^{(n)}, \mathbf{B}_r^{(n)}$ are infinite matrices that must be truncated; for most problems 20 coefficient delivers adequate accuracy. If $N = 20$, then $N + k \leq 30$ is also sufficient. Ellipses of very long aspect ratio (large F, small η_0) may require more terms,

but the calculations remain trivial on a desktop computer. For the application considered here, when $A \leq 2$, the expansion of the boundary condition in angular Mathieu functions is very accurate.

Since eigenvectors only define a direction, they must be normalized to have a length consistent with convention. Two normalization schemes are popular, the one used here is attributed to McLachlan (1947, §2.21). It consists of specifying the norms to be $1/\pi$ (simplifying the expressions for β_{2n} and γ_{2n+1}), while the other normalization, attributed to Morse and Feshbach (1953, p.1409) sets the value or slope of the angular functions at $\psi \in [0, \pi/2]$ to unity. This alternate normalization (used by Alhargan (2000b)) instead simplifies the expression for the normalization constant in the radial Mathieu functions, e.g., the coefficients outside the summation in (F.68–(F.71)).

If LAPACK routines (or equivalently Matlab calls to `eig()`) are used to compute the eigenvector matrices, only the first eigenvector of $\mathbf{A}_{2r}^{(2n)}$ must be re-scaled. The solution for $\mathrm{ce}_0(\psi, -q)$ is normalized so it degenerates to $\cos(0)$ as $q \to 0$. This requires the normalization be

$$2\left[\mathbf{A}_0^{(0)}\right]^2 + \sum_{r=1}^{\infty}\left[\mathbf{A}_r^{(0)}\right]^2 = 1, \tag{F.75}$$

where the zero-order term is included twice.

REFERENCES

J. Abate and P. P. Valkò. Multi-precision Laplace transform inversion. *International Journal for Numerical Methods in Engineering*, 60:979–993, 2003.

M. Abramowitz and I. A. Stegun, editors. *Handbook of Mathematical Functions with Formulas, Graphs and Mathematical Tables*. Number 55 in Applied Mathematics Series. National Bureau of Standards, 1964.

F. A. Alhargan. Algorithms for the computation of all Mathieu functions of integer orders. *ACM Transactions on Mathematical Software*, 26(3):390–407, 2000a.

F. A. Alhargan. Algorithm 804: subroutines for the computation of Mathieu functions of integer order. *ACM Transactions on Mathematical Software*, 26(3):408–414, 2000b.

E. Anderson, Z. Bai, J. Dongarra, A. Greenbaum, A. McKenney, J. D. Croz, S. Hammarling, J. Demmel, C. Bischof, and D. Sorensen. LAPACK: a portable linear algebra library for high-performance computers. In *Supercomputing '90: Proceedings of the 1990 ACM/IEEE Conference on Supercomputing*, pages 2–11. IEEE Computer Society, 1990.

L. C. Andrews. *Special Functions of Mathematics for Engineers*. SPIE, second edition, 1998.

H. Antia. *Numerical Methods for Scientists and Engineers*. Birkhäuser-Verlag, second edition, 2002.

N. Aquino, E. Castano, and E. Ley-Koo. Spheroidal functions revisited: matrix evaluation and generating functions. *Revista Mexicana de Fisica*, 48(3):277–282, 2002.

F. M. Arscott. *Periodic Differential Equations*. Macmillan, 1964.

F. M. Arscott. *Ordinary and Partial Differential Equations*, volume 846 of *Lecture Notes in Mathematics*, chapter The land beyond Bessel: A survey of higher special functions. Springer, 1981.

F. M. Arscott and A. Darai. Curvilinear co-ordinate systems in which the Helmholtz equation separates. *IMA Journal of Applied Mathematics*, 27:33–70, 1981.

D. H. Bailey. A Fortran-90 based multiprecision system. *ACM Transactions on Mathematical Software*, 21(4):379–387, 1995.

M. Bakker. Modeling groundwater flow to elliptical lakes and through multi-aquifer elliptical inhomogeneities. *Advances in Water Resources*, 27:497–506, 2004a.

M. Bakker. Modeling transient flow with wiggly analytic elements. In *Computational Methods in Water Resources*, volume XV, 2004b.

M. Bakker. Transient analytic elements for periodic Dupuit-Forchheimer flow. *Advances in Water Resources*, 27(1):3–12, 2004c.

M. Bakker. An analytic element approach for modeling polygonal inhomogeneities in multi-aquifer systems. *Advances in Water Resources*, 29(10):1546–1555, 2006.

M. Bakker. Transient Dupuit interface flow with partially penetrating features. *Water Resources Research*, 34(11):2911–2918, 1998.

M. Bakker and J. L. Nieber. Analytic element modeling of cylindrical drains and cylindrical inhomogeneities in steady two-dimensional unsaturated flow. *Vadose Zone Journal*, 3:1038–1049, 2004a.

M. Bakker and J. L. Nieber. Two-dimensional steady unsaturated flow through embedded elliptical layers. *Water Resources Research*, 40:1–12, 2004b.

M. Bakker and O. D. L. Strack. Analytic elements for multiaquifer flow. *Journal of Hydrology*, 271:119–129, 2003.

R. Barnes and I. Janković. Two-dimensional flow through large numbers of circular inhomogeneities. *Journal of Hydrology*, 226:204–210, 1999.

W. Barrash, T. Clemo, J. J. Fox, and T. C. Johnson. Field, laboratory, and modeling investigation of the skin effect at wells with slotted casing, Boise Hydrogeophysical Research Site. *Journal of Hydrology*, 326:181–198, 2006.

J. Bear. *Dynamics of Fluids in Porous Media*. Dover, 1988.

J. Bear and G. Dagan. The relationship between solutions of flow problems in isotropic and anisotropic soils. *Journal of Hydrology*, 3:88–96, 1965.

J. Bear and A. Verruijt. *Modeling Groundwater Flow and Pollution*. D. Reidel, 1987.

J. Bear and D. Zaslavsky. *Physical principles of water percolation and seepage*. UNESCO, 1968.

A. Ben-Menahem and S. J. Singh. *Seismic Waves and Sources*. Dover, second edition, 2000.

C. M. Bender and S. A. Orszag. *Advanced Mathematical Methods for Scientists and Engineers: Asymptotic Methods and Perturbation Theory*. Springer, 1999.

J. H. Black and K. L. Kipp. Determination of hydrogeological parameters using sinusoidal pressure tests: a theoretical appraisal. *Water Resources Research*, 17(3): 686–692, 1981.

L. S. Blackford, J. Demmel, J. Dongarra, I. Duff, S. Hammarling, G. Henry, M. Heroux, L. Kaufman, A. Lumsdaine, A. Petitet, R. Pozo, K. Remington, and R. C. Whaley. An updated set of basic linear algebra subprograms (BLAS). *ACM Transactions on Mathematical Software*, 28(2):135–151, 2002.

G. Blanch and D. S. Clemm. Mathieu's equation for complex parameters: tables of characteristic values. Technical report, Aerospace Research Laboratories, US Air Force, 1969.

N. S. Boulton. The drawdown of the water-table under non-steady conditions near a pumped well in an unconfined formation. *Proceedings of the Institution of Civil Engineers*, 3(2):564–579, 1954.

J. P. Boyd. *Chebyshev and Fourier Spectral Methods*. Dover, second edition, 2000.

C. A. Brebbia, J. C. F. Telles, and L. C. Wrobel. *Boundary Element Techniques*. Springer-Verlag, 1984.

M. Brio, P. O. Kano, and J. V. Moloney. Application of Weeks method for the numerical inversion of the Laplace transform to the matrix exponential. *Communications in Mathematical Science*, 3(3):335–372, 2005.

G. A. Bruggeman. *Analytical Solutions of Geohydrological Problems*. Number 46 in Developments in Water Science. Elsevier, 1999.

C. Canuto, M. Y. Hussaini, A. Quarteroni, and T. A. Zang. *Spectral Methods: Fundamentals in Single Domains*. Springer, 2006.

H. S. Carslaw and J. C. Jaeger. *Conduction of Heat in Solids*. Oxford, second edition, 1959.

L. Chaos-Cador and E. Ley-Koo. Mathieu functions revisited: matrix evaluation and generating functions. *Revista Mexicana de Física*, 48(1):67–75, 2002.

P.-C. Chou and N. J. Pagano. *Elasticity*. Dover, 1992.

L. J. Chu and J. A. Stratton. Elliptical and spheroidal wave functions. *Journal of Mathematics and Physics*, 20(3):259–309, 1941.

R. V. Churchill. *Operational Mathematics*. McGraw-Hill, third edition, 1972.

A. M. Cohen. *Numerical Methods for Laplace Transform Inversion*. Springer, 2007.

H. H. Cooper, J. D. Bredehoeft, and I. S. Papadopulos. Response of a finite-diameter well to an instantaneous charge of water. *Water Resources Research*, 3(1):263–269, 1967.

R. Courant and D. Hilbert. *Methods of Mathematical Physics*, volume 1 and 2. Interscience Publishers, 1962.

J. Crank. *The Mathematics of Diffusion*. Oxford, second edition, 1975.

K. S. Crump. Numerical inversion of Laplace transforms using a Fourier series approximation. *Journal for the Association for Computing Machinery*, 23(1):89–96, 1976.

G. Dagan, A. Fiori, and I. Janković. Flow and transport in highly heterogeneous formations: 1. conceptual framework and validity of first-order approximations. *Water Resources Research*, 39:1268–1280, 2003.

A. Davies and D. Crann. Parallel Laplace transform methods for boundary element solutions to diffusion-type problems. *Electronic Journal of Boundary Elements*, BETEQ 2001(2):231–238, 2002.

B. Davies. *Integral Transforms and their Application*. Springer, third edition, 2002.

B. Davies and B. Martin. Numerical inversion of the Laplace transform: a survey and comparison of methods. *Journal of Computational Physics*, 33:1–32, 1979.

G. J. de Glee. *Over grondwaterstroomingen bij wateronttrekking door middle van putten*. PhD thesis, Delft Technische Hogeschool, 1930.

F. R. de Hoog, J. H. Knight, and A. N. Stokes. An improved method for numerical inversion of Laplace transforms. *SIAM Journal of Statistical Computing*, 3(3):357–366, 1982.

W. J. de Lange. Development of an analytic element ground water model of the Netherlands. *Ground Water*, 44(1):111–115, 2006.

Delft Numerical Analysis Group. On the computation of Mathieu functions. *Journal of Engineering Mathematics*, 7(1):39–61, 1973.

J. Doherty. *PEST User's Manual*. Watermark Numerical Computing, 5 edition, 2007.

H. Dubner and J. Abate. Numerical inversion of Laplace transforms by relating them to the finite Fourier cosine series. *Journal of the Association for Computer Machinery*, 15(1):115–123, 1968.

R. J. Duffin. Yukawan potential theory. *Journal of Mathematical Analysis and Application*, 35:105–130, 1971.

D. G. Duffy. On the numerical inversion of Laplace transforms: comparison of three new methods on characteristic problems from applications. *ACM Transactions on Mathematical Software*, 19(3):333–359, 1993.

F. Durbin. Numerical inversion of Laplace transforms: an efficient improvement to Dubner and Abate's method. *The Computer Journal*, 17(4):371–376, 1973.

P. Favati, G. Lotti, and F. Romani. Algorithm 691; improving QUADPACK automatic integration routines. *ACM Transactions on Mathematical Software*, 17(2), 1991.

B. A. Finlayson. *The Method of Weighted Residuals and Variational Principles*. Academic, 1972.

A. Fiori, I. Janković, and G. Dagan. Flow and transport in highly heterogeneous formations: 2. semianalytic results for isotropic media. *Water Resources Research*, 39:1269–1278, 2003.

C. R. Fitts. Simple analytic functions for modeling three-dimensional flow in layered aquifers. *Water Resources Research*, 25(5):943–948, 1989.

C. R. Fitts. Modeling three-dimensional flow about ellipsoidal inhomogeneities with application to flow to a gravel-packed well and flow through lens-shaped inhomogeneities. *Water Resources Research*, 27(5):815–824, 1991.

R. Freund and N. Nachtigal. QMR: a quasi-minimal residual method for non-Hermitian linear systems. *Numerische Mathematik*, 60(1):315–339, 1991.

FSF. *Gnu Compiler Collection: GCC*. http://gcc.gnu.org, 4.3.0 edition, 2008.

A. Furman and S. P. Neuman. Laplace-transform analytic element solution of transient flow in porous media. *Advances in Water Resources*, 26:1229–1237, 2003.

A. Furman and S. P. Neuman. Laplace transform analytic element method for transient flow problems. In *Computational Methods in Water Resources*, volume XV, 2004.

A. Furman and A. W. Warrick. Unsaturated flow through spherical inclusions with contrasting sorptive numbers. *Vasose Zone Journal*, 4:255–263, 2005.

A. Furman, A. W. Warrick, and T. P. A. Ferré. Electric potential distributions in a heterogeneous subsurface in response to applied current: solution for circular inhomogeneities. *Vadose Zone Journal*, 1:273–280, 2002.

W. R. Gardner. Some steady state solutions of unsaturated moisture flow equations with application to evaporation from a water table. *Soil Science*, 85:244–249, 1958.

J. W. Gibbs. Fourier's series. *Nature*, 59(522):200, 1898.

N. K. Girinskii. Generalization of some solutions for wells to more complicated natural conditions. *Doklady akademii nauk SSSR*, 3:54–54, 1946.

S. Goldstein. Mathieu functions. *Transactions of the Cambridge Philosophical Society*, 23(11):303–336, 1927.

G. H. Golub and C. F. van Loan. *Matrix Computations*. Johns Hopkins, third edition, 1996.

K. F. Graff. *Wave Motion in Elastic Solids*. Dover, 1991.

D. J. Green and S. Michaelson. Series solution of certain Sturm-Liouville eigenvalue problems. *The Computer Journal*, 7:322–336, 1965.

K. E. Gustafson. *Partial Differential Equations and Hilbert Space Methods*. Dover, third edition, 1999.

J. C. Gutiérrez Vega, R. M. Rodriguez Dagnino, A. M. Meneses Nava, and S. Chávez Cerda. Mathieu functions, a visual approach. *American Journal of Physics*, 71(3):233–242, 2003.

H. M. Haitjema. An analytic element model for transient axi-symmetric interface flow. *Journal of Hydrology*, 129:215–244, 1991.

H. M. Haitjema. *Analytic Element Modeling of Groundwater Flow*. Academic, 1995.

H. M. Haitjema and V. A. Kelson. Using the stream function for flow governed by Poisson's equation. *Journal of Hydrology*, 187:367–386, 1996.

H. M. Haitjema and O. D. L. Strack. An initial study of thermal energy storage in unconfined aquifers. Technical Report PNL-5818 UC-94e, Pacific Northwest Laboratories, 1985.

M. S. Hantush. Modification of the theory of leaky aquifers. *Journal of Geophysical Research*, 65(11):3713–3725, 1960.

M. S. Hantush. Drawdown around wells of variable discharge. *Journal of Geophysical Research*, 69(20):4221–4235, 1964a.

M. S. Hantush. *Advances in Hydroscience*, chapter Hydraulics of Wells. Academic, 1964b.

T. J. Heimovaara, J. A. Huisman, J. A. Vrugt, and W. Bouten. Obtaining the spatial distribution of water content along a TDR probe using the SCEM-UA Bayesian inverse modeling scheme. *Vadose Zone Journal*, 3(4):1128–1145, 2004.

C. J. Hemker and C. Maas. Unsteady flow to wells in layered and fissured aquifer systems. *Journal of Hydrology*, 90:231–249, 1987.

R. Hempel. The MPI standard for message passing. In *HPCN Europe 1994: Proceedings of the International Conference and Exhibition on High-Performance Computing and Networking*, volume II, pages 247–252, 1994.

I. Herrera, A. Minzoni, and E. Z. Flores. Theory of flow in unconfined aquifers by integrodifferential equations. *Water Resources Research*, 14(2):291–297, 1978.

E. W. Hobson. *The Theory of Spherical and Ellipsoidal Harmonics*. University, 1931.

H. H. H. Homeier. Some applications of nonlinear convergence accelerators. *International Journal of Quantum Chemistry*, 45:545–562, 1993.

A. S. Householder. *The Theory of Matrices in Numerical Analysis*. Dover, 1975.

T. J. R. Hughes. *The Finite Element Method*. Dover, 2000.

J. A. Huisman, W. Bouten, J. A. Vrugt, and P. A. Ferré. Accuracy of frequency domain analysis scenarios for the determination of complex dielectric permittivity. *Water Resources Research*, 40(2):W02401, 2004.

R. J. Hunt, M. P. Anderson, and V. A. Kelson. Improving a complex finite-difference groundwater flow model through the use of an analytic element screening model. *Ground Water*, 36:1011–1017, 1998.

C. Hunter and B. Guerrieri. The eigenvalues of Mathieu's equation and their branch points. *Studies in Applied Mathematics*, 64:113–141, 1981.

M. J. Hvorslev. Time lag and soil permeability in ground-water observations. Technical report, Army Engineer Waterways Experiment Station Vicksburg, MS, 1951.

E. L. Ince. *Ordinary Differential Equations*. Dover, 1956.

E. Isaacson and H. B. Keller. *Analysis of Numerical Methods*. Wiley, 1966.

J. Istok. *Groundwater Modeling by the Finite Element Method*. Number 13 in Water Resources Monographs. American Geophysical Union, 1989.

C. E. Jacob. On the flow of water in an artesian aquifer. *EOS Transactions of the American Geophysical Union*, 21:574–586, 1940.

C. E. Jacob. Drawdown test to determine effective radius of artesian well. *Transactions, American Society of Civil Engineers*, 112:1047–1064, 1947.

I. Janković. *High-Order Analytic Elements in Modeling Groundwater Flow*. PhD thesis, University of Minnesota, 1997.

I. Janković and R. Barnes. Three-dimensional flow through large numbers of spheroidal inhomogeneities. *Journal of Hydrology*, 226:224–233, 1999.

I. Janković, A. Fiori, and G. Dagan. Flow and transport in highly heterogeneous formations: 3. numerical simulations and comparison with theoretical results. *Water Resources Research*, 39:1270–1283, 2003.

H. Jeffreys and B. S. Jeffreys. *Methods of Mathematical Physics*. Cambridge, third edition, 1972.

O. D. Kellogg. *Foundations of Potential Theory*. Dover, 1954.

V. A. Kelson, R. J. Hunt, and H. M. Haitjema. Improving a regional model using reduced complexity and parameter estimation. *Ground Water*, 40(2):132–143, 2002.

F. Kleinermann, N. J. Avis, and F. A. Alhargan. Analytical solution to the three-dimensional electrical forward problem for an elliptical cylinder. *Physiological Measurement*, 23:141–147, 2002.

A. Klute. A numerical method for solving the flow equation for water in unsaturated materials. *Soil Science*, 73:105–116, 1952.

S. R. Kraemer. Analytic element ground water modeling as a research program (1980 to 2006). *Ground Water*, 45(4):402–408, 2007.

S. R. Kraemer, H. M. Haitjema, and V. A. Kelson. *Working with WhAEM2000 capture zone delineation for a city wellfield in a valley fill glacial outwash aquifer supporting wellhead protection*. US Environmental Protection Agency, 2007.

F. Kucûk and W. E. Brigham. Transient flow in elliptical systems. *Society of Petroleum Engineers Journal*, 267:401–410, 1979.

K. L. Kuhlman and S. P. Neuman. Recent advances in Laplace transform analytic element method theory and application to transient groundwater flow. In *Computational Methods in Water Resources*, volume XVI, 2006.

C. Lanczos. *Discourse on Fourier Series*. Oliver & Boyd, 1966.

C. Lanczos. *Applied Analysis*. Prentice-Hall, 1956.

C. L. Lawson and R. J. Hanson. *Solving Least Squares Problems*. SIAM, 1974.

T.-C. Lee. *Applied Mathematics in Hydrogeology*. CRC, 1999.

T.-C. Lee and T. L. Henyey. Heat flow refraction across dissimilar media. *Geophysical Journal International*, 39(2):319–333, 1974.

W. R. Lepage. *Complex Variables and the Laplace Transform for Engineers*. Dover, 1980.

L.-W. Li, X.-K. Kang, and M.-S. Leong. *Spheroidal Wave Functions in Electromagnetic Theory*. Wiley, 2002.

Y. Li and S. P. Neuman. Flow to a well in a five-layer system with application to the Oxnard Basin. *Ground Water*, 45(6):672–682, 2007.

J. A. Liggett and P. L.-F. Liu. *The Boundary Integral Equation Method for Porous Media Flow*. George Allen & Unwin, 1983.

LLNL. OpenMP tutorial. https://computing.llnl.gov/tutorials/openMP/, March 2008.

T. Löfqvist and G. Rehbinder. Transient flow towards a well in an aquifer including the effect of fluid inertia. *Applied Scientific Research*, 51(3):611–623, 1993.

D. O. Lomen and A. W. Warrick. Linearized moisture flow with loss at the soil surface. *Soil Science Society of America Journal*, 42:396–400, 1978.

C. Maas. The use of matrix differential calculus in problems of multiple-aquifer flow. *Journal of Hydrology*, 88:43–67, 1986.

C. Maas. Groundwater flow to a well in a layered porous medium 2. nonsteady multiple-aquifer flow. *Water Resources Research*, 23(8):1683–1688, 1987.

C. R. MacCluer. *Boundary Value Problems and Fourier Expansions*. Dover, 2004.

R. Maertens and R. Rousseau. A new formula approach for the circumference of an ellipse. *Wiskunde & Onderwijs*, 26:249–258, 2000.

B. Malama, K. L. Kuhlman, and W. Barrash. Semi-analytical solution for flow in leaky unconfined aquifer-aquitard systems. *Journal of Hydrology*, 346(1–2):59–68, 2007.

B. Malama, K. L. Kuhlman, and W. Barrash. Semi-analytical solution for flow in a leaky unconfined aquifer toward a partially penetrating pumping well. *Journal of Hydrology*, 356(1–2):234–244, 2008.

MathWorks. *MATLAB*, 7.5 edition, 2007.

M. G. McDonald and A. W. Harbaugh. A modular three-dimensional finite-difference ground-water flow model. Techniques of Water-Resources Investigations Book 6, Chapter 1A, USGS, 1988.

N. W. McLachlan. *Theory and Application of Mathieu Functions*. Oxford, 1947.

N. W. McLachlan. *Complex Variable Theory and Transform Calculus with Technical Applications*. Cambridge, second edition, 1953.

N. W. McLachlan. *Bessel Functions for Engineers*. Oxford, second edition, 1955.

W. Menke. *Geophysical Data Analysis: Discrete Inverse Theory*. Academic, 1984.

R. J. Millington. Gas diffusion in porous media. *Science*, 130(3367):100–102, 1959.

L. M. Milne-Thompson. *Theoretical Hydrodynamics*. Dover, 1996.

A. F. Moench. Double-porosity models for a fissured groundwater reservoir with fracture skin. *Water Resources Research*, 20(7):831–846, 1984.

A. F. Moench. Transient flow to a large-diameter well in an aquifer with storative semiconfining layers. *Water Resources Research*, 21(8):1121–1131, 1985.

A. F. Moench. Flow to a well of finite diameter in a homogeneous, anisotropic water table aquifer. *Water Resources Research*, 33(6):1397–1407, 1997.

A. F. Moench and A. Ogata. A numerical inversion of the Laplace transform solution to radial dispersion in a porous medium. *Water Resources Research*, 17(1): 250–252, 1981.

A. F. Moench and A. Ogata. Analysis of constant discharge wells by numerical inversion of Laplace transform solutions. In *Groundwater Hydraulics*, Water Resources Monograph, pages 146–170. American Geophysical Union, 1984.

P. Moon and D. E. Spencer. *Field Theory for Engineers*. D. Van Nostrand, 1961a.

P. Moon and D. E. Spencer. *Field Theory Handbook: Including Coordinate Systems Differential Equations and their Solutions*. Springer-Verlag, 1961b.

E. Morales-Casique and S. P. Neuman. Laplace-transform finite element solution of nonlocal and localized stochastic moment equations of transport. *Communications in Computational Physics*, in review, 2008.

P. M. Morse and H. Feshbach. *Methods of Theoretical Physics*, volume 1 and 2. McGraw-Hill, 1953.

P. M. Morse and K. U. Ingard. *Theoretical Accoustics*. McGraw-Hill, 1968.

T. Needham. *Visual Complex Analysis*. Oxford, 1997.

S. P. Neuman and V. Di Federico. Multifaceted nature of hydrologic scaling and its interpretation. *Reviews of Geophysics*, 41(3):1014, 2003.

S. P. Neuman and P. A. Witherspoon. Theory of flow in a confined two aquifer system. *Water Resources Research*, 5(4):803–816, 1969.

D. A. Nield and A. Bejan. *Convection in Porous Media*. Springer, third edition, 2006.

A. N. M. Obdam and E. J. M. Veling. Elliptical inhomogeneities in groundwater flow – an analytical description. *Journal of Hydrology*, 95:87–96, 1987.

C. Oleksy. A convergence acceleration method for Fourier series. *Computer Physics Communications*, 96(1):17–26, 1996.

S. A. Orszag. *Science and Computers*, volume 10 of *Advances in Mathematics Supplementary Studies*, chapter Fast Eigenfunction Transforms. Academic Press, 1986.

N. M. Özişik. *Heat Conduction*. Wiley-Interscience, second edition, 1993.

I. S. Papadopulos and H. H. Cooper. Drawdown in a well of large diameter. *Water Resources Research*, 3(1):241–244, 1967.

J. R. Philip. Steady infiltration from buried point sources and spherical cavities. *Water Resources Research*, 4(5):1039–1047, 1968.

J. R. Philip. Steady infiltration from circular cylindrical cavities. *Soil Science Society of America Journal*, 48:270–278, 1984.

J. R. Philip. Multidimensional steady infiltration to a water table. *Water Resources Research*, 25(1):109–116, 1989.

R. Piessens. A new numerical method for the inversion of the Laplace transform. *Journal of the Institute of Mathematics and its Applications*, 10:185–192, 1972.

A. I. Poularikas, editor. *The Transforms and Applications Handbook*. CRC, 1996.

W. H. Press, S. A. Teukolsky, W. T. Vetterling, and B. P. Flannery. *Numerical Recipes*. Cambridge, third edition, 2007.

A. P. Prudnikov, Y. A. Brychkov, and O. I. Marichev. *Integrals and Series*, volume 4 and 5: Direct and Inverse Laplace Transforms. Gordon & Breach, 1992.

A. J. Pullan. The quasilinear approximation for unsaturated porous media flow. *Water Resources Research*, 26(6):1219–1234, 1990.

Q.-H. Qin. *The Trefftz Finite and Boundary Element Method*. Computational Mechanics, 2000.

A. Quarteroni, R. Sacco, and F. Saleri. *Numerical Mathematics*. Springer, 2000.

T. C. Rasmussen, K. G. Haborak, and M. H. Young. Estimating aquifer hydraulic properties using sinusoidal pumping at the Savannah River site, South Carolina, USA. *Hydrogeology Journal*, 11(4):466–482, 2003.

W. J. Rawls, D. L. Brakensiek, W. J. Elliot, and J. M. Laflen. Prediction of furrow irrigation final infiltration rate. *Transactions of the American Society of Agricultural Engineers*, 33(5):1601–1604, 1990.

L. A. Richards. Capillary conduction of liquid through porous mediums. *Physics*, 1:318–333, 1931.

A. Ronveaux, editor. *Heun's Differential Equations*. Oxford, 1995.

M. I. Rorabaugh. Graphical and theoretical analysis of step-drawdown test of artesian well. *Proceedings American Society of Civil Engineers*, 79(362):1–23, 1953.

T. Sakurai. Numerical inversion for Laplace transforms of functions with discontinuities. *Advances in Applied Probability*, 36(2):616–642, 2004.

M. L. Salisbury. Control equation formulation for circular inhomogeneities in the analytic element method. Master of science in civil engineering, University of Minnesota, 1992.

R. A. Schapery. Approximate methods of transform inversion for viscoelastic stress analysis. In *US National Congress on Applied Mechanics*, volume four, pages 1075–1085, 1962.

R. Schinzinger and P. A. A. Laura. *Conformal Mapping: Methods and Applications*. Dover, 2003.

T. H. Skaggs, T. J. Trout, J. Šimunek, and P. J. Shouse. Comparison of HYDRUS-2D simulations of drip irrigation with experimental observations. *Journal of Irrigation and Drainage Engineering*, 130(4):304–310, 2004.

B. F. Smith, P. E. Bjorstad, and W. Gropp. *Domain Decomposition*. Cambridge, 1996.

S. W. Smith. *The Scientist and Engineer's Guide to Digital Signal Processing*. California Technical, second edition, 1999.

J. J. Stamnes and B. Spjelkavik. New method for computing eigenfunctions (Mathieu functions) for scattering by elliptical cylinders. *Pure and Applied Optics*, 4(3): 251–262, 1995.

H. Stehfest. Algorithm 368: Numerical inversion of Laplace transforms. *Communications of the ACM*, 13(1):47–49, 1970.

J. C.-E. Sten. Ellipsoidal harmonics and their applications in electrostatics. *Journal of Electrostatics*, 64(10):647–654, 2006.

Y. M. Sternberg. Flow to wells in the presence of radial discontinuities. *Ground Water*, 7(12):17–20, 1969.

O. D. L. Strack. Theory and applications of the analytic element method. *Reviews of Geophysics*, 41(2):1005–1021, 2003.

O. D. L. Strack. The development of new analytic elements for transient flow and multiaquifer flow. *Ground Water*, 44(1):91–98, 2006.

O. D. L. Strack. A single-potential solution for regional interface problems in coastal aquifers. *Water Resources Research*, 12(6):1165–1174, 1976.

O. D. L. Strack. *Groundwater Mechanics*. Prentice-Hall, 1989.

O. D. L. Strack. Principles of the analytic element method. *Journal of Hydrology*, 226:128–138, 1999.

O. D. L. Strack and H. M. Haitjema. Modeling double aquifer flow using a comprehensive potential and distributed singularities 1. solution for homogeneous permeability. *Water Resources Research*, 17(5):1535–1549, 1981a.

O. D. L. Strack and H. M. Haitjema. Modeling double aquifer flow using a comprehensive potential and distributed singularities 2. solution for inhomogeneous permeabilities. *Water Resources Research*, 17(5):1551–1560, 1981b.

O. D. L. Strack and I. Janković. A multi-quadric area-sink for analytic element modeling of groundwater flow. *Journal of Hydrology*, 226:299–196, 1999.

O. D. L. Strack, I. Janković, and R. Barnes. The superblock approach for the analytic element method. *Journal of Hydrology*, 226:179–187, 1999.

G. Strang. *Linear Algebra and its Applications*. Thomson Learning, third edition, 1988.

J. A. Stratton. *Electromagnetic Theory*. McGraw-Hill, 1941.

E. A. Sudicky and R. G. McLaren. The Laplace transform Galerkin technique for large-scale simulation of mass transport in discretely fractured porous formations. *Water Resources Research*, 28(2):499–514, 1992.

R. M. Suribhatla. *Development and Application of AEM for Estimation of Effective Hydraulic Conductivity of Anisotropic Porous Formations*. PhD thesis, University of Buffalo, 2007.

R. M. Suribhatla, M. Bakker, K. Bandilla, and I. Janković. Steady two-dimensional groundwater flow through many elliptical inhomogeneities. *Water Resources Research*, 40:W04202, 2004.

TACC. *GotoBLAS*. http://www.tacc.utexas.edu, 1.24 edition, 2008.

G. D. Tartakovsky and S. P. Neuman. Three-dimensional saturated-unsaturated flow with axial symmetry to a partially penetrating well in a compressible unconfined aquifer. *Water Resources Research*, 43(1):W01410, 2007.

C. V. Theis. The relation between lowering of the piezometric surface and the rate and duration of discharge of a well using ground-water storage. *Transactions, American Geophysical Union*, 16:519–524, 1935.

W. Thompson. Spheroidal wave functions. *Computing in Science & Engineering*, 1 (3):84–87, 1999.

C. R. Tiedman, P. A. Hsieh, and S. B. Christian. Characterization of a high-transmissivity zone by well test analysis: steady state case. *Water Resources Research*, 31(1):27–37, 1995.

A. Torchinsky. *Real-Variable Methods in Harmonic Analysis*. Dover, 2004.

C. J. Tranter. Heat conduction in the region bounded internally by an elliptical cylinder and an analogous problem in atmospheric diffusion. *Quarterly Journal of Mechanics and Applied Mathematics*, 4(4):461–465, 1951.

A. F. van Everdingen. The skin effect and its influence on the productive capacity of a well. *Petroleum Transactions, AIME*, 198:171–176, 1953.

A. F. van Everdingen and W. Hurst. The application of the Laplace transformation to flow problems in reservoirs. *Petroleum Transactions, AIME*, 186:305–324, 1949.

J. L. Vásquez. *The Porous Medium Equation: Mathematical Theory*. Oxford, 2007.

J. A. Vrugt, S. C. Dekker, and W. Bouten. Identification of rainfall interception model parameters from measurements of throughfall and forest canopy storage. *Water Resources Research*, 39(9), 2003a.

J. A. Vrugt, H. V. Gupta, W. Bouten, and S. Sorooshian. A shuffled complex evolution metropolis algorithm for optimization and uncertainty assessment of hydrologic models parameters. *Water Resources Research*, 39(8):1201, 2003b.

A. W. Warrick. *Soil Water Dynamics*. Oxford, 2003.

A. W. Warrick and J. H. Knight. Two-dimensional unsaturated flow through a circular inclusion. *Water Resources Research*, 38:38139, 2002.

A. W. Warrick and J. H. Knight. Unsaturated flow through a spherical inclusion. *Water Resources Research*, 40:W05101, 2004.

A. W. Warrick and N. Lazarovitch. Infiltration from a strip source. *Water Resources Research*, 43:W03420, 2007.

A. W. Warrick, N. Lazarovitch, A. Furman, and D. Zerihun. Explicit infiltration for furrows. *Journal of Irrigation and Drainage Engineering*, 133(4):307–313, 2007.

G. N. Watson. *A Treatise on the Theory of Bessel Functions*. Cambridge, second edition, 1944.

E. P. Weeks. Barometric fluctuations in wells tapping deep unconfined aquifers. *Water Resources Research*, 15(5):1167–1176, 1979.

W. T. Weeks. Numerical inversion of Laplace transforms using Laguerre functions. *Journal of the ACM*, 13(3):419–429, 1966.

J. A. C. Weideman. Algorithms for parameter selection in the Weeks method for inverting the Laplace transform. *SIAM Journal of Scientific Computing*, 21(1):111–128, 1999.

E. T. Whittaker. On the functions associated with the elliptic cylinder in harmonic analysis. In E. W. Hobson, editor, *Proceedings of the Fifth International Congress of Mathematicians*, volume 1, pages 366–371, 1912.

D. V. Widder. *The Laplace Transform*. Princeton, 1946.

J. H. Wilkinson. *The Algebraic Eigenvalue Problem*. Oxford, 1965.

I. Wolfram Research. *Mathematica*. Champaign, IL, 6.0 edition, 2007.

R. A. Wooding. Steady infiltration from a shallow circular pond. *Water Resources Research*, 4(6):1259–1273, 1968.

P. Wynn. Transformations to accelerate the convergence of Fourier series. Technical Report 673, Mathematics Research Center, US Army, 1966.

M. Ye, S. P. Neuman, A. Guadagnini, and D. M. Tartakovsky. Nonlocal and localized analyses of conditional mean transient flow in bounded, randomly heterogeneous porous media. *Water Resources Research*, 40(5), 2004.

W. J. Zaadnoordijk. *Analytic elements for transient groundwater flow*. PhD thesis, University of Minnesota, 1988.

W. J. Zaadnoordijk. Transition from transient Theis wells to steady Thiem wells. *Hydrological Sciences Journal*, 43(6):859–875, 1998.

W. J. Zaadnoordijk and O. D. L. Strack. Area sinks in the analytic element method for transient groundwater flow. *Water Resources Research*, 29(12):4121–4129, 1993.

V. A. Zlotnik and H. Zhan. Aquitard effect on drawdown in water table aquifers. *Water Resources Research*, 41(6):W06022, 2005.